# The use of the Proper Orthogonal Decomposition for the characterization of the dynamic response of structures due to wind loading.

by

Rafael Flores Vera

Thesis submitted to the
Faculty of Graduate and Postdoctoral Studies
under the supervision of
Dr. Hiroshi Tanaka and Dr. Guy L. Larose

in partial fulfillment of the requirements
for the degree of
Doctor in Philosophy in Civil Engineering

Ottawa-Carleton Institute for Civil Engineering
Faculty of Engineering
University of Ottawa

# ACKNOWLEDGEMENTS

To the National Council for Science and Technology of Mexico (CONACYT), for their financial support for my doctoral studies. From the beginning to the end of the scholarship term, this institution always provided a fast, efficient and reliable support. This thesis would not have been possible without them.

To my supervisors, Hiroshi Tanaka and Guy Larose, for their guidance and support. Our meetings always brought light to my questions as well as direction and motivation in this long journey. Their complementary financial support provided peace in mind, which left the concept of money out of my list of concerns.

To the University of Ottawa, for providing an adequate environment. The professors, the staff members, the students and the facilities offered a rounded and satisfactory experience.

To the Aerodynamics Laboratory of the National Research Council, for providing me access to their facilities, where I carried out part of my research.

To all the people that I have interacted with in this period of my life. It is impossible to list all these people or to try to weight their individual influence in my life but I want to acknowledge the importance of all of them.

# ABSTRACT

This thesis presents a study of the wind load forces and their influence on the response of structures. The study is based on the capacity of the Proper Orthogonal Decomposition method (POD) to identify and extract organized patterns that are hidden or embedded inside a complex field. Technically this complex field is defined as a multi-variate random process, which in wind engineering is represented by unsteady pressure signals recorded on multiple points of the surface of a structure. The POD method thus transforms the multi-variate random pressure field into a sequence of load shapes that are uncorrelated with each other. The effect of each uncorrelated load shape on the structural response is relatively easy to evaluate and the individual contributions can be added linearly afterwards. Additionally, since each uncorrelated load shape is associated with a percentage of the total energy involved in the loading process, it is possible to neglect those load shapes with low energy content. Furthermore, the load shapes obtained with the POD often reveal physical flow structures, like vortex shedding, oscillations of shear layers, etc. This later property can be used in conjunction with classical results in fluid mechanics to theorize about the physical nature of different flow mechanics and their interactions. The POD method is well suited to be used in conjunction with the classical modal analysis, not only to calculate the structural response for a given pressure field but to observe the details of the wind-structure interaction. A detailed and complete application is presented here but the methodology is very general since it can be applied to any recorded pressure field and for any type of structure.

# CONTENTS

# LIST OF SYMBOLS AND ABBREVIATIONS

| | |
|---|---|
| A | tributary area for a pressure tap; area of the enclosure opening |
| $[\mathbf{A}]$ | matrix of oriented tributary areas |
| $B$ | bias error, bias limit |
| $B_{jk}$ | j,k-th cross-modal participation factor |
| $[\mathbf{B}]$ | cross-modal participation matrix |
| c | speed of sound |
| $C_p$ | pressure coefficient |
| Cpmin | lowest value of the mean pressure coefficients (Chapter 4) |
| $\hat{C}_p$ | zero-mean peak value of pressure coefficient |
| $\overline{C}_p$ | mean value of pressure coefficient in the definition of peak value |
| $Cov(p_i, p_j)$ | covariance of pressures $p_i$ and $p_j$ |
| $\mathbf{Cov_P}$ | covariance matrix of pressure field p(t) |
| $[\mathbf{c}]$ | modal damping matrix |
| $[\mathbf{C}]$ | viscous damping matrix |
| D | external enclosure diameter |
| $D_i$ | internal enclosure diameter |
| DMT | double modal transformation |
| $f$ | frequency |
| $f_H$ | Helmholtz frequency |
| $F_j(t)$ | external force applied along the j-th degree of freedom |
| $F_{x,j}(t)$ | external force applied along the j-th modal oscillator |

| | |
|---|---|
| $\{\mathbf{F}(t)\}$ | external load vector |
| $\Im\{y(t)\}$ | Fourier transform of $y(t)$ |
| H | vertical position of the square prism |
| $H_j(f)$ | transfer function of the j-th modal oscillator |
| $[\mathbf{I}]$ | Identity matrix |
| k | mean roughness height of enclosure; stiffness coefficients |
| $[\mathbf{K}]$ | structural stiff matrix |
| $\ell_e$ | length of air column oscillating at the cavity opening |
| L | characteristic length |
| $L_e$ | effective enclosure opening length |
| m | shear layer mode (Chapter 4); number of degrees of freedom of a structure |
| $m_j$ | mass of the j-th modal oscillator |
| M | Mach number |
| $[\mathbf{M}]$ | mass matrix |
| n | number of POD modes (Chapter 5) |
| N | integer number |
| NRC | National Research Council of Canada |
| p(t) | time history of pressure |
| $p_0$ | reference pressure for the calculation of pressure coefficients |
| $\mathbf{p}(t)$ | scalar pressure field |
| $p_x(t)$ | pressure record in modal space, image of p(t) in modal space |
| $P$ | precision error, precision limit |
| POD | proper orthogonal decomposition |

| | |
|---|---|
| PSD | power spectral density function |
| $q$ | dynamic pressure |
| Re | Reynolds number |
| RMS | root-mean square value of pressure coefficients |
| St | Strouhal number |
| $S_H$ | Helmholtz number |
| $S_{Fx,j}(f)$ | one-sided spectral density function of $F_{x,j}(t)$ |
| $S_{x,j}(f)$ | response spectrum of the j-th modal oscillator |
| $\{\mathbf{S}_x(f)\}$ | response spectrum vector for modal oscillators |
| $t$ | time |
| $U$ | wind speed; uncertainty |
| $x$ | measure value of variable X |
| $x_{true}$ | true value for variable X |
| $x_j(t)$, $\dot{x}_j(t)$, $\ddot{x}_j(t)$ | displacement, velocity and acceleration of the j-th modal oscillator |
| $\{\mathbf{x}(t)\}$, $\{\dot{\mathbf{x}}(t)\}$, $\{\ddot{\mathbf{x}}(t)\}$ | modal displacement, velocity and acceleration vectors, respectively |
| X | rectangular coordinate axis; general variable |
| $\{\mathbf{y}(t)\}$, $\{\dot{\mathbf{y}}(t)\}$, $\{\ddot{\mathbf{y}}(t)\}$ | displacement, velocity and acceleration vectors, respectively |
| Y | rectangular coordinate axis |
| $Y(\omega)$ | Fourier transform of *y(t)* |
| Z | rectangular coordinate axis |
| X'Y'Z' | rectangular local coordinate system for enclosure orientation |
| $\theta$ | azimuth orientation of enclosure (Chapter 4) |

|  |  |
|---|---|
| $\lambda$ | POD eigenvalue |
| $\Lambda$ | internal volume of the enclosure |
| $[\mathbf{\Lambda}]$ | eigenvalue matrix for POD modes |
| $\mu_x$ | mean value of a series of measurements of variable X |
| $\nu$ | kinematic viscosity or air |
| $\xi$ | structural damping ratio |
| $\rho$ | air density |
| $\sigma^2$ | variance |
| $\sigma_{x,j}^2$ | variance of displacement for the j-th modal oscillator |
| $\sigma_x$ | standard deviation for a series of measurements of variable X |
| $\phi$ | POD eigenvector; zenith rotation of enclosure (Chapter 4) |
| $[\mathbf{\Phi}]$ | eigenvector matrix for POD modes |
| $\psi$ | structural mode |
| $[\mathbf{\Psi}]$ | matrix of structural modes |
| $\omega$ | structural frequency |
| $[\mathbf{\Omega}]$ | matrix of structural frequencies |

# LIST OF FIGURES

# Chapter 1 INTRODUCTION

## 1.1 The complexities of the wind loads

The heavy and stiff structures built more than a century ago were not significantly affected by the forces of wind. Nevertheless, things started to change with the appearance of steel as a common construction material since it allowed the creation of lighter and more flexible structures. The excessive deformations and the dramatic failures cause by wind on this type of structures made clear that the wind forces needed to be studied more deeply. Certain procedures were carried out to account for the effects of the wind on civil engineering structures but it was the boom in aeronautics in the 20th century that contributed with many important ideas in the design of civil engineering structures against the adverse effects of the wind forces. Eventually, the particularities of the civil engineering structures gave origin to the field of wind engineering.

Wind engineers, thus, are concerned with the mechanical interaction between the wind and the structures built on the Earth's surface. This interaction can be used for beneficial purposes, as in the case of the power generation through wind turbines, but it can also create undesirable effects, as in the case of significant vibrations and large deformations in a bridge.

The pressure field created by wind past a building is usually very complex with abrupt changes at all times. It is impossible to predict exactly the shape and magnitude of the pressure field at any given moment and hence the challenge of modelling the wind-induced forces. To illustrate these complexities, let us imagine a building with numerous pressure gauges on its surface as indicated in Figure 1.1. Each gauge records the time history of the pressure at a specific location. The time histories (and their spectral density functions) recorded by gauges *j* and *k* are included in the figure. This grid of sensors helps us to 'take pictures' of the pressure field at different instants, like those shown in Figure 1.2. As it can be seen in the figure, the surface pressure can change significantly from one instant to another in a random fashion. Hence, the initial question would be to determine which of these surface pressures the structure should be designed against. Intuition may suggest that the structure can be designed against the mean pressure distribution, like the one shown in Figure 1.3. This is a good suggestion and in fact, many structures have been designed following this criterion.

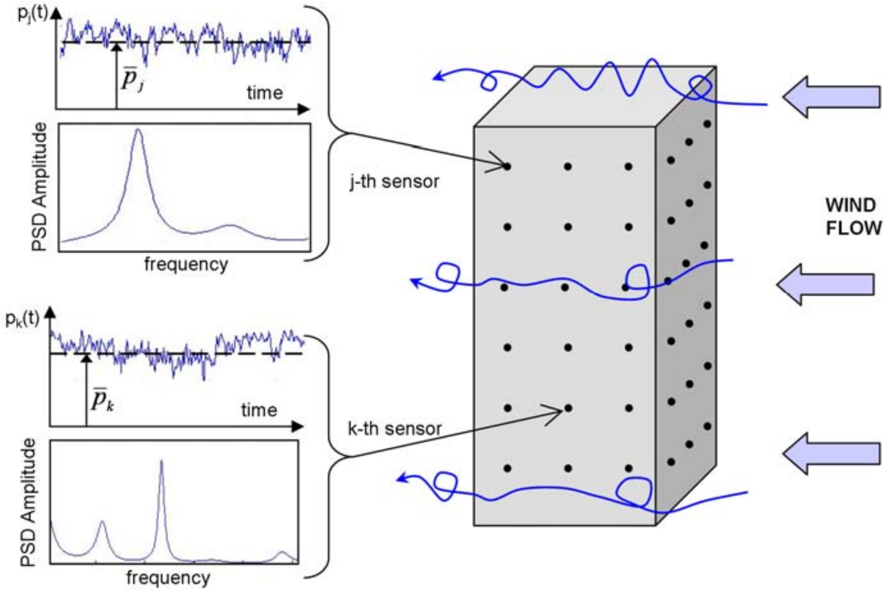

Figure 1.1 The description of the unsteady pressure field around a structure is provided by an array of pressure sensors.

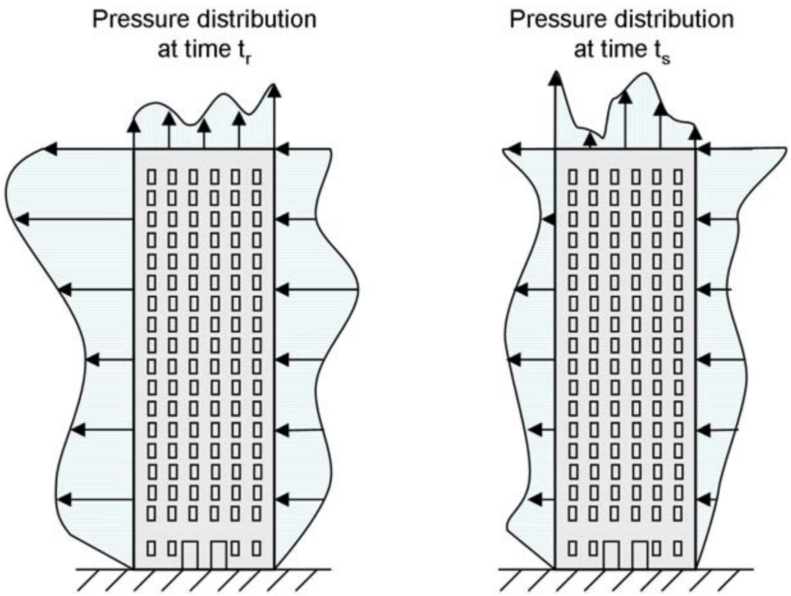

Figure 1.2 Pressure distribution on the facade of a building at two times; $t_r$ and $t_s$.

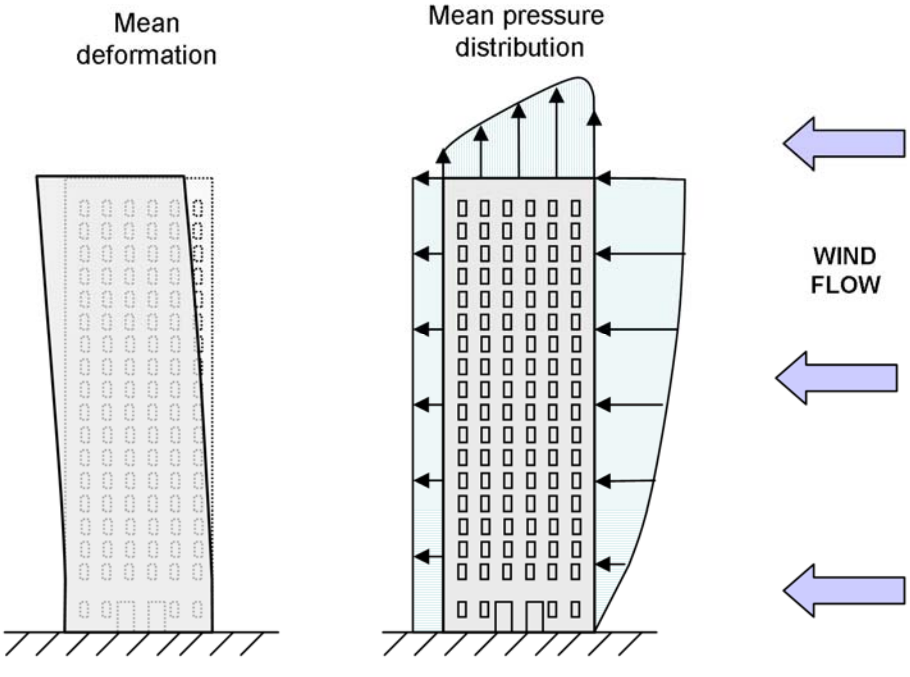

Figure 1.3 The effects of the mean pressure distribution are easily obtained from a static analysis.

Of course, the reader may wonder what happens with those instants where the pressure distribution exceeds the mean pressure distribution. Should the maximum pressure distribution be used for design? Would such a procedure be overly conservative? A more thorough reflection on the problem might suggest that not only the magnitude of the pressure field influence the structural response but also the frequency content and the shape of the pressure field are important variables when evaluating the effects of the wind load on buildings. Although in real life these two variables are combined, mathematically they can be modelled separately. The frequency content of the load refers to the time distribution of the load, while the shape of the load refers to the spatial distribution of the load. Treating these concepts separately not only facilitates the mathematical modelling but it also provides a better understanding of the physical mechanism in the wind-load interaction.

The best way to focus on the first concept –the frequency content of the load, is by studying a mechanical oscillator of one degree-of-freedom exposed to an arbitrary load. For this case, the mass and the external load are assumed to be concentrated in a single point thus eliminating the concept of the spatial distribution of the load. This type of systems has been well-studied for over a century and it is now considered as a fundamental topic in the curricula of courses like structural dynamics, mechanic vibrations, random vibrations, etc. With the use of different factors and plots, most building codes have incorporated an approximate approach to deal with the effect of the frequency content of the loads in the design of structures exposed to earthquake and wind loads.

The effects of the wind load shape on the response of structures, however, are not fully understood and therefore this topic is still open to research. This situation is considerably more complex because the ‘physical distribution of the load’ implies that the wind load is distributed on the surface of a structure that has its mass and stiffness distributed in space and therefore the structure should be modelled as a multi-degree-of-freedom-system. In other words, both the wind load and the structure should be treated as multidimensional objects.

These complexities were visualized by the author during his master’s studies on the structural response of hanging roofs due to wind action. At that time, priority was given to understand the non-linear behaviour of hanging roofs due to large displacements while the dynamic effects of the wind were taken into account by following the approximate method described in the building code of Mexico City. That experience seeded further curiosity on the characterization of wind loads on structures. A few years later, while choosing a research topic for his doctoral studies, Dr. Larose and Dr. Tanaka suggested to study the Proper Orthogonal Decomposition (POD) as a tool for achieving a better understanding of the behaviour of the wind loads.

The results of such a research are presented in this thesis. The POD method allows the decomposition of a multidimensional pressure field into a series of uncorrelated single-dimensional pressure fields. The transformation of a multidimensional pressure field into a set of uncorrelated single-dimensional pressure fields is not the only benefit of using the POD; this method also provides a possible explanation of the physical mechanisms involved in the wind-structure interaction. Furthermore, the mathematical formulation of the method is well suited to be used in combination with the classical modal analysis or the spectral analysis, thus allowing to model simultaneously the load behaviour and the structural response. The only requirement for the POD method to work is the experimental measurement of the unsteady pressure field created by wind passing a building.

## 1.2 Objectives

Two general objectives are pursued in this research. The first objective is to investigate the effectiveness of the proper orthogonal decomposition method as a tool to provide an understanding and a characterization of the wind loads on a structure. The second objective is to explore an extension of the POD method that provides an evaluation and an understanding of the effects of the wind loads on the response of the structures. This objective is to be achieved with the joint application of the POD method and the classical modal analysis.

The particular objectives are the study and description of the pressure field on specific structures: the surface of a hanging roof, the external surface of a spherical enclosure and the surface of a mirror located inside the spherical enclosure.

### 1.3 Organization of the thesis

After this introductory chapter, Chapter 2 includes the literature review, a brief introduction of the POD method and some definitions from fluid mechanics. Chapters 3 and 4 make use of the POD method for an extensive study of the pressure field around two structures: a hanging roof model and the mirror of a telescope enclosed in an open spherical shell. Chapter 5 presents the mathematical formulation for calculating the structural response by combining the POD method and the classical modal analysis. The mathematical formulations are accompanied with a numerical example to determine the structural response of a hanging roof exposed to turbulent flow. The final chapter, Chapter 6, summarizes the most significant conclusions of the research and it provides some recommendations for further studies related with the use of the POD. Finally, two appendices are included: Appendix A presents the formal definition of the proper orthogonal decomposition and Appendix B contains the measurement uncertainties related to the wind tunnel tests for the telescope model.

# Chapter 2 BACKGROUND STUDY

## *2.1 Literature Review*

Given the vast number of research papers on wind engineering, it is impossible to provide an extensive review in a few pages. Rather, this section is intended to present broad aspects of the development of the field as well as the gradual appearance of the Proper Orthogonal Decomposition in wind engineering. The review spans from the 1950's up to the present.

### 2.1.1 General studies for wind engineering.

The design of structures against the adverse effects of wind action has been a very challenging task for engineers because it requires the knowledge of diverse disciplines: fluid mechanics of turbulent flows, meteorology, structural dynamics, aerodynamics, etc. The complications increase because there is still much to learn and understand from some of the areas previously mentioned, such as turbulence and meteorology.

Wind-induced forces have been recognized and taken into account for many years by making some allowance in structural design. Despite that the adverse effects of wind speed fluctuations were known, for a long time the wind forces were modeled as static loads. New ideas and investigations in the 1950's questioned the traditional wind design practice. It was

Davenport (1961, 1964, 1967) who united many of those new ideas under a solid statistical approach. He introduced the idea of estimating structural peak response values (accelerations, stresses, displacements, etc.) not only from the mean wind speed but also from the wind velocity spectra, the mechanical and aerodynamic properties of the structures. His research included concepts such as roughness of terrain, variation of mean wind speed with height, and maps of extreme wind speed as function of return periods. These concepts were largely accepted and incorporated into design codes.

Based on new experimental and theoretical advances, more research appeared during the following years. Take the analysis of along-wind response of structures, for example. Simiu (1980) proposed a revised procedure for estimating along-wind response on tall buildings. Solari (1982, 1983a, 1983b, 1983c) developed a research program aimed to study analytically the dynamic along-wind response of structures. Solari (1989) presented another approach to estimate the dynamic along-wind response based on the response spectrum technique, similarly to the way it is used for earthquake engineering. The buffeting problem has been studied by numerous researchers. For example, Solari (1993a, 1993b) proposed a generalized solution for gust buffeting. He introduced a new expression of the power spectrum of the along-wind turbulence. Hangan and Vickery (1998, 1999) performed a semi-empirical analysis of buffeting loading based on extensive wind tunnel tests for various arrangements of 2D bluff bodies. They modelled both lift and drag spectra based on a linear wind-load dependence. Zhou et al (2000) and Zhou and Kareem (2001) proposed an alternative method to the traditional Gust Loading Factor approach for estimating buffeting loads. The new approach allows taking into account the cases with zero mean response. The suggested method is based on the base moment rather than the displacement. Piccardo and Solari (2000) proposed a closed-form solution for along-wind, crosswind and torsional vibrations of slender structures excited by the action of wind. Zhou et al (2002) made a comparative study between different international codes in regard to the along-wind response of tall buildings.

Low-rise buildings are usually rigid enough for disregarding dynamic effects caused by wind—some exceptions are long-span roofs (Fu et al 2008). Therefore, most of the attention is given to the pressure distribution on the roofs (Stathopoulos et al 1999, Uematsu and Isyumov 1999, Banks et al 2000, Baskaran and Savage 2003, Uematsu and Stathopoulos 2003, He et al 2007). Stathopoulos (1984) presented a review for the characterization of wind loads on low-rise buildings. His survey revealed that much of the information used by building codes was based on experiments performed in smooth flow, which is a misleading condition for real structures. Consequently, he emphasized the urgent need to update the codes with results obtained from full-scale measurements or from wind tunnel tests that account the effects of atmospheric turbulence. Two decades later, he wrote another review on low-rise buildings (Stathopoulos 2003) in which he discussed the most recent experiment studies that had direct impact on North American codes. In addition, he discussed the advancements of computational wind engineering and the innovative field of neural networks for the evaluation of wind loads on buildings.

Saathoff and Melbourne (1997) studied the relation between the free-stream turbulence and the large pressure fluctuations on the leading edge of bluff bodies. The free-stream turbulence is not only influenced by the topographical conditions but also by the presence of other buildings (Khanduri et al 1998).

Numerous experiments have been performed in relation to drag force reduction for common structural shapes. Lajos (1986) used add-on devices in the windward face to reduce the drag on a rectangular block. Lesage and Gartshore (1987), Igarashi (1997), Tsutsui and

Igarashi (2002), Igarashi and Terachi (2002), used a small rod located upstream to reduce the drag on flat plates, square prisms and circular cylinders. Prasad and Williamson (1997) used a flat plate located upstream of a circular cylinder in order to reduce the drag of the latter. Nakamura and Igarashi (2008) attached rings along a circular cylinder to reduce the drag forces.

Zhou and Kijewski (2003) presented a database of aerodynamic loads obtained from 27 models of tall buildings in an ultrasensitive force balance. The database is accessible via internet to the wind engineering research community. It includes analysis procedures along with a detailed example for anyone interested in the wind design of buildings with similar characteristics. The community members are invited to expand the database and also to consider the possible inclusion of the analysis procedures in codes.

### 2.1.2 Experimental wind engineering.

Given the theoretical complications of turbulence, experiments have been, are and will be key tools for developing and validating theories and methods related to fluid mechanics. Most wind engineering research is based on experimental data, which can be obtained either from wind tunnel tests or from full-scale measurements.

Wind tunnels give a valuable opportunity to test models in different configuration in order to estimate an approximate response of full-scale structures. An important observation to bring closer wind tunnel results with full-scale measurements is the consideration of the model law (Jensen 1958). This law emphasizes the need to perform wind tunnel tests with the simulation of the atmospheric turbulence. A description of the parameters involved in characterizing the atmospheric turbulence can be found, for example, in the works by Eaton et al (1974, 1975) and Lawson et al (1985). Also the textbooks by Simiu and Scanlan (1996) and Holmes (2007) are a good source for understanding the mechanics of the atmospheric turbulence. Additionally, some guidelines for wind tunnel tests can be found in section 6.6 of the standard ASCE-7-05.

While wind tunnel tests are valuable for predicting the behavior of structures, the ultimate tests are the full-scale measurements. Davenport (1975) expressed that despite their importance, the number of full-scale measurements was small and needed to be increased and shared among the research community.

It is also important to recognize the significant advances in instrumentation and measurement techniques, which are closely related to the development of electronics. It is out of the scope of this review to cover those areas. The textbook by Tavoularis (2005) presents some measurement techniques in fluid mechanics and it contains a large list of references for more details.

### 2.1.3 Numerical studies in wind engineering.

As computer resources increase, more people from different fields see the potential of numerical analysis as an alternate tool to give solutions for their areas. Wind engineering is not an exception.

The determination of an appropriate turbulence model is the main challenge in numerical simulations of wind past obstacles. Murakami et al (1992) made a numerical study of velocity and pressure fields around bluff bodies using three turbulence models ($k$-$\varepsilon$ Eddy Viscosity Model, Algebraic Stress Model and Large Eddy Simulation). His research indicates that the Large Eddy Simulation model provides results in close agreement to wind tunnel tests. Song and Park (2008) used the Partially Averaged Navier-Stokes (PANS) model to simulate the flow past a square prism. Sun et al (2009) applied the $\kappa$-$\omega$ turbulence model for wind-induced vibration in bridge deck sections. Paterson and Apelt (1990), Delaunay et al (1995) and Lim et al (2009) investigated the ability to predict wind forces on buildings by using numerical simulation on a cube model. Yu and Kareem (1997) performed both 2D and 3D numerical simulations of flow around a rectangular prism. They estimated mean pressure, RMS coefficients, lift and drag forces and the correlation coefficients at different locations. Most of the previous works were satisfactorily compared with parallel experimental studies.

More extensive reviews are available in the literature. Stathopoulos (1997) and Murakami (1997) pointed out the achievements and challenges of computational wind engineering. Tamura (2008) presented a more recent review of the practical use of the Large Eddie Simulation technique for different wind engineering problems.

Despite the growing development of CFD, there is still a need to validate the numerical results with experimental data.

### 2.1.4 The origin of the Proper Orthogonal Decomposition, its evolution and its use in wind engineering.

#### The origin of the POD and its use in other fields

The Proper Orthogonal Decomposition (POD) technique refers to a mathematical decomposition based on eigenvectors. Here the word ‘proper’ is the English translation for the German word ‘eigen’ and the word ‘orthogonal’ refers to the fact that eigenvectors are orthogonal to each other. In the particular case of statistical analysis, two variables are said to be orthogonal if they are uncorrelated. Thus, the eigenvectors of a covariance matrix provide a mathematical base that allows the transformation of correlated variables into uncorrelated variables. The POD is intended to reveal hidden regular patterns from irregular phenomena by using a recorded set of simultaneous time histories of the phenomena.

This procedure was first proposed by Kosambi (1943). It was later re-discovered independently by Loeve in 1945 and Karhunen in 1946 and therefore the technique is also known as the Karhunen-Loeve expansion.

Lorenz (1959) applied the POD in meteorology. Lumley (1967) introduced it in the field of turbulence, which enjoys a rich amount of research related to the use of the POD. Aubry et al (1988) used the POD method to model the wall region in a boundary layer region by expanding the instantaneous velocity field in empirical eigenfunctions. Moin and Moser (1989) applied the POD to extract coherent eddies in a turbulent flow channel. Glezer et al (1989) extended the classic POD methodology in order to deal with flows that do not meet statistical stationarity. Arndt et al (1997) used the POD for pressure measurements in the outer edge of a jet mixing layer in order to deduct the stream-wise structure of the flow. Del Ville et al (1999) recognized that the lower POD modes in a plane turbulent mixing layer resembles well known stream-wise and span-wise flow structures. An extensive review of the POD in turbulent flows as well as a sound description of its mathematical background is given by Berkooz et al (1993). In addition, the textbook of Holmes et al (1996) contains a whole chapter about the POD.

The POD technique has been also used for pattern recognition (Ahmed and Rao 1975), image processing (Devijver and Kittler 1982), non-linear mechanics systems (Fenny and Kappagantu 1998, Alaggio and Rega 2000) and earthquake engineering (Carassale et al 2000). Chatterjee (2000) presented a tutorial for the computational implementation of the POD. The use of the POD for studying the aerodynamics of an oscillating wing was discussed by Tang et al (2001). Pettit and Beran (2001) used the POD for the numerical simulation of a fluid in the transonic regime. Rathinam and Petzold (2003) investigated the properties of the POD as a tool for data compression and model reduction of non-linear systems.

## Dawn of the POD in wind engineering

Since long time ago, it was clear for structural engineers that the fluctuations of the wind speed greatly affected the behaviour of certain structures exposed to wind forces. They also knew that such fluctuations could be characterized with parameters like the variance or the co-variance. Therefore, it was logical to develop methods for analyzing the effects of the wind on structures that made use of the variance or co-variance. The following paragraphs discuss the evolution of such methods until they converged with the POD technique.

Armitt (1968) was the first applying eigenvector analysis of pressure measurements in a full-scale structure. Although this work was not published in the open literature, the idea was taken up since then by several authors in the field of wind engineering. Stathopoulos (1981) used Legendre functions to model accurately the distribution of mean pressure coefficients and the respective RMS for the particular case of flat roofs. Holmes and Best (1981) used the covariance integration method for the determination of the fluctuating and the peak values of structural effects due to wind loads on low-rise buildings. Their aerodynamic data were obtained from wind tunnel tests on a single-storey house model. The covariance of the pressure coefficients and the static structural influence coefficients were combined in order to obtain the RMS value of a structural effect. The restriction of the method is that it neglects any resonant dynamic effects, an assumption that is normally valid for low-rise buildings. Later, Best and Holmes (1983) extended their work published two years earlier by using eigenvalues obtained from the covariance matrix. This approach resembles the POD but there were some aspects not taken into account before calculating the covariance matrix: the mean value of pressure signals was not subtracted, there was no emphasis in the zero time lag condition and there was not information about signal correction due to tubing effects. Nevertheless, they pointed out the importance of the eigenvalues and eigenvectors as a significant insight in the wind load mechanisms. Later, Holmes (1990) calculated the eigenvectors of the covariance matrix obtained from a set of pressure histories. He oberserved that the eigenvectors are a convenient way to reveal the mixed structures of a turbulent flow. Kasperski and Niemman (1992) introduced the LRC (Load-response-correlation) method. This method goes one step further by considering the correlation of the fluctuating pressures over the whole structure. Additional refinements of the method converged with the POD technique for studying wind-induced unsteady pressure fields. Holmes (1992) extended Kasperski's work. He combined linearly the peak-load distributions of a few eigenvector modes in order to obtain the overall peak-load distribution.

### The use of the POD in wind engineering

The POD was formally used by Bienkiewicz et al (1993), who aimed to decompose the unsteady pressure field on a flat roof. Bienkiewicz et al (1995), Jeong and Bienkiewicz (1997) and Tamura et al (1997) worked also on a flat roof model but with a larger number of pressure taps. The fine grid allowed them to describe more accurately the POD modes. The results of these studies should be analyzed with caution since the mean pressure was not removed during the POD analysis, which affects the shape of the POD mode, the energy distribution per mode and the accuracy of the mean pressure reconstruction after truncation of higher modes.

Davenport (1995) presented some reflections in an attempt to simplify and generalize the way we deal with wind loads. He pointed out three key functions that determine the magnitude of structural responses: the influence lines, the structural mode shapes and the pressure distributions. He made use of the POD for modeling the pressure distribution.

Bienkiewicz (1996) discussed some of the new technological, numerical and theoretical tools available in wind engineering. Among the novel analysis methods, he outlined the usefulness of the POD.

Holmes et al (1997) applied the POD for a low-rise building model, pointing out that the mathematical requirements of orthogonality play a dominant role in determining the shape of every mode, which may not necessarily represent real flow structures. Similar conclusions were reached by Baker (1999), who commented that probably the more energetic modes represent actual flow structures while the less energetic modes only adjust to the mathematical requirements of the method. In fact, it is possible that all POD modes are a mix of physical and mathematical structures.

The works by Solari and Carassale (2000) and Carassale et al (2001) showed the conceptual aspects of double modal transformations, i.e., the simultaneous use of structural modal analysis and the POD for continuous and discrete systems. For the cases when the structural and loading systems can be represented in closed form, the application of the double modal transformations is quite effective (Carassale and Solari 2002). Nevertheless, for discrete systems its implementation requires a considerable amount of computation. Tubino and Solari (2007) also made use of double modal transformations to study gust buffeting in long span bridges.

Crémona et al (2002) and Amandolèse and Crémona (2005) analyzed the aeroelastic behaviour of three bridge deck-like sections. They combined a numerical approach with experimental measurements, concluding that the POD is a convenient tool to highlight the relationship between the body shapes and motion characteristics with the aeroelastic pressure response and the resulting flutter derivatives. Similarly, Ricciardeli et al (2002b) used the POD to analyze wind loads on bridge deck sections. Once again they remarked that despite no general rule can be derived from the POD analysis, some POD modes can be associated to flow patterns.

Holmes (2002) wrote a paper dedicated to simplify the design of wind loads through the use of effective static load distribution. He used the POD to decompose the background loading distribution. He established that the contribution of each POD mode to the total effective static load distribution is dependent on the similarity with the influence line.

Han and Fenny (2002, 2003) applied the POD for structural vibration analysis by using experimental data obtained in a simply-supported beam.

Rocha et al (2000) compared the POD with the Monte Carlo simulation method for characterizing wind-induced pressure. They concluded that the POD is convenient for modeling global effects but not for the local effects, which are highly dependent on the number of measurement points.

Jeong et al (2000) compared how the distribution of pressure taps affect the results obtained by the POD. In a similar way, Cohen et al (2004) used the POD to define heuristically the most convenient location of sensors for the feedback control suppression of the wake instability behind a circular cylinder.

Xu (2004) and Chen and Letchford (2005) successfully used the POD to detect flow structures in studies related with high intensity winds, such as tornados and downbursts.

Chen and Kareem (2005) used the POD as the base for modeling, analysis and simulation of dynamic wind effects on structures.

Different than the double modal transformations mentioned above, the double POD procedure (Tubino and Solari 2005) is the joint application of the single-point and the multipoint POD technique.

The list of papers where the POD has been used for wind engineering applications is vast and keeps growing. The present work shows the application of the POD for two particular cases but the author targets in the final chapter, by linking all the information available, to propose a rational wind load design based on the results of the POD analysis.

## 2.2 Proper Orthogonal Decomposition

The POD techquique is intended to reveal hidden regular patterns from irregular phenomena by using a recorded set of simultaneous time histories of the phenomena.

The POD has been rediscovered several times since the 1940's and it has been used in a wide variety of disciplines: random variables, process identification and control in chemical engineering, signal analysis, image processing, turbulence, etc. Other names used for the POD are Karhunen-Loève decomposition and principal component analysis (PCA). For wind engineering applications, the POD is used to decompose a turbulent pressure field into several 'regular' pressure fields.

The POD has a solid mathematical theory behind, which gives confidence for its use. Although the mathematical formulation may not be easy to follow in a first reading, it is worth mentioning that the numerical implementation of the POD is not complicated and the physical interpretation of the results is straightforward. A detailed mathematical description is given by Berkooz et al (1993) and Holmes et al (1996). A simplified version addressed to its numerical implementation for wind engineering is given below.

Although the POD method does not impose any conditions on the data to be analyzed, the interpretation of the results and the manipulation of data become easier if we consider some assumptions that are normally valid for wind engineering applications. Therefore, it is a common practice to apply the POD method to an n-variate pressure field that is assumed to be a Gaussian stationary random process with zero mean. It is convenient to write a few lines about these assumptions.

It is said that a pressure field is an n-variate random process because it is defined through the measurement of pressure histories by N pressure taps. Thus the pressure field is mathematically represented by the vector $\mathbf{p}(t) = \{p_1(t), p_2(t), \cdots, p_n(t)\}^T$. In general, the pressure signals have mean values different from zero but it is a convenient practice to subtract them and use them for static analysis, while the fluctuating part is treated separately for dynamic analysis.

A random process is called strictly stationary if its probability distribution does not evolve with time. A weakly stationary process occurs when only the mean and the variance of a random variable do not appear to change during time intervals of interest for engineering applications. This more relaxed definition of stationarity is satisfactory for most wind engineering problems and it has been widely used since the 1960's, as can be seen in the work by Davenport (1961).

The assumption that the pressure signals have a Gaussian probability distribution is not always true, especially for pressure taps located in regions where flow separation occurs. The probability distribution curves of the pressure histories in these regions usually show slanted profiles, like those of extreme value distributions. Nevertheless, these discrepancies are small compared with the benefits of using the simplifications related to Gaussian distributions.

Before applying the POD method, the pressure signals must be corrected for tubing dynamic distortion and zero time lag condition.

The POD method can be based either on the covariance matrix or on the power spectral density matrix (Solari and Carassale 2000, Carassale et al 2001, Cosentino and Benedetti

2005). The use of the covariance matrix is widely preferred and all results in this thesis are based on it. The covariance matrix of **p**(t) is defined as:

$$\mathbf{Cov_P} = \begin{bmatrix} Cov(p_1, p_1) & Cov(p_1, p_2) & \cdots & Cov(p_1, p_n) \\ Cov(p_2, p_1) & Cov(p_2, p_2) & \cdots & Cov(p_2, p_n) \\ \vdots & \vdots & \ddots & \vdots \\ Cov(p_n, p_1) & Cov(p_n, p_2) & \cdots & Cov(p_n, p_n) \end{bmatrix}$$

Since each pressure history consist of *k* samples obtained simultaneously, the covariance elements are $Cov(p_i, p_j) = \frac{1}{k}\sum_{r=1}^{k} p_i(t_r)p_j(t_r)$. Notice that the covariance must be calculated after the mean pressure has been removed.

The eigenvalue problem can be expressed as $(\mathbf{Cov_P} - \lambda_i\mathbf{I})\boldsymbol{\varphi}_i = \mathbf{0}$, where $\lambda_i$ and $\varphi_i$ are the *i*-th eigenvalue and eigenvector, respectively. The collection of all these values, for $i = 1, \cdots, n$, in matrix form is:

$$[\Lambda] = \begin{bmatrix} \lambda_1 & & 0 \\ & \ddots & \\ 0 & & \lambda_n \end{bmatrix}, \qquad [\Phi] = [\varphi_1 \quad \cdots \quad \varphi_n]$$

The eigenvector set $[\Phi]$ forms an orthogonal basis that defines a vector space called the modal space. This means that $[\Phi]$ can be used to transform the original pressure field p(t) into another pressure field $p_x(t)$. The new pressure field in the modal space has the convenient property that is uncorrelated; i.e., $Cov(p_{xi}, p_{xj}) = 0$ for $i \neq j$. In fact, the only non-zero values are the diagonal values of $[\Lambda]$. Each eigenvector $\varphi_i$ defines a mode shape (wind load pattern) which is associated with certain amount of ‘energy’ $\lambda_i$.

The POD has some attractive features for its application in wind engineering. First of all, an n-variate correlated pressure field can be decomposed into *n* uncorrelated signals, where every signal is associated with a POD mode ( $\varphi_i$ ) and some of these modes strongly suggest real phenomena, such as fluctuating lift and drag, or acoustic wave resonance in cavities. Another important advantage of the POD method arises because the load pattern of every POD mode can be applied independently to a structure and, if the structure is a linear system, the effects of every POD mode on the structure can be added in a linear fashion. Finally, since every POD mode is associated with an amount of kinetic energy, it is advantageous to disregard those modes with low energy content, thus simplifying the structural analysis due to wind forces.

The author points out that there is a degree of controversy about the physical meaning of the mode shapes. Based on the considerations of orthogonality and non-correlation, Baker (1999) suggested that the most energetic modes would represent to some extent specific flow mechanisms but any particular mode might also have some degree of influence from other mechanisms. He also reasons that the least energetic modes (higher modes) do not necessarily represent real flow mechanisms but they may actually represent the interaction between different mechanisms. Since the least energetic modes account for small pressure fluctuations, they are susceptible to measurement accuracy. The higher modes, with their many inflections points, depend on the amount and distribution of pressure taps (Jeong et al 2000 and Cohen et al 2004).

The POD method has very interesting features but it should be noted that the method depends exclusively on the covariance matrix of a pressure field, and therefore it is necessary to have a good understanding of the covariance concept, what it measures, which kind of information it gives and, very importantly, which information it does not give.

The covariance is a measure of joint dispersion of two variables. Its definition makes it a useful parameter to measure the degree of **linear** correlation between two variables but it says nothing about non-linear relationships. Misunderstanding the last sentence may cause confusion in interpreting the results obtained by the POD. A simple example is given below to show the point.

Let $P_1(t)$ and $P_2(t)$ be the pressure histories obtained at two pressure taps. Further, let us assume both histories are described by sine functions that differ only by a phase angle $\varphi$.

$$P_1(t) = \sin(\omega t) \text{ and } P_2(t) = \sin(\omega t + \varphi)$$

Obviously, the two variables are mathematically related. It is also possible to imagine a phenomenon where the two variables have a physical relationship. However the covariance of $P_1(t)$ and $P_2(t)$ gives three different values depending exclusively on the phase angle. For $\varphi = 0, \mathrm{cov} = 0.50$; for $\varphi = 45°, \mathrm{cov} = 0.35$; and for $\varphi = 90°, \mathrm{cov} = 0.00$. Figure 2.1 shows the graphical relationship between $P_1(t)$ and $P_2(t)$ for these three cases. From the figure, it can be seen that it would be incorrect to conclude that $\mathrm{cov} = 0$ implies a nil physical or mathematical relationship between $P_1(t)$ and $P_2(t)$, it rather implies zero linear statistical correlation.

There are many more examples of non-linearity where the covariance concept is not the most effective tool for determining physical relations. It is feasible to develop models that take into account the non-linear relationships. By using a 'non-linear covariance' matrix, the POD would be more efficient in extracting real load modes but all the benefits of linear operations would be lost. The author believes this is the reason why such idea has not become popular.

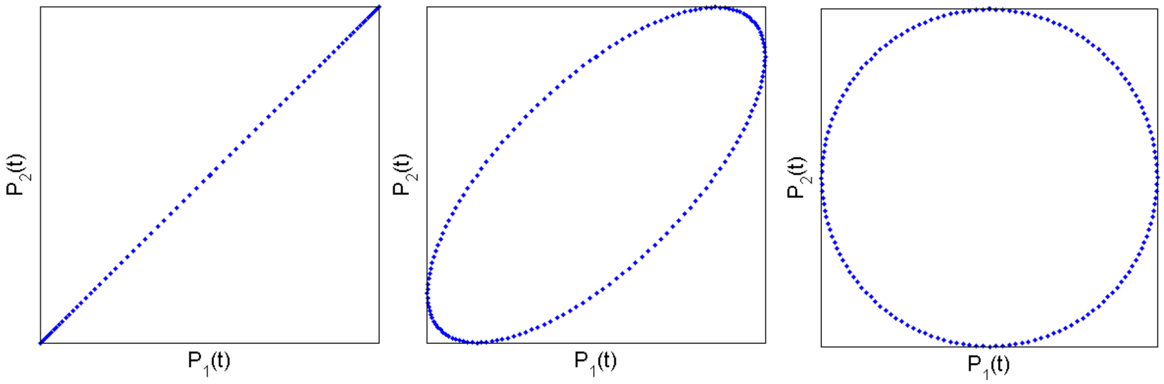

Figure 2.1 $P_1(t)$ vs $P_2(t)$ for three phase angles. From left to right: $\varphi = 0$, $\varphi = 45°$ and $\varphi = 90°$.

## 2.3 Similarity and non-dimensionalization

Although measurements over full-scale structures (prototypes) are occasionally carried out, it is much more common to perform experiments on scale models and then use the results for predictions on full-scale structures. Nevertheless, the correct application of the experimental results obtained from scale models towards the design of full-scale structure requires the observance of the concept of similarity. There are three types of similarity and they are briefly explained in the next paragraphs.

The geometrical similarity between a model and its prototype is an essential condition. It is difficult to define a priori the necessary level of refinement for a model. In general, it can be said that large flow structures are sensitive to the global shape of the models, while small flow structures are sensitive to small physical details. Nevertheless, some small physical features like surface roughness have significant impact on global response like drag force.

The kinematic similarity condition establishes that the velocity vector fields around the model and the prototype should remain proportional at all times or at least in statistical terms. This implies the need to model accurately the oncoming flow field, as well as the effect of obstacles surrounding the model.

In order to achieve full similarity between a prototype and its model, a third condition must be met. This is the dynamic similarity condition, which establishes that the forces in the model and the prototype should remain proportional at all times or at least in statistical terms. One possible way to achieve dynamic similarity is by using the same construction materials for both the model and the prototype, with the same level of construction detail.

Achieving full similarity can be extremely difficult, impractical or even impossible. Thus, judgment and experience are necessary to determine the level of refinement while designing an experiment. In civil engineering applications it is common to use aeroelastic models, which are models designed to represent the most significant geometric and dynamic features of flexible structures, where the interaction fluid-structure is of the utmost importance.

The three types of similarity conditions give rise to a large amount of dimensionless numbers. Non-dimensionalization is a common practice that allows to compare data that comes from two similar flows that were originated in different testing conditions—different flow speed, different physical and time scales, different viscosity, etc. Among the large amount of dimensionless numbers available in fluid mechanics, only a few are used during the present work. They are the pressure coefficient, Reynolds number, the Strouhal number and the Helmholtz number.

### 2.3.1 Pressure coefficient (Cp)

The pressure field around an object is usually better described in terms of dimensionless numbers called pressure coefficients rather than reporting the actual values of pressure. The pressure coefficient, Cp, represents the ratio of pressure and inertia forces. It is mathematically defined as:

$$Cp = \frac{p - p_0}{\frac{1}{2}\rho U^2}$$

where:

$p$ = measured pressure, Pa.

$p_0$ = reference pressure, usually the atmospheric pressure or the static pressure, Pa.

$\rho$ = air density, kg/m$^3$.

$U$ = wind speed, m/s.

### 2.3.2 Reynolds number (*Re*)

The Reynolds number represents the ratio of the inertia forces to the viscous forces. In most practical cases Re>>1, but this does not imply that viscosity could be considered as zero. In fact, the viscosity is present in all real fluids and is responsible for the non-slip condition, which in turn is responsible for the formation of boundary layers. The boundary layers are very complex and unstable flow structures that directly affect the object/obstacle that creates them, as well as other objects located downstream. The appearance and evolution of several flow structures is closely connected with the magnitude of the Reynolds number, which is defined as:

$$\mathrm{Re} = \frac{U \cdot L}{\nu}$$

where:

$L$ = characteristic length, m.

$\nu$ = $1.46\times10^{-5}$ m$^2$/s is the kinematic viscosity of air.

### 2.3.3 Strouhal number (*St*)

The Strouhal number is associated to vortex shedding from bluff bodies. It is calculated as follows:

$$St = \frac{f \cdot L}{U}$$

where *f* is the frequency, in Hz, at which the vortices are shed.

There are different vortex mechanisms associated to every particular bluff body. In fact, it has been shown that different vortex mechanisms coexist for certain bluff bodies. The particular description of these mechanisms will be explained at the pertinent section within this work.

### 2.3.4 Helmholtz number ($S_H$)

The Helmholtz number is related to the acoustic resonance inside a cavity. It is calculated as follows:

$$S_H = \frac{f_H L}{U}$$

where $f_H$ is the Helmholtz frequency in Hz.

The specific values for U, L and f will be defined in the proper section of the thesis.

# Chapter 3 REFERENCE CASE: POD analysis for a hanging roof model

## 3.1 Introduction

In order to validate the POD method, it was deemed necessary to apply first the POD to a simple model from which the pressure field was already well known and to which published results on POD analysis could be compared. The time and the costs were also part of the considerations while selecting a reference case.

The roof model described in this chapter was chosen because it was already used for the author's previous studies on the static effects of wind loads on hanging roofs (Flores-Vera 2003). Thus, the time and costs of building a model were already saved and the author was familiarized with the static pressure field around the model. Nonetheless, there were no publications on the use of the POD for this type of buildings. Hence the idea to include another simple structure for the POD validation: the square prism.

The square prism was a convenient choice for different reasons. It has been extensively studied for general purposes. It is a 'well-behaved' vortex generator, i.e., the Strouhal number is constant in a wide range of Reynolds number. One additional benefit is that the flow past a square prism has already been analyzed with the POD method (Kareem and Cermak 1984, Kikuchi et al 1997 and Cosentino and Benedetti 2005).

The factors described above set the conditions for the experiments described in this chapter. First, the POD was used to analyze the unsteady pressure field over the roof model in smooth flow. Later, the roof model was placed in the vortex trail of the square prism. At this stage, it was possible both to evaluate the influence of the square prism on the pressure field over the roof and to verify the results of the POD analysis for flow past a square prism.

## 3.2 Model description and experimental conditions

It was required to study the dynamic pressure field over the hanging roof of a sports facility. A rigid model was built in acrylic at a geometrical scale of 1:200. The footprint of the model covered approximately a square area of 50 cm per side. The height at the centre of the model was 11.6 cm. It should be noted that the vertical wall in the XZ-plane (see Figure 3.1) over-passes the parabolic edge, which causes a slight asymmetry to the building and to the pressure field.

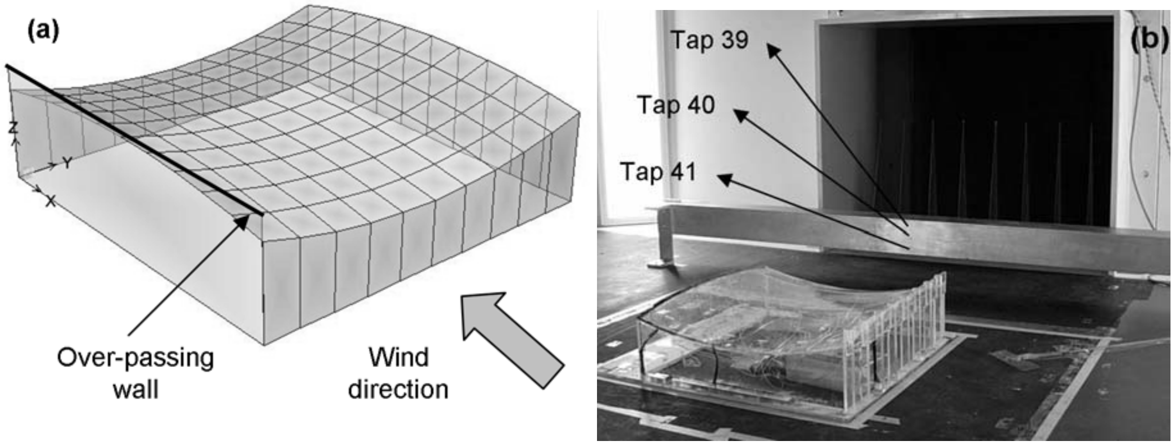

Figure 3.1 Roof model (a). The roof model and the square prism inside the wind tunnel (b).

The model was tested in the Pilot Wind Tunnel of the National Research Council Canada. The tunnel has a nozzle that is 1.0m-wide and 0.8m-high. The air in the test section travels from the upstream nozzle to a downstream collector. The test section has larger dimensions than the nozzle, forming a large plenum. The roof model was placed 80 cm downstream of the nozzle. The tests were performed in smooth flow and in a simulated sub-urban turbulent flow created with spires. Nevertheless, the use of the spires did not bring outstanding additional information when compared with the case of smooth flow. For the sake of simplicity only two configurations are presently discussed: 1) the roof model immersed in smooth flow, and 2) the roof model immersed in the vortex trail of a square prism. For the second configuration, a square prism of 10 cm per side was located horizontally between the nozzle and the roof model. Figure 3.1 (right) shows the model and the square prism inside the wind tunnel and Figure 3.2 indicates the distances, in millimetres, of the experimental set up.

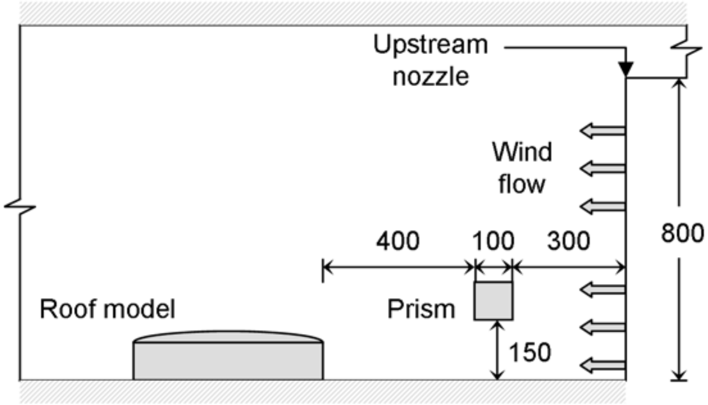

Figure 3.2 Longitudinal view of the roof model and the square prism inside the wind tunnel.

Unsteady pressure measurements were carried out simultaneously at 44 pressure taps, 32 of them on the surface of the roof model and 12 around the mid-section of the square prism. All 2-D figures in this chapter showing the roof model or the square prism are oriented as in Figure 3.3, which shows the identification and distribution of the pressure taps. Pressure data acquisition was carried out with a Scanivalve Hyscan System. The pressure taps on the roof model were connected to a pressure-scanning module ZOC33/64Px, which was housed into a thermal control unit. The pressure taps on the prism were connected to a pressure-scanning module ZOC23B, which was housed into the square prism in order to minimize sensor mis-calibration due to temperature effects. Both pressure scanning modules have a full-scale range (FS) of $\pm 10 \cdot inch$ $H_2O$ ($\pm 2500$ Pa) and an accuracy of $\pm 0.20\%$FS ($\pm 5$ Pa). The accuracy of the sensors defines the lower limit of the wind speed for the tests. For example, the dynamic pressure at the lowest speed (U=14 m/s) is $q_{14} = 0.5 \rho U^2 = 196 \pm 5 Pa$. Since the dynamic pressure is used as reference for the calculation of pressure coefficients, a value of Cp=1.0 has 2.5% accuracy, which is considered good. Pressure coefficients as low as 0.1 have 25.5% accuracy, which is considered poor. Therefore, lower wind speed would imply poorer measurement accuracy. The full-scale range of the sensors defines the upper limit of wind speed for the tests. For example, the dynamic pressure at the largest wind speed (U=38 m/s) is $q_{38} = 0.5 \rho U^2 = 837 \pm 5 Pa$. Since it is possible to have instantaneous pressure peaks of Cp=-3.0, the full-scale range can be reached. Despite the fact that the sensors are protected for eventual pressure peaks beyond the full-scale range, it is advisable to remain under the designed limit (2500 Pa).

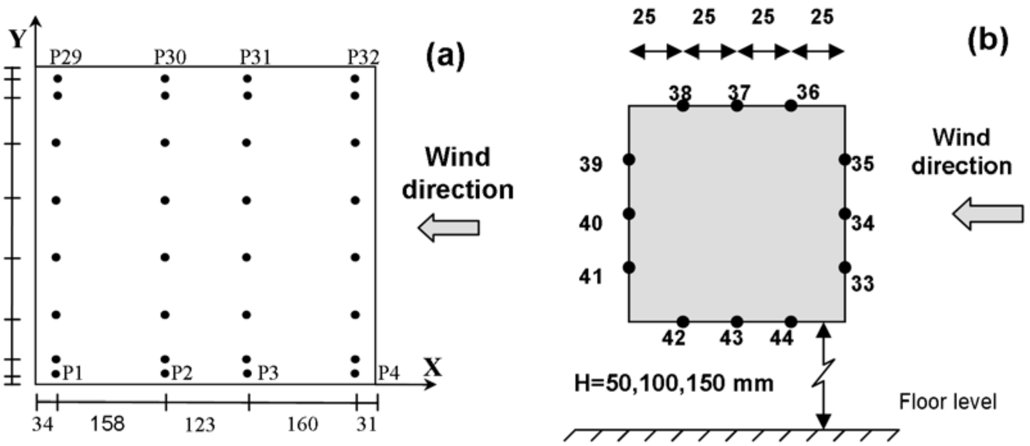

Figure 3.3 Pressure tap distribution. Plan view of the roof model (a). Cross section of the square prism (b). Dimensions in mm.

The sampling frequency was set to 400 Hz, which allowed to identify flow mechanisms with frequency content up to 200 Hz. The sampling interval was set to 90 seconds, which provided enough information for a reliable statistical database. Corrections for the tubing frequency response and time delay between channels were made. A single orientation of the roof was studied with velocities ranging from 14 to 38 m/s. The square prism was located in three vertical positions at 5, 10 and 15 cm from the floor of the wind tunnel, being the height H=15cm the position that provides the best information due to a smaller interaction between the floor and the vortices.

In addition to the pressure measurements, wind velocity profiles such that shown in Figure 3.18 were obtained with a TFI Cobra probe. The Cobra probe is a 4-hole pressure device that is able to resolve wind velocity into three orthogonal components within a ± 45° acceptance cone (see Figure 3.4). The probe features a linear frequency response from 0 Hz to 1500 Hz and it is adequate to measure wind speeds ranging from 2 m/s to 55 m/s. The accuracy of the probe is ± 0.3 m/s for wind speed and ± 1.0° for velocity direction. The probe traversed vertically, measuring the velocity magnitude and the velocity direction. The time histories were recorded at 25 locations at a sampling rate of 2000 Hz with a duration of 30 s each.

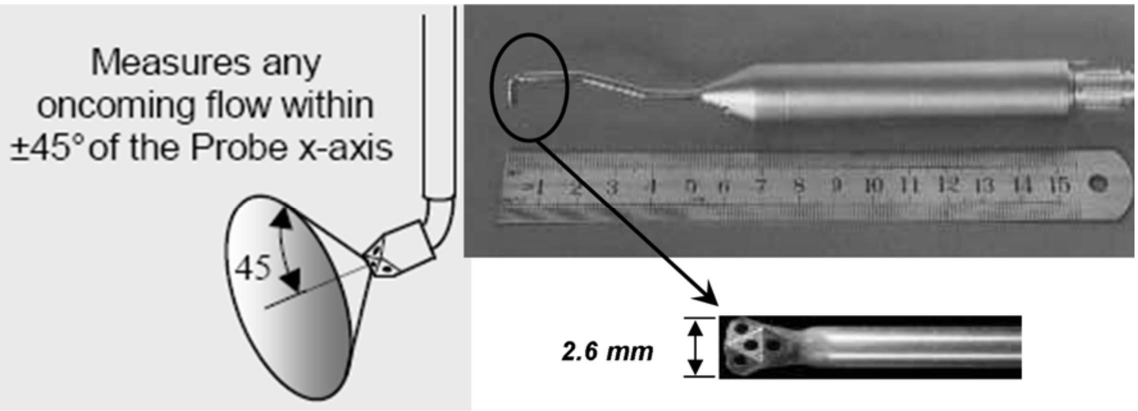

Figure 3.4 Cobra probe, Turbulent Flow Instrumentation.

## 3.3 Data reduction

### 3.3.1 Time delay correction

The pressure signals were recorded with a Scanivalve Corp. multiplexer system. This means that there was a time delay between pressure recordings from one channel to the next. Although the time delay is very small (78 and 57 $\mu s$ when using 32 and 44 channels respectively), a correction has to be made in order to apply the POD analysis which requires a zero time lag between pressure signals. Since the sampling intervals between channels were fixed, the time delay correction was easily carried out by linear interpolation. It is considered that all important features of the flow were properly captured because the fraction of time between samples is small compared with the time scale of the flow phenomena studied.

### 3.3.2 Tubing effects on pressure signals

In order to evaluate the effects of dynamic wind loading on structures, wind tunnel tests often involve unsteady pressure measurements at certain points on the models. Due to technical and economic reasons, it is impractical to place sensors exactly on these points. It is more often the case where orifices are drilled on the model and then connected to the sensors through urethane tubes. The tubing system is a dynamic system itself that amplifies or attenuates the pressure signals that travel through it. It should be noted that the tubing system consists not only of the urethane tubes but also of the tubulation, which are short metallic tubes that allow the physical connection between the urethane tubes and the sensors on one end and between the urethane tubes and the model on the other end.

In order to take into account the signal distortion caused by the tubing, as well as to perform the respective corrections, it was necessary to measure the transfer functions of the tubing system. This was achieved by measuring the response of every tube line to a white noise signal using the method described by Larose et al (2003). The instrumentation necessary for the determination of the transfer functions is shown in Figure 3.5 and the procedure is described briefly here for completeness. The starting point was the generation of the white-noise signal with an oscilloscope. Then, the electrical signal was amplified and sent to a horn driver, which transformed the electrical signal into pressure pulsations. The pressure pulsations were measured directly at the base of the horn driver by a Kulite fast response pressure transducer and indirectly, through a urethane tube, by a ZOC pressure transducer. Thus, the Kulite sensor measured the exciting pressure at the source while the ZOC sensor, located at the other end of the tubing, measured the response. The signals from the Kulite and ZOC sensors were sent simultaneously to a spectrum analyzer, which calculated their Fourier spectra as well as the transfer function (the ratio of both spectra). The process was repeated for all pressure taps, obtaining thus the transfer functions shown in Figure 3.6 and Figure 3.7. It was not possible to measure the transfer function of the pressure taps 1 to 4 due to the inability to reach the taps with the loudspeaker. Therefore, the first four taps were assigned an average transfer function. All these functions were later used to correct the pressure measurements of the actual wind tunnel tests, by using the method described by Irwin and Cooper (1980), which corrects both the magnitude and the phase angle.

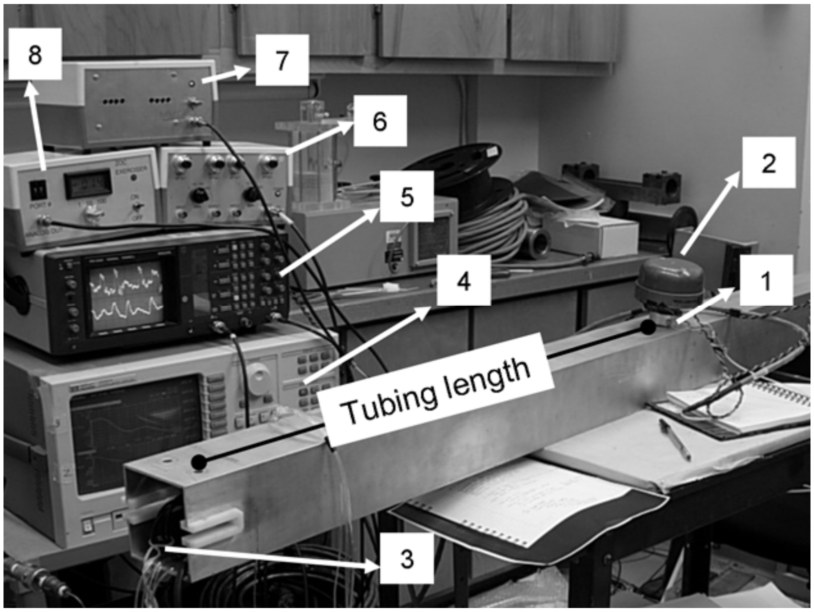

Figure 3.5 Components for measuring the transfer function of pressure tubing. Kulite pressure transducer (1), horn driver (2), ZOC pressure transducers (3), spectrum analyzer (4), oscilloscope (5), instrumentation amplifier for Kulite sensor (6), noise signal amplifier (7), ZOC exerciser (8).

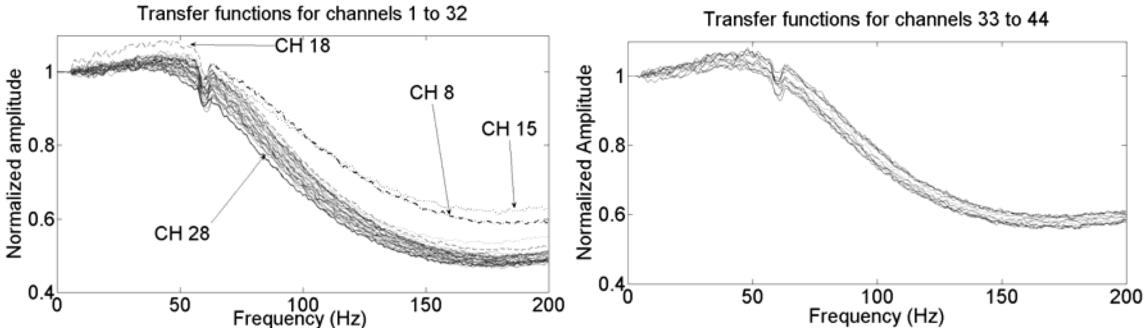

Figure 3.6 Transfer function (magnitude) for all tubes. Channels 1 to 32 (left) and channels 33 to 44 (right).

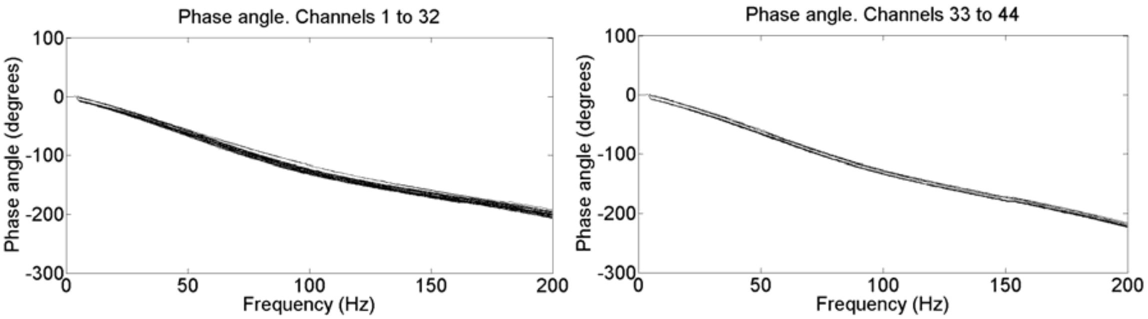

Figure 3.7 Transfer function (phase angle) for all tubes. Channels 1 to 32 (left) and channels 33 to 44 (right).

The tubing lines for the 32 pressure taps were intended to be dynamically similar by using tubes of the same length (50 cm) and same internal diameter (1.02 mm). For the same reason, the tubes for the 12 pressure taps on the square prism all were 75 cm long. Nevertheless, it is possible to observe some differences among the transfer functions. Such differences are more notorious for the pressure taps connected to the scanning module ZOC33 mainly because of the arrangement of the connecting tubes inside the module.

Since the transfer functions indicate how every exciting frequency is distorted when it travels along the tubing, it can be concluded from Figure 3.6 that frequencies below 70 Hz are not affected significantly but higher frequencies experienced a considerable attenuation. The strange behaviour around 60 Hz is attributable to the electric noise.

The tubing had no effect on the mean values of the pressure coefficients but it had a slight influence on the root-mean-square value of the pressure coefficients as can be seen in Figure 3.8. Except for pressure taps 1 to 4—the taps with an average transfer function, the RMS values of the raw data are larger than those for the corrected data. This observation implies that the tubing slightly increases the dispersion of data around the mean value.

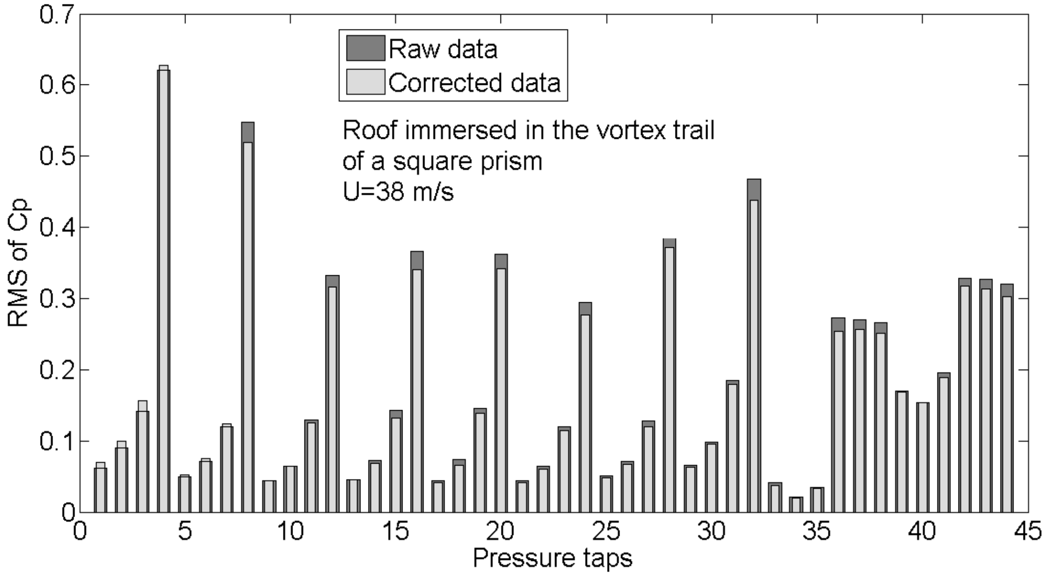

Figure 3.8 Effects of data correction on the RMS values of the pressure coefficients

Before discussing the physical meaning of Figure 3.9, which shows the effect of tubing correction on the power spectral densities (PSD), it is convenient to recall the concepts of the variance, the power spectral density and their mutual connection. Firstly, the variance is a measure of the dispersion of data around the mean value. In the case of the time history of a physical process like a pressure history, the variance is also an indicator of the energy involved in the process. A larger value of the variance implies larger pressure variations and thus more energy involved. On the other hand, the power spectral density of a time history is a very useful representation of how the variance (energy) is distributed according to the frequency content of the time history. Consequently, the area under the power spectral density function equals the variance of the process.

By linking these concepts with the discussion of the transfer function (Figure 3.6), it is possible to justify that the power spectral densities of the raw and corrected data intersect about 70 Hz, which is the approximate frequency where the transfer functions become equal to 1.0 and start to decay rapidly. An additional observation of Figure 3.9 can be done by comparing the differences between the four plots, which represent the PSD on pressure taps 5, 6, 7 and 8. The four taps are aligned in the direction of the wind flow, being the tap number 5 the closest to the trailing edge and the tap number 8 the closest to the leading edge. Since the oncoming flow is the result of vortices shed at a frequency equal to 44 Hz, the PSD of tap number 8 clearly indicates that most of the energy is concentrated at 44 Hz. Both, raw and corrected data on that tap look practically the same because the transfer function at 44 Hz is close to 1.0. On the other hand, the PSD functions of tap number 5 are no longer concentrated in a narrow frequency band, thus showing more appreciable differences between raw and corrected data for frequencies beyond 70 Hz.

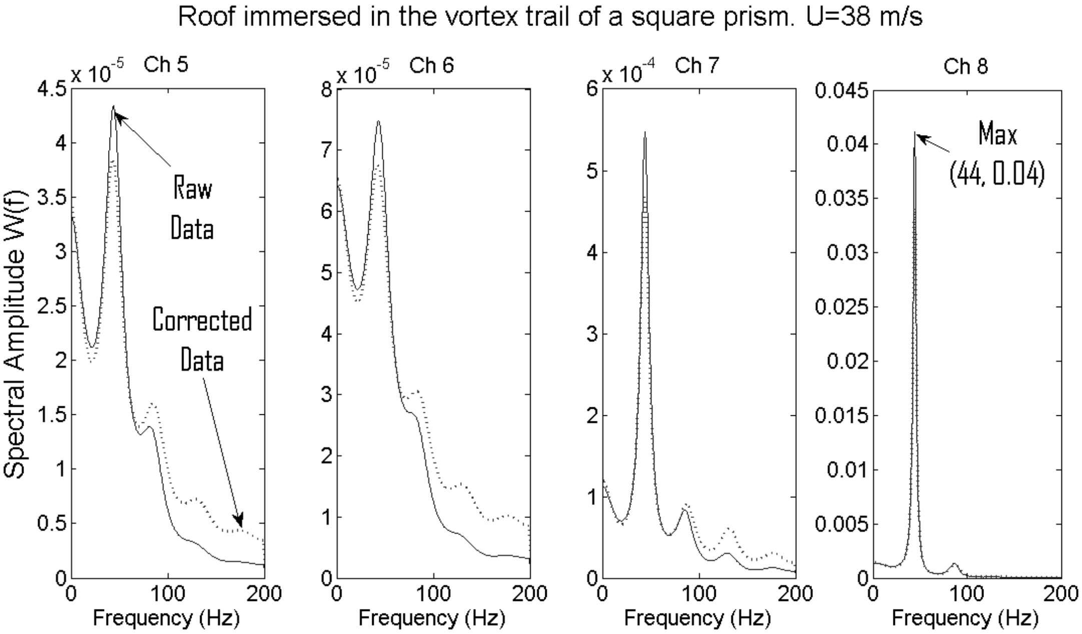

Figure 3.9 Effects of tubing correction on the power spectral densities.

### 3.3.3 Normalization of power spectral densities (PSD)

Normalization of the power spectral densities is a common process that allows the comparison of results obtained from different testing conditions (different scale, wind speed, etc). It was decided to work with one-sided spectral densities functions with both axis normalized. The horizontal axis (frequency axis) was multiplied by a factor L/U, where L is a characteristic length taken as the side of the square prism (0.10 m) and U is the wind speed. The vertical axis (spectral amplitude axis) was multiplied by a factor $f / \sigma^2$, where $f$ is the frequency and $\sigma^2$ is the variance of the pressure signal. The normalized spectral densities are presented in the following sections for describing the frequency content of the POD modes.

## *3.4 Roof model immersed in smooth flow*

**Mean pressure coefficients, Cp.**

The mean pressure coefficients obtained during this study were found similar to those reported by Bienkiewicz et al (1995) for flat rectangular roofs. As it is commonly observed for bluff body shapes, higher suction values occur near the leading edge, in the separation bubble. The mean pressure coefficients shown in Figure 3.10 remain practically constant for the 14-33 m/s range of wind speed analyzed. The corresponding Reynolds number range is 96,000<Re<220,000, based on a characteristic length of 0.10 m, equal to both, the height of the model at the middle of the leading edge and the side length of the square prism.

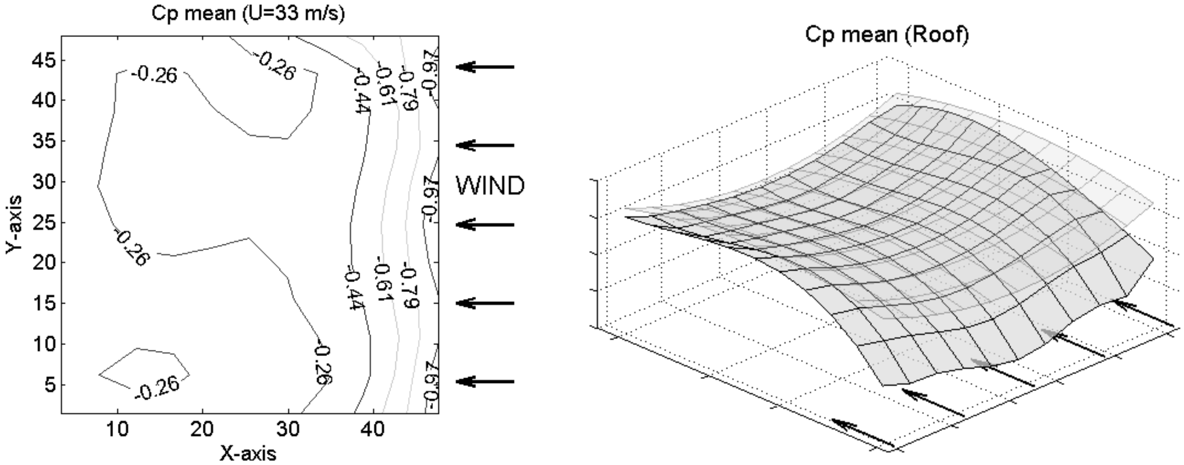

Figure 3.10 Mean pressure coefficients. Roof model immersed in smooth flow.

### Root-mean square values of pressure coefficients, RMS.

The root-mean-square value (RMS) of the pressure coefficients is an indicator of the level of unsteadiness in the flow field. Figure 3.11 shows the distribution of the RMS on the roof. Also the RMS values remain practically constant for the whole wind speed range (14-33 m/s). There is a very important difference between the RMS values reported here and those reported by Bienkiewicz et al (1995), the former are much lower than the latter. The major difference is due to the fact that the cited paper did not subtract the mean values neither for calculating the RMS values nor for constructing the covariance matrix, which lead to very different results in the POD analysis.

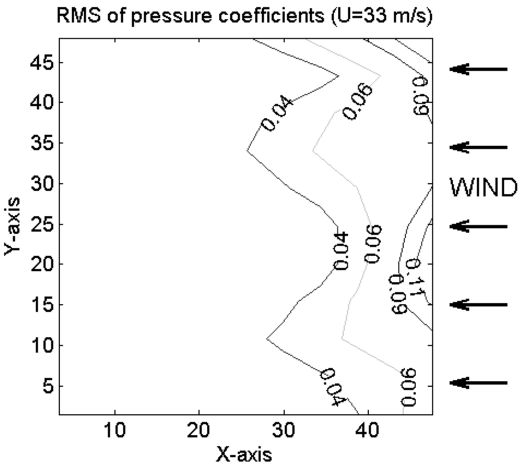

Figure 3.11 Root-mean-square of pressure coefficients. Roof model immersed in smooth flow. 14≤U≤33m/s.

**Peak values.**

Strictly speaking, an instantaneous peak value of pressure is the highest or lowest value recorded at a pressure sensor. Nevertheless, since there are nearly 35000 values recorded per sensor in each run there is a possibility that the highest or lowest value is an outlier, i.e., an instantaneous misreading of the measuring device. Even if the highest value is not an outlier, the influence of an individual peak on the structure is questionable since only a number of repetitions of large values can have a noticeable effect on the object. Therefore, for the cases studied in this chapter, a peak value $\hat{C}_p$ is calculated as the average of the 35 (0.1%) highest absolute values recorded at a pressure tap. Figure 3.12 (left) show the peak values of pressure coefficients for a wind speed equal to 33 m/s. The peak value distributions for all other wind speeds are very similar to this figure. Figure 3.12 (right) shows the ratio of the zero-mean peak value and the rms value, $\hat{C}_p - \overline{C}_p \big/ \sigma_{Cp}$. It can be observed that for the most part the ratio ranges between four and seven, which is a common value observed in many measurements in the field of wind engineering.

The peak values of pressure can be calculated more formally with the use of extreme value distributions but these methods require additional information about the nature of the wind and the length of the averaging time. The description of the formal procedure is out of the scope of this work but the interested reader can find more information in the papers by Mayne and Cook (1978) and Mayne (1979).

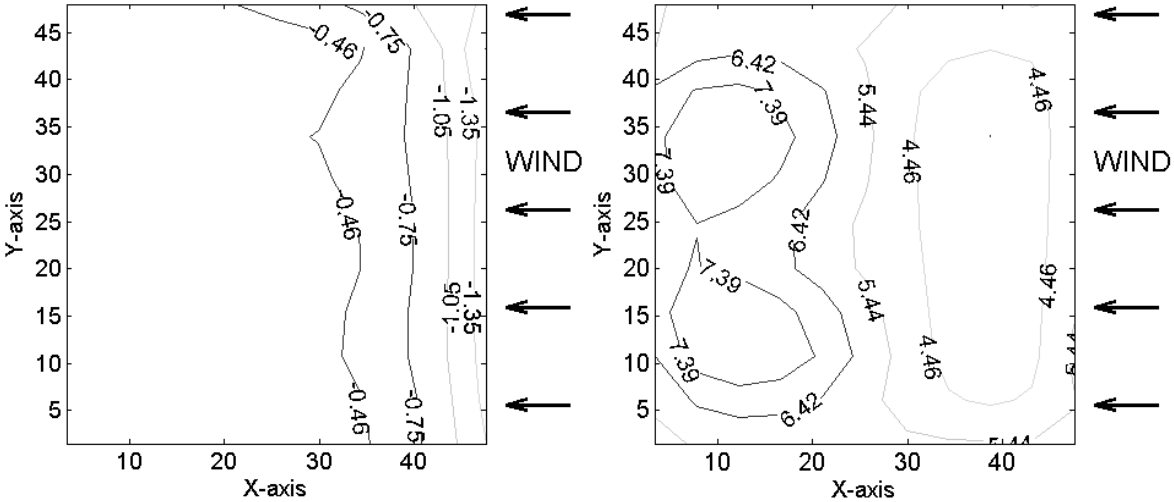

Figure 3.12 Peak values of pressure coefficients (left). Ratio zero-mean peak/rms (right). Roof model immersed in smooth flow, 14≤U≤33m/s.

**Energy distribution (eigenvalues).**

Since the RMS values obtained for the hanging roof are small, it is assumed that the characteristics of the turbulence observed are mainly local; i.e., the eddies created by the flow separation at the leading edge are small and/or remain stationary and/or do not travel coherently along the roof. Given the curvature of the roof in two directions, it is likely that the flow reattached before reaching the trailing edge of the roof. It is apparent that the aerodynamic-like shape of the roof model not only contributed to a small amount of turbulence but also in the organization of the POD modes and their respective energy contribution. As can be seen in Figure 3.13, the energy is not concentrated in any particular mode and consequently there is no dominant mode. The same energy distribution was observed for the whole wind speed range studied.

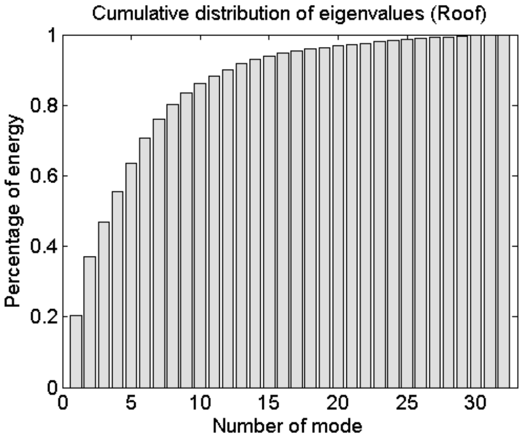

Figure 3.13 Cumulative energy distribution per POD mode. Roof model immersed in smooth flow.

**POD modes (eigenvectors).**

The first POD mode and its respective spectral density function are shown in Figure 3.14 and Figure 3.15. As an obvious consequence of the RMS distribution discussed on Figure 3.11, the largest pressure oscillations in the first POD mode occur on areas near the leading edge, with maximum coefficients around 0.43 at the center and 0.60 at the corner, while most of the roof experience small pressure oscillations. The asymmetrical behaviour is most likely due to the uneven boundary conditions set by the over-passing wall on one side of the roof. Additionally, the power spectral density does not have a significant peak; it rather resembles the spectrum of white noise. These descriptions agree with the weak flow organization discussed in the previous paragraph.

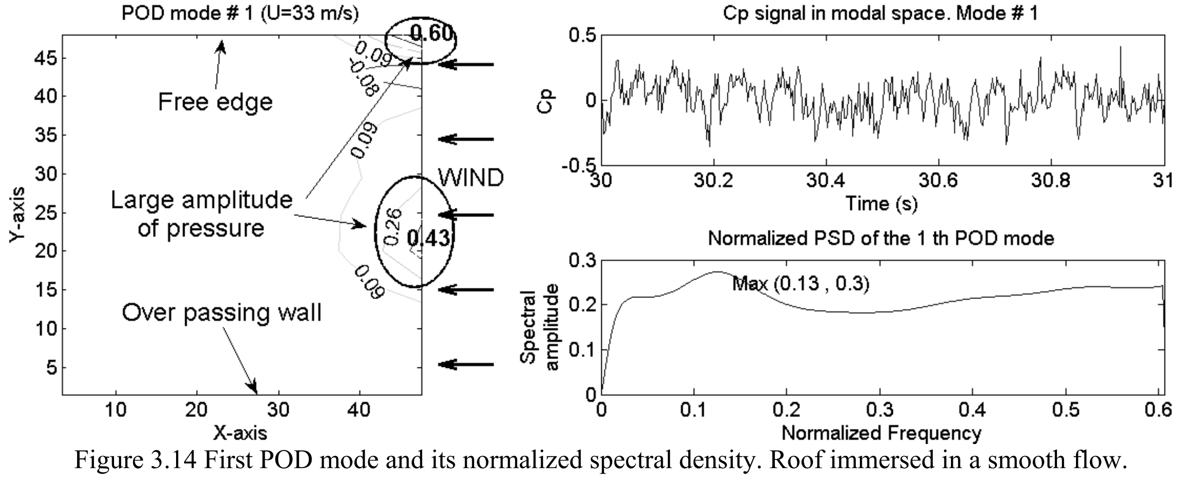

Figure 3.14 First POD mode and its normalized spectral density. Roof immersed in a smooth flow.

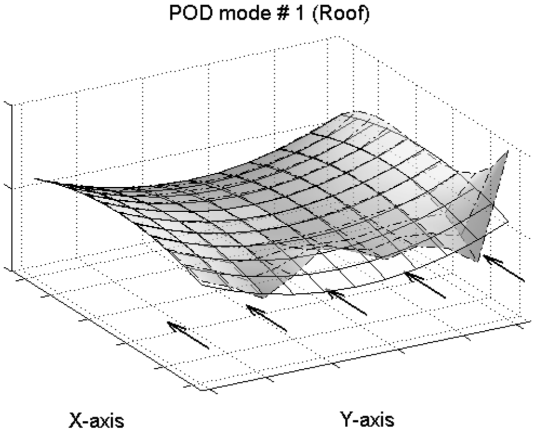

Figure 3.15 First POD mode in a 3D-view.

The second POD mode and its respective spectral density function are shown in Figure 3.16 and Figure 3.17. The behaviour is similar to that of the first POD mode, with the largest pressure oscillations occurring on the leading edge and with a spectral density function resembling that of white noise. Even the energy contribution is also similar for the first two modes (20% and 17%). The only distinction is that the second POD mode has an additional inflection point.

The higher POD modes not only are less energetic but they seem even more disorganized. It was decided not to show higher modes since no significant information can be obtained from them.

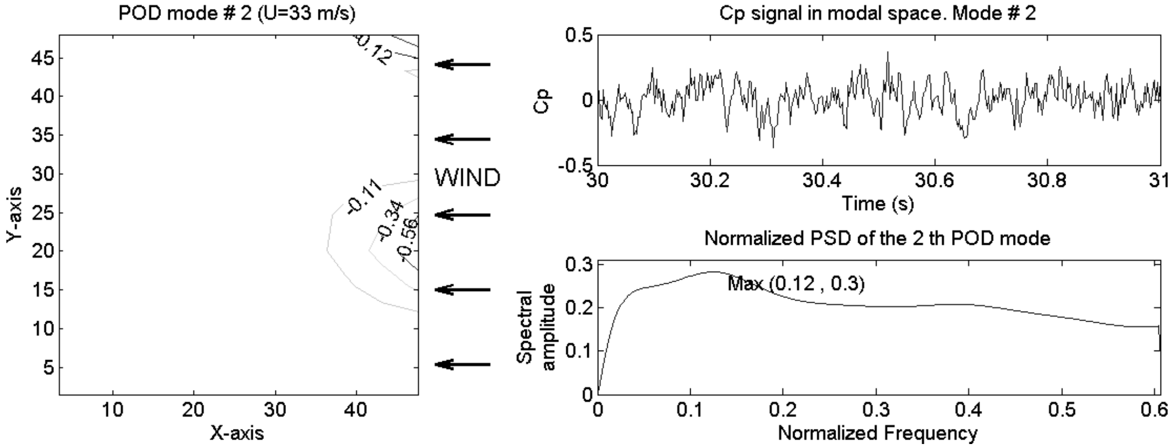

Figure 3.16 Second POD mode and its normalized spectral density. Roof immersed in a smooth flow.

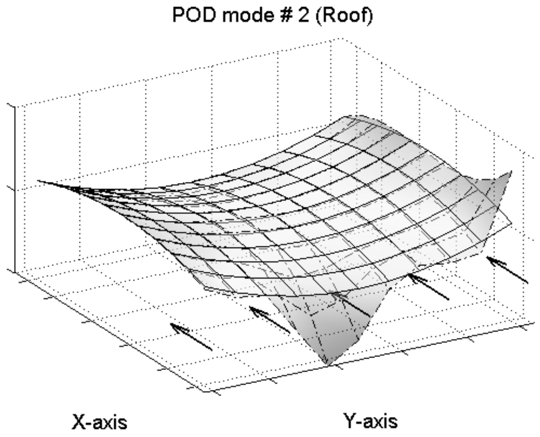

Figure 3.17 Second POD mode in a 3D-view.

## 3.5 Roof model immersed in the vortex trail of a square prism

The presence of the square prism created mean-velocity and turbulence profiles like those shown in Figure 3.18. A schematic representation of the location of the square prism and the roof model are included in the figure. It is possible to observe a dramatic reduction of mean wind speed behind the square prism. This velocity gradient causes a highly turbulent wake, characterized by vortex shedding. An extensive review of vortex shedding from bluff bodies can be found in the papers by Berger and Wille (1972) and Bearman (1984).

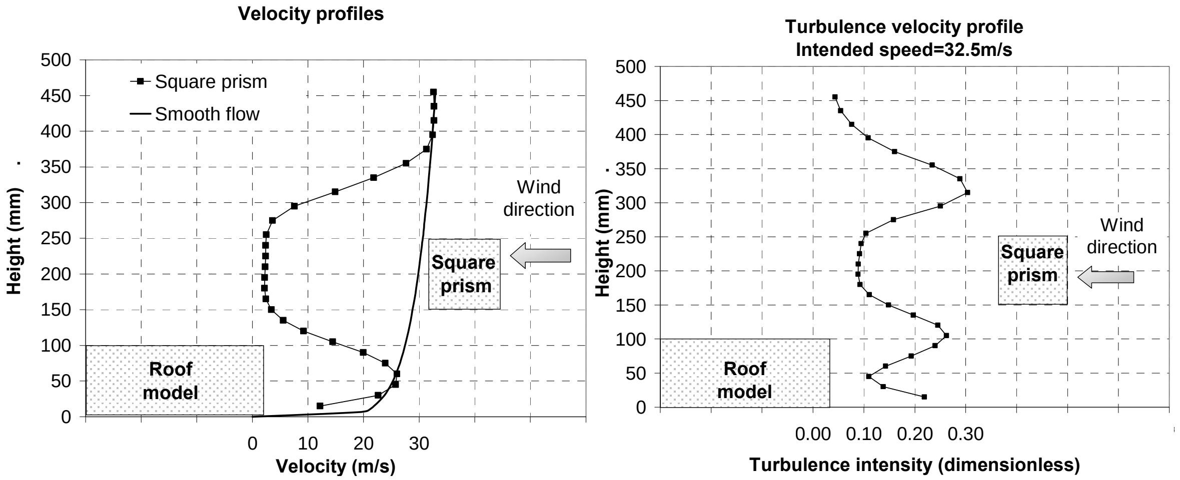

Figure 3.18 Left: velocity profiles for smooth flow and for wind past a square prism. Right: Turbulence profile for wind past a square cylinder

The experiments were performed for three different vertical positions (H) of the square prism. It was observed that the proximity of the prism to the floor affected the formation of vortices, their travelling and the way they impinge the roof model located downstream. The proximity of the floor tends to destroy the vortices shed from the bottom face and probably creates other flow structures that affect the vortices shed from the upper face. Even more important is the fact that a low position of the bottom face with respect to the leading edge of the roof prevents a natural vortex rolling over the roof surface. In fact, the vortices shed from the bottom face of the prism are stopped by the front wall of the roof model. Since the highest position of the prism (H=15cm) provides the best vortex rolling over the roof surface and also diminishes the floor interaction, such configuration is the most convenient study. All the following results were obtained from experiments with the square prism located at H=15cm from the floor.

Although the POD analysis was carried out from simultaneous pressure measurements on all 44 pressure taps, it is convenient to show separately the results obtained for the square prism and for the roof model. Before proceeding with the detailed analyses of the roof and the prism, some concepts about the use of the POD have to be highlighted in order to better understand the scope of the method and the meaning of the results.

The POD analysis is fully based on the covariance matrix obtained from the pressure histories. Whether the POD results have a physical meaning or not depends on the ability of the covariance to measure a physical correlation between every pair of pressure signals. If one aspires to capture real flow structures with the POD method, the construction of the covariance matrix should involve only those pressure taps that are considered affected by the same flow structures. Unfortunately, there is no method for such decision and the best guidance is the experience and intuition on fluid mechanics problems.

For the current case, there was a doubt if the covariance matrix should include all 44 pressure taps or the problem should be split into two independent analyses: one for the 32 pressure taps on the roof and another one for the 12 pressure taps on the prism. In fact, the two possibilities were studied. Figure 3.19 and Figure 3.20 present the comparison of the cumulative energy distribution obtained with the POD method when the analysis was based on the 44-by-44 covariance matrix, the 32-by-32 covariance matrix and the 12-by-12 covariance matrix. The POD analysis based on the 44-by-44 covariance matrix provided less efficiency in extracting the energy. Furthermore, there was an additional deficiency by realizing that the 32 pressure taps on the roof do not weight the same as those 12 pressure taps on the prism. The taps have a different tributary area and the fluctuations (and thus the variances) on the prism are higher than the fluctuations on the roof model. The use of the 44-by-44 covariance matrix represented a forced combination of flow structures that the POD was unable to identify. Therefore, it was decided to perform the POD analysis based on two independent covariance matrices and then the results were reviewed a posteriori in order to infer the interaction of the prism and the roof.

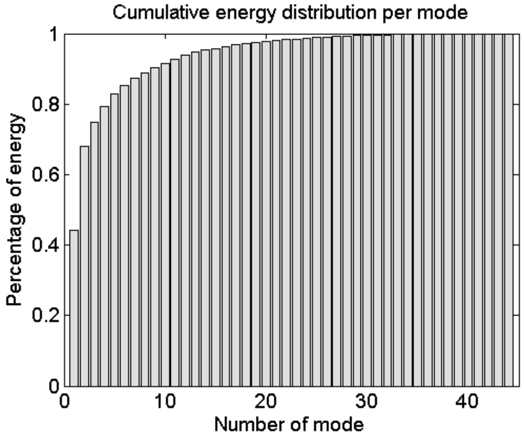

Figure 3.19 Cumulative energy distribution per mode based on the 44-by-44 covariance matrix (U=38 m/s)

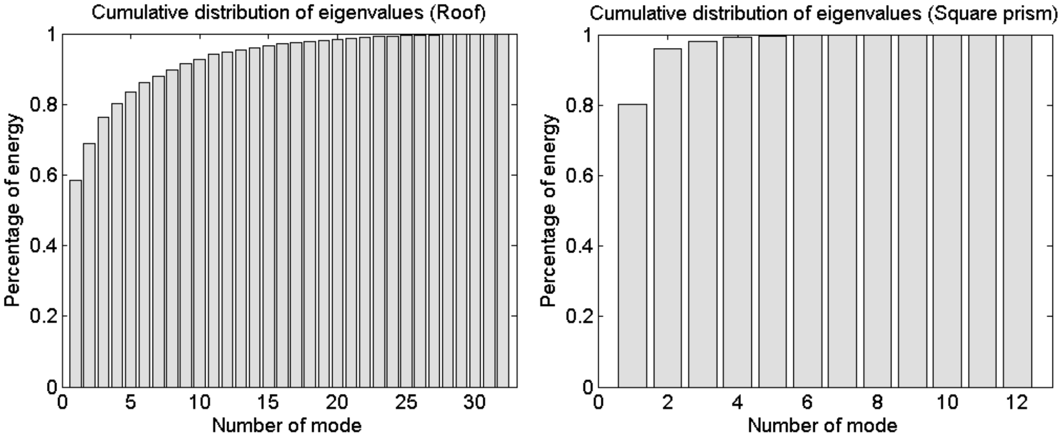

Figure 3.20 Cumulative energy distribution per mode based on 32-by-32 and 12-by-12 covariance matrices (U=38 m/s).

## 3.5.1 POD analysis for the square prism

The POD revealed flow structures over the surface of the square prism. The analysis was based on the unsteady pressure measurements obtained from 12 pressure taps arranged around the mid-span of the prism, with three taps per side.

**Mean pressure coefficients, Cp.**

The mean pressure coefficients (Cp's) are plotted on Figure 3.21. These values are practically the same for wind speeds ranging from 14 m/s to 33 m/s but there is a 50% increment in the absolute values recorded in channels 36 to 44 for wind speed of 38 m/s.

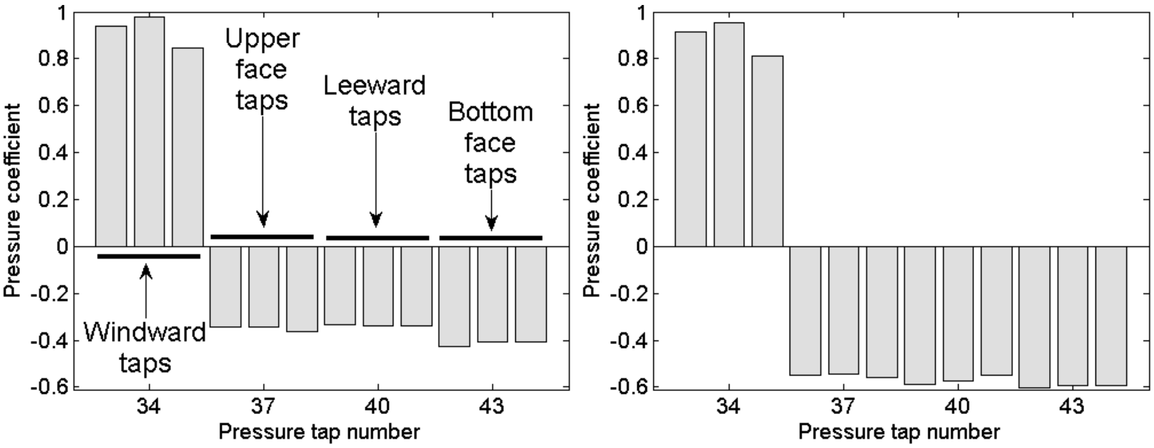

Figure 3.21 Mean pressure coefficients for the square prism. 14<U<33m/s (left) and U=38m/s (right)

### Root-mean square values of pressure coefficients, RMS.

The RMS values of pressure coefficients for the lowest and highest wind speed (14 and 38 m/s) are shown in Figure 3.22. One may expect a smooth transition between these two graphs, implying that gradual changes in wind speed will produce gradual changes in dynamic loading (measured by RMS). Nevertheless, this was not true. Figure 3.23 shows the variation of RMS as a function of wind speed. It is possible to observe that RMS values remain almost constant for 15m/s<U<35m/s, and so the respective eigenvalues and eigenvectors. However, there is a sudden increment in RMS at U=38m/s.

The abrupt changes in mean and RMS values of pressure coefficients at U=38 m/s suggest that a critical speed was reached. This behaviour could be attributed to the *lock-in phenomenon,* which appears when the vortex shedding frequency matches the natural frequency of the vortex generator (Simiu and Scanlan 1996). Although the natural frequency for the square prism was not measured, its numerical estimation is 50±10 Hz— where the plus-minus ±10 Hz depend on the actual support conditions. The Strouhal number for flow past a square prism has been reported between 0.12 and 0.14 (Yu and Kareem 1997) and it is considered invariant with Reynolds number. The power spectral densities of the pressure taps located in the square prism have a sharp spectral peak at St=0.12. This number, combined with U=38 m/s and L=0.10 m, gives a vortex shedding frequency of 45 Hz. The close match of the estimated structural frequency vibration of the prism and that of the vortex shedding strongly suggests that the lock-in phenomena took place at U=38 m/s.

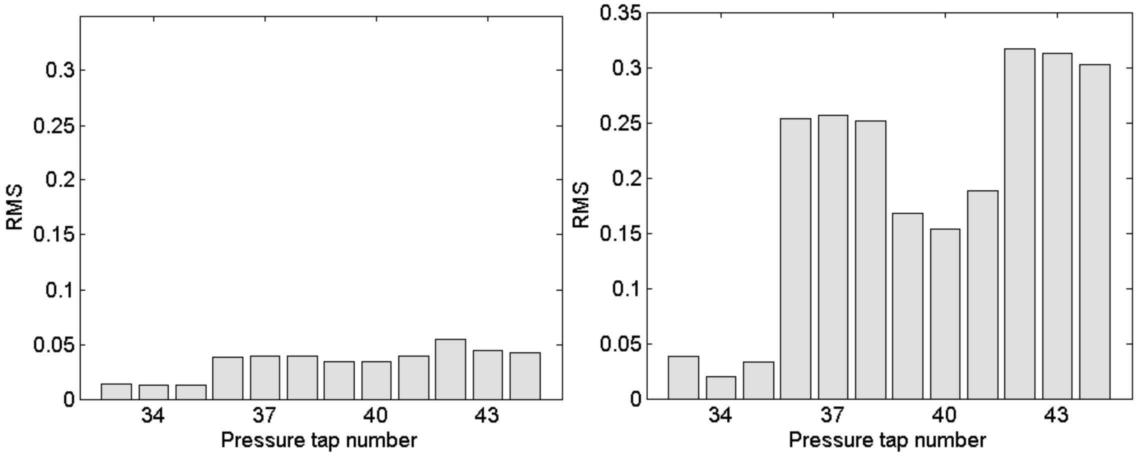

Figure 3.22. RMS values of pressure. U=14 m/s (left). U=38 m/s (right)

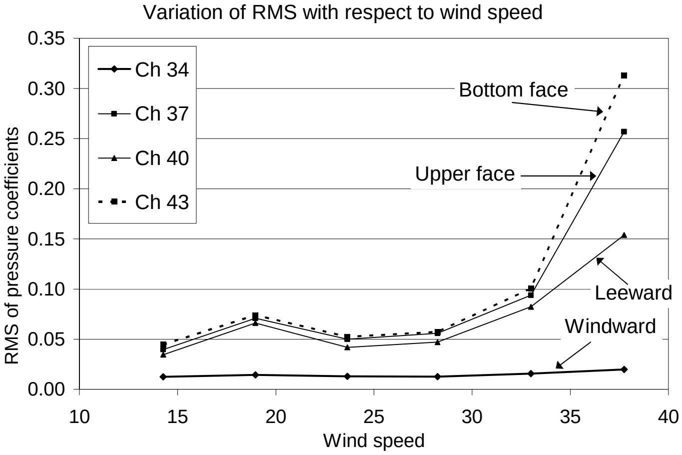

Figure 3.23. Variation of RMS pressure coefficients at the center of each face with respect to wind speed.

The lock-in phenomena not only increased the RMS values—and so the variances, but it actually had a greater effect on the off-diagonal elements of the covariance matrix of pressure coefficients. This non-proportional changes in the co-variances led to different eigenvalues and eigenvectors.

### Energy distribution (eigenvalues).

As stated before, the eigenvalues are indicators of the amount of energy related to their corresponding POD modes (eigenvectors). The energy distribution for flow past a square prism is shown in Figure 3.24. The histogram on the left is valid for 14<U<33m/s, while the histogram on the right is valid for the lock-in condition, at U=38m/s. In either case, it is evident that only a few modes are necessary to account for most of the energy. It is worth mentioning that the energy distribution shown on the right histogram is completely congruent with that reported by Cosentino and Benedetti (2005). This validates the numerical program developed by the author.

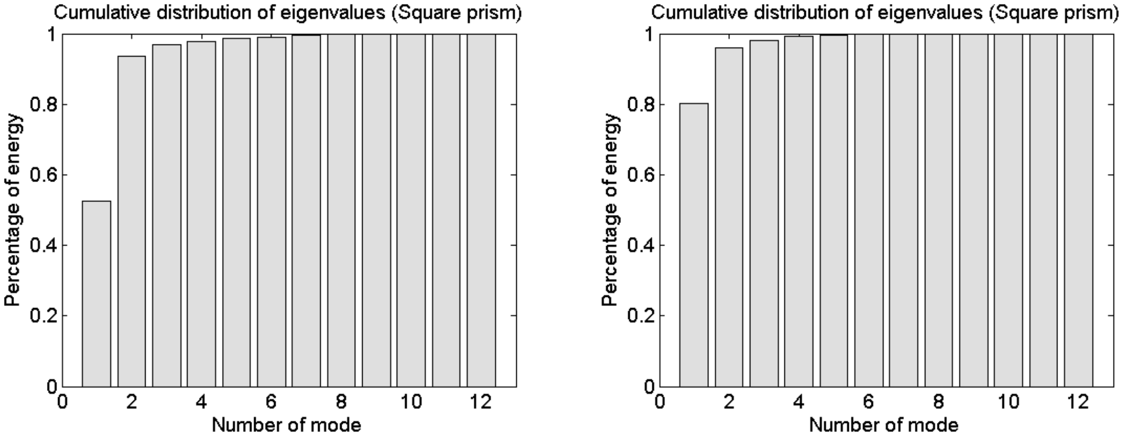

Figure 3.24 Energy distribution per mode. Left: 14≤U≤33m/s. Right: U=38m/s.

**POD modes (eigenvectors).**

The POD analysis confirmed that the dominant structure for flow past a square prism is the vortex shedding. Such conclusion was also reached by Kikuchi et al (1997) and Cosentino and Benedetti (2005). Figure 3.25 shows the first POD mode and its spectral density function, which remain practically constant in the whole wind speed range (14≤U≤38m/s). It can be seen that while the upper side of the prism experiences negative pressure (suction) the bottom face experiences positive pressure. The windward and leeward faces indicate a linear transition between positive and negative pressure. The windward face is the one with the lowest absolute values of pressure. The slight asymmetry on the mode shape is due to the influence of the wind tunnel floor on the vortices formation. The mode shape oscillates harmonically at a specific frequency of St=0.12. The narrow peak of the spectral density function indicates that most of the energy is concentrated around the Strouhal frequency.

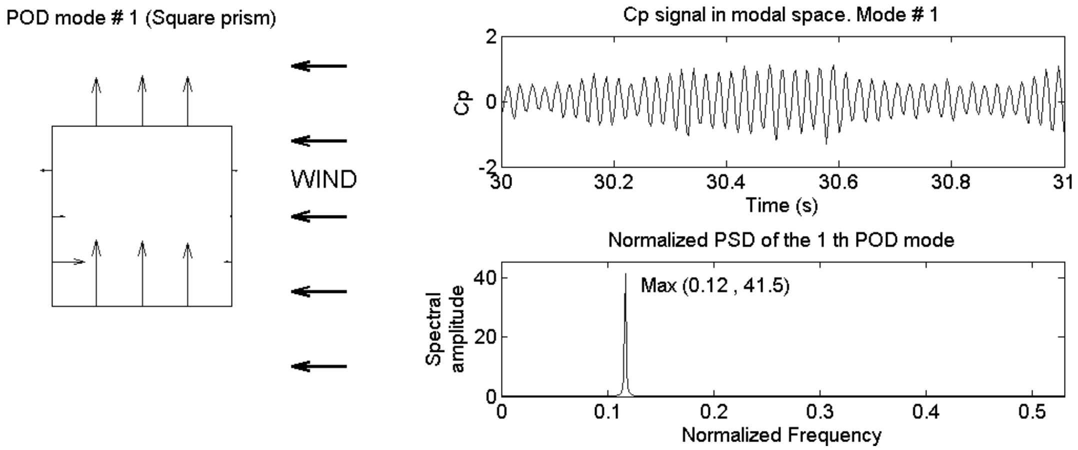

Figure 3.25 First POD mode for square prism. Similar for all wind speed range: 14≤U≤38m/s

The shape of the second POD mode had minor variations with respect of wind speed but the power spectral density was dependent on wind speed. In all cases, the second mode shape appeared to be the result of pressure pulsations. All faces were simultaneously either under compression or suction, with the windward face having the smallest absolute value of pressure. Figure 3.26 shows the second POD mode and its power spectral density for 14≤U≤28m/s. At this wind speed range, the energy was mostly located at the low frequencies. Nevertheless, the situation of the spectral density function changed for larger values of wind speed. At U=33 m/s and 38 m/s, the energy were concentrated at frequencies around one or twice the value of the Strouhal number, as can be seen in Figure 3.27. It must be clarified that St=0.12 corresponds to the frequency at which one vortex is shed from one side of the prism while a peak at twice this frequency represented the combined effect of vortex shedding from the two faces of the prism.

It is important to point out that the similarities of the present results with those obtained by Kikuchi et al (1997) and Cosentino and Benedetti (2005) are much more important than the differences; the latter are attributable to different test conditions. First of all, the aforementioned references placed the square prism vertically, having thus a reduced effect of the proximity between the prism and the walls of the wind tunnel. Other differences in the testing conditions are the Reynolds number, the oncoming flow turbulence and the presence of the roof model inside the wind tunnel.

The current experiment and analysis provided confidence in the POD data reduction program elaborated for this study.

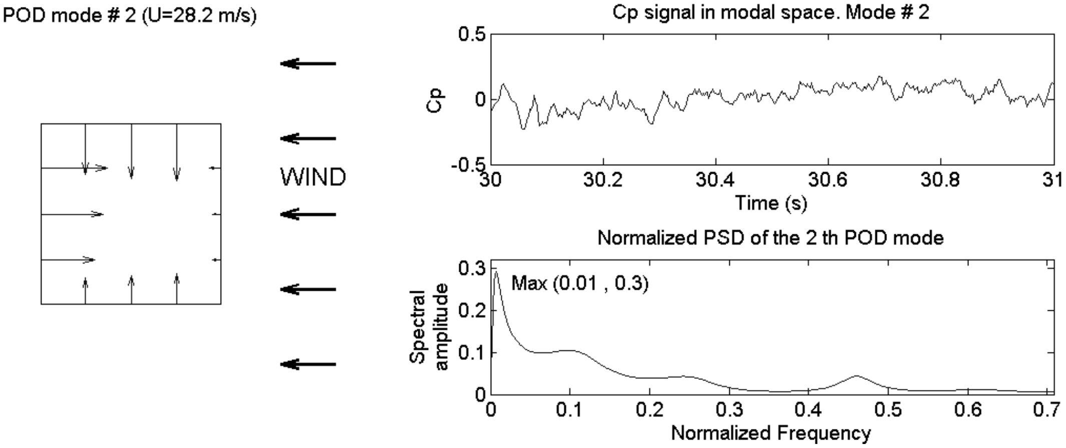

Figure 3.26 Second POD mode for the square prism. Similar for wind speed range 14≤U≤28m/s.

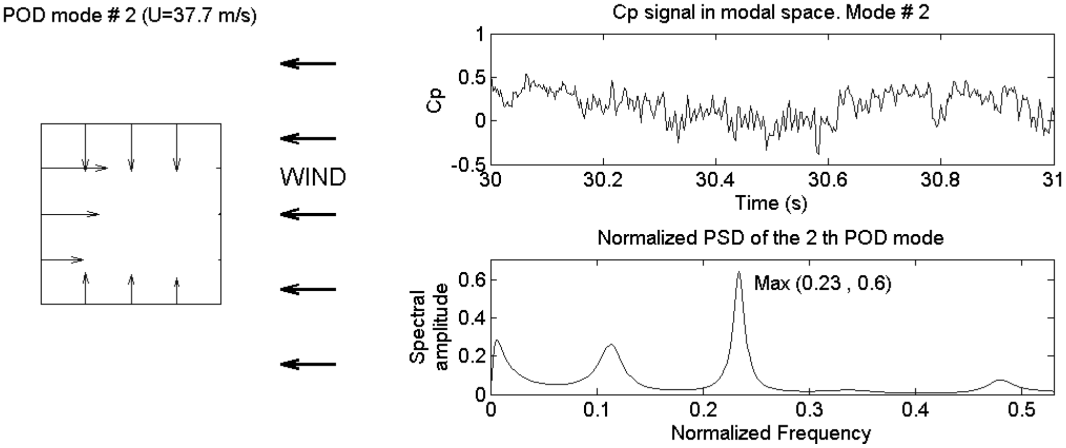

Figure 3.27 Second POD mode for the square prism. U=33 m/s and U=38 m/s.

### 3.5.2 POD analysis of the roof model in the vortex trail of the square prism

Since the roof model was immersed in the vortex trail of the square prism, the following results have to be observed in parallel with those just described in the previous section. Particularly, it was observed again that all results remain practically unchanged in the wind speed range of 14-33 m/s but there are some noticeable differences when the wind speed reached 38 m/s.

**Mean pressure coefficients, Cp.**

The mean pressure coefficients (Cp's) are plotted on Figure 3.28. The Cp's on the roof remain unchanged for wind speeds between 14 m/s and 33 m/s (left graph). There is a slight variation on the pressure coefficients obtained for wind speed U=38 m/s (right graph). Such variation seems related to the lock-in phenomena, which increased the strength of the vortices and thus affected the width of the wake behind the prism. The mean pressure coefficients on the roof immersed in the vortex trail of the square prism are significantly lower than those obtained in smooth flow because the mean wind speed behind the square prism was reduced (see Figure 3.18) while the reference pressure was still based on the wind speed of the free flow ahead of the prism.

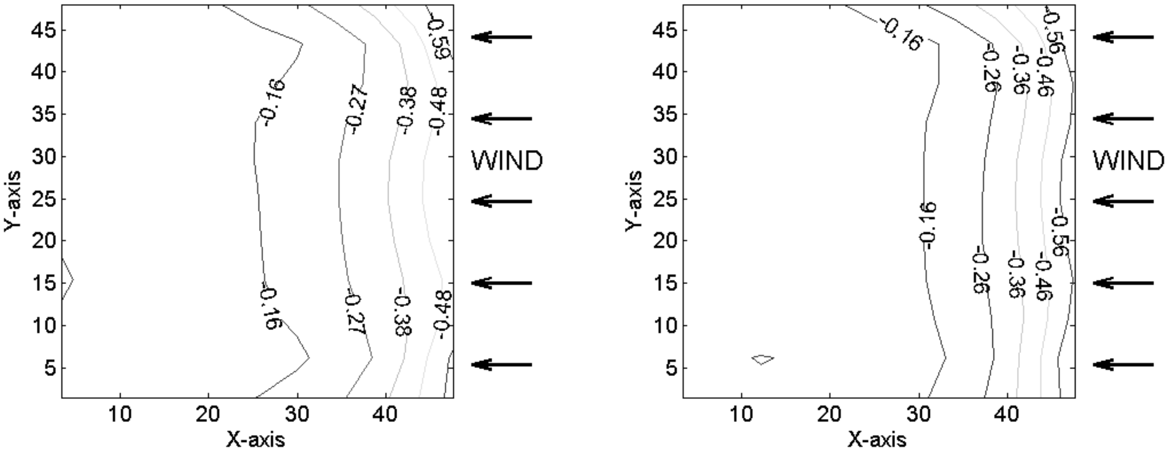

Figure 3.28 Mean pressure coefficients for the hanging roof. Left: 14<U<33m/s. Right: U=38m/s.

**Root-mean square values of pressure coefficients, RMS.**

The RMS values are shown in Figure 3.29. These values remain practically unchanged for 14<U<33 m/s (left graph). The slight changes in the distribution of the RMS values when the wind speed reaches 38 m/s (right graph) do not seem to be sufficient reason to justify the significant changes in the energy distributions obtained with the POD analysis, which are shown in Figure 3.31 and discussed below. Similarly to the previous section, the reason was found in non-proportional changes in the off-diagonal covariance matrix elements, most likely caused by the lock-in phenomena discussed above.

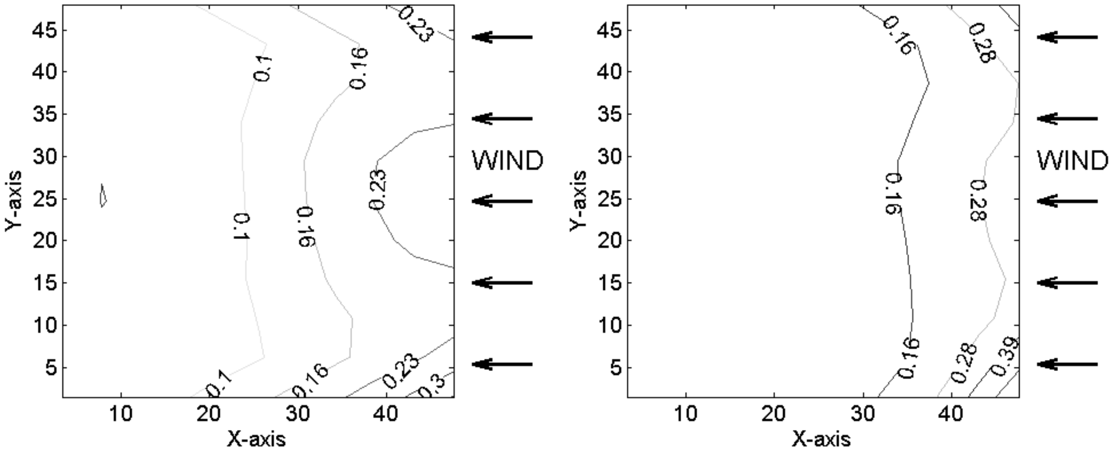

Figure 3.29 RMS values of pressure for the roof model. Left: 14<U<33m/s. Right: U=38m/s.

**Peak values.**

The distribution of the peak values of the pressure coefficients are practically identical for wind speeds ranging between 14m/s and 33m/s. This distribution is indicated in Figure 3.30 (left). The peak value distribution for the case of U=38m/s is shown in Figure 3.30 (right), which differs slightly from the previous figure in the values reported at the corners of the leading edge. The ratios between the zero-mean peak values and the rms values of pressure coefficients are similar to those discussed for the case of smooth flow.

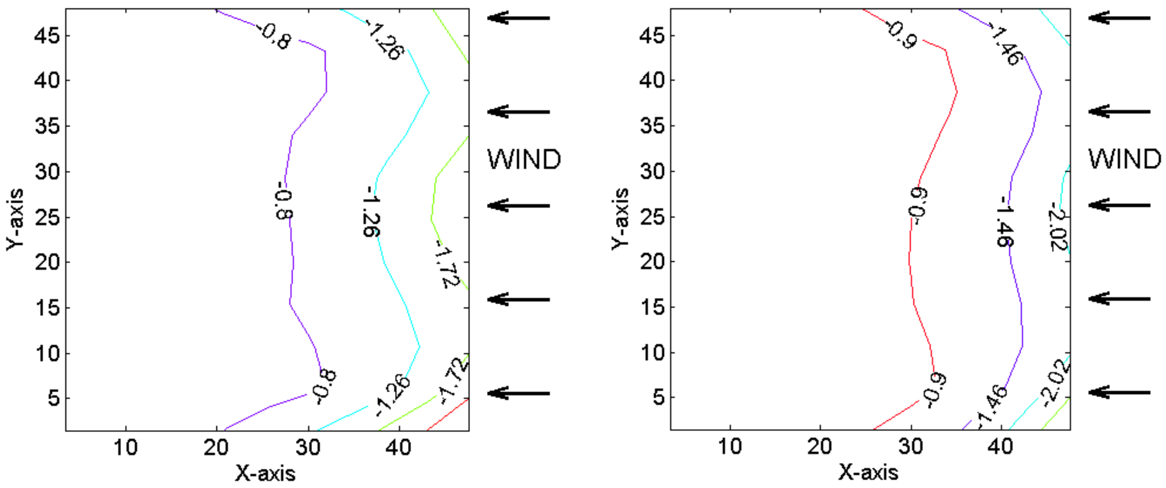

Figure 3.30 Peak values of pressure coefficients for the hanging roof. Left: 14<U<33m/s. Right: U=38m/s.

**Energy distribution (eigenvalues).**

The energy distribution of the POD modes is shown in Figure 3.31. As it can be seen on the left graph, the first POD mode has an energy contribution of 35% out of the total kinetic energy involved, for wind speeds between 14 m/s and 33 m/s. When the wind speed reached 38 m/s the first POD mode increased its energy content up to 60%, as shown on the right graph.

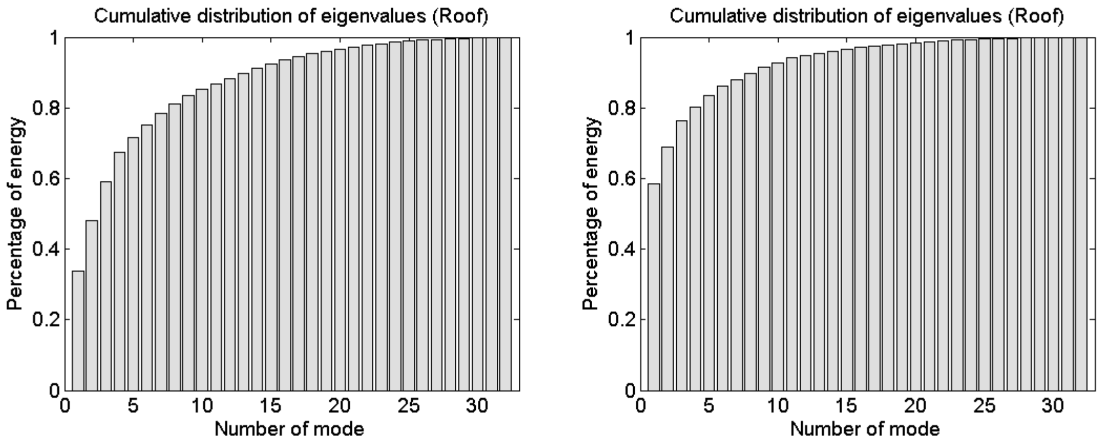

Figure 3.31 Cumulative energy distribution per mode. Left: 14<U<33m/s. Right: U=38m/s.

The first POD mode and its corresponding spectrum density function for U=38 m/s are shown in Figure 3.32. A 3D view of the mode is depicted in Figure 3.33. The sharp peak of the spectrum reflects the quasi-harmonic behaviour of the mode with most of the energy contained near the Strouhal frequency (St=0.12). The shape of the mode is fairly symmetric with respect to the direction of the wind flow. Large pressure oscillations can be seen at the leading edge, especially on the corners.

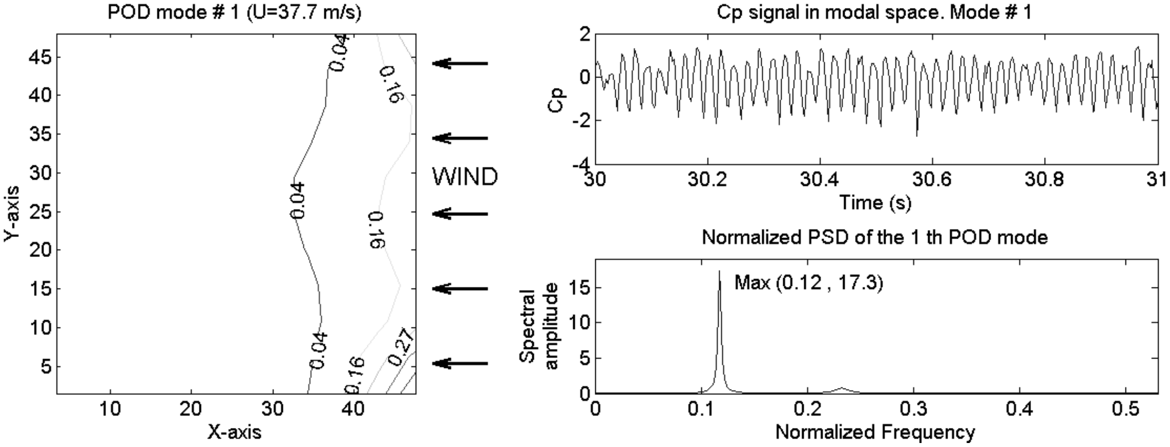

Figure 3.32. First POD mode and its corresponding spectral density at U=38m/s.

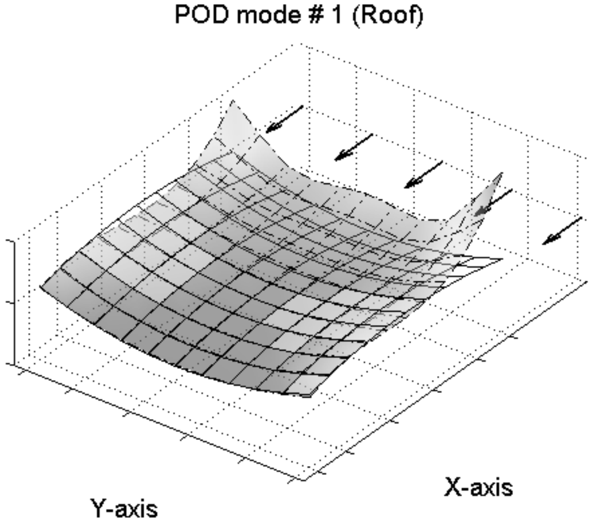

Figure 3.33. First POD mode in 3D view. U=38m/s.

The second and third POD modes are shown in Figure 3.34 to Figure 3.36. The mode shapes seem to be the mirror of each other with very similar spectral densities that indicate a high-energy content concentrated around the Strouhal frequency. The pressure fluctuations are more significant at the leading edge.

The fact that the three first POD modes have spectral peaks at the Strouhal frequency is an indication that all three modes are related to the vortices shed from the square prism. As stated at the beginning of the section, the results should be examined in parallel with those of the previous section ("POD analysis for the square prism"). Once again, it should be noted that the cases of the roof and the prism were analyzed from two independent covariance matrices. The reader should not deduct that the i-th POD mode on the roof is in direct connection with the i-th POD mode on the prism. In fact, several modes shown in this chapter indicate that they are related to the same phenomenon (vortex shedding), which means that the POD method was not able to completely isolate the vortex shedding in one single mode.

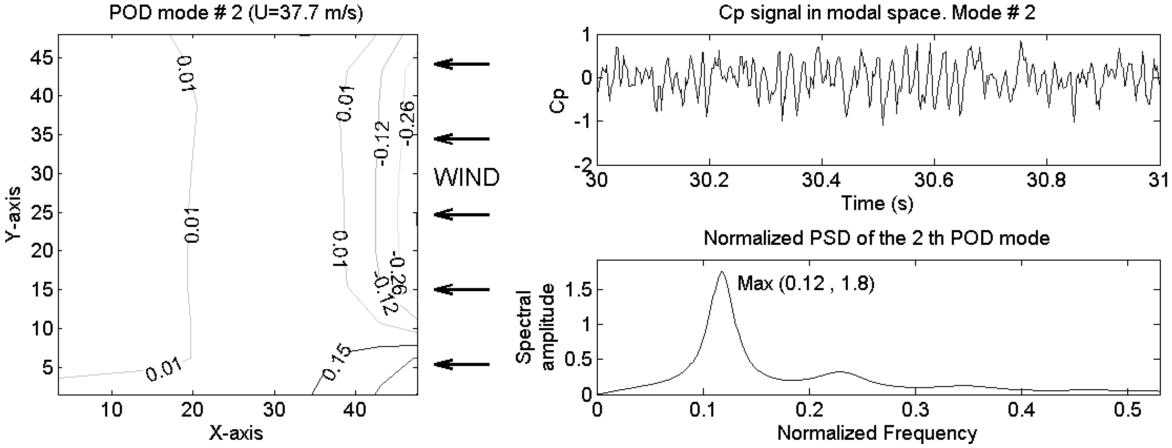

Figure 3.34. Second POD mode for U=38m/s.

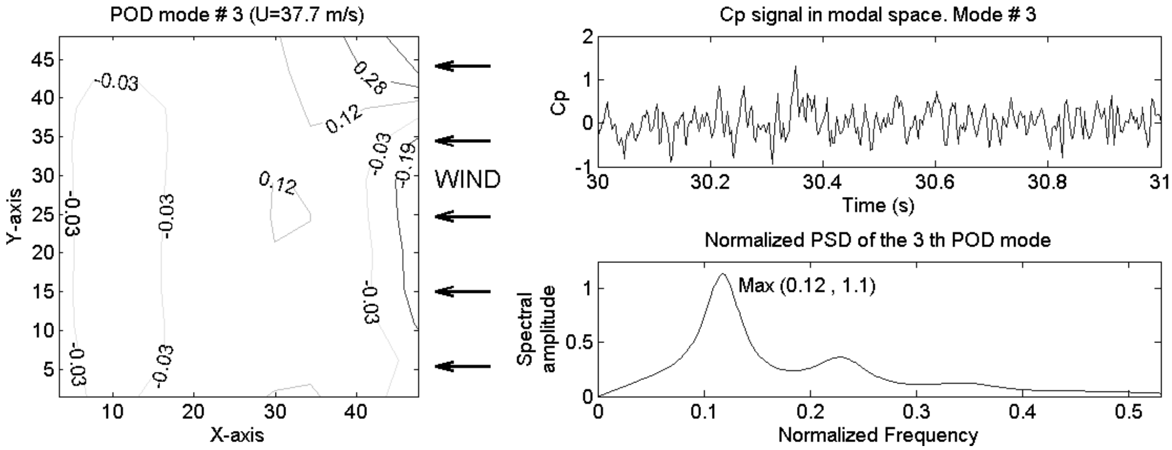

Figure 3.35. Third POD mode for U=38m/s.

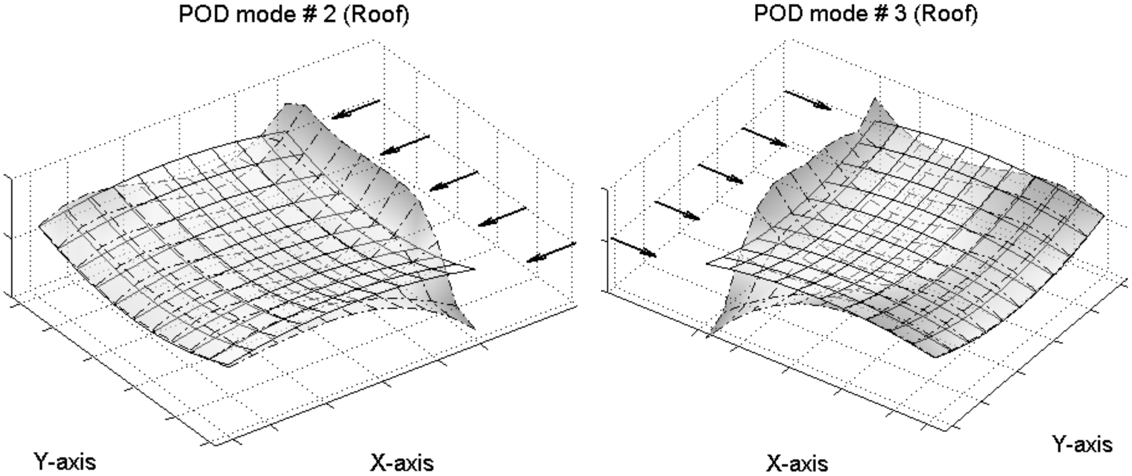

Figure 3.36. Second and third POD modes in 3D view. U=38m/s.

## 3.6 Conclusions

- The proper orthogonal decomposition was used to study the unsteady pressure field on the surface of a roof model under smooth flow conditions and also for the case of the roof immersed in the vortex trail of a square prism. This latter case allowed the study of the pressure field around a square prism as well.
- Data analysis of these experiments provided a good insight for the use of the POD in wind engineering.
- It was possible to validate the present results with those available in the literature, thus, providing confidence in the numerical code written by the author.

- The POD method provides mode shapes that suggest real physical flow structures in some cases but in other cases the mode shapes are only mathematical structures. Experience and intuition are necessary for the interpretation of the results.
- The slight asymmetry caused by the over-passing wall on the roof model was large enough to produce notorious asymmetries on some POD modes.

# Chapter 4 POD ANALYSIS ON A TELESCOPE

## 4.1 Introduction

The Hertzberg Institute for Astrophysics of the National Research Council Canada (NRC) required a series of wind tunnel tests on the model of a Very Large Optical Telescope (VLOT). The tests were performed in a 1:100 scale model of the 51m-diameter spherical enclosure and 20m-diameter mirror assembly. The study was performed in the ¾-open-jet pilot wind tunnel of the Aerodynamics Laboratory of the NRC. This wind tunnel is the same facility where the experiments of the roof model of the previous chapter took place, except that the experiments on the telescope model do not include a plenum chamber.

The purpose of these experiments was to evaluate the effects of wind-induced forces on the mirror assembly. Given its large dimensions in real scale, the mirror cannot be built in a single piece but from smaller segments of 1 to 2 $m^2$. In order to ensure that the segments are properly levelled at all times, each segment must be controlled by an actuator connected to a feedback system. The physical design of the supporting system along with the algorithm for controlling its response will require a good understanding of the wind load patterns and their frequency content. Thus, the POD was considered a possible convenient tool for revealing the hidden flow structures around and inside the telescope, which in turn would assist in the definition of the control algorithm of the actuators.

It was necessary to cover a wide range of combinations of wind speed and orientation. Additionally, a few physical modifications to the spherical enclosure were performed in order to reduce the effects of wind loads. Small modifications consisting in alterations to the opening lip did not reduce the wind effects. Therefore, it was decided to drill big holes around the enclosure, which produced a new set (called the ventilated case) of experiments. All these configurations produced a large database consisting of over a thousand wind tunnel runs.

The preliminary reports of Cooper et al (2004a, 2004b) provided a significant insight to the problem and it allowed to reduce the number of cases to be analyzed with the POD method. Nevertheless, the amount of combinations is still in the order of a few hundreds and the presentation of results needs to be done methodologically. Given their significant differences, the sealed and ventilated cases are treated separately.

## 4.2 Telescope model and the testing conditions

### 4.2.1 Model description

The geometrical scale of the model was 1:100. The external diameter of the enclosure was 0.51 m and the mirror diameter was 0.20 m. The opening of the enclosure had a radius of 0.12 m. The model was built using a stereo-lithographic manufacturing process (SLA), which allows the tubing system to run within the walls of the enclosure and the mirror. The telescope ensemble and its installation in the wind tunnel are shown in Figure 4.1.

There were a total of 149 effective pressure taps. Twenty-four of them were distributed on the inner side of the enclosure, eighty-nine taps on the outer side of the enclosure and thirtysix taps on the mirror (Figure 4.2). The tubing system was connected to three HyScan ZOC™ 33 and one ZOC™ 23B pressure scanners. The sampling frequency was set to 400 Hz. As with the roof model tests, corrections were made in order to take into account the time delay between channels and the signal distortion due to the tubing system. Additionally, blockage correction was performed.

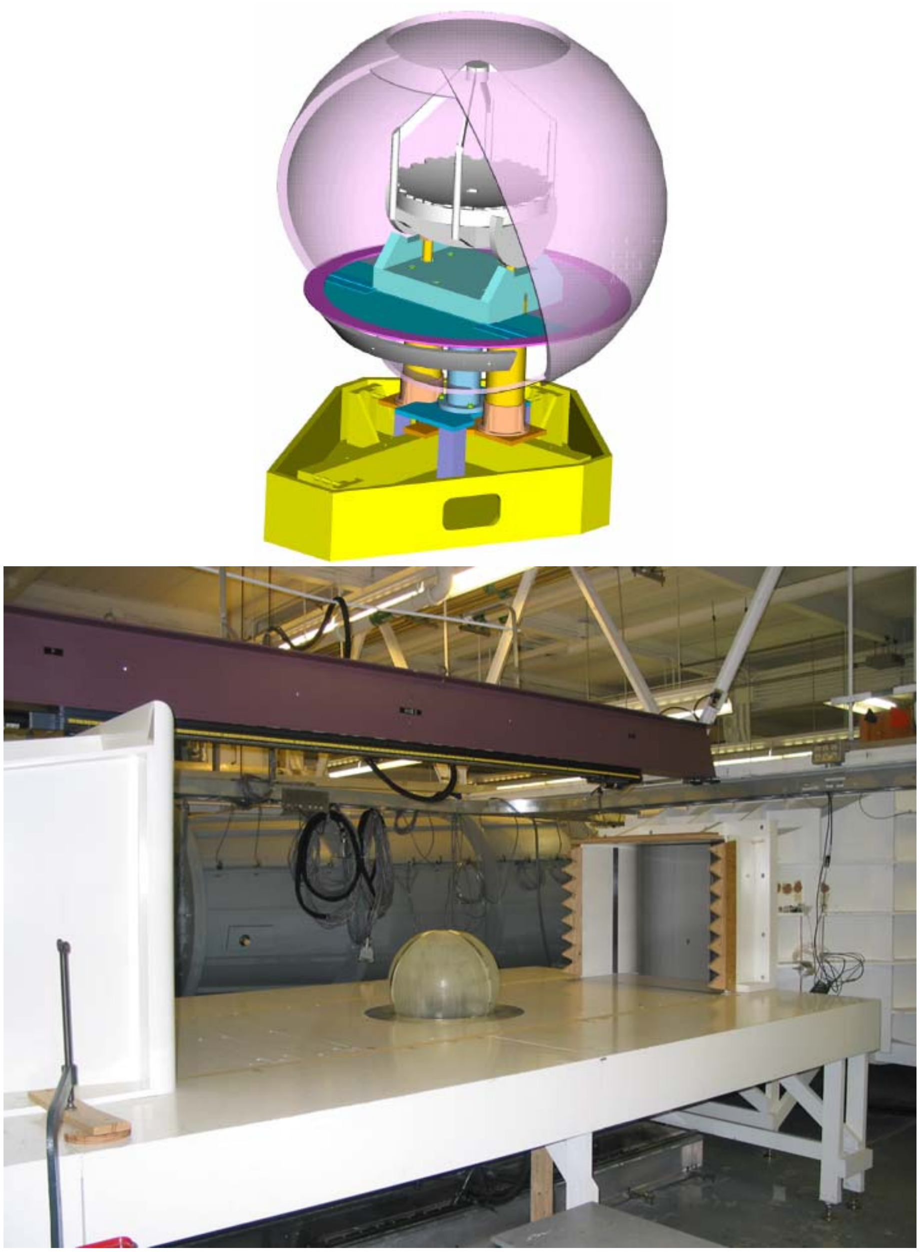

Figure 4.1 The telescope ensemble and its position inside the pilot wind tunnel (after Cooper et al 2004).

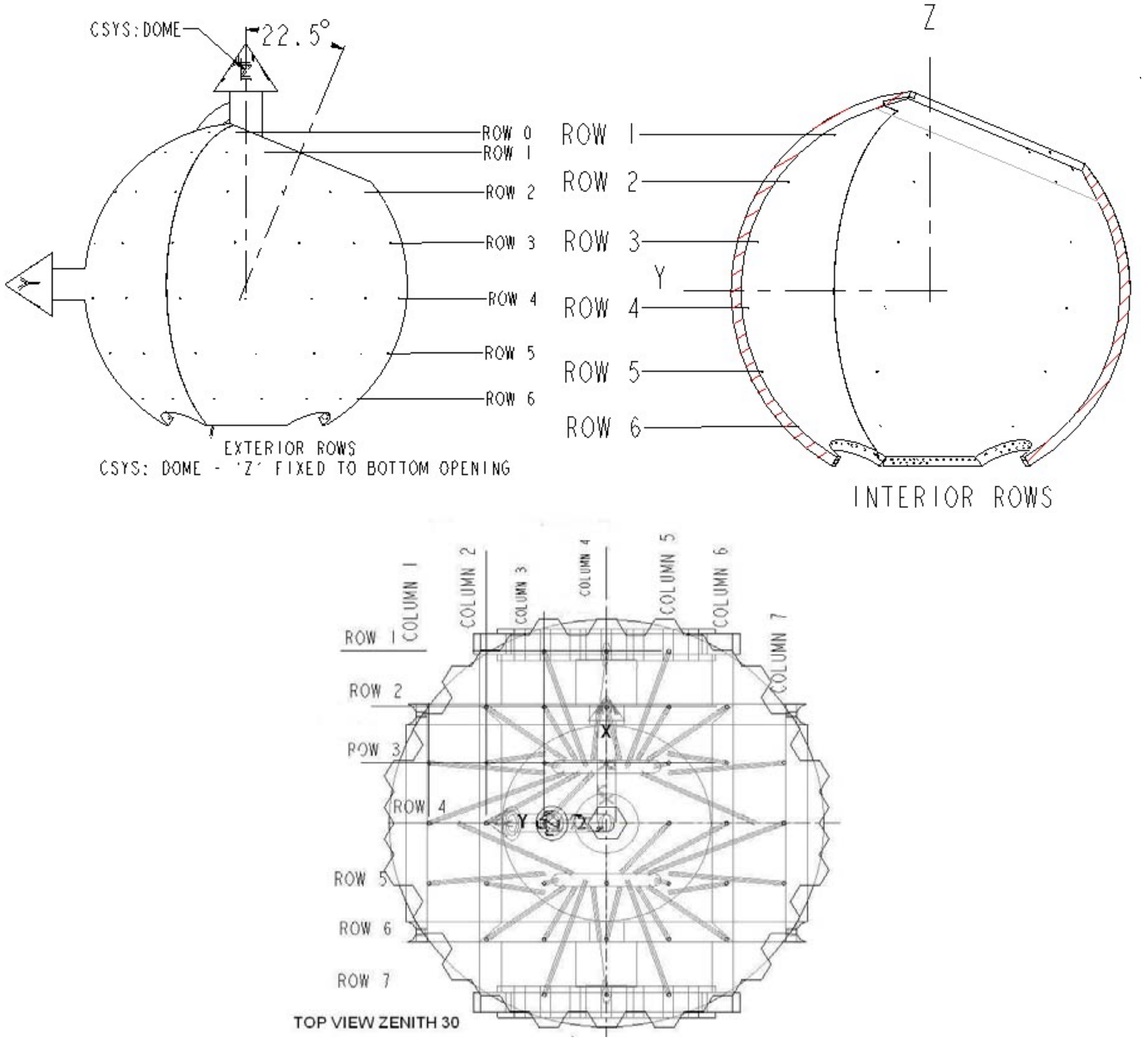

Figure 4.2 Pressure tap distribution. From left to right: outer enclosure, inner enclosure, mirror (after Cooper et al 2004).

Two coordinate systems were used, a global system fixed to the wind tunnel and a local system attached to the enclosure. The global coordinate system XYZ was fixed to the wind tunnel. The X-axis was horizontal and perpendicular to the wind flow. The Y-axis indicated the direction of the wind flow, with the wind approaching from Y=-∞. The Z-axis was the vertical axis. The local coordinate system X'Y'Z' was attached to the enclosure and it coincided with the global system in the initial position at θ=0° and ϕ=0°, that is, when the opening was horizontal (Figure 4.3 left).

The enclosure and the mirror sit on a cradle, which in turn sits on a turntable. The cradle allows zenith rotations around the X'-axis at fixed angles ϕ=0, 15, 30, and 45°. The turntable allows azimuth rotations around the Z-axis from θ=0 to 180° with increments of 15 degrees. Therefore, there are 40 different enclosure orientations. Notice that, because of symmetry, there is no need for azimuth rotation at ϕ=0°. Figure 4.3 shows three orientations.

Since the local environment for the full-scale structure was not known, the tests were carried out in smooth flow conditions for $10\,m/s \le U \le 40\,m/s$. Each combination of wind speed, zenith and azimuth rotation defined a test configuration.

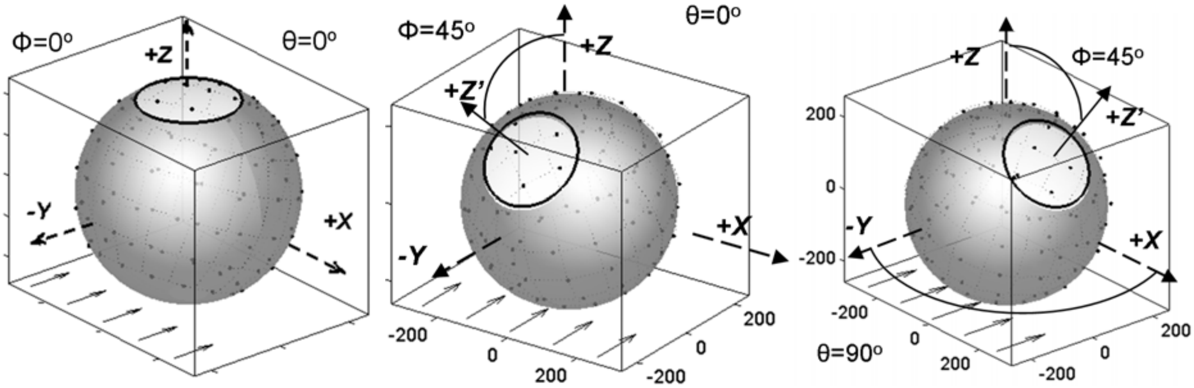

Figure 4.3 Coordinate systems and some enclosure orientations.

### 4.2.2 Similarity and non-dimensionalization

The telescope model was conceived to satisfy the geometrical similarity condition only, including the effects of the enclosure's surface roughness. The kinematic similarity condition could not be met since, as stated before, the local environment for the prototype is not known. The model was not intended to be dynamically similar to the prototype, only the dynamic loads on the mirror were measured.

The three dimensionless numbers described in section 2.3 (Re, St and $S_H$) are used in the current chapter. The following paragraphs indicate the range of values adopted for these numbers during the tests on the telescope model.

**Reynolds number (*Re*)**

The calculation of the Reynolds number was based on the external diameter (D) of the enclosure as the characteristic length. For D=0.51m, ν=1.46x$10^{-5}$ $m^2$/s and a wind speed range of $10\, m/s \le U \le 40\, m/s$, the Reynolds number ranged from $3.5 \times 10^5$ to $1.4 \times 10^6$.

The critical Reynolds number is identified by a sudden drop in the drag forces exerted by the fluid on an object immersed in it. This critical number is not only a function of the global geometry of the object but also of its surface roughness. The roughness of the sphere used in the experiments was measured as k/D=25x$10^{-5}$, where k is the mean roughness height. Figure 4.4 shows the critical Reynolds number for spheres with three different roughnesses. From the figure it can be seen that the critical Re for a sphere with roughness of 25x$10^{-5}$ occurs at Re=2.5x$10^5$ and therefore all the tests involved in this chapter are above the critical Reynolds number.

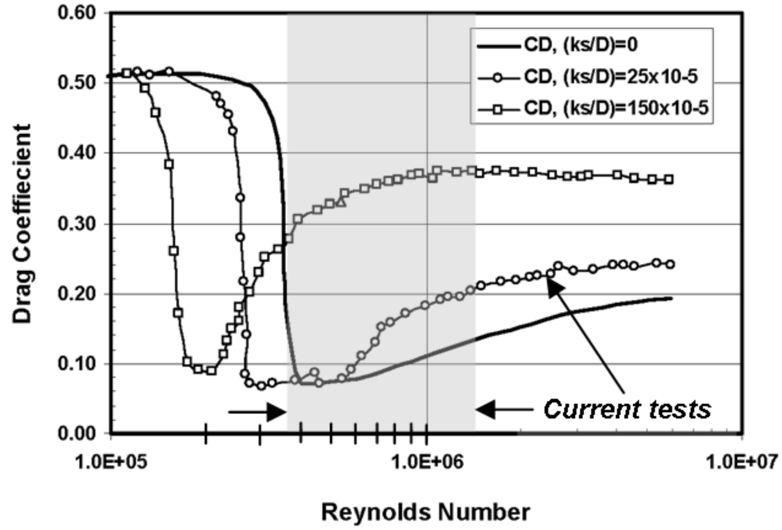

Figure 4.4 Critical Reynolds number for spheres with different roughness; after Cooper et al (2004).

**Strouhal number (*St*)**

The Strouhal number is associated to vortex shedding from bluff bodies. In dealing with flow past a sphere, Sakamoto and Haniu (1990) provided a collection of Strouhal numbers from several sorces for Reynolds number ranging from 400 to 1x$10^5$. These results are shown in Figure 4.5 and they indicate that more than one Strouhal number can coexist for flow past a sphere. The two types of Strouhal numbers used in this chapter are classified as low-frequency Strouhal number and high-frequency Strouhal number.

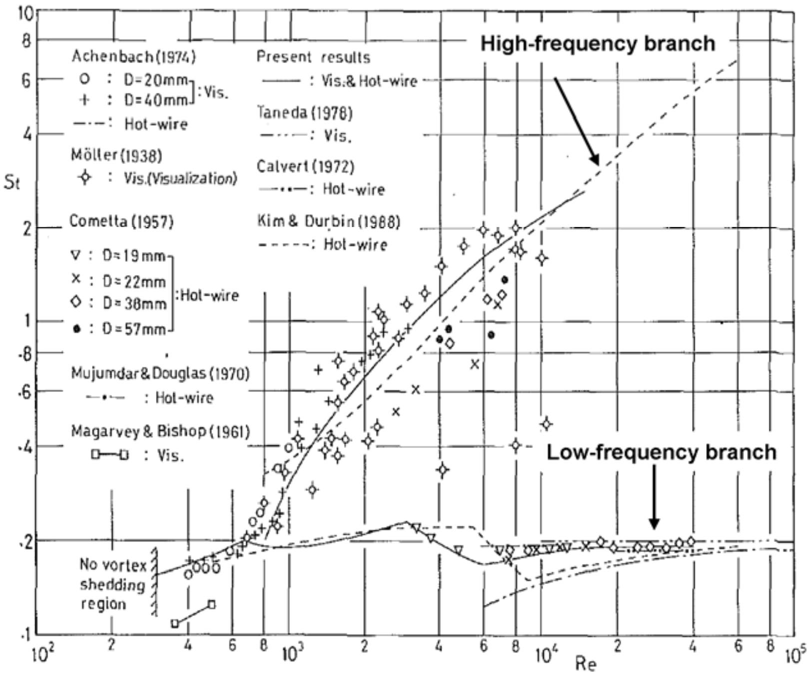

Figure 4.5 Strouhal number vs Reynolds number for flow past a sphere in the range 400<Re<1x$10^5$; after Sakamoto and Haniu (1990).

### *Low-frequency Strouhal number.*

The low-frequency Strouhal number is related to large-scale instabilities in the vortex wake and most references agree that its value remains in a narrow range of 0.13 and 0.20 for Reynolds numbers between 400 and 3x$10^5$.

The low-frequency Strouhal number is based on the external diameter of the sphere,

$$St = f \cdot D/U$$

where *f* is the frequency, in Hz, at which the vortices are shed.

Achenbach (1974) performed a series of measurements with hot-wire anemometers for detecting vortex shedding from spheres in Reynolds numbers ranging from 6x$10^3$ to 5x$10^6$. Nevertheless he was unable to measure any prevailing frequency associated with the low-frequency vortex shedding at Reynolds numbers greater than 3x$10^5$. He could not establish the reason for the lack of periodic vortex shedding after this value but he pointed out that this value coincided with the critical Reynolds number discussed in the previous section (Figure 4.4). The author could not find references reporting low-frequency vortex shedding past a sphere for Reynolds number beyond this critical value but the results of the POD analysis discussed in this chapter indicate the existence of weak low-frequency vortex shedding at Strouhal numbers of the order of 0.25.

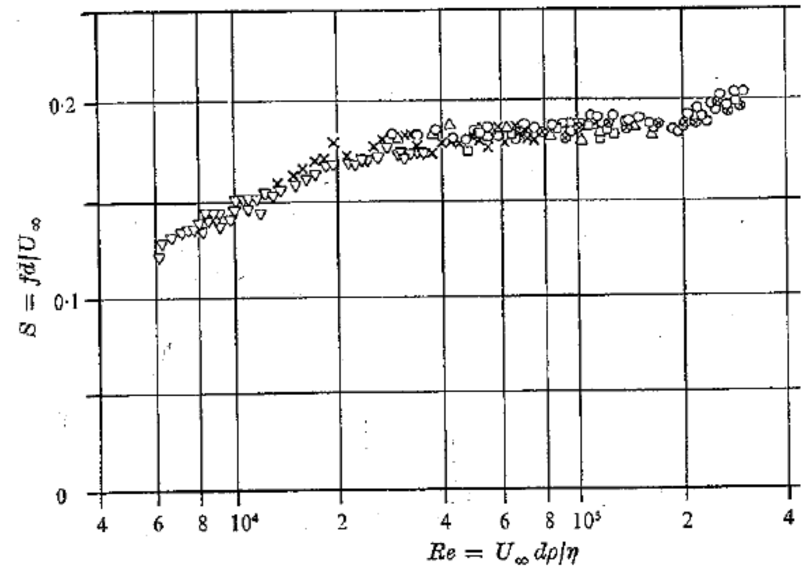

Figure 4.6 Strouhal number vs Reynolds number for flow past a sphere in the range $6x10^3<Re<3x10^5$; after Achenback (1974).

Achenbach also provided a schematic representation of the low-frequency vortex shedding for flow past a sphere. His drawings shown in Figure 4.7 represent the flow structure as observed from two perpendicular directions. He explained that as the Reynolds number increases, "...the loops lose their individual character immediately after the rolling-up of the vortex sheet. They grow together and penetrate each other." Achenbach also noticed that when the lower critical Reynolds number was exceeded, the Strouhal number incresead by one order of magnitude. He could not find an explanation for this phenomenon but as it is described below, new flow structures occur in what is presently called high-frequency Strouhal number.

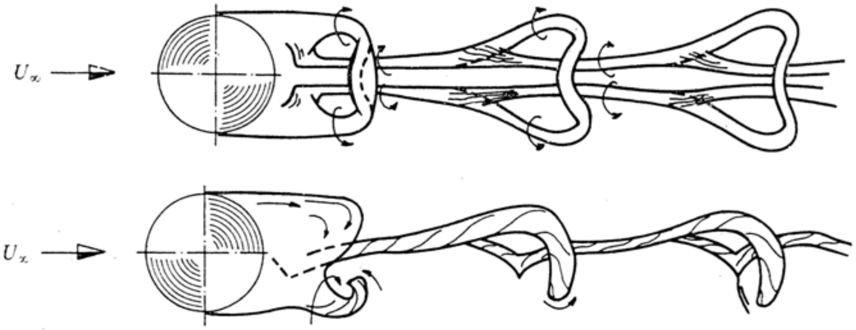

Figure 4.7 Schematic representation of the vortex configuration in the wake of spheres at Re=$10^3$; after Achenback (1974).

### *High-frequency Strouhal number.*

The high-frequency Strouhal numbers, $St_s$, are associated to small-scale instabilities in the shear layer. It is known that the free shear layer rolls up into a series of coherent eddies that are shed periodically at a frequency $f_s$. In fact, it has been recognized that this type of vortex shedding is organized in free-shear-layer modes.

In the particular case of spheres with openings, the frequency $f_s$ can be calculated as follows (Rossiter 1966):

$$f_s = \frac{U(m-\gamma)}{L_e\left(M+\dfrac{1}{\kappa}\right)}$$

where

$L_e$ = effective enclosure opening length, here chosen as 0.155m in order to match the observed frequencies,

m = shear layer mode number, 1,2,3,...,

$\gamma$ = 0.25 (phase lag, in fractions of a wavelength of the vortex flow, between the vortex impinging on the downwind edge of the opening and the arrival of the resulting pressure pulsation at the vortex formation location), M = Mach number,

$\kappa$ = proportion of free-stream velocity at which the shed vortices travel over the cavity; decreasing from 0.72 for mode 1 to 0.60 for mode 2 and then to a constant 0.57 for mode 3 and higher (Naudascher and Rockwell 1994).

The continuous straight lines in Figure 4.8 represent the theoretical values provided by the formula above for predicting the frequency at which the shear layers are shed from the enclosure. The figure shows theoretical and experimental values for the first four shear layer modes and for the low-frequency vortex shedding mechanism. The experimental values are represented by markers and the size of the markers is a quantitative indication of the magnitude of their respective spectral peaks. Furhter discussion of this figure will be given in the following sections but for now, its purpose is to present a comparison between the theoretical and experimental values of low-frequency and high-frequency vortex shedding.

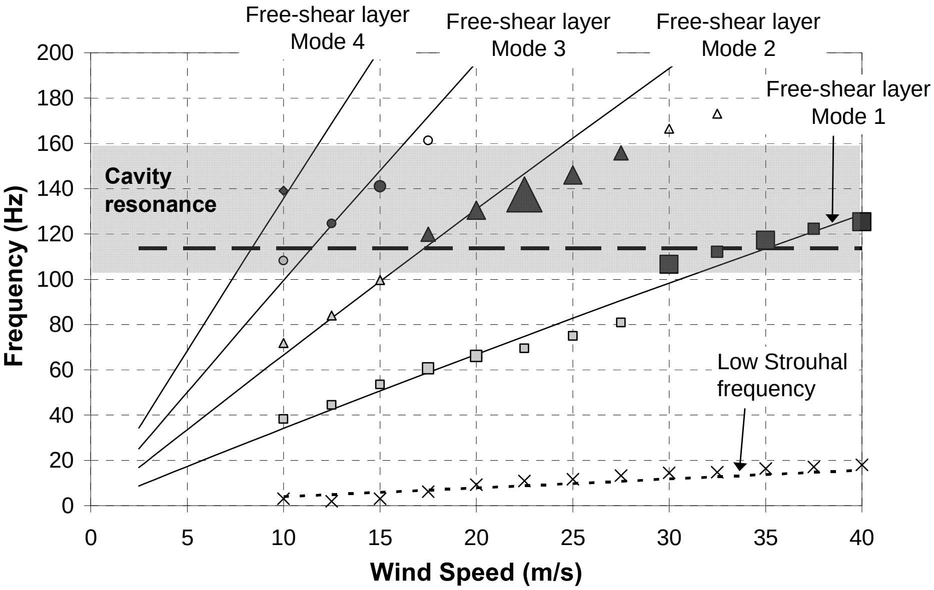

Figure 4.8 Characteristic frequencies for different flow structures. The straight lines represent the theoretical predictions and the markers indicate experimental values obtained with the first POD mode on the mirror. The size of the marker is an indication of the magnitude of the spectral amplitude.

It is important to mention that the shear layers may separate and impinge on other parts of the enclosure. In particular they may impinge over the opening, causing an acoustic excitation inside the cavity. This possibility is depicted in Figure 4.9. The curved arrow in the figure indicates that the wake is in fact oscillating. The oscillations or instabilities in the wake occur with a mixture of the frequencies discussed in the paragraph above.

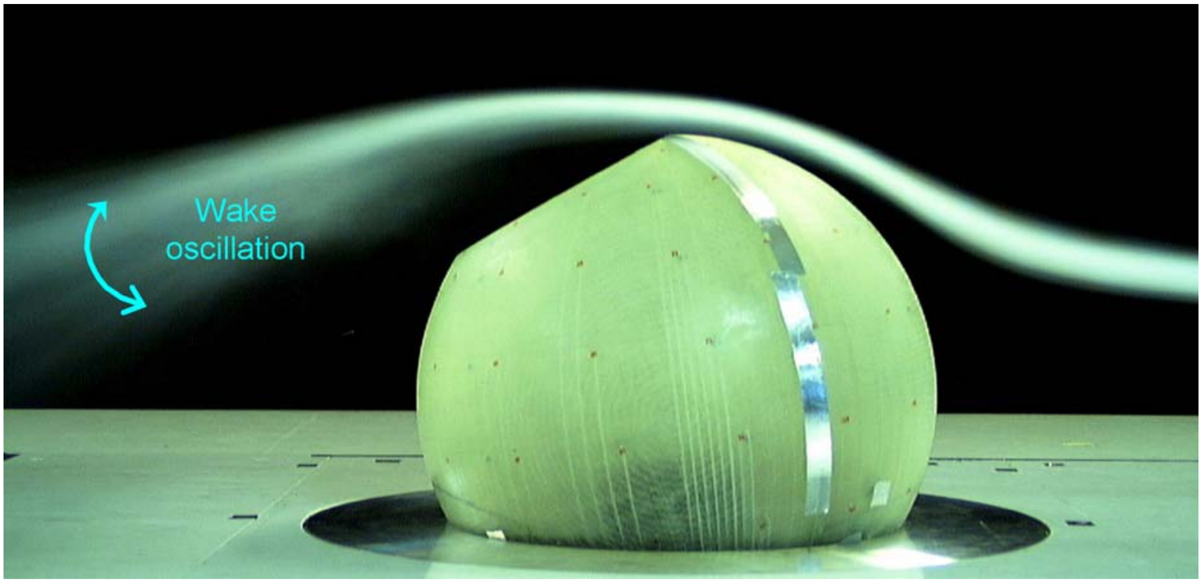

Figure 4.9 Shear layer separation from upstream lip: after Cooper et al (2004).

**Helmholtz number ($S_H$)**

The Helmholtz number is related to the acoustic resonance in the enclosure cavity. It can be calculated as follows:

$$S_H = \frac{f_H D_i}{V} = \frac{D_i}{2\pi}\sqrt{\frac{A}{\Lambda \ell_e}}\left(\frac{c}{U}\right)$$

where:

Di = enclosure internal diameter, 0.50 m at model scale,

$\Lambda$ = $5.86\text{x}10^{-2}$ m$^3$ is the internal volume of the enclosure,

$f_H$ = Helmholtz frequency, Hz,

c = speed of sound, 343 m/s at 20°C in the wind tunnel,

A = area of the enclosure opening, $4.52 \times 10^{-2}$ m$^2$ at model scale,

$\ell_e$ = length of air column oscillating at the cavity opening. It is estimated as the entrance passage length plus the effective length of the air column on either side of the opening that moves with the air in the opening.

= d + 2(0.75)r = 0.01+0.18 = 0.19 m.

(U/c) = the flow Mach number.

This phenomena may cause strong pressure pulsations inside the enclosure that propagate in all directions. In particular, these pulsations can affect the upstream shear layer separation mentioned previously, thus generating a vibrating system that is self-amplified.

From the expression and values described above, the Helmholtz frequency is estimated as follows: $f_H = \frac{c}{2\pi}\sqrt{\frac{A}{\Lambda \ell_e}} = 113.6$ Hz. Note that this frequency is independent of wind speed. The intensity of the acoustic resonance depends weather or not the shear layer separation impinges the enclosure opening at a frequency near this value. Although the theoretical estimation of the Helmholtz frequency is 113.6 Hz, the experimental results show significant acoustic amplifications between 106 Hz and 156 Hz, with the largest peak occurring at 137 Hz (see Figure 4.8). The difference between the latter value and the numerical estimation may reside in the calculation of the length of air column oscillating at the cavity opening.

### *Application to full-scale.*

Given that the model/prototype velocity scale to 1:1 and that the length scale is 1:100, the time runs hundred times faster at model scale. Thus, the 400 Hz sampling rate at model scale is equivalent to a 4 Hz sampling rate at full-scale. Given that each record contains 15330 samples, each record represents just over 1 hr of pressure data at full-scale. In order to use the recorded pressure coefficients for different wind speeds than those at which the wind tunnel tests took place, it is necessary to multiply the pressure coefficients by the dynamic pressure $0.5\rho U^2$. Notice that the properties of flow past a sphere change significantly at different wind speeds and therefore it is not recommended to extrapolate far from the wind speed range at which the tests were carried out originally ($10 \leq U \leq 40$m/s).

## *4.3 POD analysis for the sealed case*

As mentioned before, there are a large number of combinations of wind speed, azimuth and zenith rotations. The results of each combination are summarized in several graphs. The presentation of this large amount of graphs is impractical and therefore, only a selected number of cases are described in detail. The understanding of these few cases is necessary in order to discuss more abstract graphs that condense the most significant information obtained from all cases. As for the case of the roof, the discussion of flow past the telescope enclosure includes the description of the mean pressure coefficients, the root-mean-square values of pressure, and the POD modes with their spectral density functions.

In a similar way to the case of the roof model and the square prism, the POD analysis for the telescope model was split into different analyses. The low correlation between the outer taps and the inner taps provided a reason to construct three independent covariance matrices—one for the outer taps, one for the inner enclosure taps and a third matrix for the mirror taps. This decision is believed to improve the efficiency of the POD method in extracting the flow structures that are specifically related to the mirror. Although the flow past a sphere shows an interesting behaviour (Achenbach 1974), it has to be clear that the ultimate purpose in this chapter is to evaluate the wind loading on the mirror.

### 4.3.1 Zero-zenith angle and zero-azimuth angle

The first case to be analyzed is the enclosure in a zero-zenith and zero-azimuth orientation (Figure 4.3-left). Since this orientation provides complete symmetry around the Z-axis, it was unnecessary to perform azimuth rotations. The only parameter that changed was the wind speed. This case is a good opportunity to get familiar with the graphics that will be referred for all other orientations.

**Mean pressure coefficients, Cp.**

The distribution of mean pressure coefficients (Cp) for the enclosure is shown in Figure 4.10. The distribution is in agreement with previous studies for wind past a sphere. The highest positive pressure coefficient always occurs at the stagnation point and it has a value of 1.0. The collection of points with nil-pressure defines a circle at about 42 degrees from the stagnation point. The circle of nil-pressure is represented by the transition between the blue and green tones. The lowest value of the mean pressure coefficients is here defined as **Cpmin** and it is used to identify the combination of orientation and wind speed that produced the highest suction (in the mean sense).

There is no need to show the mean pressure distribution on the mirror because it is practically constant over the whole surface of the mirror, with values of $Cp = -1.12 \pm 0.05$. Thus, for this orientation, the enclosure opening acts as a big pressure tap.

The distribution of the mean pressure coefficients for both, the enclosure and the mirror, remained practically constant in the whole wind speed range (10<U<40 m/s). Figure 4.11 shows the variation of Cpmin as a function of wind speed. Since the variations are small with no apparent functional pattern, it is concluded that the mean pressure coefficients were insensitive to wind speed for zero-zentih and zero-azimuth orientation.

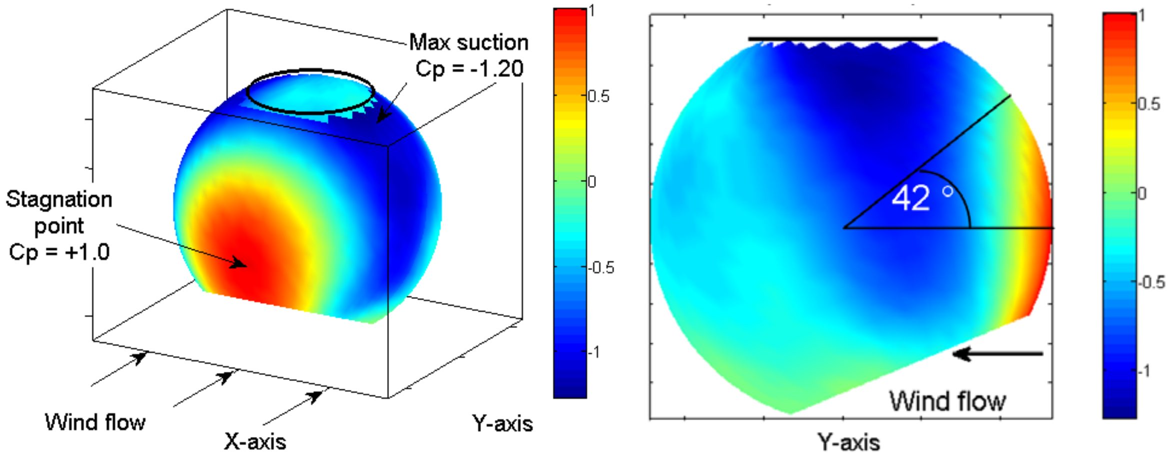

Figure 4.10 Mean pressure coefficients for the enclosure. ϕ=0°, θ=0°, 10≤U≤40m/s.

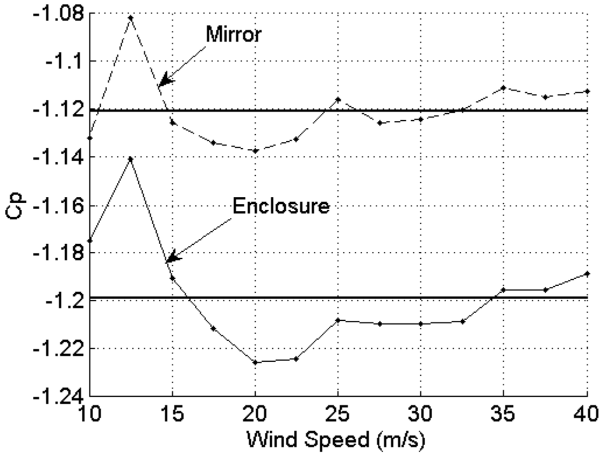

Figure 4.11 Variation of Cpmin with respect to wind speed. ϕ=0°, θ=0°, 10≤U≤40m/s.

## Root-mean square values of pressure coefficients, RMS.

The RMS values of pressure coefficients are shown in Figure 4.12 and Figure 4.13 for the lowest and highest wind speeds, respectively. The figures show the leeward side of the enclosure because the highest values of RMS occur on this side, while the windward side has very low values of RMS. At a first glance, the two graphs look very similar, but a more careful observation evidences two significant differences. First of all, the highest values of RMS on the enclosure moved from one location to another, as indicated in the figures. The second outstanding difference between the two plots is the magnitude of the RMS values on the mirror.

The transition between Figure 4.12 and Figure 4.13, i.e. for 10≤U≤40 m/s, is represented by Figure 4.14. It can be seen that the RMS values obtained from the pressure taps on the enclosure were relatively insensitive to wind speed, while the pressure taps on the mirror experienced an increment of RMS values as the wind speed increased.

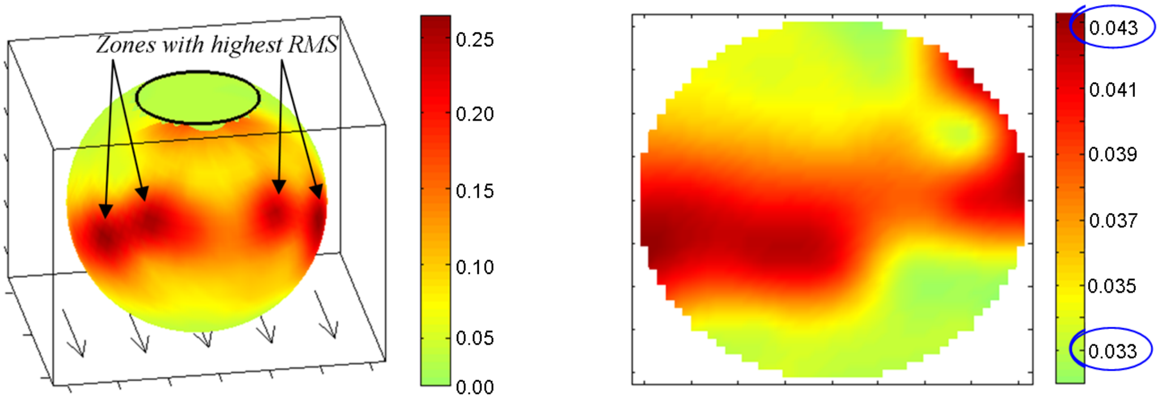

Figure 4.12 RMS values of pressure coefficients for the enclosure (left) and the mirror (right). ϕ=0°, θ=0°, U=10m/s.

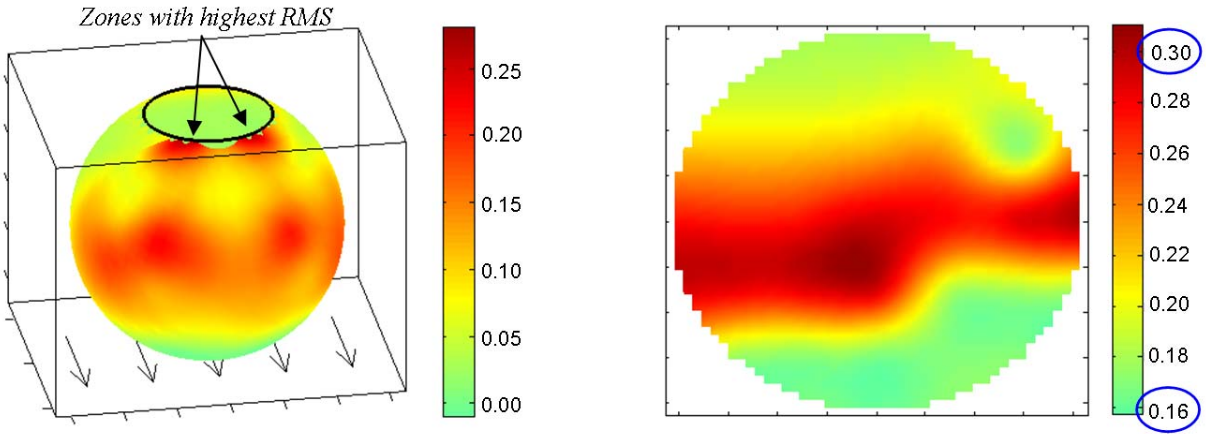

Figure 4.13 RMS values of pressure coefficients for the enclosure (left) and the mirror (right). ϕ=0°, θ=0°, U=40m/s.

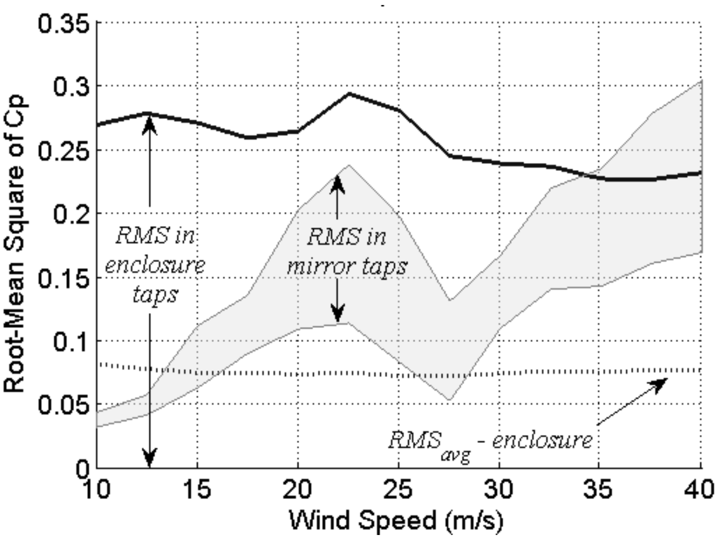

Figure 4.14 Root-mean square value of pressure coefficients as function of wind speed. ϕ=0°, θ=0°, 10≤U≤40m/s.

**Energy distribution (eigenvalues).**

The cumulative energy distribution of the POD modes is shown in Figure 4.15 for wind speed equal to 40m/s. For the case of the mirror, it is evident that the first POD mode accounts for most of the energy (99%) and that the remaining modes can be disregarded. The situation is different for the enclosure, where there is no clear dominant mode. It would be necessary to take into account about 20 POD modes for representing 90% of the kinetic energy involved in the wind loading on the enclosure, but this is an impractical number of modes to be managed for structural analysis and design purposes.

The energy content of the first POD mode gives and indication of how effective the POD method is for simplifying a turbulent field. Thus, Figure 4.16 shows the energy contribution of the first POD mode for 10≤U≤40 m/s at zero-zenith and zero-azimuth orientation. Since the RMS values and the kinetic energy are related, it is not surprise to realize that the energy content of the first POD mode on the enclosure has little variation with respect to wind speed. Nevertheless, the energy content of the first POD mode on the mirror has an increment from 80% to 98% when the wind speed increased from 10 to 15 m/s. Above 15 m/s, the energy content of the first POD mode on the mirror remains very close to 100%.

The paragraph above establishes that the wind load on the mirror can be accurately determined by using only the first POD mode. On the contrary, the wind load on the enclosure is not accurately represented by a few number of POD modes. Nevertheless, as it will be explained below, the POD modes on the enclosure suggest the underlying flow structures that finally produce the acoustic resonance inside the cavity. Thus, it is worth to study in parallel the pressure field around the enclosure and on the mirror.

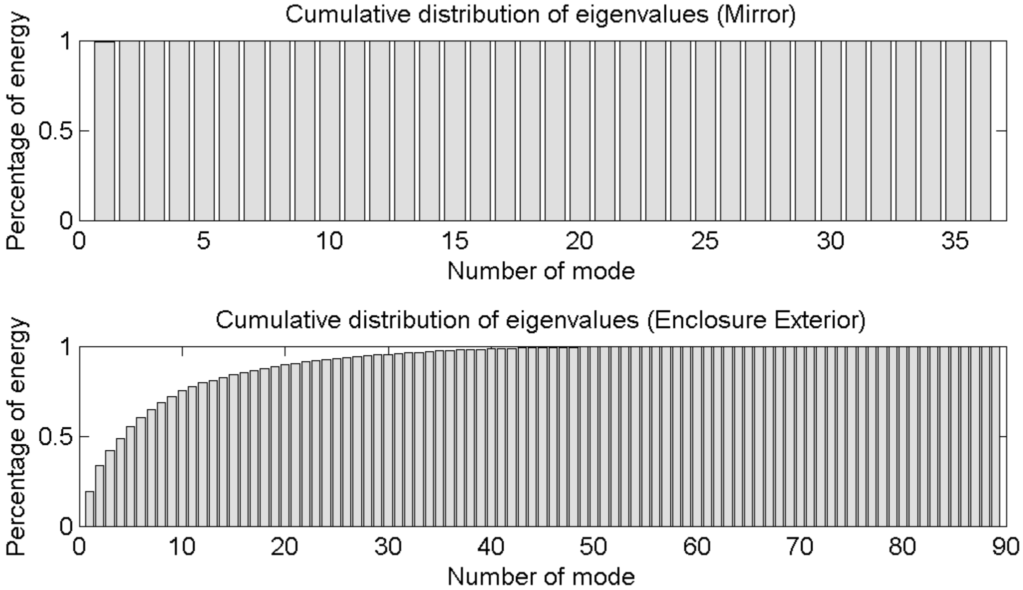

Figure 4.15 Cumulative energy distribution of the POD modes. ϕ=0°, θ=0°, U=40 m/s.

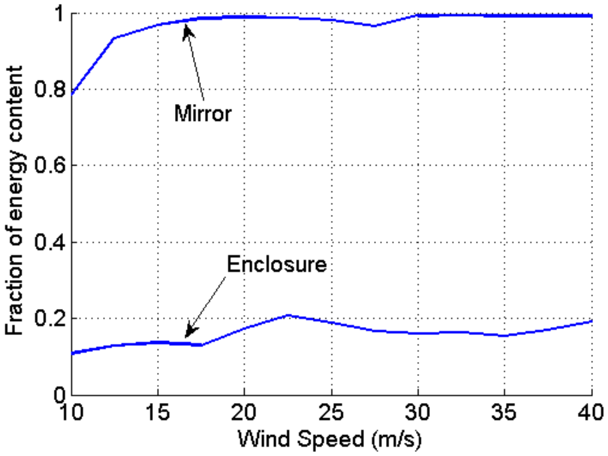

Figure 4.16 Variation of the energy content of the first POD mode as a function of wind speed. ϕ=0°, θ=0°, 10≤U≤40m/s

**POD modes (eigenvectors).**

The evolution, with respect to wind speed, of the first POD mode over the enclosure is described with the joint observation of Figure 4.17, Figure 4.18 and Figure 4.19. All spectral peaks are in good correspondence to flow structures predicted by the theory of flow past a sphere (Figure 4.19). Such flow structures are the vortex shedding at a low Strouhal frequency and the free-shear layer modes. The amplitude of every spectral peak changes with respect to wind speed, which means that the energy contribution of each flow structure is dependent of wind speed. The dominant flow structure in the interval 10 m/s≤U≤17.5 m/s is the vortex shedding at a low Strouhal frequency, although the spectral peak is neither too high nor too narrow. The spectral density function at U=17.5 m/s shows the incipient appearance of three peaks that correspond to the first three free-shear layer modes predicted by the theory. At U=20 m/s, there is a significant increment in the spectral amplitude at the frequency that corresponds to the second free-shear layer mode. The spectral increment is accompanied by an evident change in the shape of the first POD mode. Since the amplitude of the spectral peak of the second free-shear layer mode (at 130 Hz) is much greater than any of the other spectral peaks (11 Hz, 66 Hz, 187 Hz), it is concluded that the shape of the first

POD mode must correspond to the shape of second free-shear layer. This mode shape is held for 20≤U≤25 m/s. There is another change in the POD mode shape and its spectral density for 27.5≤U≤35 m/s. This time the figures suggest a combination of the first free-shear layer modes with the vortex shedding at a low Strouhal frequency. Finally, for a wind speed of 37.5 m/s and 40 m/s, the dominant flow structure is the one corresponding to the first free-shear layer mode. All this numerical information is condensed in Table 4.1.

It should be noted that the largest spectral peaks occur in a range near the cavity resonance frequency, which proves the strong connection between the pressure field on the outer enclosure and inside the cavity.

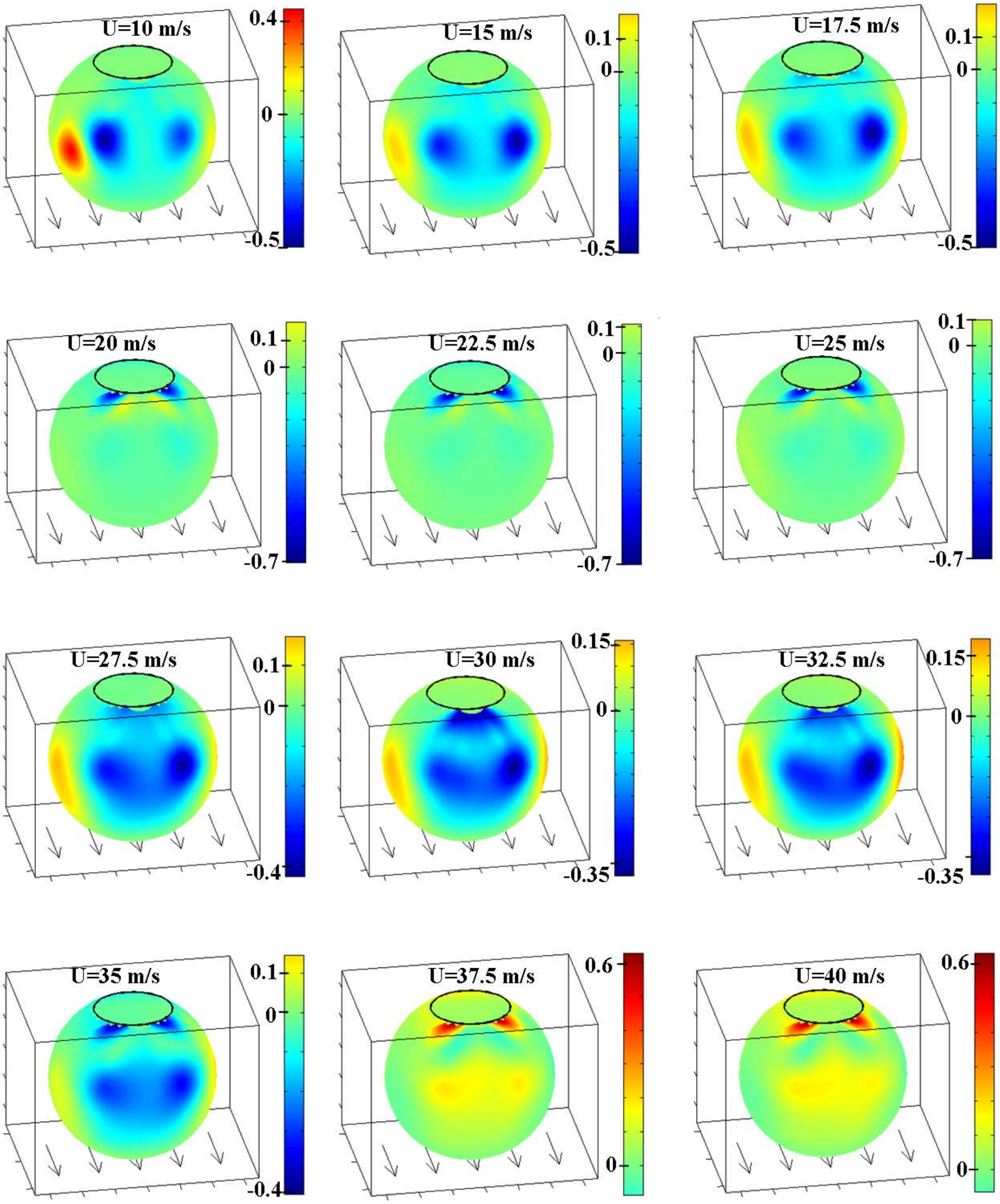

Figure 4.17 First POD mode on the enclosure. ϕ=0°, θ=0°, 10≤U≤40m/s.

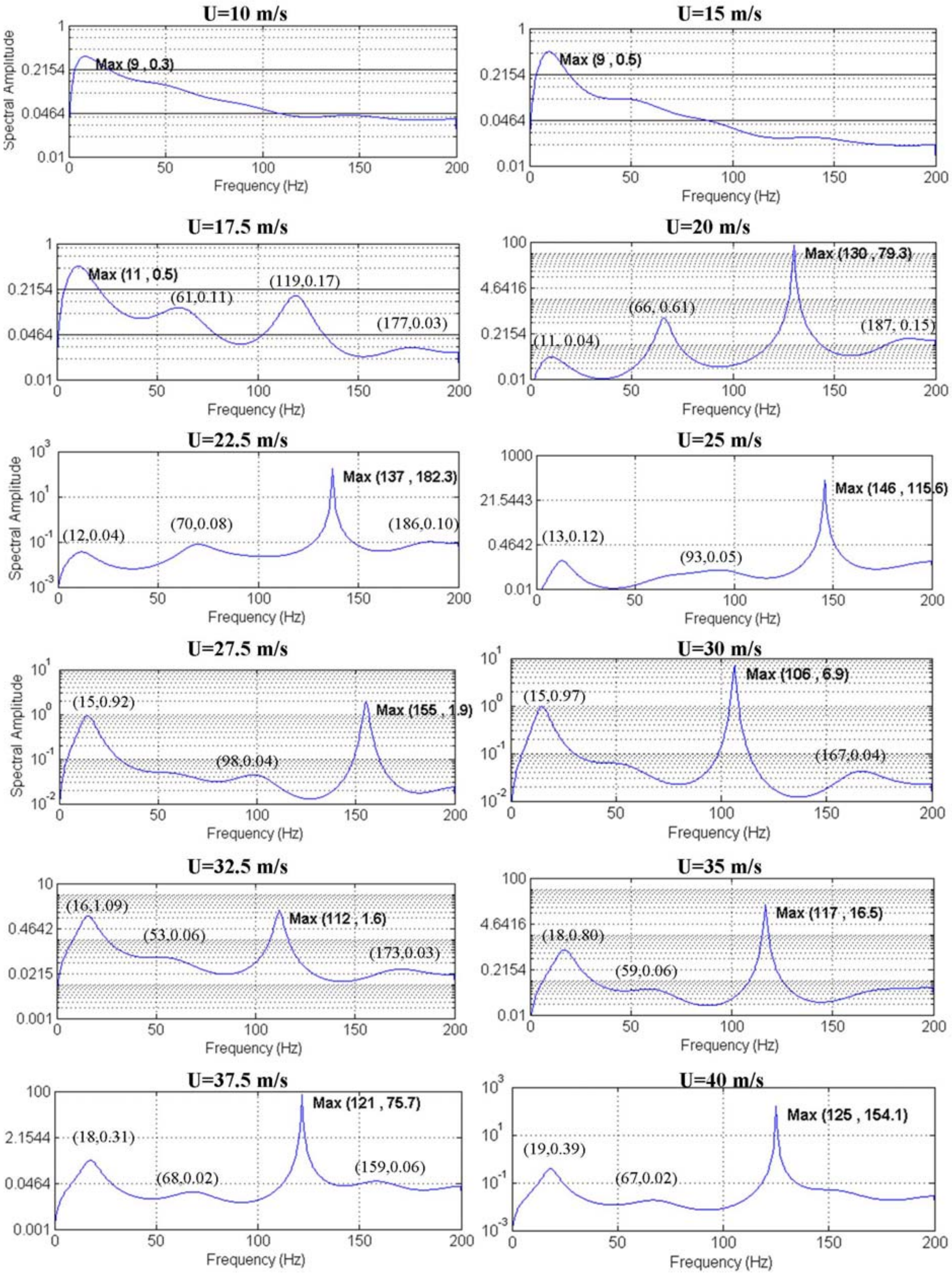

Figure 4.18 Power spectral densities of the first POD mode on the enclosure. ϕ=0°, θ=0°, 10≤U≤40m/s.

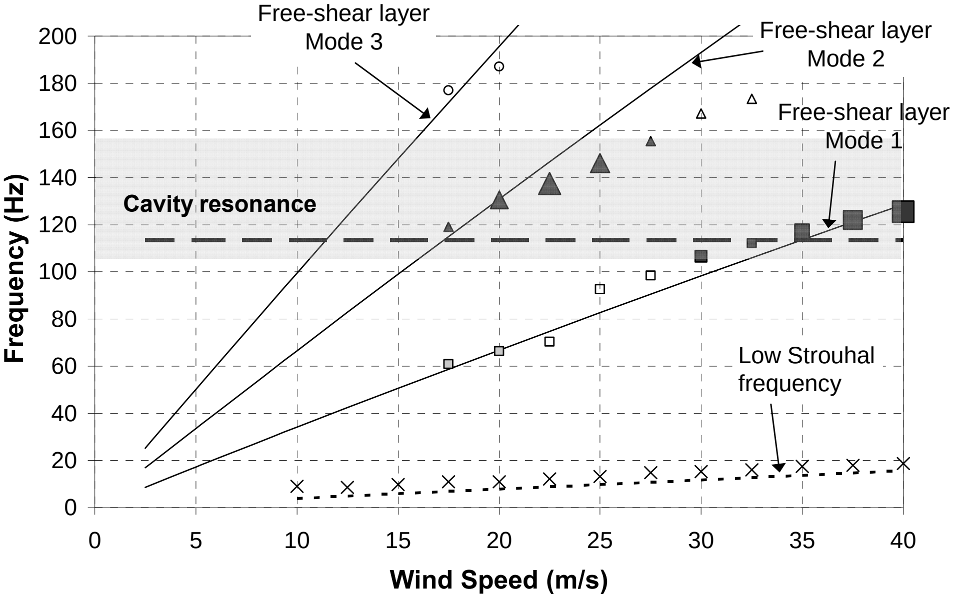

Figure 4.19 Characteristic frequencies for different flow structures. The straight lines represent the theoretical predictions and the markers indicate experimental values obtained with the first POD mode on the enclosure. The size of the marker is an indication of the magnitude of the spectral amplitude.

Table 4.1 Spectral peaks of the first POD mode on the enclosure. ϕ=0°, θ=0°, 10≤U≤40m/s.

| | Low St frequency | | 1st FSLM | | 2nd FSLM | | 3rd FSLM | | Dominant flow structure |
|---|---|---|---|---|---|---|---|---|---|
| U (m/s) | f (Hz) | Spectral amplitude | f (Hz) | Spectral amplitude | f (Hz) | Spectral amplitude | f (Hz) | Spectral amplitude | |
| 10.0 | **9** | **0.34** | | | | | | | St |
| 12.5 | **9** | **0.40** | | | | | | | St |
| 15.0 | **10** | **0.46** | | | | | | | St |
| 17.5 | **11** | **0.47** | *61* | *0.11* | *119* | *0.17* | 177 | 0.03 | St + 2nd + 1st FSLM |
| 20.0 | 11 | 0.04 | 66 | 0.61 | **130** | **79.26** | 187 | 0.15 | 2nd FSLM |
| 22.5 | 12 | 0.04 | 70 | 0.08 | **138** | **182.25** | | | 2nd FSLM |
| 25.0 | 13 | 0.12 | 93 | 0.05 | **146** | **115.56** | | | 2nd FSLM |
| 27.5 | *15* | *0.92* | 98 | 0.04 | **155** | **1.88** | | | 2nd FSLM + St |
| 30.0 | *15* | *0.97* | **107** | **6.88** | 167 | 0.04 | | | 1st FSLM + St |
| 32.5 | *16* | *1.09* | **112** | **1.57** | 173 | 0.03 | | | 1st FSLM + St |
| 35.0 | *18* | *0.80* | **117** | **16.49** | | | | | 1st FSLM + St |
| 37.5 | 18 | 0.31 | **122** | **75.73** | | | | | 1st FSLM |
| 40.0 | 19 | 0.39 | **125** | **154.09** | | | | | 1st FSLM |

* FSLM=Free-shear layer mode

The evolution of the second POD mode on the enclosure has a similar description as the one given for the first POD mode. In fact, the second POD mode essentially has the same underlying physical flow structures described for the first POD mode but with different spectral amplitudes. The second POD mode is fully described with the joint observation of Figure 4.20, Figure 4.21 and Figure 4.22. Figure 4.20 shows the shapes of the second POD mode for different wind speeds, while Figure 4.21 presents their respective spectral density functions. Figure 4.22 compares the theoretical and experimental values of the frequencies associated with the flow structures in flow past a sphere. Table 4.2 summarizes the spectral peaks observed in Figure 4.22. From Figure 4.22, it can be seen that the dominant flow structures for $10 \leq U \leq 15$ m/s are in the low frequency range—although not coincident with the Strouhal frequency. When the wind speed increased to $17.5 \leq U \leq 25$ m/s, the dominant flow structure was the second free-shear layer mode. At $U=30$ m/s and higher wind speeds, the second free-shear layer mode could not longer be sustained and then the first free-shear layer mode became the dominant flow structure. Once again, the spectral amplitudes increased significantly when they were in the vicinity of the cavity resonance. From Figure 4.17 and Figure 4.21, it can be seen that the shapes of the first and second POD modes are alternating when the wind speed changes. This is easily explained by noticing that the first two POD modes have similar energy content.

Higher POD modes for the enclosure are not shown since they have a more reduced participation in the energy content.

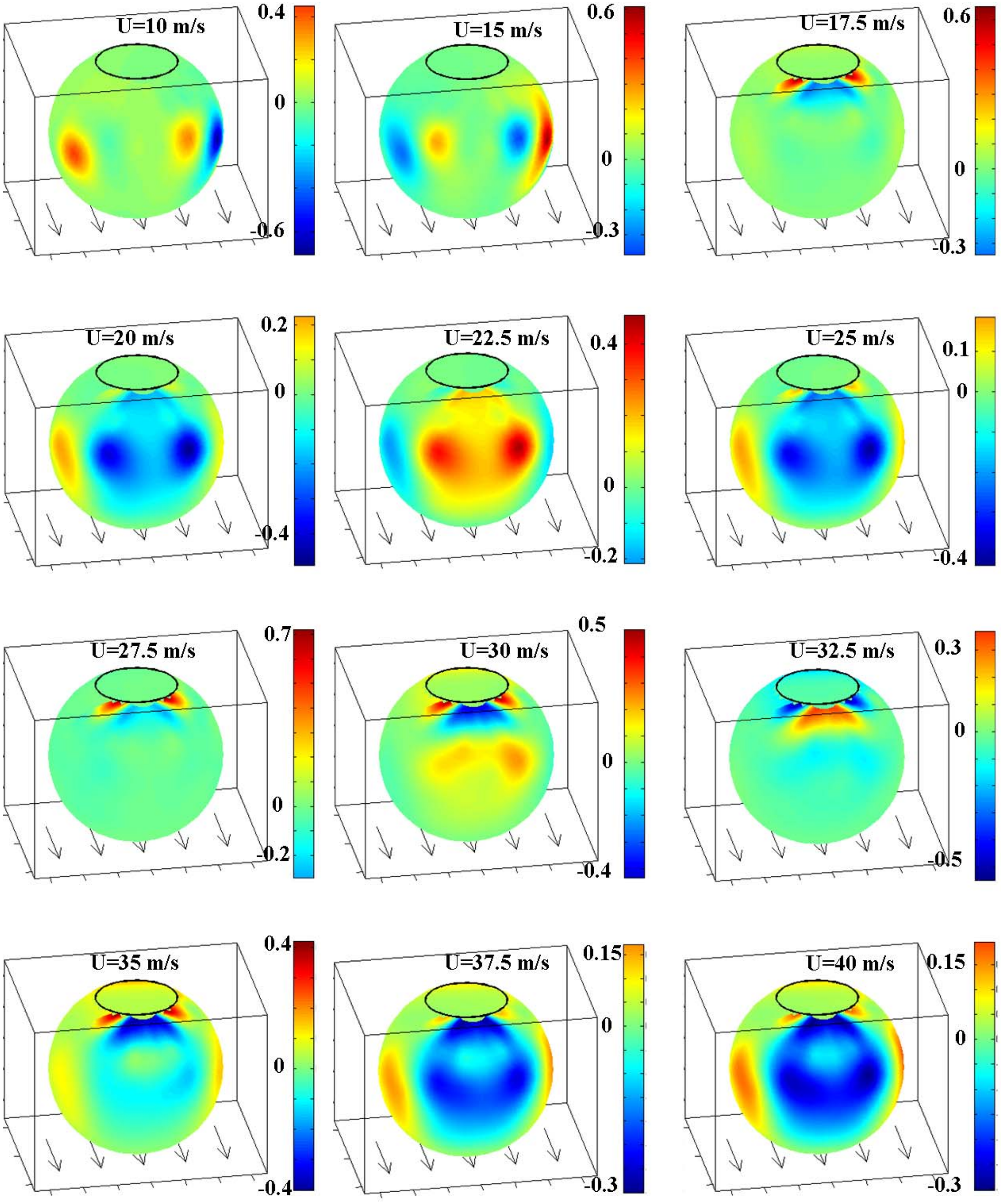

Figure 4.20 Second POD mode on the enclosure. ϕ=0°, θ=0°, 10≤U≤40m/s.

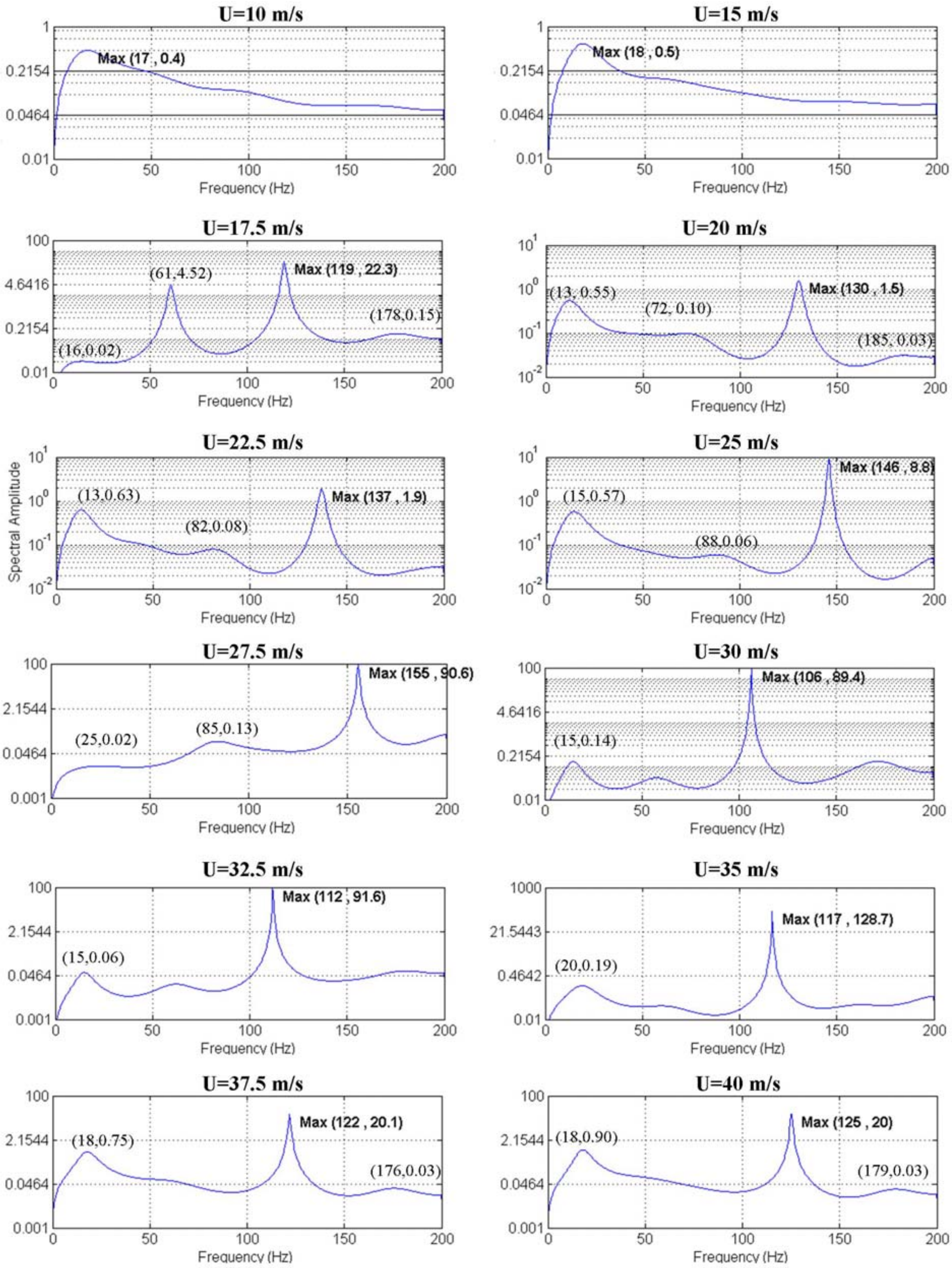

Figure 4.21 Power spectral densities of the second POD mode on the enclosure. ϕ=0°, θ=0°, 10≤U≤40m/s.

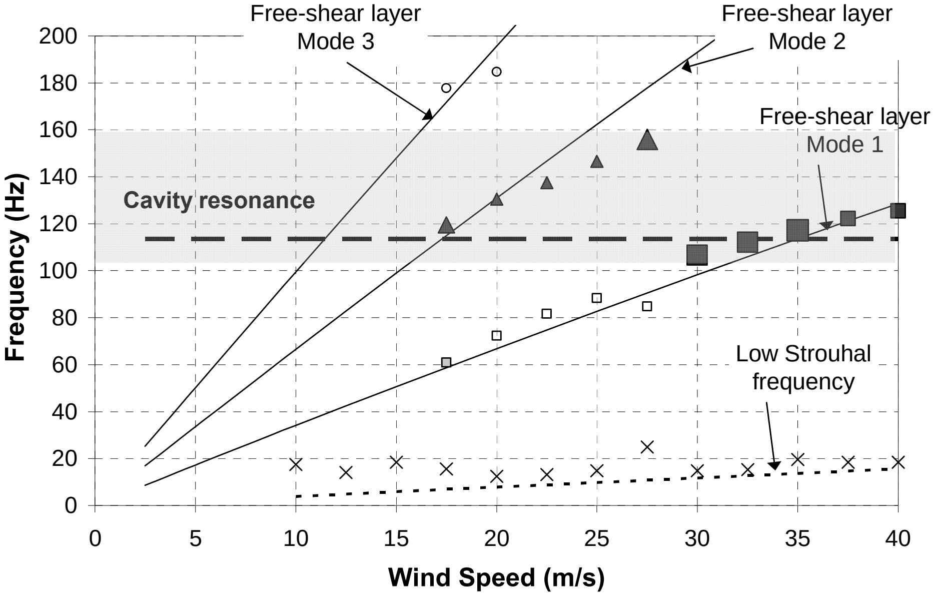

Figure 4.22 Characteristic frequencies of different flow structures. The straight lines represent the theoretical predictions and the markers indicate experimental values obtained with the second POD mode on the enclosure. The size of the marker is a qualitative indication of the magnitude of the spectral amplitude.

Table 4.2 Spectral peaks of the second POD mode on the enclosure. ϕ=0°, θ=0°, 10≤U≤40m/s.

| | Low St frequency | | 1st FSLM | | 2nd FSLM | | 3rd FSLM | | Dominant flow structure |
|---|---|---|---|---|---|---|---|---|---|
| U (m/s) | f (Hz) | Spectral amplitude | f (Hz) | Spectral amplitude | f (Hz) | Spectral amplitude | f (Hz) | Spectral amplitude | |
| 10.0 | **18** | **0.44** | | | | | | | St |
| 12.5 | **14** | **0.41** | | | | | | | St |
| 15.0 | **18** | **0.55** | | | | | | | St |
| 17.5 | 16 | 0.02 | *61* | *4.52* | **120** | **22.33** | 178 | 0.15 | 2nd + 1st FSLM |
| 20.0 | *13* | *0.55* | 72 | 0.10 | **130** | **1.55** | 185 | 0.03 | 2nd FSLM + St |
| 22.5 | *13* | *0.63* | 82 | 0.08 | **138** | **1.85** | | | 2nd FSLM + St |
| 25.0 | 15 | 0.57 | 88 | 0.06 | **146** | **8.83** | | | 2nd FSLM |
| 27.5 | 25 | 0.02 | 85 | 0.13 | **156** | **90.64** | | | 2nd FSLM |
| 30.0 | 15 | 0.14 | **107** | **89.44** | | | | | 1st FSLM |
| 32.5 | 15 | 0.06 | **112** | **91.55** | | | | | 1st FSLM |
| 35.0 | 20 | 0.19 | **117** | **128.75** | | | | | 1st FSLM |
| 37.5 | 18 | 0.75 | **122** | **20.09** | | | | | 1st FSLM |
| 40.0 | 18 | 0.90 | **125** | **20.01** | | | | | 1st FSLM |

* FSLM=Free-shear layer mode

The wind loading on the mirror is described very accurately with only the first POD mode. Following the same procedure as with the enclosure, the pressure field on the mirror is described with the joint observation of three figures and one table. Figure 4.8 shows the relation of the frequencies of the spectral peaks with respect to wind speed. The spectral peaks are associated to the flow structures described above. The figure is a convenient comparison between theoretical estimations and experimental results. Figure 4.23 shows the shape of the first POD mode, which remains practically constant for the whole wind speed range studied. The mode shape indicates that the whole mirror's surface is exposed to pressure of the same sign. The mode shape and the power spectral density functions, which are shown in Figure 4.24, indicate that the mirror is subjected to pressure pulsations with very specific frequency content. The energy contribution of every flow structure varies with the wind speed. At U=10 m/s, there are five peaks, one related to the vortex shedding of flow past a sphere at a low frequency and the remaining four peaks are related to the first four free-shear layer modes of flow past a sphere. At this speed, none of the peaks is significantly greater than the others. At U=15 m/s, the fourth free-shear layer mode can not be longer sustained and it disappears, while the spectral peak associated to the third free-shear layer mode increases up to ninety times the magnitude of the other peaks. At U=17.5 m/s, the third free-shear layer mode practically disappears and then the second free-shear layer mode becomes the dominant mechanism. This pattern holds for a wind speed between 17.5 m/s and 27.5 m/s. The maximum spectral amplitude occurs at U=22.5 m/s, with a value that is almost 3000 times greater than the other peaks. The flow mechanism changes again at U=30 m/s, when the first free-shear layer mode becomes the dominant flow structure and it remains like that up to the maximum wind speed of 40 m/s. Table 4.3 summarizes the values of the frequencies of the spectral peaks and their amplitude.

It should be noted that the exciting forces on the mirror are originated from flow structures perfectly identified in the studies of flow past a sphere. Such flow structures have frequency contents that vary linearly with wind speed. The magnitude of the spectral peak associated to a particular flow structure is determined by the proximity of the exciting frequency with the Helmholtz frequency. The theoretical estimation of the Helmholtz frequency was of 113 Hz, but the experiments show that the larger spectral peaks occur at a frequency of 137 Hz. The frequency range where the spectral amplitudes increase notoriously is between 105 Hz and 155 Hz, which is indicated in the shaded area of Figure 4.8, Figure 4.19 and Figure 4.22.

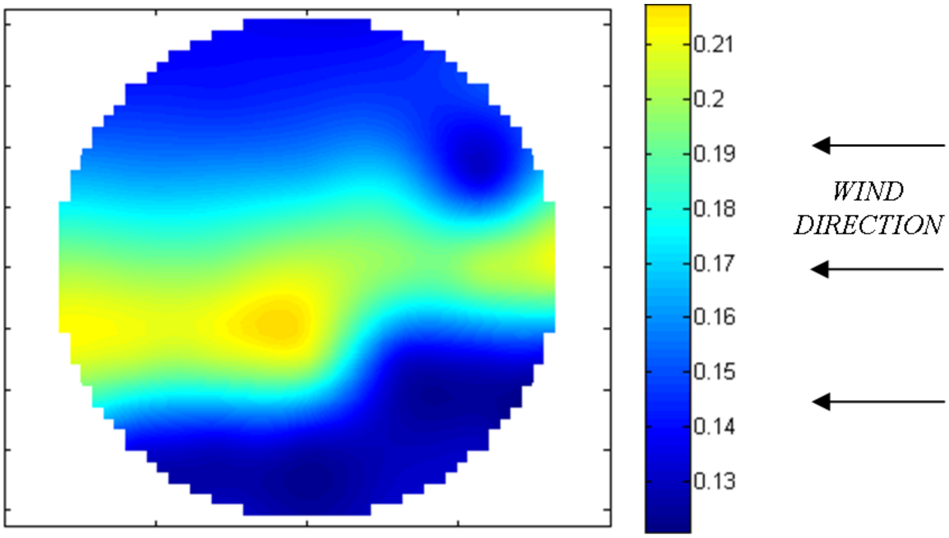

Figure 4.23 First POD mode on the mirror. $\phi=0°$, $\theta=0°$, $10\leq U\leq 40$m/s.

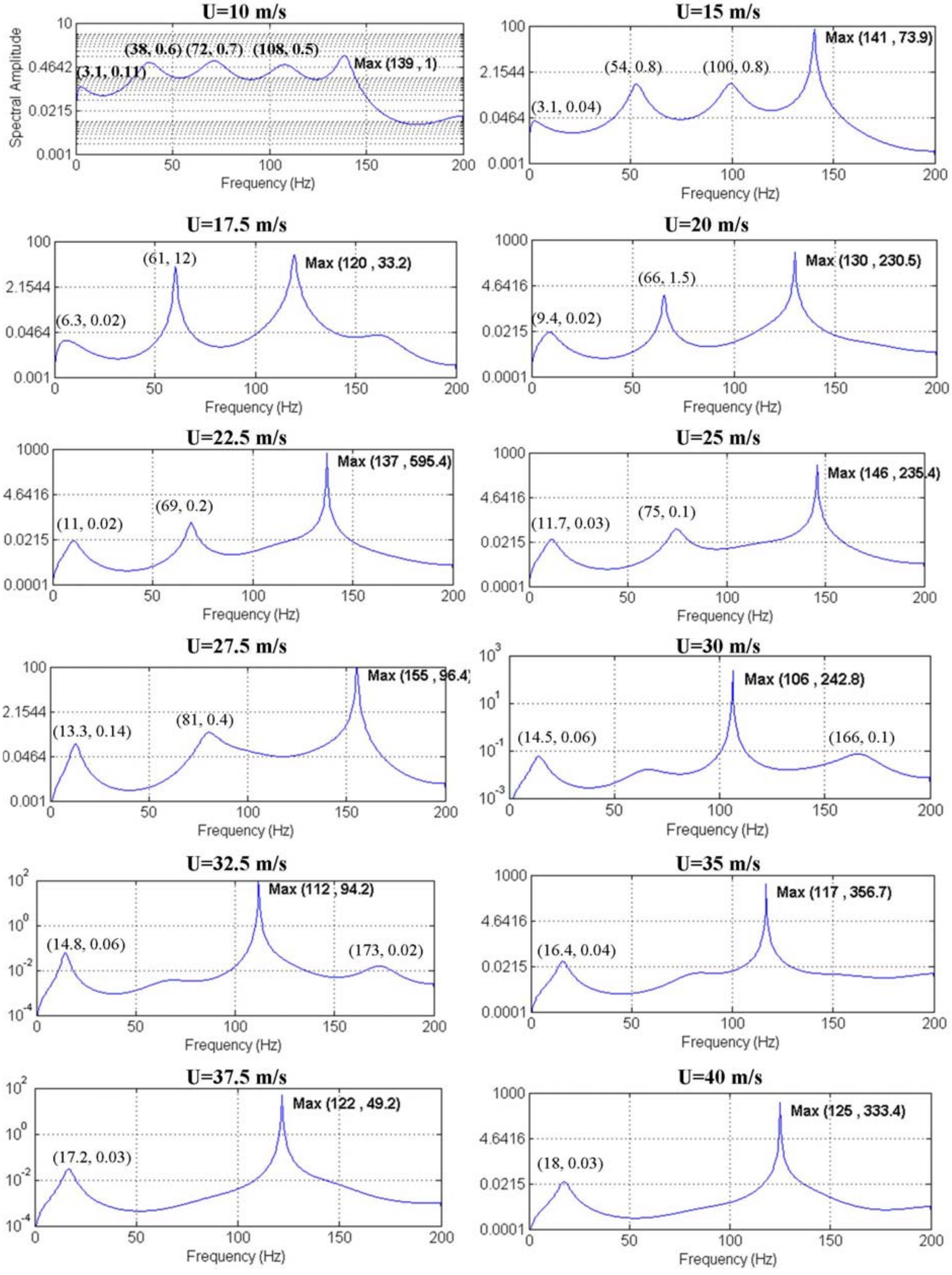

Figure 4.24 Power spectral densities of the first POD mode on the mirror. ϕ=0°, θ=0°, 10≤U≤40m/s.

Table 4.3 Spectral peaks of the first POD mode on the mirror. $\phi=0^\circ$, $\theta=0^\circ$, $10 \leq U \leq 40$m/s.

| | Low St frequency | | 1st FSLM | | 2nd FSLM | | 3rd FSLM | | Dominant flow structure |
|---|---|---|---|---|---|---|---|---|---|
| U (m/s) | f (Hz) | Spectral amplitude | f (Hz) | Spectral amplitude | f (Hz) | Spectral amplitude | f (Hz) | Spectral amplitude | |
| 10.0 | 3.1 | 0.11 | 38.3 | 0.62 | *71.9* | *0.70* | 108.2 | 0.53 | No particular |
| 12.5 | 2.0 | 0.07 | 44.5 | 1.66 | 84.0 | 2.45 | *124.6* | *3.19* | No particular |
| 15.0 | 3.1 | 0.04 | 53.5 | 0.77 | 99.6 | 0.79 | **141.0** | **73.91** | 3rd FSLM |
| 17.5 | 6.3 | 0.02 | 60.5 | 12.01 | **119.9** | **33.20** | 161.3 | 0.04 | 2nd FSLM |
| 20.0 | 9.4 | 0.02 | 66.0 | 1.53 | **130.5** | **230.46** | | | 2nd FSLM |
| 22.5 | 10.9 | 0.02 | 69.5 | 0.16 | **137.5** | **595.44** | | | 2nd FSLM |
| 25.0 | 11.7 | 0.03 | 75.0 | 0.10 | **146.1** | **235.38** | | | 2nd FSLM |
| 27.5 | 13.3 | 0.14 | 80.9 | 0.36 | **155.9** | **96.36** | | | 2nd FSLM |
| 30.0 | 14.5 | 0.06 | **106.6** | **242.81** | 166.4 | 0.07 | | | 1st FSLM |
| 32.5 | 14.8 | 0.06 | **112.1** | **94.25** | 173.0 | 0.02 | | | 1st FSLM |
| 35.0 | 16.4 | 0.04 | **117.2** | **356.68** | | | | | 1st FSLM |
| 37.5 | 17.2 | 0.03 | **122.3** | **49.20** | | | | | 1st FSLM |
| 40.0 | 18.0 | 0.03 | **125.4** | **333.41** | | | | | 1st FSLM |

* FSLM=Free-shear layer mode

### 4.3.2 Enclosure at different orientations: $15^\circ \leq \Phi \leq 45^\circ$, $0^\circ \leq \theta \leq 180^\circ$

The effects of the wind on the enclosure and on the mirror for a zero-zenith orientation (Figure 4.3-left) were discussed in detail in the previous section. Such orientation provided the ideal conditions to study the unsteady pressure field, using the POD method, as a function of wind speed. This section provides a more general view of the pressure field behaviour for different combinations of wind speed, azimuth and zenith orientations. Nevertheless, the large amount of information obtained from these combinations obliges to find an alternative presentation of the results. Hence the idea to present the results in 3D graphics that contain the most important values of the items discussed in the previous section.

**Mean pressure coefficients, Cp.**

A visual inspection at the mean pressure fields on the enclosure for every test configuration confirms that the pressure pattern of flow past a sphere is maintained similar to that shown in Figure 4.10. Nevertheless, the location of the enclosure opening with respect to wind direction affects the maximum mean suction value, which was previously defined as

Cpmin. Therefore, the description of the mean pressure field on the enclosure is properly described with the observation of the Cpmin as a function of zenith and azimuth orientation as well as wind speed. Figure 4.25, Figure 4.26 and Figure 4.27 condense this information. From the figures, it is clear that Cpmin (and also the rest of the pressure coefficients) are practically insensitive to wind speed. The values of Cpmin are kept in a narrow range between -1.1 to -1.3 in most of the test configurations, except for the case where the opening is inclined 45 degrees towards the approaching wind (Φ=45°, θ=0°). In such configuration, Cpmin reaches values of -1.9. The highest suction occurred in the top part of the sphere, as shown in Figure 4.28.

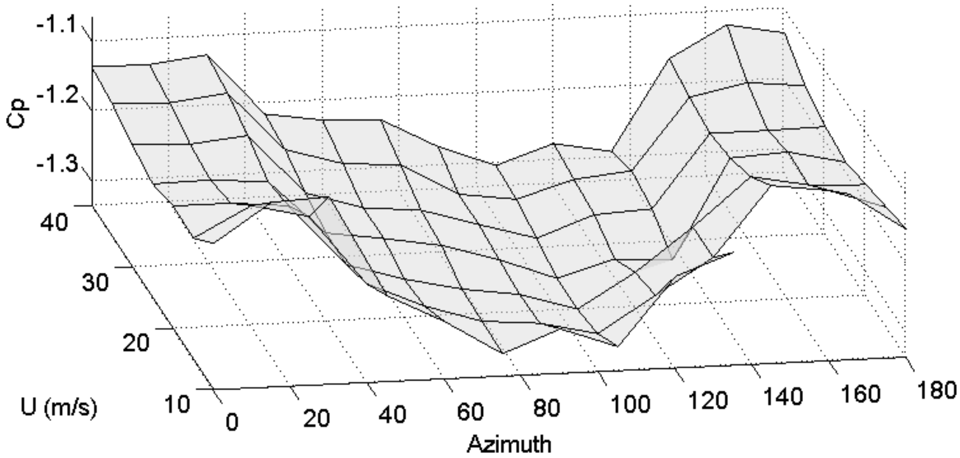

Figure 4.25 Cpmin on the enclosure. Φ=15°, 0°≤θ≤180°, 10≤U≤40m/s.

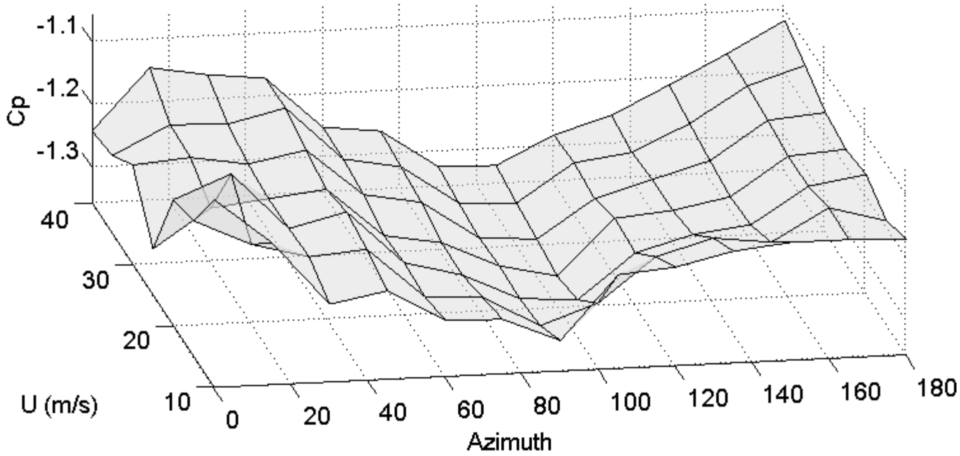

Figure 4.26 Cpmin on the enclosure. Φ=30°, 0°≤θ≤180°, 10≤U≤40m/s.

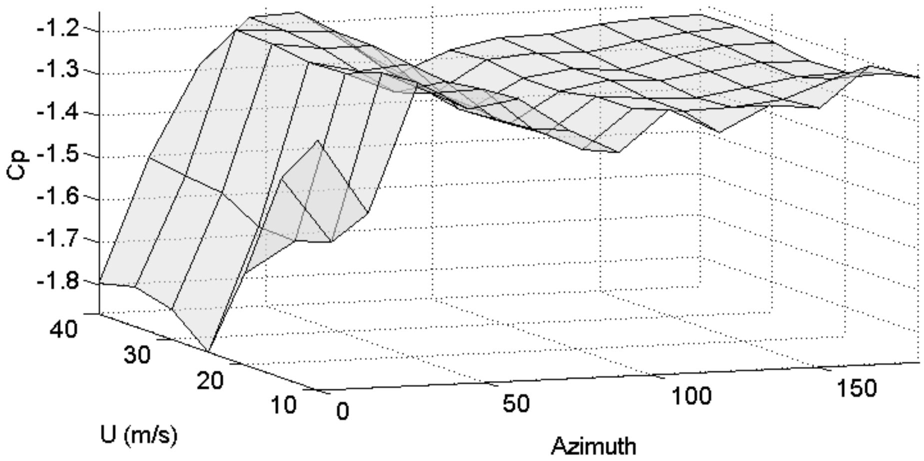

Figure 4.27 Cpmin on the enclosure. Φ=45°, 0°≤θ≤180°, 10≤U≤40m/s.

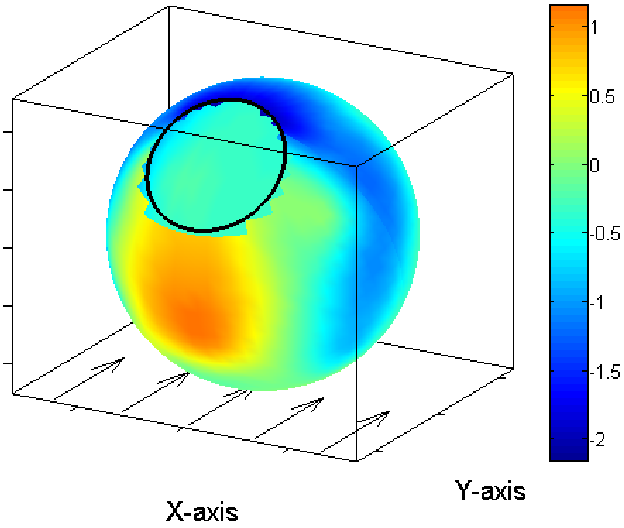

Figure 4.28 Mean pressure coefficients for the enclosure. Φ=45°,θ=0°, U=25m/s.

All pressure taps on the mirror recorded similar values for any particular orientation of the telescope, but there were significant changes from one orientation to another. The changes of the mean pressure coefficients on the mirror with respect to the enclosure orientation are well understood if the enclosure opening is considered as a big pressure tap. The description of the mean pressure field on the mirror is accurately represented by the mean pressure value at any single pressure tap on it, in particular the one that recorded the maximum mean suction (Cpmin). Figure 4.29, Figure 4.30 and Figure 4.31 provide a graphical representation of the variation of Cpmin as a function of the enclosure orientation and wind speed. It can be observed that, similarly to the case of the enclosure, Cpmin is insensitive to wind speed. At Φ=15° the value of Cpmin gradually changes from -0.7 at θ=0° to a maximum suction of $-1.2$ at θ=90°, then the suction reduces again to -0.7 at θ=180°. At Φ=30° the value of Cpmin gradually changes from -0.3 at θ=0° to a maximum suction of $-1.2$ at θ=90°, then the suction reduces to -0.6 at θ=180°. At Φ=45° the pressure coefficients have a positive value near +0.3 at θ=0° but as the enclosure rotates the coefficients turn into negative values up to a maximum suction of $-1.2$ at θ=90°, then suction reduces again to -0.5 at θ=180°. It is noticeable the fact that the highest suction is always, for any zenith value, near the value of $-1.2$ when the enclosure is oriented at θ=90°.

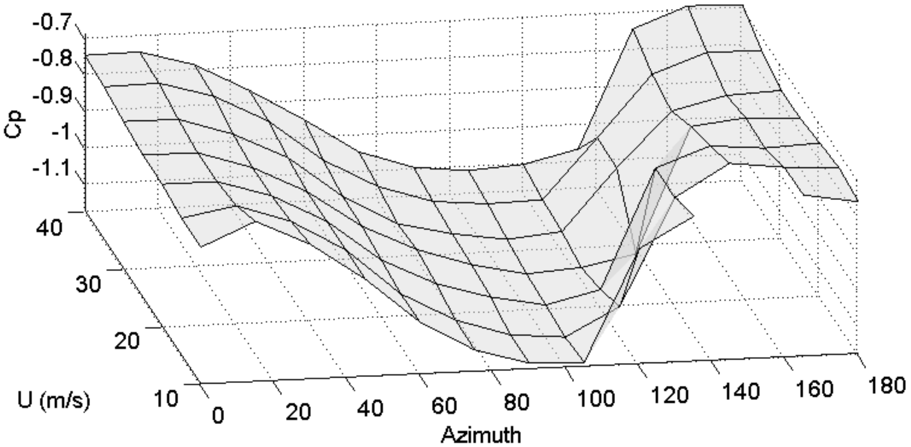

Figure 4.29 Cpmin on the mirror. Φ=15°, 0°≤θ≤180°, 10≤U≤40m/s.

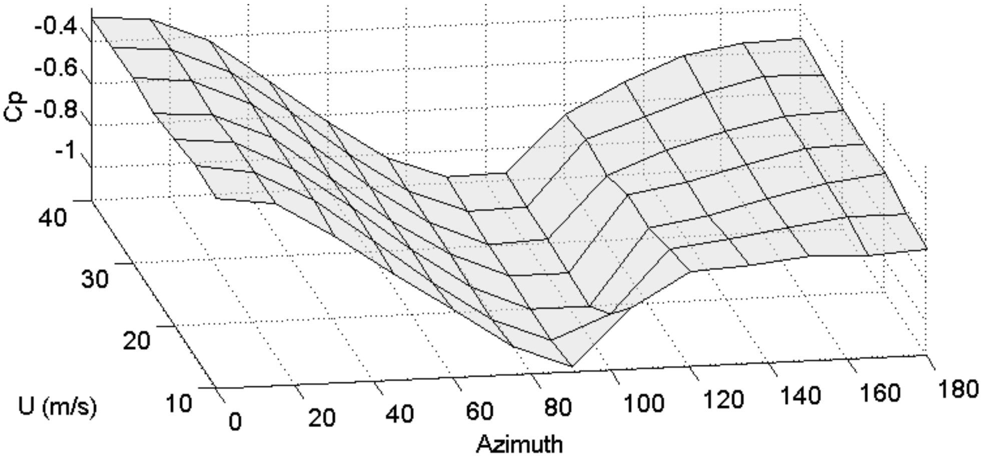

Figure 4.30 Cpmin on the mirror. Φ=30°, 0°≤θ≤180°, 10≤U≤40m/s.

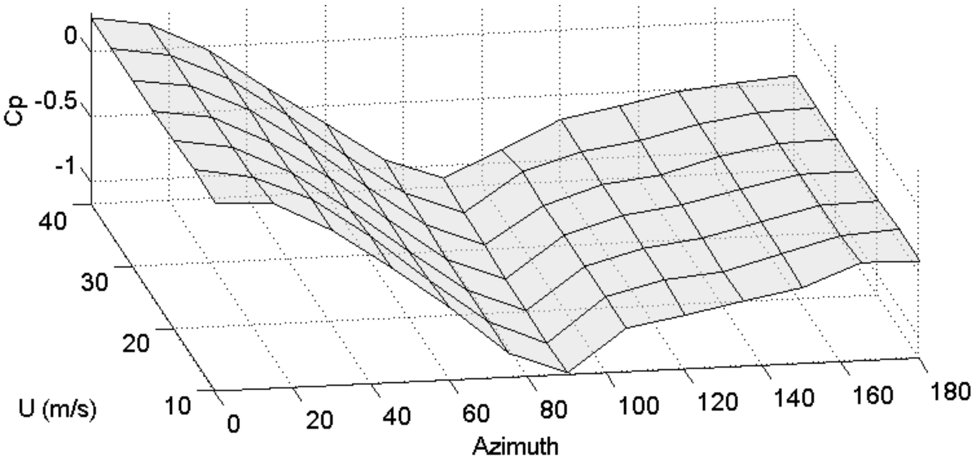

Figure 4.31 Cpmin on the mirror. Φ=45°, 0°≤θ≤180°, 10≤U≤40m/s.

**Root-mean square values of pressure coefficients, RMS.**

The root-mean square values of pressure coefficients on the enclosure have a slight dependence on wind speed but a significant dependence on the enclosure orientation, particularly on the azimuth rotations. Figure 4.32, Figure 4.33 and Figure 4.34 show the variation of the RMS values as a function of wind speed and enclosure orientation. The figures follow similar patterns, which means that the zenith angle does not make an important difference in the RMS values. Each of the three figures includes two surfaces; the upper surface is defined by the maximum RMS values and the lower surface is defined by the average RMS values. The substantial differences between the upper and lower surfaces implies that the large RMS values are concentrated in small regions of the sphere, as indicated in Figure 4.35, while most of the pressure taps on the sphere recorded pressure histories with small RMS. The surfaces of maximum RMS have the largest values when the enclosure opening is directly exposed to the oncoming wind flow (0°≤θ≤60), reaching values as high as 0.50. The average RMS values on the enclosure never exceed 0.10.

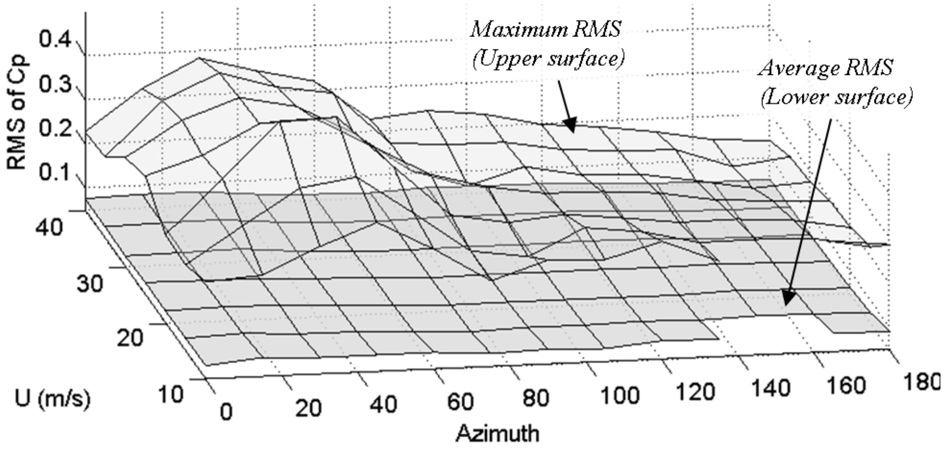

Figure 4.32 Average and maximum RMS values of pressure coefficients on the enclosure. Φ=15°, 0°≤θ≤180°, 10≤U≤40m/s.

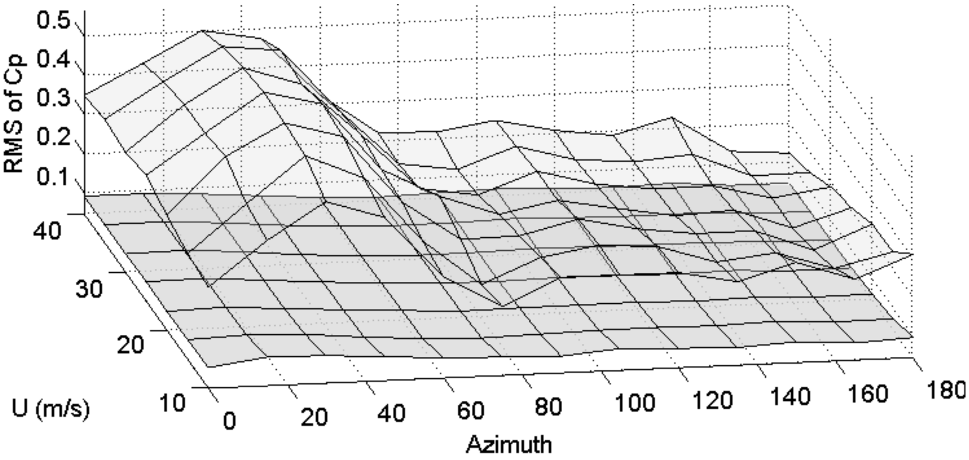

Figure 4.33 Average and maximum RMS values of pressure coefficients on the enclosure. Φ=30°, 0°≤θ≤180°, 10≤U≤40m/s.

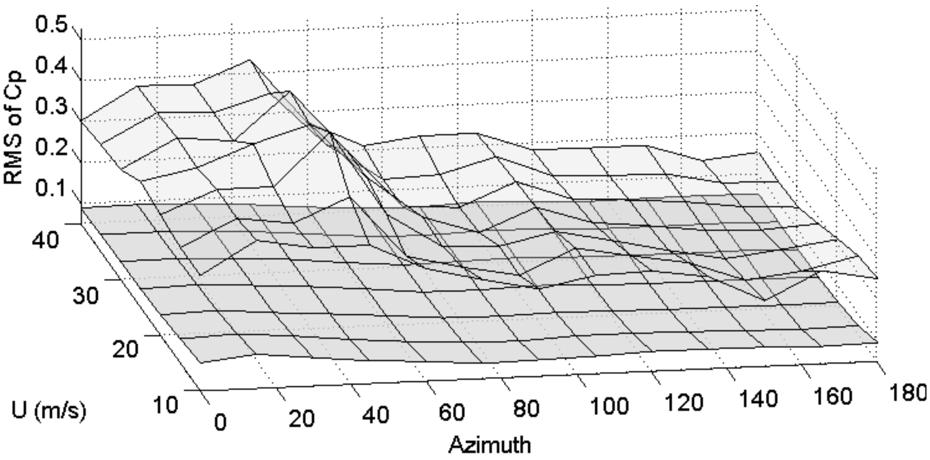

Figure 4.34 Average and maximum RMS values of pressure coefficients on the enclosure. Φ=45°, 0°≤θ≤180°, 10≤U≤40m/s.

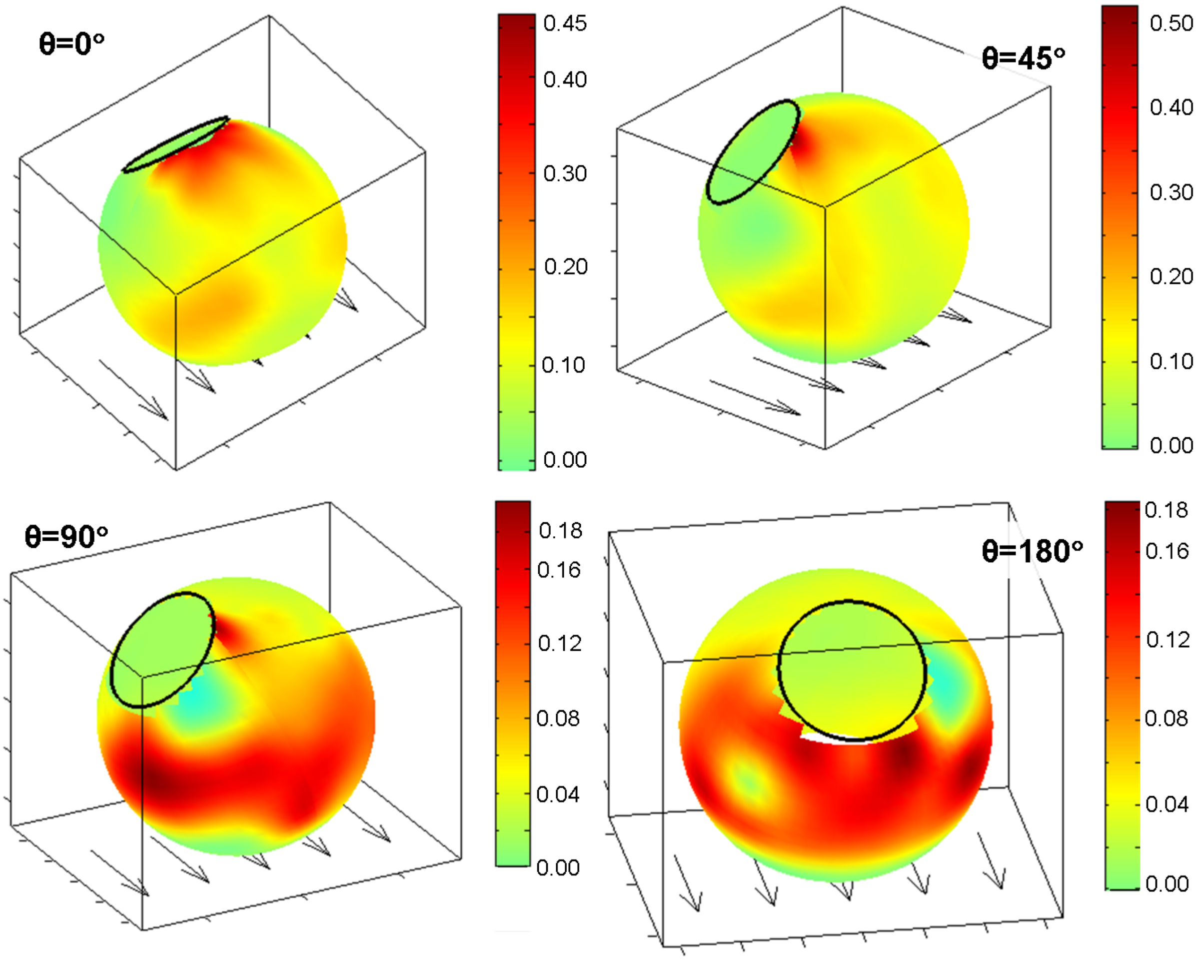

Figure 4.35 RMS values of pressure coefficients on the enclosure for Φ=45°, U=25m/s and θ=0°, 45°, 90°, 180°.

The variation of the RMS values of pressure coefficients on the mirror, with respect to wind speed and azimuth rotation, is also represented graphically in three figures: Figure 4.36, Figure 4.37 and Figure 4.38. Each figure contains two surfaces, one defined by the maximum RMS values and the other by the average RMS values. It can be seen that both surfaces are very close to each other as a direct consequence of the fact that all pressure taps on the mirror recorded similar pressure histories for any wind tunnel test case. Unlike the case of the enclosure, the magnitude of the RMS on the mirror is highly dependent on wind speed since at higher wind speeds the acoustic resonance inside the cavity increased and consequently the RMS values also increased. This trend, though, have an irregularity at

U=30 m/s, where there is a change of the dominant flow mechanism. Figure 4.8 and Table 4.3 show that, at U=30 m/s, the dominant flow mechanism switched from the second to the first free-shear layer mode. A final observation from the three figures is that the RMS values on the mirror reduced considerably when the enclosure opening was on the leeward side.

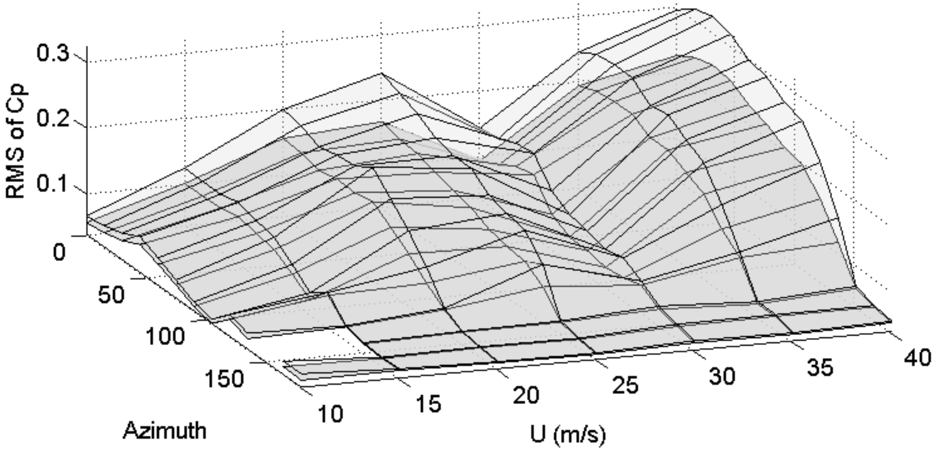

Figure 4.36 Average and maximum RMS values of pressure coefficients on the mirror. Φ=15°, 0°≤θ≤180°, 10≤U≤40m/s.

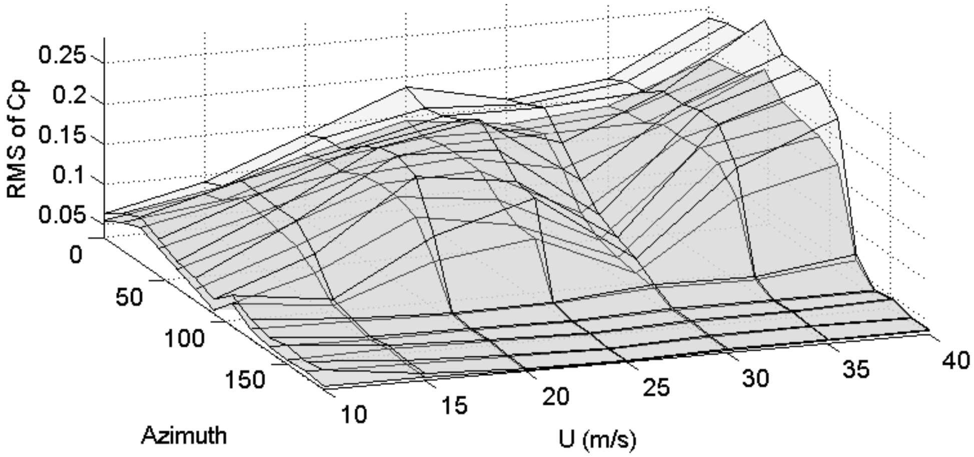

Figure 4.37 Average and maximum RMS values of pressure coefficients on the mirror. Φ=30°, 0°≤θ≤180°, 10≤U≤40m/s.

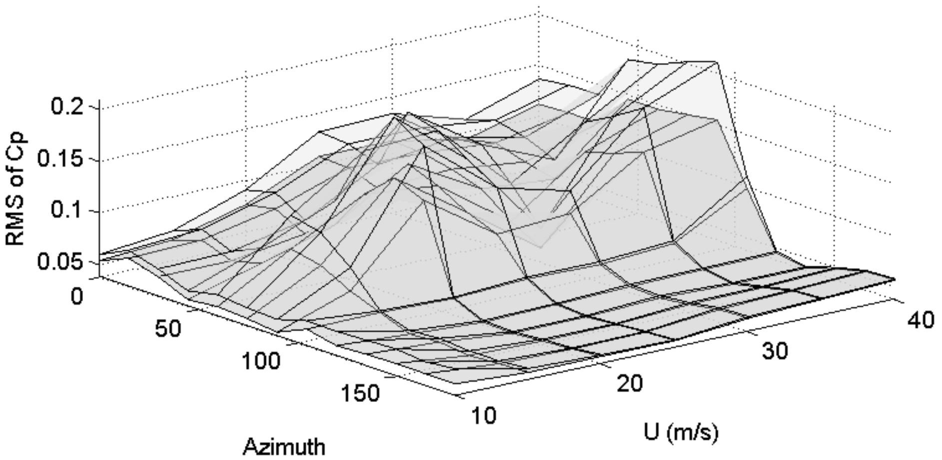

Figure 4.38 Average and maximum RMS values of pressure coefficients on the mirror. Φ=45°, 0°≤θ≤180°, 10≤U≤40m/s.

**Energy distribution (eigenvalues).**

The cumulative energy distribution shown in Figure 4.15 is a typical distribution of the energy content of the POD modes for most test configurations. In all cases, the energy contribution of the first POD mode on the enclosure is always below 35% out of the total kinetic energy, which means that several modes are needed to accurately reproduce the real pressure field. On the other hand, the energy contribution of the first POD mode on the mirror is always greater than 70% and it goes above 99% for most cases, allowing the accurate representation of the real pressure field with only the first POD mode. Thus, the energy content of the first POD mode is a good indicator of how efficient the POD method is for extracting energy in a few POD modes. Figure 4.39, Figure 4.40 and Figure 4.41 show the variation of the energy content of the first POD mode on the enclosure, as a function of enclosure orientation and wind speed. The figures for zenith inclination Φ=15°, 30° are very similar. The energy content of the first POD mode increases as the wind speed increases. There is a peculiar increment of the energy content for azimuth rotation θ=45°. The third figure, which refers to the maximum zenith inclination Φ=45°, indicates that the energy content of the first POD mode on the enclosure increased for θ=0°, 45°, 90°, 180°.

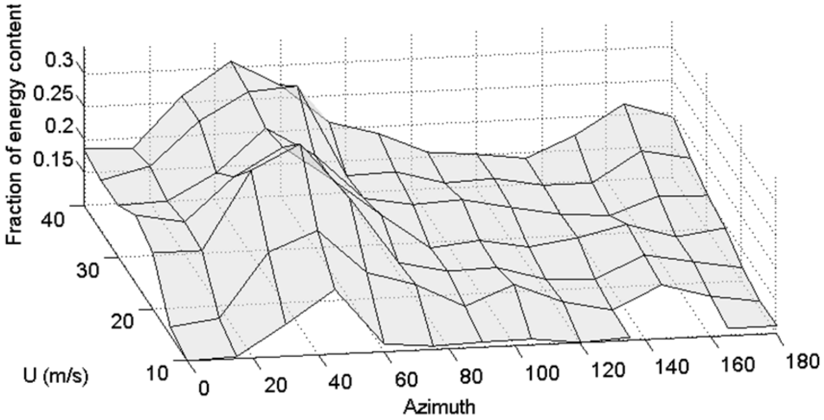

Figure 4.39 Variation of the energy content of the first POD mode on the enclosure. Φ=15°, 0°≤θ≤180°, 10≤U≤40m/s.

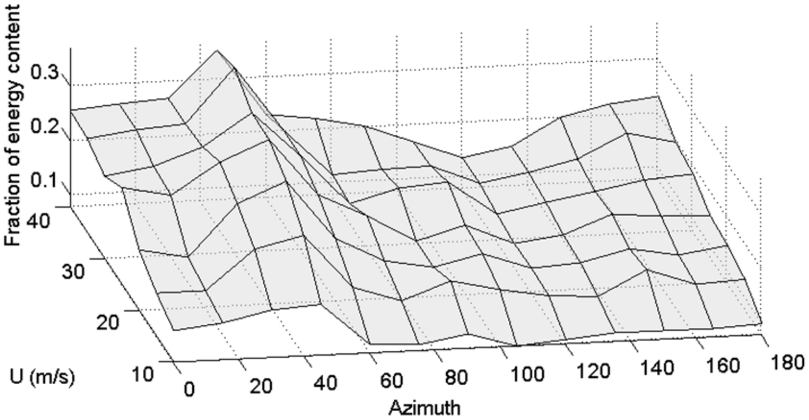

Figure 4.40 Variation of the energy content of the first POD mode on the enclosure. Φ=30°, 0°≤θ≤180°, 10≤U≤40m/s.

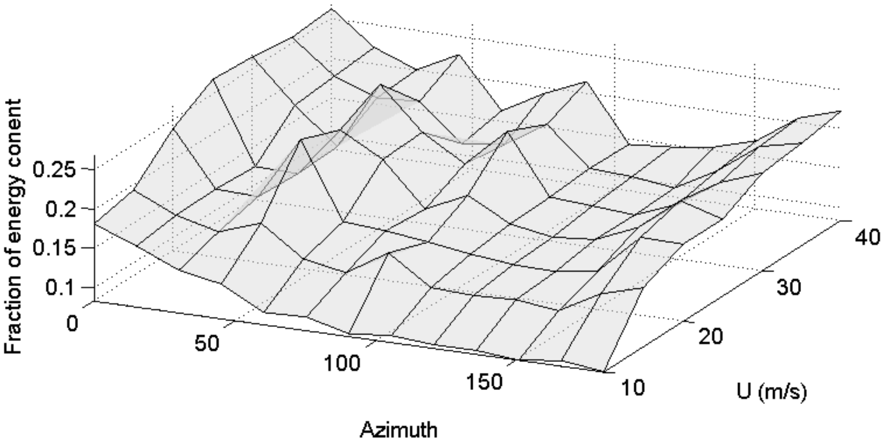

Figure 4.41 Variation of the energy content of the first POD mode on the enclosure. Φ=45°, 0°≤θ≤180°, 10≤U≤40m/s.

As mentioned before, all test configurations provided a very high energy content of the first POD mode on the mirror. In all cases, the consideration of only the first POD mode is enough to represent accurately the real pressure field on the mirror. Figure 4.42, Figure 4.43 and Figure 4.44 show the variation of the energy content of the first POD mode on the enclosure, as a function of orientation and wind speed. The three figures are similar. It can be observed that the lowest values were obtained at the lowest wind speed, U=10m/s. Almost all configurations with a wind speed greater than 10 m/s caused a strong first POD mode, with energy content above 98%.

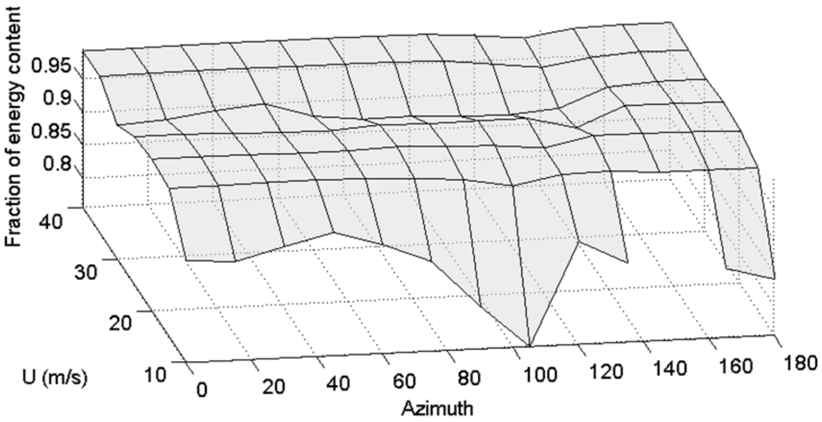

Figure 4.42 Variation of the energy content of the first POD mode on the mirror. Φ=15°, 0°≤θ≤180°, 10≤U≤40m/s.

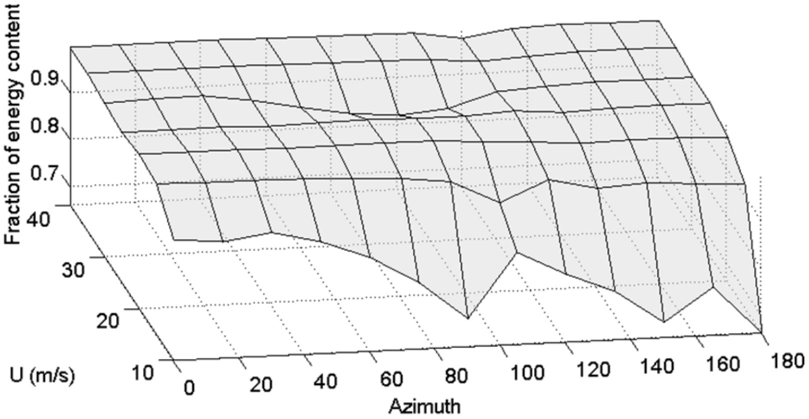

Figure 4.43 Variation of the energy content of the first POD mode on the mirror. Φ=30°, 0°≤θ≤180°, 10≤U≤40m/s.

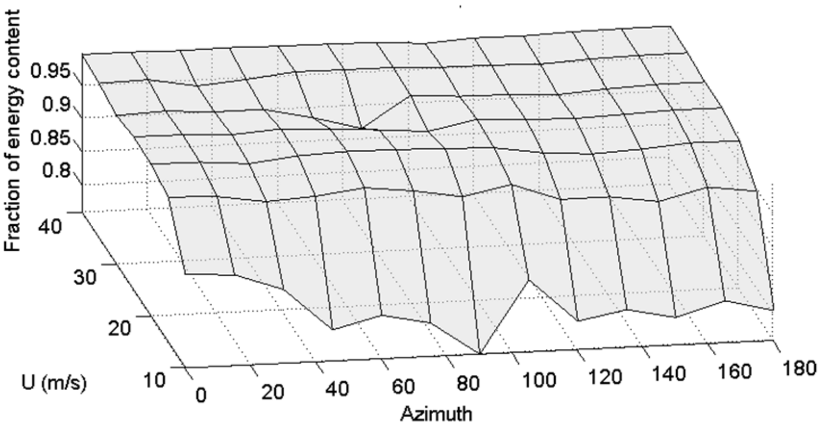

Figure 4.44 Variation of the energy content of the first POD mode on the mirror. Φ=45°, 0°≤θ≤180°, 10≤U≤40m/s.

The results of this section show clearly the effectiveness of the POD in detecting dominant modes on the mirror. Nevertheless, they also show that the POD is unable to detect a clear dominant POD mode for the case of the enclosure.

**POD modes (eigenvectors).**

The presentation of the POD modes in a compact form is a more challenging task since there are two important non-scalar entities from every particular POD mode: the mode shape and the spectral density function of the pressure history in modal space. The flow mechanisms detected by the POD in the analysis of the zero-zenith inclination are the same mechanisms at any other enclosure orientation. The POD analysis for the case of zero-zenith orientation provided an opportunity to observe how the flow mechanisms evolve with respect to wind speed. In this section, the evolution of the POD mode shapes on the enclosure with respect to azimuth orientation is shown in Figure 4.45 and the evolution of the respective spectral densities is shown in Figure 4.46. The two figures contain a sequence of plots obtained from twelve tests performed at a fixed zenith orientation of Φ=45° and at a fixed wind speed of U=25m/s. The azimuth orientation was changed from 0° to 180° in increments of 15°. The figures indicate that for 0°≤θ≤75° the dominant flow mechanisms are the free-shear layer modes, with the larger pressure oscillations occurring on the edge of the enclosure opening. At θ=90°, when the opening is hidden from the oncoming flow, the mode shape changes notoriously and this is accompanied by a change in the respective spectral density function, which now shows a higher spectral amplitude at the low Strouhal frequency. At θ=105°, there is a non-identified mechanism at 73 Hz which does not fully develop as indicated by the low spectral amplitude. From 120°≤θ≤180°, the only identifiable flow mechanism is the low-frequency Strouhal vortex shedding, which have modest spectral amplitude.

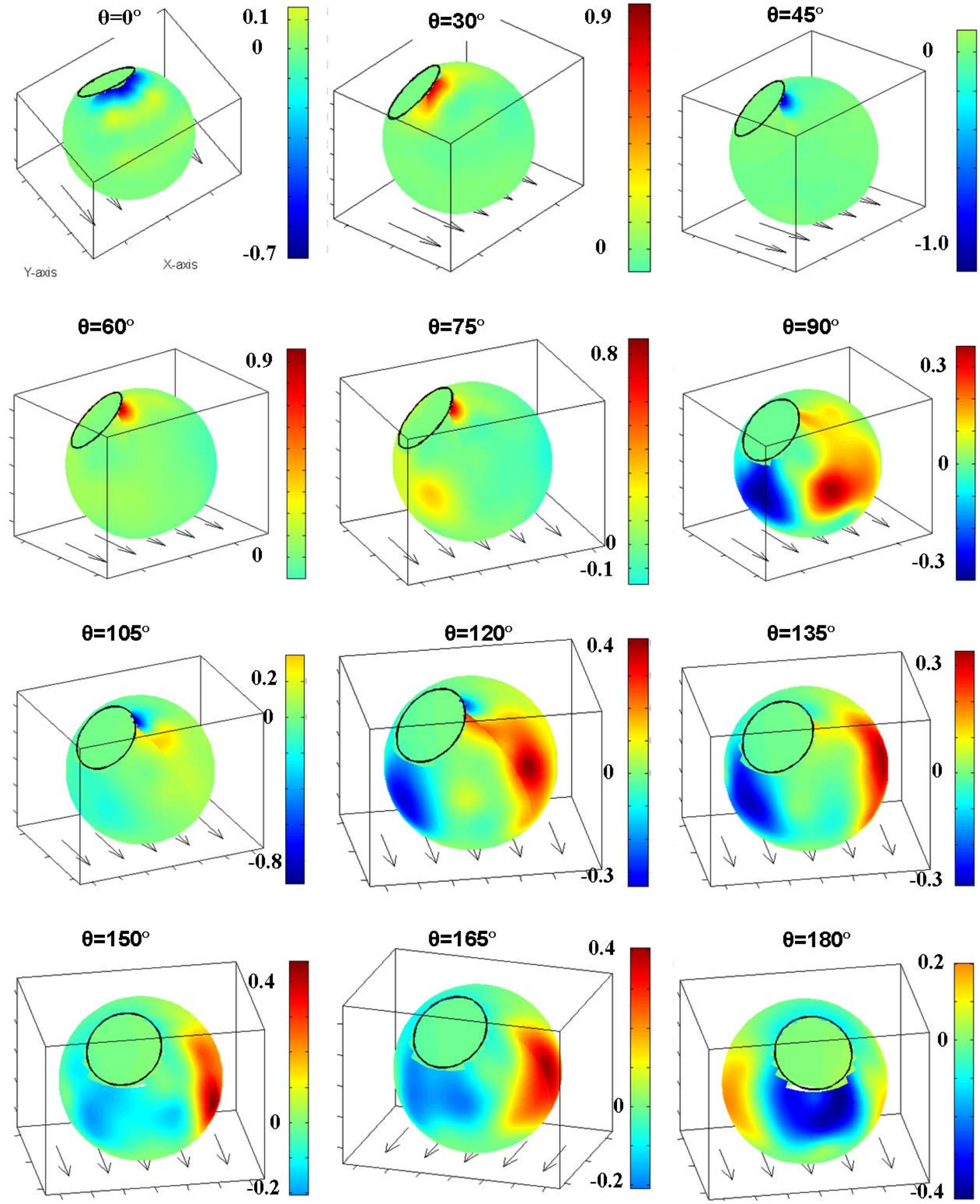

Figure 4.45 First POD mode on the enclosure. ϕ=45°, 0°≤θ≤180°, U=25m/s.

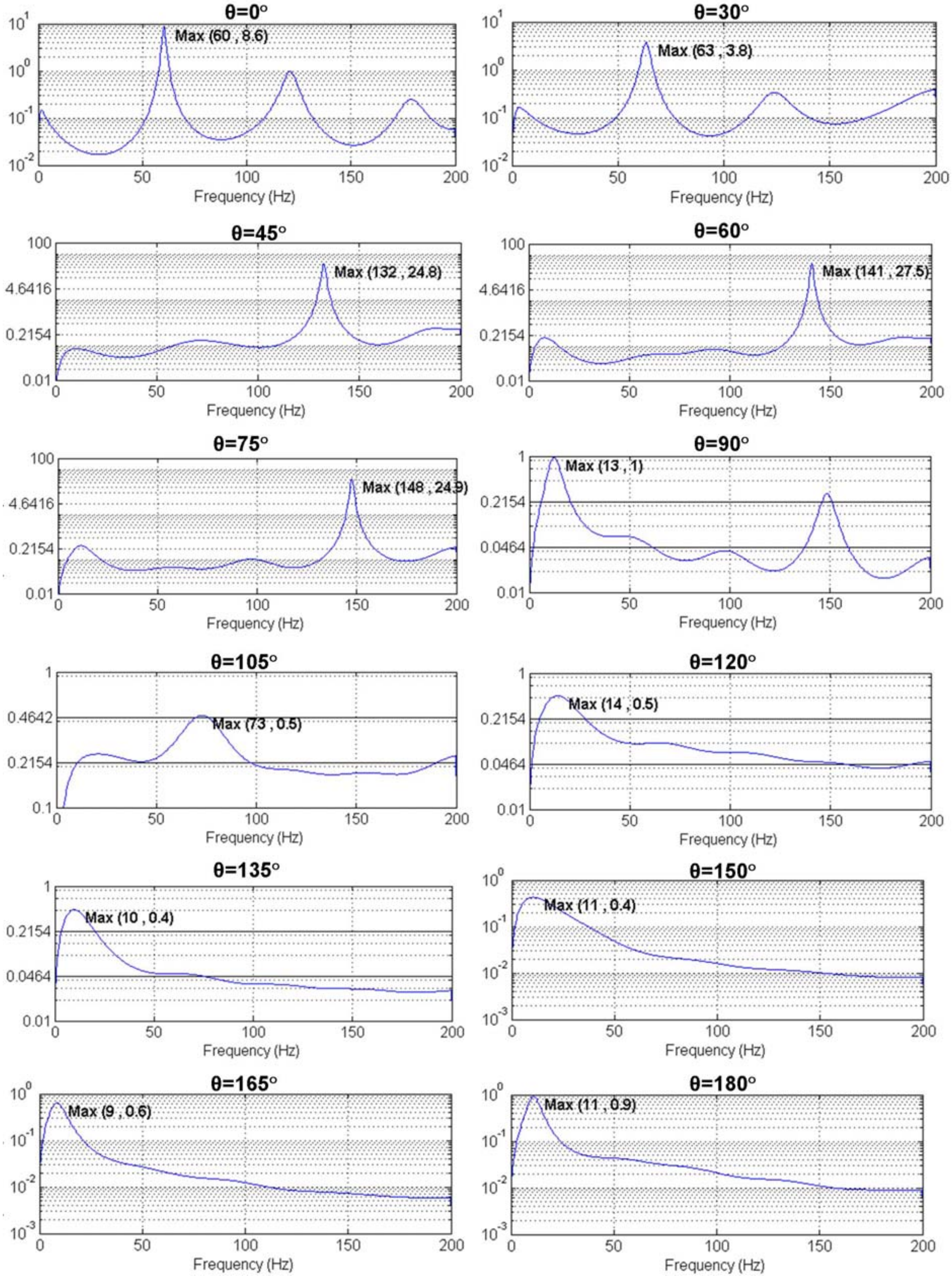

Figure 4.46 Power spectral densities of the first POD mode on the enclosure. ϕ=45°, 0°≤θ≤180°, U=25m/s.

By definition, the spectral density function is a detailed description of how the kinetic energy of certain phenomena is distributed according to its frequency content. Since the present study produced hundreds of spectral density functions, it was considered necessary to extract from them only the largest spectral peak. Thus, Figure 4.47, Figure 4.48 and Figure 4.49 show the spectral amplitude of the most energetic flow mechanism, detected by the first POD mode, for each test configuration. Although these figures do not provide information about the frequency associated with the spectral peaks, they are a convenient tool to spot the test configurations that produce the more energetic flow structures. The direct comparison of the spectral amplitudes is possible because they are normalized with respect to the factor $f / \sigma^2$, as indicated in section 3.3.3. The three figures indicate that the spectral amplitudes reduce considerably (notice that the vertical axis is in logarithmic scale) when the enclosure opening is not exposed to the oncoming flow, i.e. for azimuth rotations greater than 90°. It can be observed that the wind speed is a secondary factor in determining the magnitude of the spectral amplitudes.

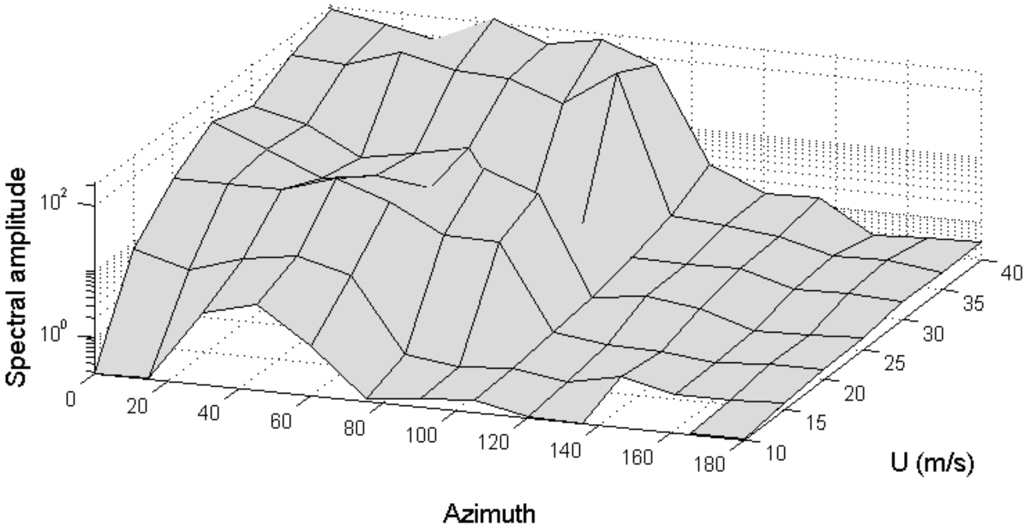

Figure 4.47 Maximum spectral amplitude of the first POD mode on the enclosure. ϕ=15°, 0°≤θ≤180°, 10≤U≤40m/s.

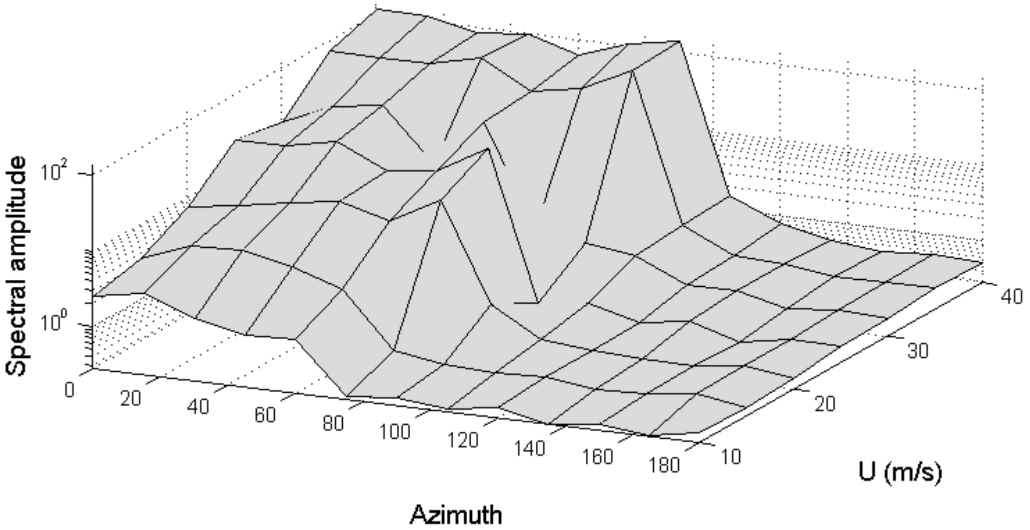

Figure 4.48 Maximum spectral amplitude of the first POD mode on the enclosure. ϕ=30°, 0°≤θ≤180°, 10≤U≤40m/s.

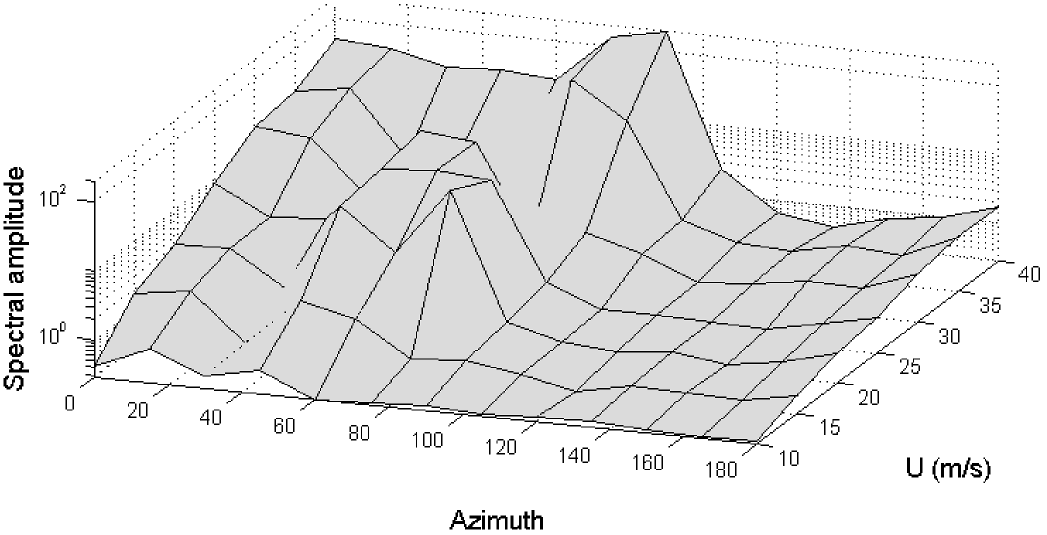

Figure 4.49 Maximum spectral amplitude of the first POD mode on the enclosure. ϕ=45°, 0°≤θ≤180°, 10≤U≤40m/s.

The previous lines in this section have provided a description of how the first POD mode on the enclosure evolves with respect to wind speed and enclosure orientation. The remaining of the section is dedicated to present a similar description for the first POD mode on the mirror.

The shape of the first POD mode on the mirror always represents a pressure pulsation mechanism similar to the one shown in Figure 4.23, and therefore, no additional figures are required to describe it. In order to understand how the spectral density functions evolve with respect to azimuth orientation, a series of twelve spectral density functions are shown in Figure 4.50 for fixed wind speed and zenith orientation. It can be seen that for 0°≤θ≤90°, the higher spectral peaks are associated with the free-shear layer modes caused by flow past a sphere. There is an outstanding strong spectral peak associated to the second free-shear for 45°≤θ≤90°. At θ=105°, there is a sudden decrement in the height of the spectral peaks. The dominant participation of the low-frequency flow mechanisms is held from 105°≤θ≤180°.

Figure 4.51, Figure 4.52 and Figure 4.53 show the amplitudes of the largest spectral peak of the first POD mode on the mirror, for each test configuration. There are some similarities between these figures and their counterparts for the case of the enclosure; in particular, the fact that the spectral amplitudes reduce when the enclosure opening is in the leeward side.

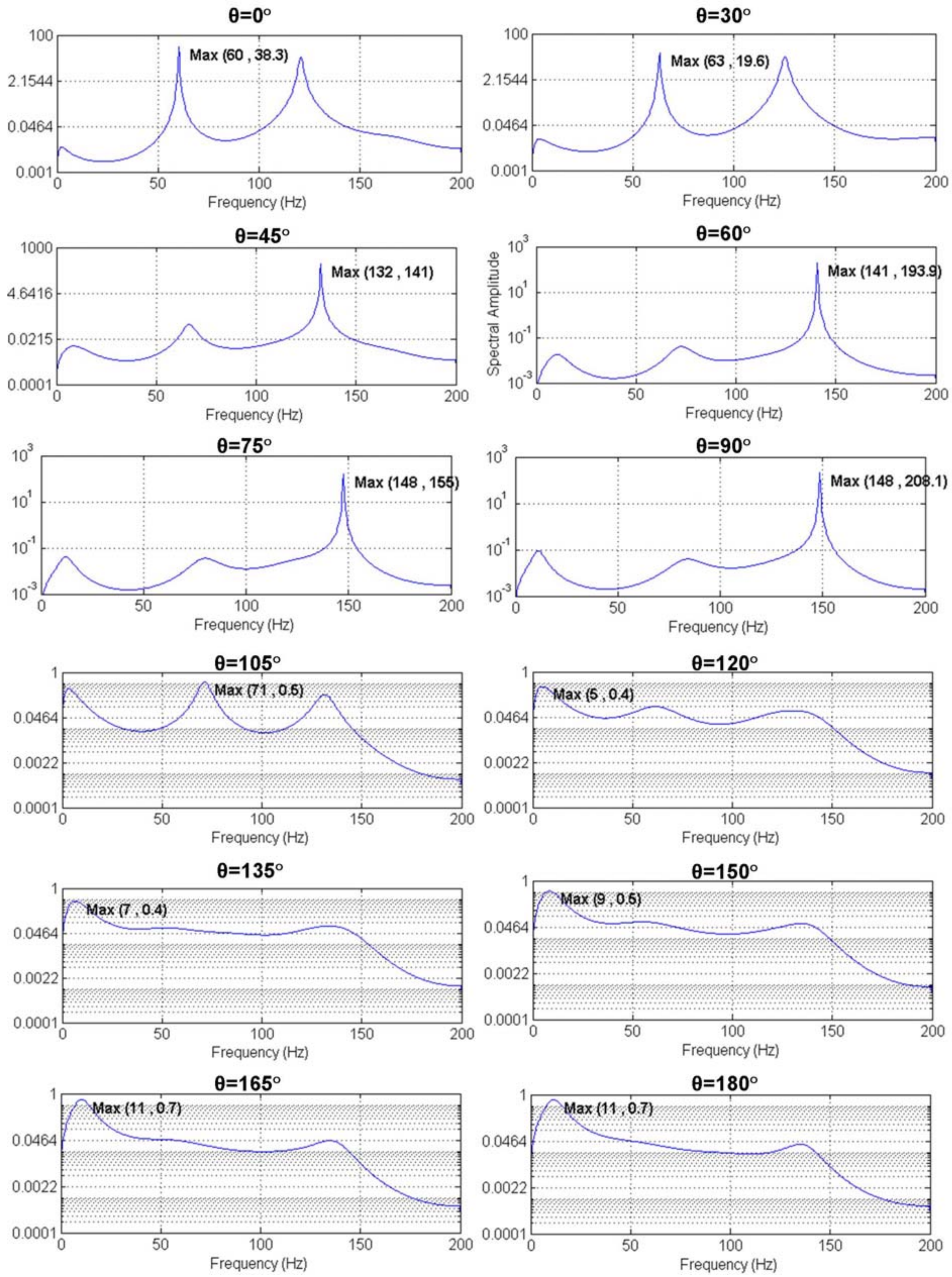

Figure 4.50 Power spectral densities of the first POD mode on the mirror. ϕ=45°, 0°≤θ≤180°, U=25m/s.

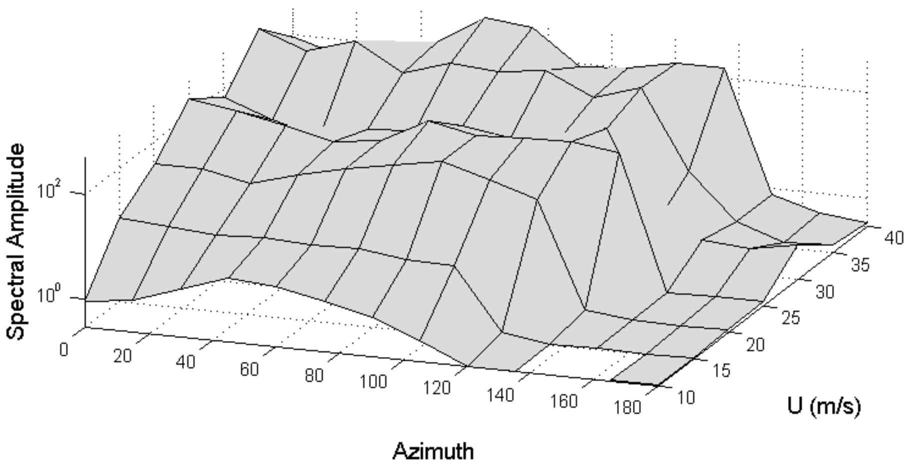

Figure 4.51 Maximum spectral amplitude of the first POD mode on the mirror. ϕ=15°, 0°≤θ≤180°, 10≤U≤40m/s.

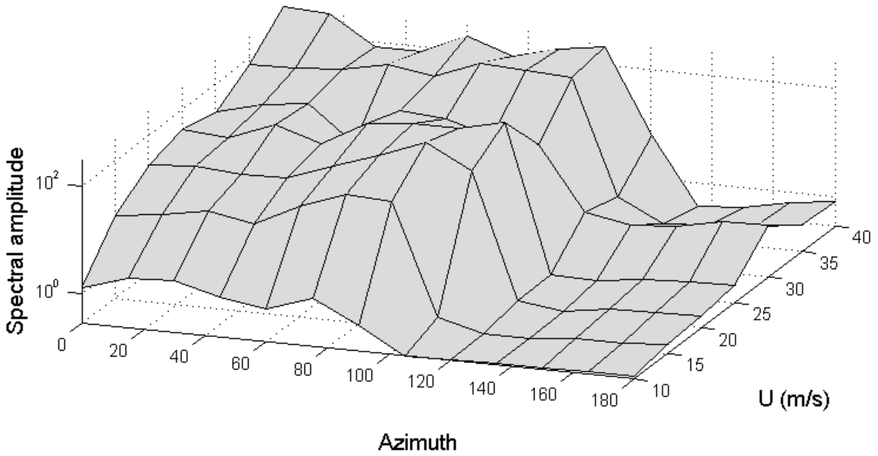

Figure 4.52 Maximum spectral amplitude of the first POD mode on the mirror. ϕ=30°, 0°≤θ≤180°, 10≤U≤40m/s.

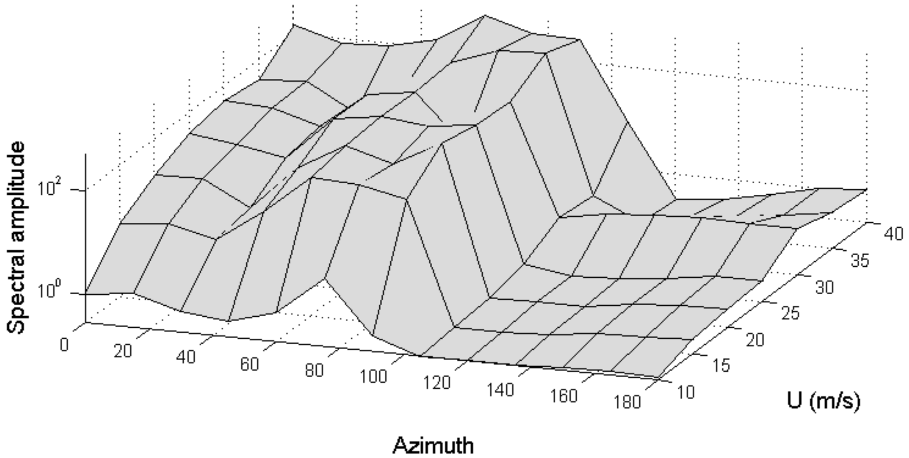

Figure 4.53 Maximum spectral amplitude of the first POD mode on the mirror. ϕ=45°, 0°≤θ≤180°, 10≤U≤40m/s.

As it has been observed, the flow mechanisms created by the outer enclosure are the exciting forces of the pressure pulsations on the mirror, inside the cavity. Nevertheless, one should not conclude that the first POD mode observed on the enclosure is the only exciting force that produces the first POD mode on the mirror. In other words, the pressure field on the mirror described by the first POD mode is caused by flow mechanisms not fully represented by the first POD mode on the enclosure.

The discussion of the POD modes in this sub-section finishes the POD analysis for the sealed case. The next section presents the results of the POD analysis for the ventilated case.

## 4.4 POD analysis for the ventilated case

Since the strong acoustic resonances inside the cavity could significantly distort the mirror's surface, some physical modifications on the enclosure were performed in order to reduce these pressure pulsations. The first two modifications, consisting in altering the edge of the enclosure opening (Figure 4.54), did not reduce the acoustic resonance inside the cavity. Therefore, a more complex modification was necessary, which consisted in creating a row of circular openings on the enclosure, as shown in Figure 4.55.

Figure 4.54 1 cm-high opening lip (left) and 1 cm-high-serrated lip (right).

Figure 4.55 Ventilated enclosure at Φ=30°, θ=30°(left) and Φ=0°, θ=0° (right).

The number of test cases was reduced in the ventilated case. The present study only considered a fixed zenith rotation, a variable azimuth rotation from 0° to 180° and only three wind speeds (13.4m/s, 20m/s and 35m/s). The study also included a variable percentage of porosity on the enclosure, which was achieved by opening and sealing some holes. The test configurations are summarized in Table 4.4. Due to the multiple openings, there were no pressure taps drilled on the enclosure and therefore only the pressure histories on the mirror were recorded.

Table 4.4 Test configurations.

| Porosity | | | Zenith (deg) | Azimuth (deg) | Wind Speed (m/s) |
|---|---|---|---|---|---|
| Case | Upstream | Downstream | | | |
| A | 100% | 100% | 30 | 0, 15, ..., 180 | 13.4, 20, 35 |
| B | 100% | 50% | 30 | 0, 15, ..., 180 | 13.4, 20, 35 |
| C | 50% | 50% | 30 | 0, 15, ..., 180 | 13.4, 20, 35 |
| D | 50% | 100% | 30 | 0, 15, ..., 180 | 13.4, 20, 35 |
| E | 0% | 100% | 30 | 0, 15, ..., 180 | 13.4, 20, 35 |

**Mean pressure coefficients, Cp.**

The largest positive and negative values of the mean pressure field for all test configurations were collected and plotted in Figure 4.56 and Figure 4.57. This means that the mean pressure value of any tap in any test configuration remains between the pair of surfaces shown in the figures. Figure 4.56 was obtained for porosity A, but it is very good description of cases B, C and D. It is noticeable the sharp peak at an azimuth angle of 75°. Figure 4.57 was obtained for porosity E. It follows the same trend of Figure 4.56 but with a smooth transition at θ=75°. In all cases, the mean pressure coefficients remained between 0 and -0.6, which is a more favourable situation than the sealed case, where the mean pressure coefficients reached values up to -1.8. Since the mean pressure field does not follow a particular pattern, there is no need to show images of it.

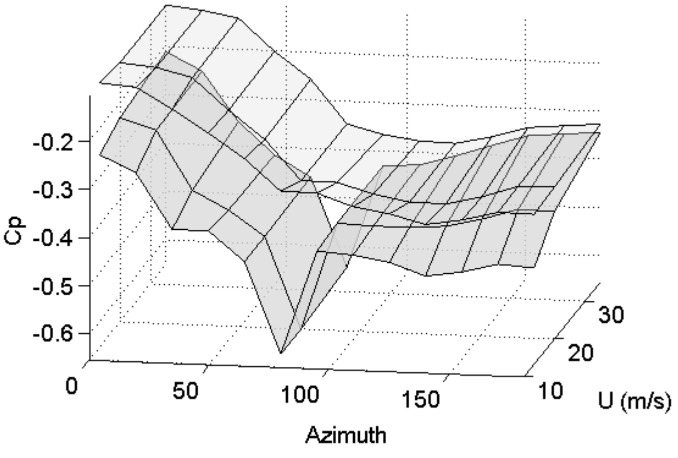

Figure 4.56 Maximum and minimum mean pressure coefficients. $\Phi=30°$, $0°\leq\theta\leq180°$, $13.4m/s\leq U\leq35m/s$. Porosity: upstream=100% & downstream=100%.

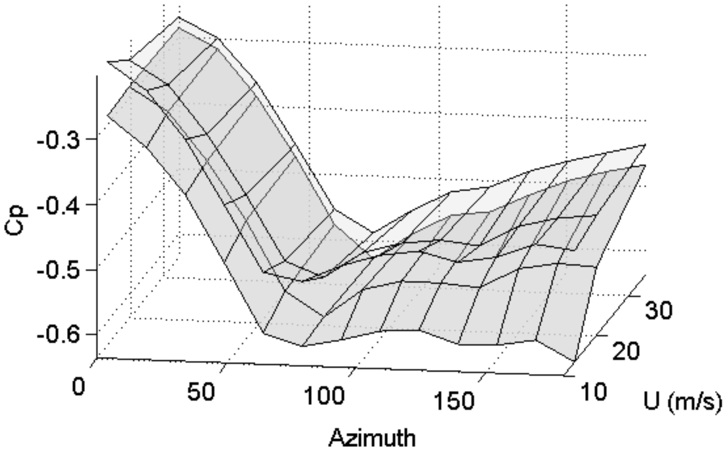

Figure 4.57 Maximum and minimum mean pressure coefficients. Φ=30°, 0°≤θ≤180°, 13.4m/s≤U≤35m/s. Porosity: upstream=0% & downstream=100%.

**Root-mean square values of pressure coefficients, RMS.**

Figure 4.58 and Figure 4.59 show two surfaces that correspond to the average and maximum RMS of pressure coefficients for all test configurations. The porosity of the enclosure notoriously reduced the RMS values of the pressure coefficients on the mirror. While the sealed case reached average and maximum values up to 0.23 and 0.33 respectively (Figure 4.36), the venting case only reached values up to 0.06 and 0.15. Figure 4.58 was obtained for porosity A but it is also a good description for cases B, C and D. As for the case of the mean pressure coefficients, there is a sharp peak at θ=75°. Figure 4.59 was obtained for porosity E. The two surfaces vary smoothly and they remain close to each other with values lower than 0.09.

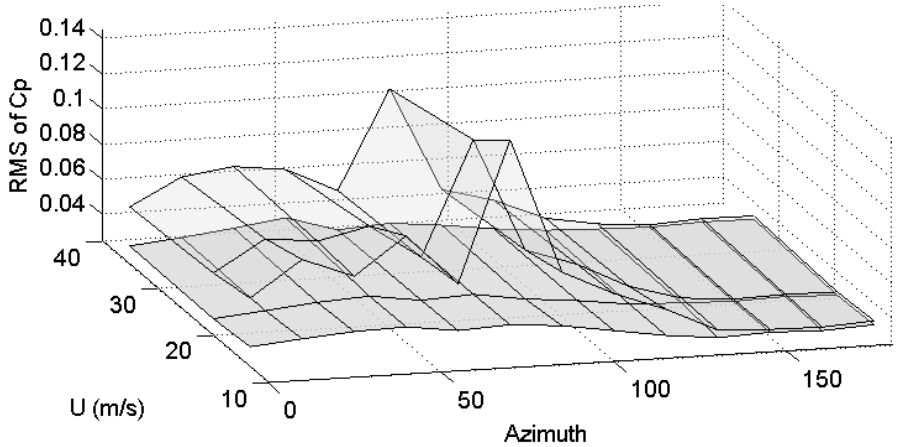

Figure 4.58 Average and maximum RMS of pressure coefficients. Φ=30°, 0°≤θ≤180°, 13.4m/s≤U≤35m/s. Porosity: upstream=100% & downstream=100%.

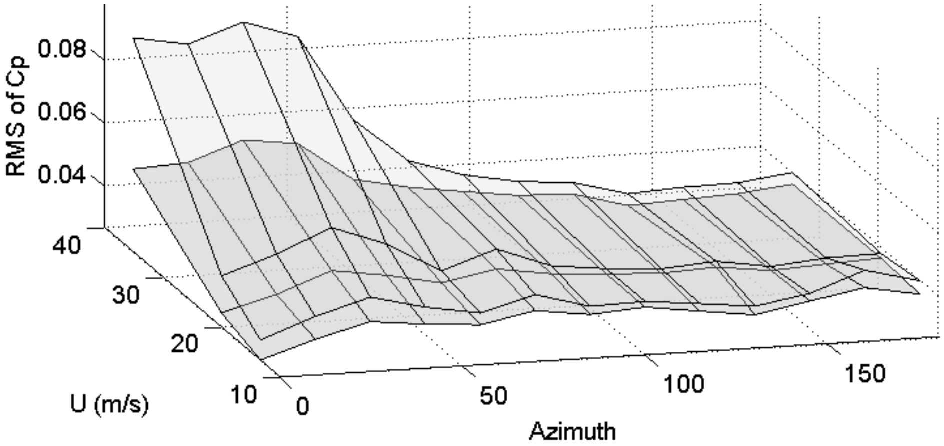

Figure 4.59 Average and maximum RMS of pressure coefficients. Φ=30°, 0°≤θ≤180°, 13.4m/s≤U≤35m/s. Porosity: upstream=0% & downstream=100%.

**Energy distribution (eigenvalues).**

The pressure pulsations observed in the sealed case were the most dominant wind-induced load inside the cavity. For most test configurations, the first POD mode accounted up to 99% of the total energy content. The ventilated case promoted different wind-induced loads inside the cavity, other than the pressure pulsations. The dominance of the first POD mode in the ventilated case is not as strong as in the sealed case. Depending on porosity, wind speed and enclosure orientation, the values for the energy content of the first POD mode ranged from 39% up to 95%. Additional POD modes are required to account for a significant fraction of the total energy content. In most cases, three or less POD modes were enough to account for

70% or more of the total energy content. Depending on porosity, wind speed and enclosure orientation, the cumulative energy content of the first three POD modes ranged from 59% up to 99.5%. These sets of two values are plotted as surfaces in Figure 4.60 and Figure 4.61. The lower surfaces indicate the energy content of the first POD for different test configurations. The upper surfaces indicate the cumulative energy content of the first three POD modes for different test configurations. Figure 4.60 was obtained for porosity A but it is also representative of the cases B, C and D. It can be seen that the energy content is practically independent of wind speed. The variation of the surfaces depends mostly on azimuth orientation. Figure 4.61 was obtained for porosity E. The upper surface has an almost constant value around 96%. The lower surface also has a near constant value except for the region determined by the interval [0°≤θ≤90°, U=35m/s].

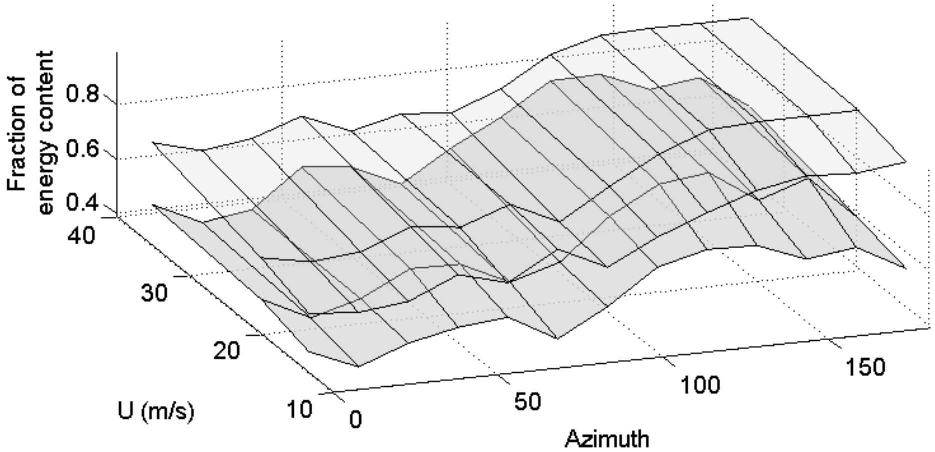

Figure 4.60 Fraction of energy content for the first POD mode and the first three POD modes. Φ=30°, 0°≤θ≤180°, 13.4m/s≤U≤35m/s. Porosity: upstream=100% & downstream=100%.

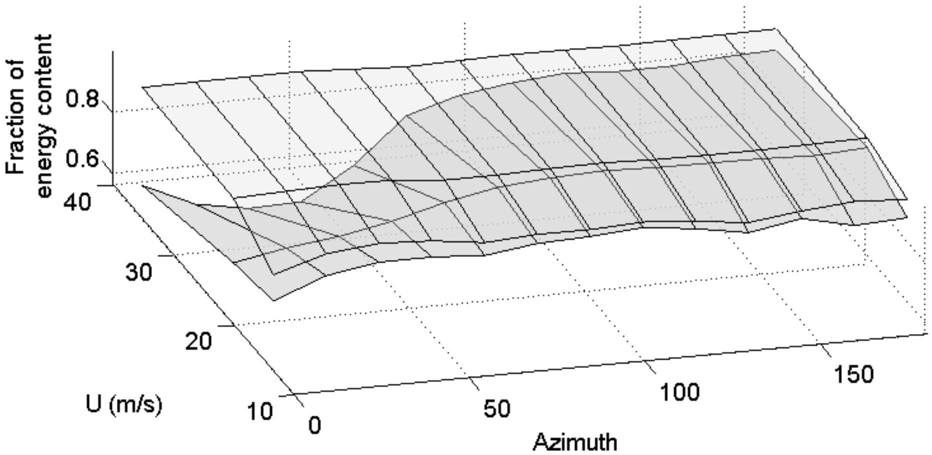

Figure 4.61 Fraction of energy content for the first POD mode and the first three POD modes. Φ=30°, 0°≤θ≤180°, 13.4m/s≤U≤35m/s. Porosity: upstream=0% & downstream=100%.

**POD modes (eigenvectors).**

The flow structures described by the POD modes are no longer associated with the free-shear layer modes observed in the sealed case. At Φ=30° and U=35m/s, the spectral peaks observed in the first three POD modes, for different azimuth angles, occurred at 10±5 Hz, 90±5 Hz and 185±5 Hz. From these frequencies, only the low frequency spectral peaks can be related to the Strouhal number for flow past a sphere, while the higher frequencies cannot be presently related with any well-known flow structure. Figure 4.62, Figure 4.63 and Figure 4.64 show the first, second and third POD modes, respectively, for Φ=30°, θ=0°, U=35m/s and porosity case A. The first and third mode shapes tend to form symmetric patterns with respect to the wind flow, which approaches horizontally from the left. The second mode shape tend to be antisymmetric.

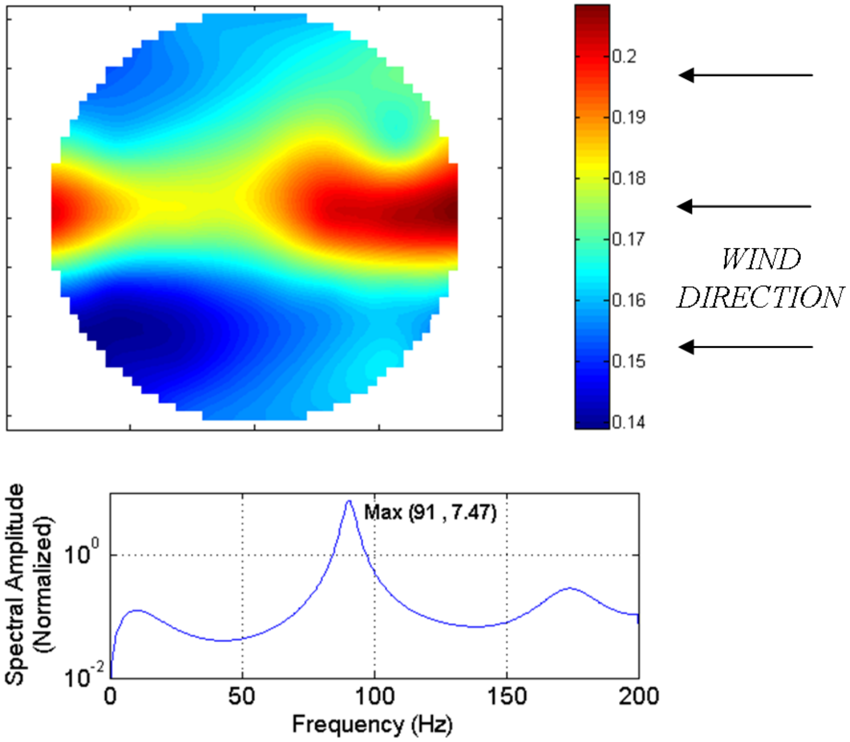

Figure 4.62 First POD mode. Φ=30°, θ=0°, U=35m/s. Porosity: upstream=100% & downstream=100%.

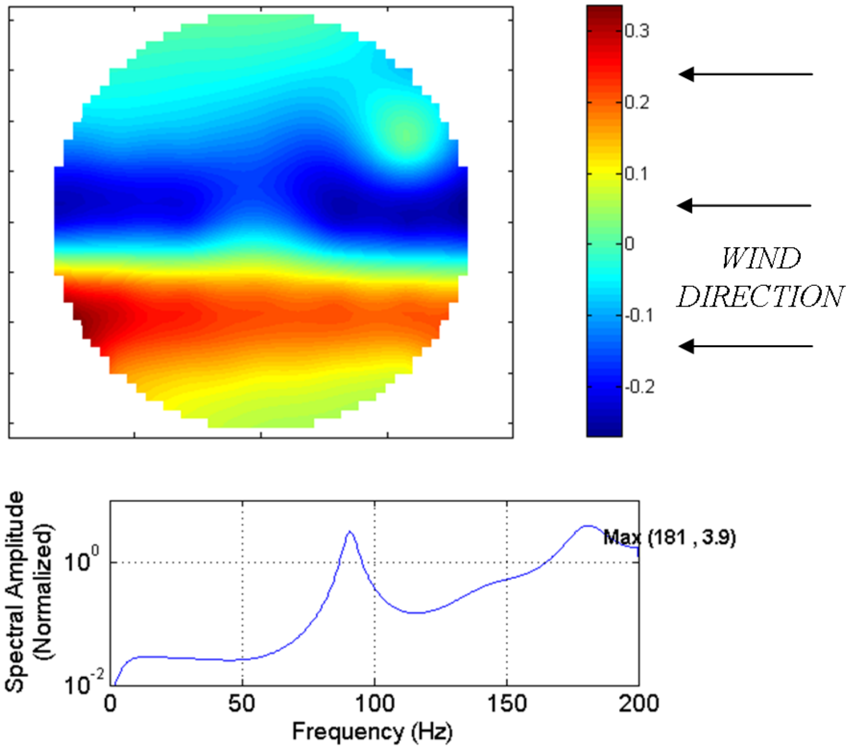

Figure 4.63 Second POD mode. Φ=30°, θ=0°, U=35m/s. Porosity: upstream=100% & downstream=100%.

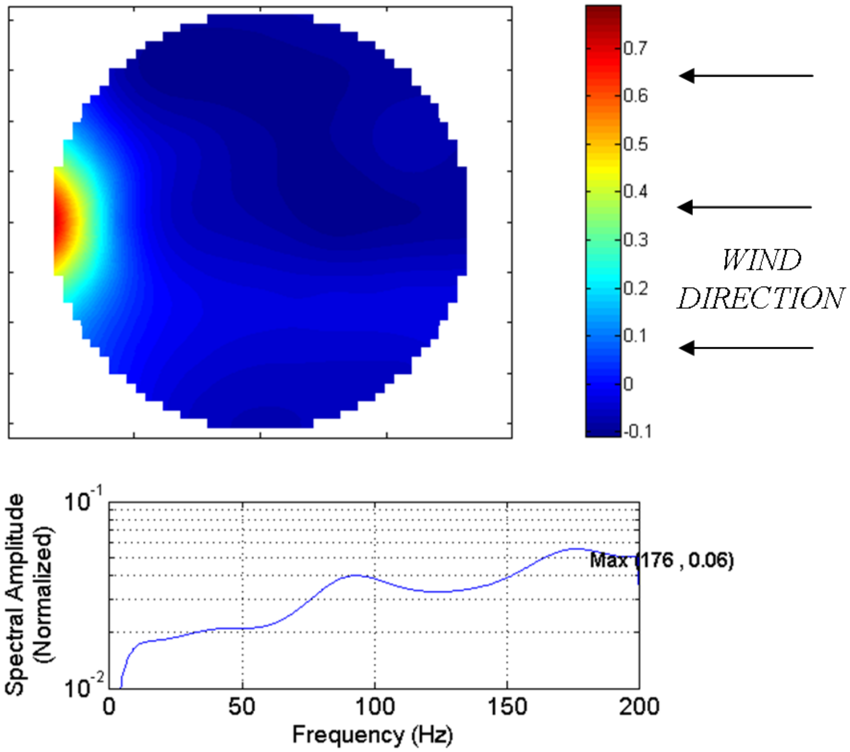

Figure 4.64 Third POD mode. Φ=30°, θ=0°, U=35m/s. Porosity: upstream=100% & downstream=100%.

There are different mode shapes that depend on the percentage of porosity and the azimuth orientation. Nevertheless, the power spectral densities of the POD modes have similar patterns to those shown in the three previous figures. Figure 4.65 to Figure 4.69 show the spectral amplitudes of the first POD mode for all test configurations. It can be seen that the porosity cases A, B, C and D have a similar pattern, with higher amplitudes at 0°≤θ≤45°. Porosity case E has small spectral amplitudes except in the interval [0°≤θ≤5°, U=35m/s].

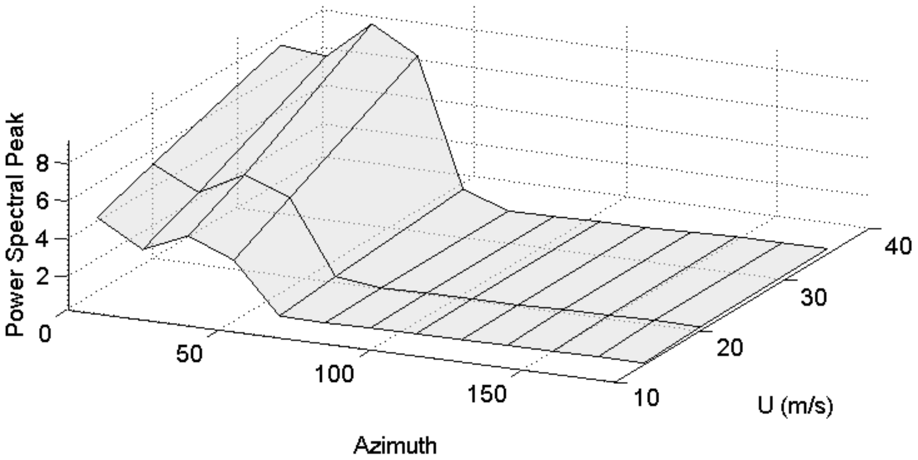

Figure 4.65 Spectral peaks of the first POD mode. Φ=30°, 0°≤θ≤180°, 13.4m/s≤U≤35m/s. Porosity: upstream=100% & downstream=100%.

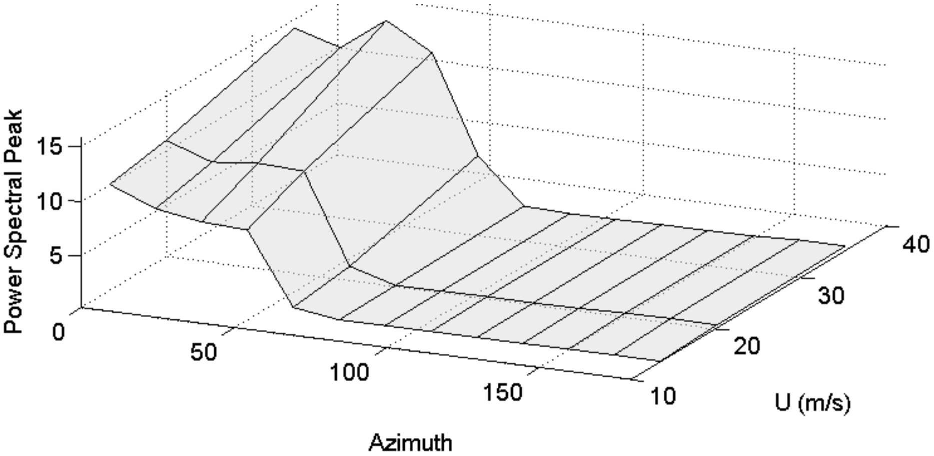

Figure 4.66 Spectral peaks of the first POD mode. Φ=30°, 0°≤θ≤180°, 13.4m/s≤U≤35m/s. Porosity: upstream=100% & downstream=50%.

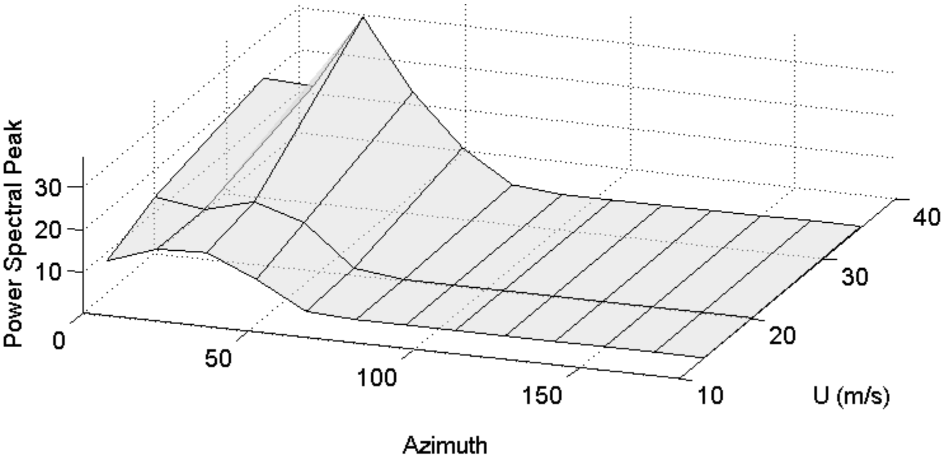

Figure 4.67 Spectral peaks of the first POD mode. Φ=30°, 0°≤θ≤180°, 13.4m/s≤U≤35m/s. Porosity: upstream=50% & downstream=50%.

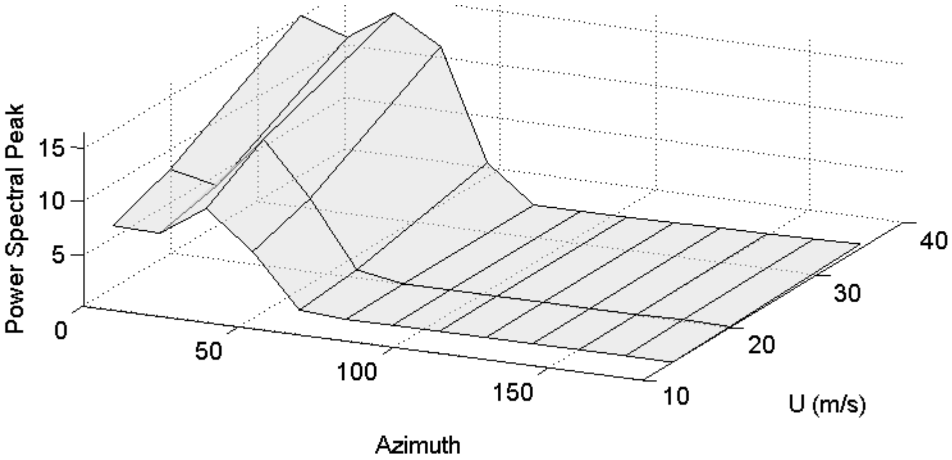

Figure 4.68 Spectral peaks of the first POD mode. Φ=30°, 0°≤θ≤180°, 13.4m/s≤U≤35m/s. Porosity: upstream=50% & downstream=100%.

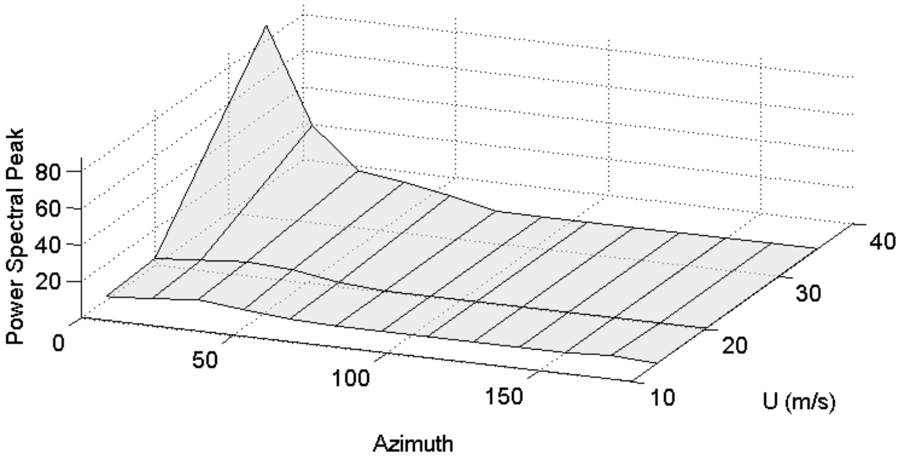

Figure 4.69 Spectral peaks of the first POD mode. Φ=30°, 0°≤θ≤180°, 13.4m/s≤U≤35m/s. Porosity: upstream=0% & downstream=100%.

## *4.5 Conclusions*

- The proper orthogonal decomposition was used to study the unsteady pressure field on the model of an optical telescope. The objective was to determine the static and dynamic characteristics of the wind-induced loads on the mirror assembly located inside a spherical enclosure.
- The wind tunnel tests were carried for smooth flow in a wind speed range of 10≤U≤40m/s and for several enclosure orientations.

- Two different models for the enclosure were considered: the sealed case and the ventilated case. The two models provided pressure fields with different characteristics.
- The sealed case included pressure measurements on both the enclosure and the mirror. The POD modes on the enclosure and their spectral densities revealed flow structures that matched the theoretical descriptions of the free-shear layers modes associated to flow past a sphere. Such flow structures were the source of the acoustic resonances measured on the mirror.
- The POD analysis on the mirror, for the sealed case, indicated that only the first POD mode is enough to describe accurately the wind-induced forces on the mirror.
- The ventilated case included pressure measurements only on the mirror. The porosity on the enclosure decreased significantly the resonance effects observed in the sealed case and therefore both the static and dynamic wind-induced forces on the mirror were considerably smaller than those observed in the sealed case.
- The flow patterns detected on the mirror were dependent on the porosity configuration. For example, in the case of 100% porosity upstream and downstream, the first POD mode indicated regular pulsations of small spectral amplitude. The second POD mode indicated an alternation between pressure on one half of the mirror and suction on the other half. Both POD modes have their spectral peaks at a frequency that is not related to any of the free-shear layer modes, which is evidence of new flow patterns not related with flow past a solid sphere. In fact, it is apparent that a high percentage of porosity on the enclosure

promote flow patterns on the mirror similar to those detected for the hanging roof in Chapter 3.

- The different configurations of porosity in the ventilated case provided similar spectral amplitudes, with slightly more beneficial results in the case of 100% porosity.
- Since the pressure field on the mirror can be reproduced with a few POD modes, one mode for the sealed case and three modes for the ventilated case, it is concluded that the POD method is an appropriate tool to determine the dynamic information needed to design the algorithm control for the actuators of the mirror segments.

# Chapter 5 DOUBLE MODAL TRANSFORMATION

## 5.1 Introduction

The previous chapters have discussed in detail the technique of the proper orthogonal decomposition for understanding and modelling the wind forces that act on two structures: a hanging roof and a telescope. Nevertheless, the results obtained so far cannot be applied directly in the estimation of the structural response of neither of the two structures. Since the final objective of structural engineers is to provide a full description of the structural response, it is reasonable to ask for the link between the structural analysis and the analysis of wind forces using the POD technique. This chapter presents this link through the Double Modal Transformation (DMT) method, which consists of the joint application of the structural modal analysis with the POD analysis.

Solari and Carassale (2000) and Carassale et al (2001) introduced the mathematical aspects of the DMT method. The final part of their papers includes the results of applications to cantilever elements exposed to simulated turbulent flows. Tubino and Solari (2007) presented the results of an application of the DMT method for a long-span bridge immersed in a simulated turbulent flow. The references aforementioned are valuable resources to understand the general aspects of the method but the author of this thesis believes they lack a discussion of how the method must be implemented. By providing a detailed discussion of every mathematical step and a fully-explained application of the DMT method, the author expects to clarify all aspects of the method and promote its use for more wind engineering applications.

The double modal transformation is an elegant method that can be applied to describe the dynamic response of structures that are modelled as multi degree-of-freedom systems and are subject to concentrated or distributed stationary random loads. The method is suitable to be solved either in time domain or in frequency domain.

The solution in time domain is given in section 5.2 and the solution in frequency domain is given in section 5.3. The solution in frequency domain requires the knowledge of the response spectral analysis of single-degree-of-freedom systems, which is discussed in subsection 5.3.1. Subsection 5.3.2 continues the solution of the double modal transformation in frequency domain for multi-degree-of-freedom systems. The last section of the chapter provides an example of the application of the double modal transformation method, which is solved in the frequency domain.

Since the DMT method uses two modal transformations, there are two sets of eigenvectors and eigenvalues and special attention is required to avoid confusion. The structural eigenvalues are denoted with the Greek letter omega at the power of two $\left(\omega^2, \mathbf{\Omega}^2\right)$ and the structural eigenvectors are denoted with the Greek letter psi $(\psi, \mathbf{\Psi})$. The POD eigenvalues are denoted with the Greek letter lambda $(\lambda, \mathbf{\Lambda})$ and the POD eigenvectors are denoted with the Greek letter phi $(\phi, \mathbf{\Phi})$.

## 5.2 Solution in the time domain

The structural modal analysis is a well-known method that can be found in most textbooks of structural dynamics. In order to unify notation with the POD method, the main aspects of the structural modal analysis are described below.

The differential equations of motion of a structure with m-degrees-of-freedom are expressed in matrix form as:

$$[\mathbf{M}]\{\ddot{\mathbf{y}}(t)\} + [\mathbf{C}]\{\dot{\mathbf{y}}(t)\} + [\mathbf{K}]\{\mathbf{y}(t)\} = \{\mathbf{F}(t)\} \qquad \textbf{Eq. 5-1}$$

where [**M**], [**C**] and [**K**] are the mass, viscous damping and stiffness matrices respectively; $\{\mathbf{y}(t)\}$, $\{\dot{\mathbf{y}}(t)\}$ and $\{\ddot{\mathbf{y}}(t)\}$ are the displacement, velocity and acceleration vectors of the structure, respectively; $\{\mathbf{F}(t)\}$ is the loading vector where the force $F_j(t)$ is the force applied along the j-th degree of freedom.

In order to de-couple the differential equation system defined by Eq. 5-1, it is necessary to transform the equations of motion from the physical space (Lagrangian coordinates) to the modal (or principal) space defined by the eigenvectors of the following characteristic equation:

$$\left([\mathbf{K}] - \omega_j{}^2[\mathbf{M}]\right)\{\boldsymbol{\psi}_j\} = \{\mathbf{0}\} \qquad (j = 1,2,\cdots,m) \qquad \textbf{Eq. 5-2}$$

where the eigenvalues $\omega_1{}^2,\cdots,\omega_m{}^2$ correspond to the natural circular frequencies and the eigenvectors $\{\boldsymbol{\psi}_1\},\cdots,\{\boldsymbol{\psi}_m\}$ define the vibration mode shapes of the structure.

Since [**M**] and [**K**] are real, symmetric and positive definite matrices, the eigenvalues obtained from Eq. 5-2 are real and positive. For eigenvectors normalized with respect to the mass matrix, the orthonormal conditions apply:

$$[\boldsymbol{\Psi}]^T[\mathbf{M}][\boldsymbol{\Psi}] = [\mathbf{I}]; \qquad [\boldsymbol{\Psi}]^T[\mathbf{K}][\boldsymbol{\Psi}] = \left[\boldsymbol{\Omega}^2\right] \qquad \textbf{Eq. 5-3}$$

where $[\boldsymbol{\Psi}] = [\{\boldsymbol{\psi}_1\}, \cdots, \{\boldsymbol{\psi}_m\}]$ is an m-by-m matrix containing the structural mode shapes in its columns; **[I]** is the identity matrix; $[\boldsymbol{\Omega}^2]$ is a diagonal m-by-m matrix containing the eigenvalues $\omega_1{}^2, \cdots, \omega_m{}^2$.

The transformation rule that allows to switch from the modal space X to the physical space Y (Lagrangian coordinates) and vice versa is given by:

$$\{\mathbf{y}(t)\} = [\boldsymbol{\Psi}]\{\mathbf{x}(t)\} \qquad \textbf{Eq. 5-4}$$

where {**x**(t)} is the image of {**y**(t)} in modal space. The vector {**x**(t)} contains the displacements referred to the structural principal coordinates, which are displacement histories in modal space.

In order to de-couple the equations of motion it is necessary both, to substitute Eq. 5-4 in Eq. 5-1 and to perform a left-multiplication with the matrix $[\boldsymbol{\Psi}]^{T}$. In matrix form this is expressed as follows:

$$[\boldsymbol{\Psi}]^T[\mathbf{M}][\boldsymbol{\Psi}]\{\ddot{\mathbf{x}}(t)\} + [\boldsymbol{\Psi}]^T[\mathbf{C}][\boldsymbol{\Psi}]\{\dot{\mathbf{x}}(t)\} + [\boldsymbol{\Psi}]^T[\mathbf{K}][\boldsymbol{\Psi}]\{x(t)\} = [\boldsymbol{\Psi}]^T\{\mathbf{F}(t)\} \qquad \textbf{Eq. 5-5}$$

Applying the orthonormality conditions, the matrix equation is reduced to:

$$\{\ddot{\mathbf{x}}(t)\} + [\mathbf{c}]\{\dot{\mathbf{x}}(t)\} + [\boldsymbol{\Omega}^2]\{\mathbf{x}(t)\} = [\boldsymbol{\Psi}]^T\{\mathbf{F}(t)\} = \{\mathbf{F}_x(t)\} \qquad \textbf{Eq. 5-6}$$

If classical damping is considered, matrix [**c**] is diagonal and it contains the modal damping ratios $2\xi_j\omega_j$ ($j$=1,2,...,m). Thus, the j-th differential equation of motion in modal space can be defined as:

$$\ddot{x}_j(t) + 2\xi_j\omega_j\dot{x}_j(t) + \omega_j{}^2x_j(t) = \{\boldsymbol{\psi}_j\}^T\{\mathbf{F}(t)\} = F_{x,j}(t) \qquad (j = 1, \cdots, m) \qquad \textbf{Eq. 5-7}$$

where $\{\boldsymbol{\psi}_j\}$ is the j-th structural eigenvector, whose elements are $\psi_{ij}$ ($i$=1,2,...,m).

It is a customary practice to express the structural response as the contribution of a reduced number of structural modes. Therefore, Eq. 5-7 can be solved for $j = 1, \cdots, m_t$ (with $m_t<m$) and then these solutions are substituted into Eq. 5-4 to return back into physical space.

During the modal structural analysis, the external load vector {**F**(t)} follows passively the mathematical transformations imposed by [**Ψ**], without providing any physical meaning of its nature. It is at this point that the POD analysis is included, providing information about the underlying physical mechanisms of a stochastic pressure field. Moreover, the joint application of the structural modal analysis and the POD analysis reveals the interaction between the external loads and the structural response. Thus, the double modal transformation method provides a full description of the wind-load interaction, both qualitatively and quantitatively.

A brief introduction of the POD was given in Chapter 2. The same notation is used here to facilitate the discussion of the double modal transformation.

In order to connect the ideas of the structural modal analysis and the POD method, it is assumed that the vector force {**F**(t)} in Eq. 5-1 is related to the wind-induced pressure field {**p**(t)} in the following way:

$$\{\mathbf{F}(t)\} = [\mathbf{A}]\{\mathbf{p}(t)\} \qquad \textbf{Eq. 5-8}$$

As mentioned in Chapter 2, the pressure field $\{\mathbf{p}(t)\} = \{p_1(t), p_2(t), \cdots, p_n(t)\}^T$ is determined by n pressure histories recorded at n different locations on the structure. The new mathematical element [**A**] is an m-by-n deterministic matrix that defines a correspondence between the pressure obtained in every pressure tap and the force acting on every degree of freedom of the structure. It is known that the correspondence between pressure and force is a tributary area and that is the basic function of matrix [**A**]. Nevertheless, for tridimensional structures, this correspondence is not as simple as in the scalar case because the wind-induced pressure might act on a curved surface. If the pressure (scalar amount) acting on curved surface is to be interpreted as vector force, then the pressure should be multiplied by differential elements of area and their normal components. The resultant force, if desired, can be obtained as a vector addition or vector integration. Thus, matrix [**A**] is not only a matrix of tributary areas, it also contains information of the components of the unit normal vector associated with each tributary area. The simplest form of matrix [**A**] is by defining it as a diagonal matrix m-by-m but this procedure will be explained during the numerical example provided at the end of the chapter.

It was established in Chapter 2 that the real pressure field {**p**(t)} can be expressed as a linear combination of n uncorrelated pressure signals $\{\mathbf{p}_x(t)\} = \{p_{x,1}(t), p_{x,2}(t), \cdots, p_{x,n}(t)\}^T$. The pressure field {$\mathbf{p}_x$(t)} is the mathematical image of the real pressure field {**p**(t)} in the modal space defined by the eigenvectors $\{\phi_k\}$ (k=1, 2, ...n) of the covariance matrix. In matrix form, this is stated as $\{\mathbf{p}(t)\} = [\mathbf{\Phi}]\{\mathbf{p}_x(t)\}$. Substituting this expression and Eq. 5-8 into Eq. 5-7, we obtain a de-coupled system of m differential equations.

$$\{\ddot{\mathbf{x}}(t)\} + [\mathbf{c}]\{\dot{\mathbf{x}}(t)\} + \left[\mathbf{\Omega}^2\right]\{\mathbf{x}(t)\} = [\mathbf{\Psi}]^T[\mathbf{A}][\mathbf{\Phi}]\{\mathbf{p}_x(t)\} = [\mathbf{B}]\{\mathbf{p}_x(t)\} = \{\mathbf{F}_x(t)\} \qquad \textbf{Eq. 5-9}$$

where [**B**] is an m-by-n matrix called the cross-modal participation matrix. From the equation above it is readily seen that:

$$[\mathbf{B}] = [\mathbf{\Psi}]^T[\mathbf{A}][\mathbf{\Phi}] \qquad \textbf{Eq. 5-10}$$

The j, k-th element of [**B**] is calculated as $B_{jk} = \{\psi_j\}^T[\mathbf{A}]\{\phi_k\}$ and it determines the influence of the k-th POD mode (loading mode) on the j-th structural mode.

Thus, the j-th differential equation of Eq. 5-9 is expressed as follows:

**Eq. 5-11**

$$\ddot{x}_j(t) + 2\xi_j\omega_j\dot{x}_j(t) + \omega_j^{\,2}x_j(t) = \sum_{k=1}^{n} B_{jk}\,p_{x,k}(t) = F_{x,j}(t) \qquad (j = 1,\cdots,m)$$

Notice that the use of letter F reminds that the pressure has been transformed into force. The tributary areas are included in the calculation of the cross-modal participation factors and therefore the units are coherent. Eq. 5-11 indicates that the response of the j-th mode of vibration is affected by the weighted participation of all the loading modes (POD modes).

Several numerical methods have been developed to give accurate solutions to second order differential equations like Eq. 5-11. Once the response **x**(t) is obtained, it is possible to return back to the Lagrangian equations or real space by means of Eq. 5-4, thus concluding the procedure of the double modal transformation in the time domain. The solution in time domain provides an exact description of the displacement, velocity and accelerations experienced by every joint in the structure at any time. Nevertheless, this level of detail is often unnecessary and it comes at the expense of a large computation time. This and other reasons explained below justify the use of an alternate solution, a solution in the frequency domain.

## *5.3 Solution in the frequency domain*

Obtaining the exact solution in the time domain is possible with the double modal transformation but there are a few reasons why the frequency domain solution is preferred. First, the solution in time domain for any particular vector field {**p**(t)} is unique and does not represent a solution for any other pressure distribution. Another reason for limiting the time-domain solution is that it requires more computation time. Finally, the detailed description of the structural response is often unnecessary since engineers are usually concerned about the peak values.

The peak values of the structural response can be determined, through probabilistic models, if the mean and standard deviation of the structural response are known. The question is how to obtain the mean and standard deviation of the response of a structure subjected to a random load without going through the whole path of the time-domain solution. The procedure to achieve that goal is called the Response Spectrum Analysis and the double modal transformation is suitable to be solved in combination with the response spectral analysis. Nevertheless, it should be noticed that the advantages of using the frequency-domain solution applies only for structures that behave linearly. More complex analyses, that might require a time-domain solution, have to be used for non-linear structures.

The Response Spectrum Analysis is a method broadly discussed in many sources; Chopra (2000), Simiu and Scanlan (1996) and Wirsching et al (1995) are a few examples. The method allows to estimate 'exactly' the peak value of the response of a single-degree-of-freedom (SDOF) system subjected to an arbitrary load for which its spectrum is known. In the case of a multi-degree-of-freedom system (MDOF), the solution is not exact because there is uncertainty in the combination of the individual responses of every degree of freedom and because the common truncation of modes. Fortunately, several combination methods have been developed in order to provide an accurate estimation of the peak value of the response.

There are important reasons why the frequency-domain solution is preferred in many times over the time-domain solution. Firstly, there is steadiness in the spectrum of a random process and this allows to predict results for similar random processes. In the second place, the spectrum of a random process is defined with less points than its time history, thus allowing faster numerical calculations. Additionally, the solution in the frequency domain reveals some features of the random process that are hidden in the time-domain solution. Finally, the frequency-domain solution provides directly the standard deviation values used to predict the peak values.

From the discussion thus far, it is apparent that there is a connection between the spectrum of a random process and the variance of the process. In fact, the connection is very direct: the area under the spectral density function of a random process is exactly the variance of the process. Furthermore, the spectral density function of a random process is a fine description of how the variance is distributed according to its frequency content.

Without further comments, let us start the discussion of the Response Spectral Analysis for a single degree-of-freedom system. These results are useful for the frequency-domain solution of the double modal transformation method.

### 5.3.1 Spectral Analysis for Single-Degree-of-Freedom Systems

Let start the discussion by reviewing the most important aspects of the response spectral analysis of a SDOF system with mass $m_j$, damping coefficient $c_j$ and stiffness subjected to the action of a random load $F_j(t)$. The differential equation of motion can be established as:

$$m_j \ddot{x}_j(t) + c_j \dot{x}_j(t) + k_j x_j(t) = F_{x,j}(t) \qquad \textbf{Eq. 5-12}$$

By dividing all terms by $m_j$ and substituting $\frac{c_j}{m_j} = 2\xi_j \omega_j$, $\frac{k_j}{\omega_j} = \omega_j^2$ and $\omega_j = 2\pi f_j$ the equation above is transformed into:

$$\ddot{x}_j(t) + 2\xi_j (2\pi f_j) \dot{x}_j(t) + (2\pi f_j)^2 x_j(t) = \frac{1}{m_j} F_{x,j}(t) \qquad \textbf{Eq. 5-13}$$

If $m_j$=1, then this equation is the same as Eq. 5-11 for a system that is under the action of only one random load, $F_{x,j}(t)$.

One of the most important results of spectral analysis states that the response spectrum is equal to the product of two real-valued functions, where one function contains information of the structural properties and the other function contains the information of the load characteristics. Mathematically, this is expressed as follows:

$$S_{x,j}(f) = \left|H_j(f)\right|^2 S_{Fx,j}(f) \qquad \textbf{Eq. 5-14}$$

where $S_{Fx,j}(f)$ is the one-sided spectral density function of $F_{x,j}(t)$ with the frequency f in Hz, $H_j(f)$ is a complex function called the transfer function and its magnitude $\left|H_j(f)\right| = \sqrt{H(f)H^*(f)} = \sqrt{(\mathrm{Re}\,H)^2 + (\mathrm{Im}\,H)^2}$ is called the gain function (also known as the mechanical admittance function or dynamic amplification function). In order to understand what Eq. 5-14 represents, it should be remembered that the spectral density function of the load $S_{Fx,j}(f)$ defines how the energy of the exciting force is distributed according with its frequency content, while the gain function describes the sensitivity of the structure to respond to individual exciting frequencies.

Eq. 5-14 is so important that it is worth to make a short parenthesis to look at it from a graphical point of view. Figure 3.1 shows that the amplitude of the response spectrum is highly sensitive to the location of the spectral peaks of the gain function and the force spectrum. In Figure 3.1a, the force spectrum has a peak coinciding with the peak of the gain function, which produces a response spectrum with a large peak. In Figure 3.1b the peaks of the force spectrum and the gain function do not coincide, which leads to a response spectrum with small amplitude. It should be noticed that in the two cases the amplitudes of the gain function and the load spectrum do not change, the only difference is the location of their peaks.

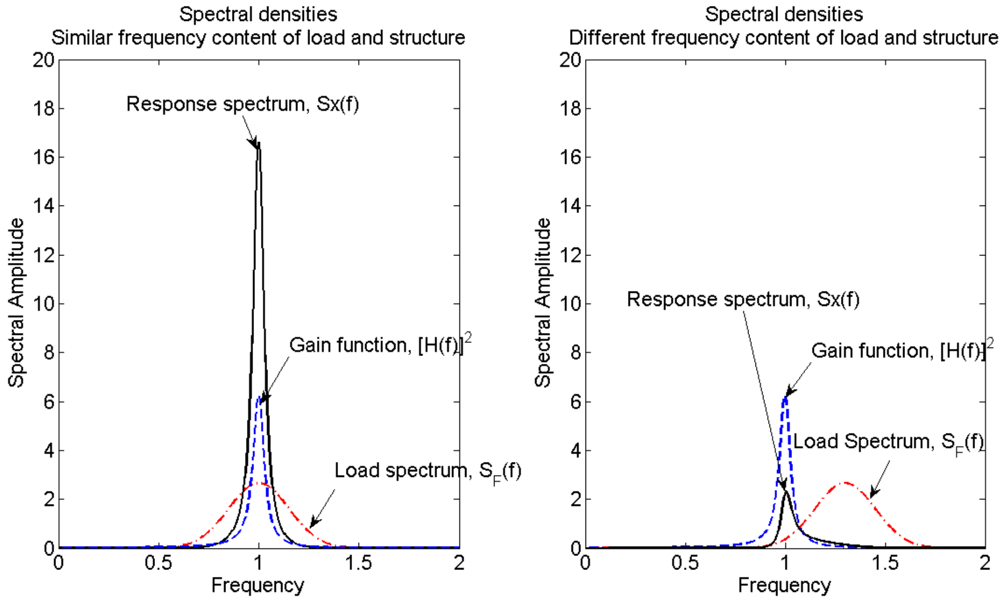

Figure 5.1 Graphical representation of Eq. 5-14 for two cases: (a) Similar frequency content of load and structure, and (b) Different frequency content of load and structure.

Depending on the particular requirements and conditions of a problem, it is possible to define different expressions for the gain function. Thus, it is possible to obtain different gain functions for absolute displacement, velocity and acceleration and for relative displacement, velocity and acceleration. For example, the gain function of the absolute displacement of a SDOF system is calculated as follows:

$$\left|H_j(f)\right| = \frac{1}{4\pi^2 f_j{}^2 m_j \sqrt{\left(1 - r_j^2\right)^2 + \left(2\xi_j r_j\right)^2}} \qquad \textbf{Eq. 5-15}$$

where $m_j$ is the modal mass of the system ($m_j$=1 in Eq. 5-11 and Eq. 5-13), $\xi_j$ is the modal damping ratio and $r_j = f/f_j$ is the ratio of the exciting frequencies f to the natural frequency $f_j$. The factor $4\pi^2$ indicates that this expression should be used in conjunction with single-sided load spectral densities that have values of frequencies in Hertz. Wirsching et at (1995) provide a complete table of gain functions.

Intensive research and numerous experimental measurements have provided mathematical models for the estimation of $S_{Fx,j}(f)$ for different scenarios of atmospheric turbulence and site conditions. Nevertheless, some problems require a precise measurement of the spectral density function of the load.

Once the response spectrum $S_{x,j}(f)$ is obtained, the variance of the response is finally obtained by calculating the area under the response spectrum:

$$\sigma_{x,j}^2 = \int_0^{+\infty} S_{x,j}(f)df \tag*{Eq. 5-16}$$

### 5.3.2 Multi-degree-of-freedom systems (MDOF)

The double modal transformation method can be used in conjunction with the response spectral analysis of a single-degree-of-freedom system in order to provide a frequency-domain solution.

It is observed that the exciting force of the j-th uncoupled equation of motion is a linear combination of n signals, i.e., $F_{x,j}(t) = \sum_{k=1}^{n} B_{jk} p_{x,k}(t)$, then the spectral density function of $F_{x,j}(t)$ can be calculated as:

$$S_{Fx,j}(f) = \sum_{k=1}^{n} B_{jk} S_{px,k}(f) \tag*{Eq. 5-17}$$

where the $S_{px,k}(f)$ (for k=1,...,n) are the spectral density functions of each POD mode.

Notice that once the cross-modal participation matrix [**B**] is defined, there are no difficulties in calculating $S_{Fx,j}(f)$ for j=1,...,m. Similarly, the gain functions of all modal oscillators are fully determined with Eq. 5-15 with the knowledge of the modal frequencies, modal damping ratios and modal masses. Thus, the application of Eq. 5-14 to each modal oscillator (Eq. 5-11) provides the solution in frequency domain of all uncoupled modal oscillators $\{\mathbf{S}_x(f)\} = \{S_{x,1}(f), \cdots, S_{x,m}(f)\}$.

In classical modal analysis, once the solution in modal space is determined for {**x**(t)}, it is possible to obtain the solution in Lagrangian space for {**y**(t)} by means of Eq. 5-4. The problem is to verify if a similar transformation applies to {$\mathbf{S}_x$(t)}.

Let us start by assuming that the solution {**x**(t)} can be obtained from numerical methods. Eq. 5-4 provides the connection between the solution in modal space {**x**(t)} and the solution in real space {**y**(t)}. In particular, let us focus on the i-th de-coupled equation of motion:

$$y_i(t) = \sum_{j=1}^{m} \psi_{ij} x_j(t) \tag*{\textbf{Eq. 5-18}}$$

or in expanded form,

$$y_i(t) = \psi_{i1}x_1(t) + \psi_{i2}x_2(t) + \cdots + \psi_{im}x_m(t) \tag*{\textbf{Eq. 5-19}}$$

The Fourier transform is applied on both sides of Eq. 5-19 in order to change the analysis from the time domain to the frequency domain:

$$\Im\{y_i(t)\} = \Im\{\psi_{i1}x_1(t) + \psi_{i2}x_2(t) + \cdots + \psi_{im}x_m(t)\} \tag*{\textbf{Eq. 5-20}}$$

Since the Fourier transformation is a linear operation, the sum of m time histories is equal to the sum of the individual transforms of the m time histories. In mathematical terms this stated as:

$$\Im\{y_i(t)\} = \Im\{\psi_{i1}x_1(t)\} + \Im\{\psi_{i2}x_2(t)\} + \cdots + \Im\{\psi_{im}x_m(t)\} \tag*{\textbf{Eq. 5-21}}$$

Since the $\psi_{ir}$ are constants, they are not affected by the Fourier transform, therefore we obtain:

$$Y_i(\omega) = \psi_{i1}X_1(\omega) + \psi_{i2}X_2(\omega) + \cdots + \psi_{im}X_m(\omega) \tag*{\textbf{Eq. 5-22}}$$

or in compact form:

$$Y_i(\omega) = \sum_{j=1}^{m} \psi_{ij} X_j(\omega)$$ **Eq. 5-23**

Now we make the observation that the power spectral density of a signal x(t) is basically obtained from splitting x(t) in r segments of length T, taking the Fourier transform of each segment and averaging the square of the magnitude of Fourier transforms of all segments. In numerical applications, the power spectral density function is estimated as follows:

$$\hat{S}_x(\omega) = \frac{1}{2\pi T} \frac{1}{r} \sum_{k=1}^{r} |X_k(\omega)|^2$$ **Eq. 5-24**

The circumflex sign is used to denote a numerical estimation of the spectral density function while $S_x(f)$ denotes its formal definition with the frequency in hertz. The latter notation is used throughout this work.

In a few words, the power spectral density of x(t) is a smooth Fourier transform from which the phase angle can not be recovered. By assuming that the Fourier transform $X_j(\omega)$ can be substituted by the power spectral density function $S_{x,j}(f)$, we obtain:

$$S_{y,i}(f) = \sum_{j=1}^{m} \psi_{ij} S_{x,j}(f)$$ **Eq. 5-25**

Since the variance of a signal x(t) is the area under its power spectral density function, i.e. $\sigma_x^2 = \int S_x(f) df$ , we extend the result as:

$$\sigma_{y,i}^2 = \sum_{j=1}^{m} \psi_{ij} \sigma_{x,j}^2$$ **Eq. 5-26**

Notice that if these operations are valid for the i-th degree-of-freedom, then they are also valid for all degrees-of-freedom. Therefore, Eq. 5-25 can be generalized as:

$$\{\mathbf{S}_y(f)\} = [\mathbf{\Psi}]\{\mathbf{S}_x(f)\} \qquad \textbf{Eq. 5-27}$$

This expression states that if we can solve Eq. 5-11 in the frequency domain for $j = 1, \cdots, m_t$, then it is possible to determine the spectrum density function of $\{\mathbf{y}(\mathrm{t})\}$.

Naturally, once the spectral density functions $\{\mathbf{S}_x(f)\}$ are obtained, it is possible to calculate their variances $\{\boldsymbol{\sigma}_x^2\}$ and thus Eq. 5-26 can also be generalized as follows:

$$\{\boldsymbol{\sigma}_y^2\} = [\mathbf{\Psi}]\{\boldsymbol{\sigma}_x^2\} \qquad \textbf{Eq. 5-28}$$

This concludes the method of the double modal transformation based on the classical modal analysis and the covariance proper orthogonal decomposition. The method is strongly appealing from a theoretical point of view since it gives a precise description of the interaction of every loading mode shape on every structural mode shape. The cross-modal participation matrix [**B**] condenses the information of the interaction between the shape of the load eigenvectors and the shape of the structural eigenvectors. The interaction between the frequency content of the load and natural frequencies of the structural modes is estimated through equation Eq. 5-14: $S_{x,j}(f) = \left|H_j(f)\right|^2 S_{Fx,j}(f)$.

The practical application of the double modal transformation method is restricted to the access of the equations of motion of the structure (Eq. 5-1) and, of course, to the collection of experimental pressure data. The output of certain commercial software for structural analysis gives enough information to perform, independently, the double modal transformation. For example, the structural eigenmodes and eigenvalues provided by SAP2000 can be combined with the POD modes to establish Eq. 5-11 and then the equation can be solved with the assumption of a damping ratio for each structural mode.

The previous discussion of the double modal transformation was stated for structures that can be modelled as discrete systems but the method can also be established for continuous structures. In fact, the method can provide a closed-form solution for a few continuous structures subjected to particular wind load patterns.

## 5.4 Numerical application

The POD analysis of the unsteady pressure field on the hanging roof, presented in Chapter 3, is now combined with the structural analysis of the roof model studied by Flores-Vera (2003) in order to demonstrate how to apply the double modal transformation method discussed in this chapter. There is no intention for describing thoroughly the structural response of the hanging roof for all wind tunnel tests studied in Chapter 3. Therefore, only one case is studied; the roof immersed in the vortex trail of a square prism at U=37.7 m/s at model scale.

### 5.4.1 Similarity requirements

Before applying the double modal transformation method, it is convenient to discuss how the results obtained from wind tunnel tests should be used in the prediction of the prototype behaviour.

According to the theory of models, any dimensionless number based on model scale parameters should be equal to the same dimensionless number based on the prototype scale parameters. There are many dimensionless numbers and a true model should meet all similarity requirements. If at least one similarity requirement is not met, then it is said that the model is distorted.  Given the difficulties to meet all the similarity requirements, it is more common to use distorted models rather than true models. Valuable information can be obtained from distorted models but the interpretation of results should be done carefully.

The example presented in this section includes the use of only four dimensionless numbers and the reader can see the difficulties in trying to meet these few similarity requirements. The four dimensionless quantities are the length scale, Strouhal number, Reynolds number and the normalized spectral amplitude.

- *Length scale*. The length scale is calculated as the ratio of two different characteristic lengths for the model and the prototype. For example, if $L_{x,m}$ and $L_{y,m}$ are the dimensions of the sides of the hanging roof model along the x and y axis and $L_{x,p}$ and $L_{y,p}$ are the corresponding dimensions of the prototype, then the ratio $L_{x,m}/L_{x,p} = L_{y,m}/L_{y,p} = 1/200$ is the length scale. For true models there is only one length scale but it will be seen shortly that other length scale might be more convenient when dealing with the effects of the vortex generator.
- *Reynolds number*. This dimensionless group establishes the following relationship:

$$U_m \frac{L_{2m}}{\nu_m} = U_p \frac{L_{2p}}{\nu_p} \qquad \text{or}$$

**Eq. 5-29**

$$U_p = U_m \frac{L_{2m}}{L_{2p}} \text{ for } \nu_m = \nu_p$$

where $\nu_m$ and $\nu_p$ are the kinematic viscosity of the moving fluid at model and prototype scale, respectively. Since the physical properties of the air used in the wind tunnel are practically the same used for the prototype, then $\nu_m = \nu_p$. $U_m$ and $U_p$ are the wind speed at the model and prototype scales, respectively. The length scale used for the Reynolds number is $L_{2m}/L_{2p}$. Notice that if the length scale is 1/200 and $U_m$=37.7 m/s, then, in order to hold the same Reynolds number the wind speed at prototype scale should be $U_p$=0.19 m/s. Such small wind speed is never used for wind engineering applications. In fact, according to the construction code of Mexico City, Flores-Vera (2003) determined that the design wind speed for the hanging roof is $U_p$=35.8 m/s. We will continue this example with a wind speed equal to $U_m$=$U_p$=35.8 m/s and we assume that despite that the Reynolds number is almost 200 times larger at the prototype scale than at model scale the results obtained from the wind tunnel tests are applicable to the prototype. In a real application, this assumption can be serious since the characteristics of the pressure field might change significantly at different Reynolds numbers, especially for structures with curved surfaces.

- *Strouhal number*. This dimensionless group refers to vortex shedding and its similarity requirement is stated as follows:

$$f_m \frac{L_{1m}}{U_m} = f_p \frac{L_{1p}}{U_p} \qquad \text{or}$$

$$f_p = \left( f_m \frac{L_{1m}}{U_m} \right) \frac{U_p}{L_{1p}} \qquad \textbf{Eq. 5-30}$$

where 0 Hz<$f_m$<200 Hz refers to the values of the frequencies observed at the model scale and $L_{1m}$=0.10m is the characteristic length of the vortex generator at model scale. The value inside the brackets is the normalized frequency reported in the results of the POD analysis. In order to satisfy the length scale requirement of $L_{1m}/L_{1p} = 1/200$ the length of the vortex generator at the prototype scale should be $L_{1p}$=20 m. The square prism at model scale shed vortices at 45 Hz. Maintaining the length scale as 1:200 and $U_p$=35.7 m/s, the vortices from a square prism of 20 m per side would shed vortices at 0.21 Hz, i.e. every 4.66 seconds. If the prototype is expected to be excited at different frequencies then the values of $f_p$ should be aligned accordingly.

- *Normalized spectral density function*. The spectral density functions S(f) reported in Chapters 3 and 4 were normalized based on the variance $\sigma^2$ and the frequency. The similarity requirements for the spectral density functions is stated in the next form:

$$S_m(f_m)\frac{f_m}{\sigma_m^2} = S_p(f_p)\frac{f_p}{\sigma_p^2} \qquad \text{or}$$

$$S_p(f_p) = S_m(f_m)\frac{f_m}{\sigma_m^2}\frac{\sigma_p^2}{f_p} \qquad \textbf{Eq. 5-31}$$

where $S_m(f)$ and $S_p(f)$ are the spectral density functions at model and prototype scale, respectively. Since the wind speeds $U_m$ and $U_p$ do not change, it is reasonable to assume that the variances of the pressure signals at the model and prototype scale do not change either. The frequency $f_p$ is the one determined by Eq. 5-30.

### 5.4.2 The structural model and the structural vibration modes [Ψ]

The non-linear response of hanging roofs subjected to static forces is described in detail by Flores-Vera (2003). In fact, there is a thorough analysis for the prototype of the hanging roof model studied in Chapter 3. The necessary information to reproduce the structural model is listed below.

- The footprint of the prototype covers approximately a square area, with 101.60 m along the side parallel to the X-axis and 99.60 m along the perpendicular side.
- The geometry of the surface is described by the function

$$f(x,y) = \frac{125}{41334}\left(y - \frac{99.6}{2}\right)^2 - \frac{125}{64516}\left(x - \frac{101.6}{2}\right)^2 + 23.315$$ **Eq. 5-32**

- The roof is supported by a uniform network of pre-stressed steel cables, which are the main source of rigidity of the structure. The roof is accurately modeled with an arrangement of 31 equidistant loading cables running parallel to the Y-axis and 23 equidistant shape cables running parallel to the X-axis. Each loading cable has a cross section area of 924 $mm^2$ and a nominal pre-stress of 531 MPa, which makes a total pretension force of 490 kN. Each shape cable has a cross section area of 308 $mm^2$ and a nominal pre-stress of 300 MPa, which makes a total pretension force of 92 kN.
- There are $31 \times 23 = 713$ free joints, each with a tributary area equal to $1.02 \times 3.175m \times 4.15m = 13.44m^2$. The factor 1.02 accounts for the curvature of the surface. The mass distribution was estimated as 84 $kg/m^2$.

The structural model was created with the information listed above. The program SAP 2000 allows the user to save, among other information, the modal shapes. The number of structural modes that can be obtained for a structure with m degrees of freedom can be as large as m. Nevertheless, it is a customary practice to truncate the number of structural modes to a smaller number $m_t$. It was decided that for the purposes of this example only the first 20 structural modes were going to be considered (Figure 5.2 to Figure 5.4).

It is important to notice that SAP2000 provides the structural modes normalized with respect to the mass matrix and therefore the modal masses are equal to one. In this example, the units of force were tons and thus the unitary masses are equal to 1000 Kg.

The structural analysis was carried out with all six degrees of freedom activated for each joint. However, the wind-induced forces acting on each joint does not have angular components and therefore the rotational degrees of freedom of the structural mode shapes can be discarded. Thus, each structural vector mode has $713 \times 3 = 2139$ elements. Consequently, the modal matrix [**Ψ**] containing the first 20 mode shapes has 2139 rows and 20 columns. Alternatively, the modal shapes can be stored and manipulated into different matrices, each referring to the three orthogonal directions X,Y and Z. This latter arrangement is preferred and therefore the structural modes shapes are arranged in submatrices $[\boldsymbol{\Psi}_x]$, $[\boldsymbol{\Psi}_y]$ and $[\boldsymbol{\Psi}_z]$ each having 713 rows and 20 columns. Thus, the structural eigenvectors are arranged as:

$$[\boldsymbol{\Psi}] = \begin{bmatrix} [\boldsymbol{\Psi}_x] \\ \hdashline [\boldsymbol{\Psi}_y] \\ \hdashline [\boldsymbol{\Psi}_z] \end{bmatrix}$$

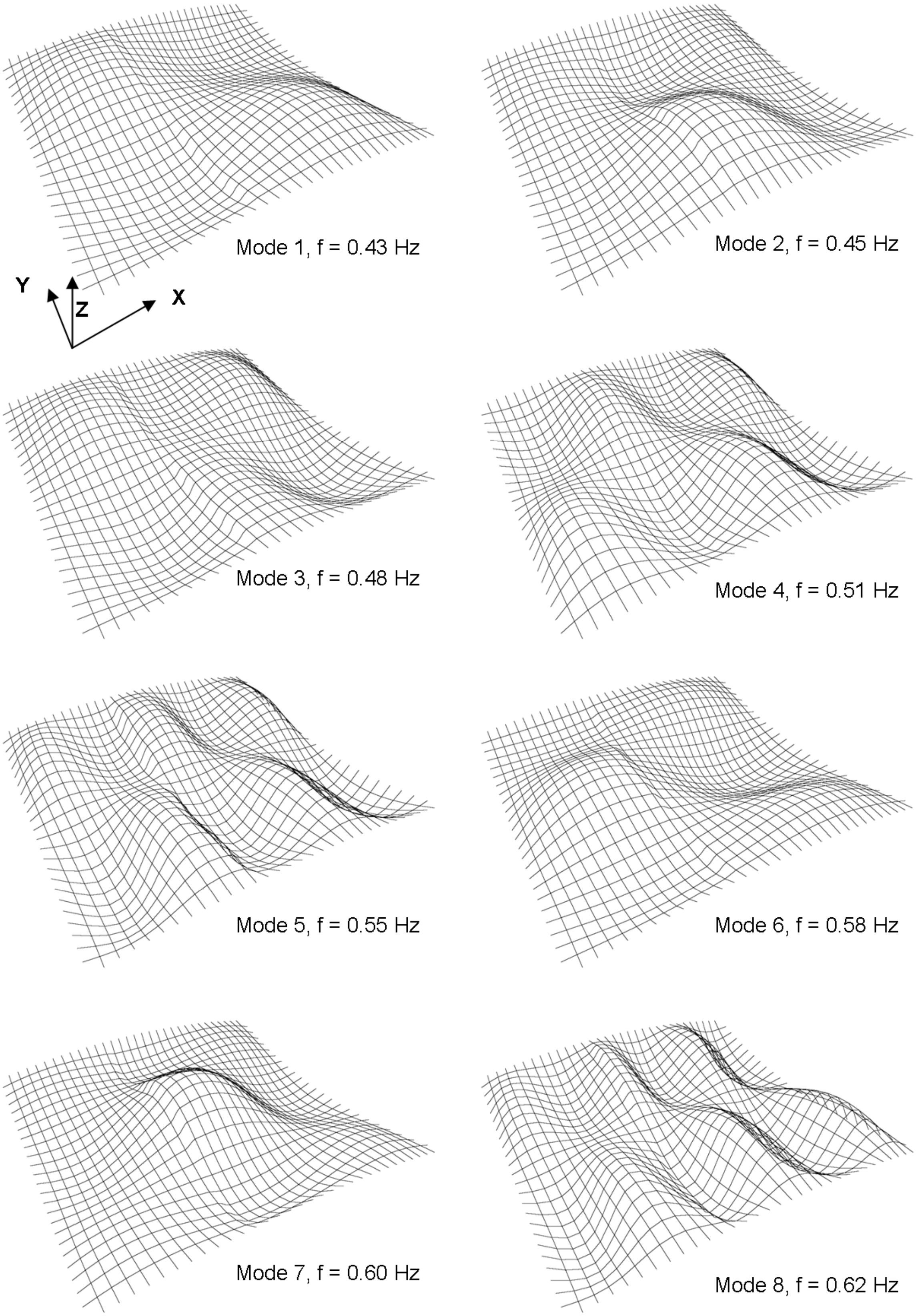

Figure 5.2 Structural modes 1 to 8.

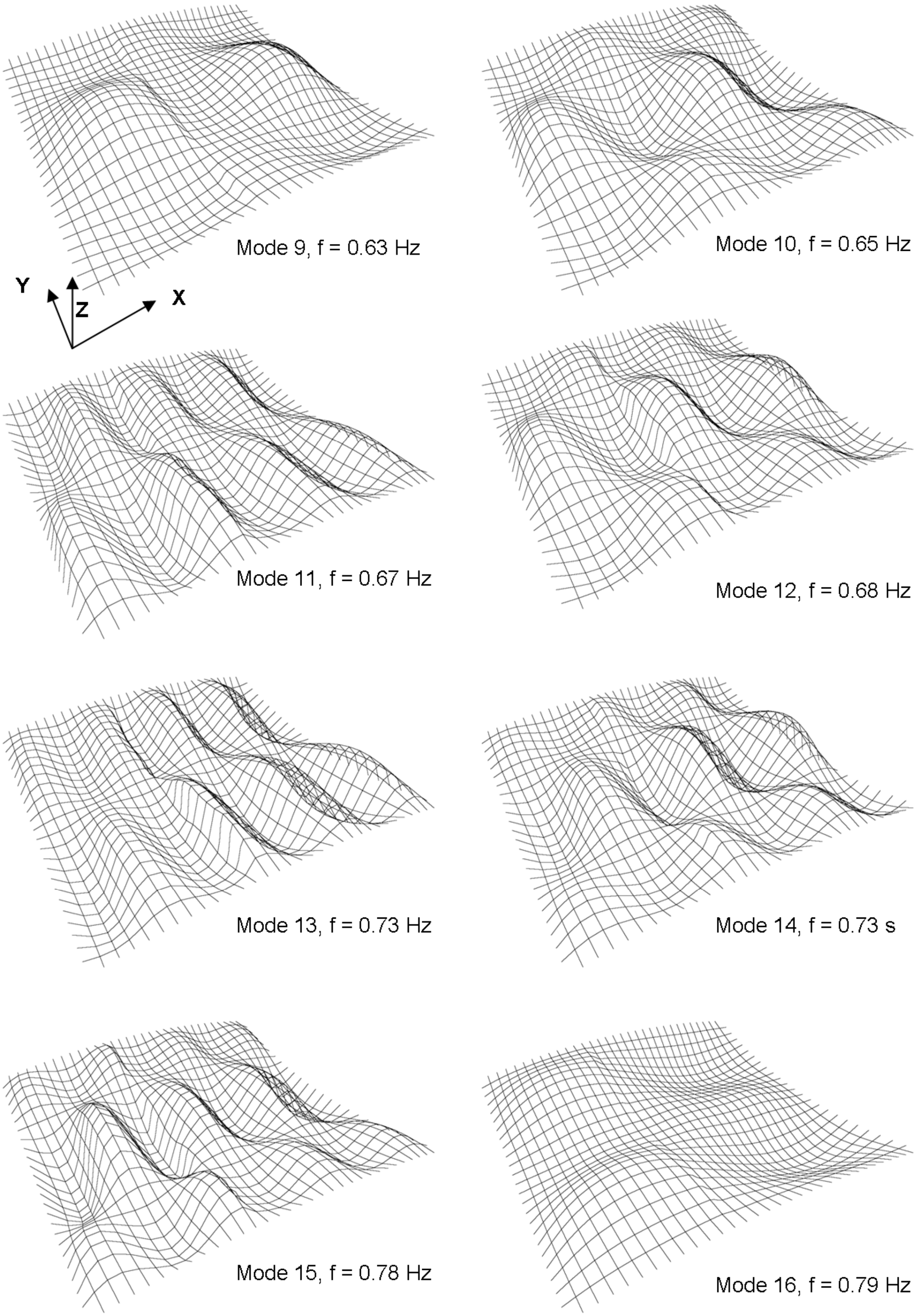

Figure 5.3 Structural modes 9 to 16.

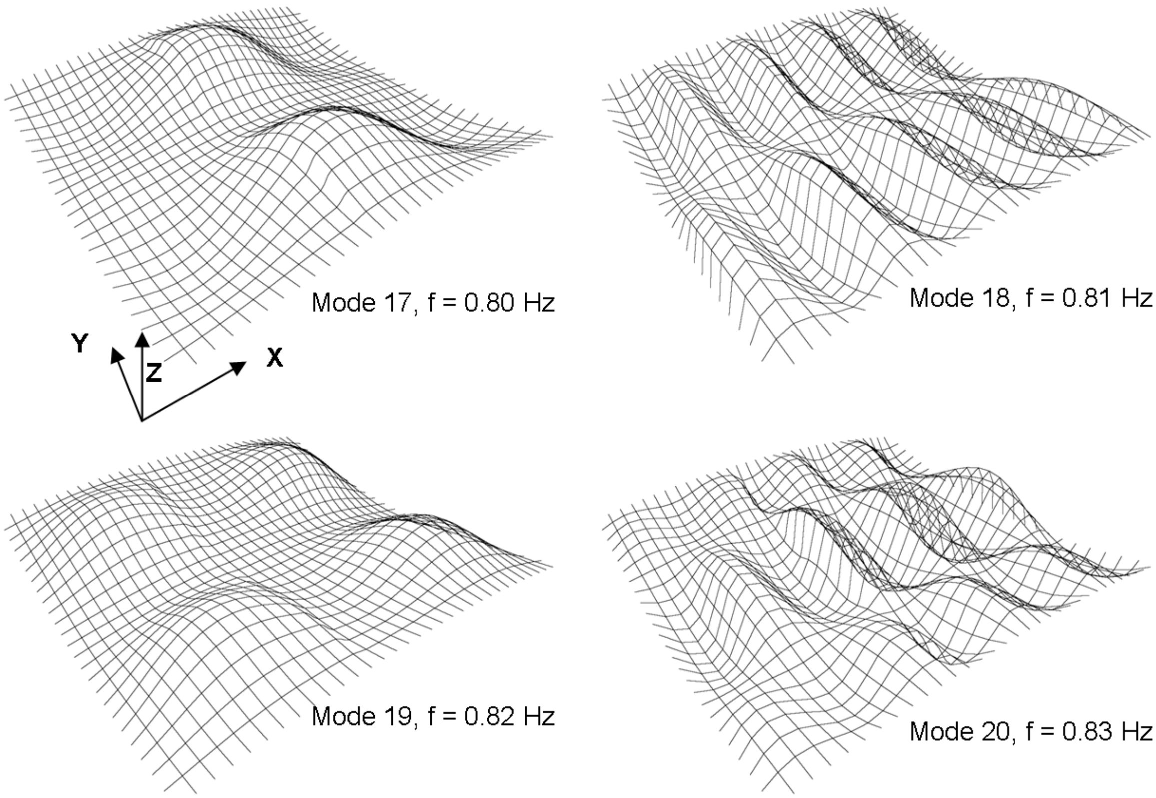

Figure 5.4 Structural modes 17 to 20.

### 5.4.3 The wind load modes [Φ] obtained from the POD analysis

The pressure field over the hanging roof immersed in the vortex trail of a square prism was studied with the POD method in Chapter 3.

It is pointed out that a POD analysis based on the pressure history of n=32 pressure taps can provide a maximum of 32 eigenvectors (or POD modes) with 32 elements each vector. Thus, the matrix [**Φ**] that collects all the POD modes has 32 rows and 32 columns, where element $\phi_{ij}$ indicates the value of the j-th eigenvector at the location of the i-th pressure tap. Nevertheless, by means of interpolation, it is possible to increase the number of elements that define each eigenvector. In particular, it is very convenient that the POD modes are interpolated at the same location where the structural joints are defined. This greatly simplifies the calculation of the inner product of vectors $\{\phi_j\}$ and $\{\psi_k\}$ in the calculation of the cross-modal coefficients $B_{jk}$.

As stated before, the number of POD modes can also be truncated for the purpose of simplifying the structural analysis. Instead of using n=32 POD modes, it is possible to use a smaller number $n_t$ of POD modes. There might be different criteria for selecting particular POD modes for the study of the structural response. For example, it might be convenient to choose only those POD modes that have significant contribution to drag, overturning or lift effects. The criteria used for the example treated in this chapter was to consider only the first POD modes for which the energy content accumulated up to 90% of the total kinetic energy. For the case of the hanging roof immersed in the vortex trail of a square prism at a wind speed of U=38 m/s only 9 POD modes were necessary to account for 90% of the total energy.

With the interpolation of the POD modes and their truncation up to $n_t=9$, the dimensions of matrix $[\mathbf{\Phi}]$ is 713-by-9. The first three POD modes have been shown in Chapter 3 and the remaining 6 POD modes are shown in Figure 5.5. It is noticed that the larger variations of the POD modes occur near the leading edge.

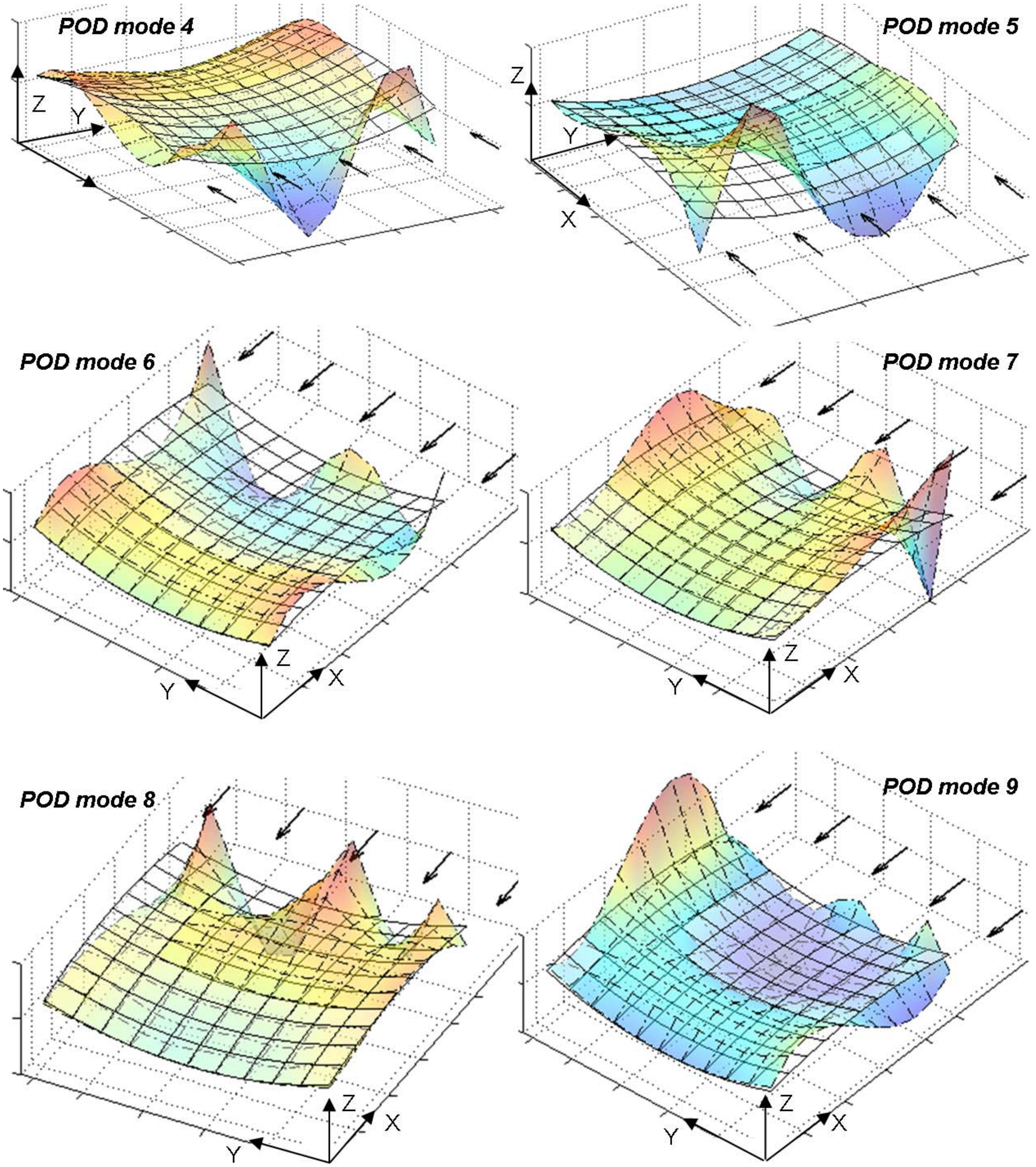

Figure 5.5 POD modes 4 to 9 for roof model immersed in the vortex trail of a square prism at U=38 m/s.

### 5.4.4 The cross-modal participation matrix, [B]

Eq. 5-8 indicates that the connection between the scalar pressure field {**p**(f)} and the vector force field {**F**(t)}, both in the Lagrangian coordinates, is {**F**(t)}= [**A**]{**p**(f)}. In order to transform the scalar field into a vector field, it is evident than the connecting element [**A**] cannot be only a matrix of tributary areas but rather a matrix of *oriented tributary areas*. At this point it is not obvious how the elements of [**A**] must be arranged in order to perform such transformation. Nevertheless, this arrangement becomes clearer after the double transformation imposed by $[\mathbf{\Psi}]^T$ and [**Φ**].

After the double modal transformation $\{\mathbf{F}_x(t)\} = [\mathbf{B}]\{\mathbf{p}_x(t)\}$, where $\{\mathbf{p}_x(t)\}$ is the image of {**p**(f)} in the space defined by [**Φ**] and $\{\mathbf{F}_x(t)\}$ is the image of {**F**(t)} in the space defined by $[\mathbf{\Psi}]^T$. In a similar way, [**B**] is the image of [**A**] in a space defined by both modal matrices as stated in Eq. 5-10. The cross-modal participation matrix is a connector between two entities that belong to different mathematical spaces.

As discussed earlier, the POD modes should be interpolated[1]at the same coordinates where the joints of the structure are defined. In this way matrix [**A**] becomes diagonal and each of its element is an *oriented tributary area*. In the present example the network of cables is uniform and all tributary areas are equal to A=13.44 $m^2$. Nevertheless, the projection of this constant area in the three orthogonal axes changes according to the location (x, y) of each joint.

As stated above, it was deemed convenient to use different matrices to arrange and manipulate the components x,y,z of the forces applied at each joint. In the current example matrix [**A**] is subdivided into three matrices $[\mathbf{A}_x]$, $[\mathbf{A}_y]$ and $[\mathbf{A}_z]$ as follows:

$$[\mathbf{A}] = \left[\begin{array}{c:c:c} [\mathbf{A}_x] & [\mathbf{0}] & [\mathbf{0}] \\ \hdashline [\mathbf{0}] & [\mathbf{A}_y] & [\mathbf{0}] \\ \hdashline [\mathbf{0}] & [\mathbf{0}] & [\mathbf{A}_z] \end{array}\right]$$

where each submatrix is a diagonal matrix with dimensions $713 \times 713$. Each of its elements contains the *orientated tributary areas* defined as follows:

---

[1] This procedure is carried out easily with a software like Matlab.

$$a_{ij,x} = n_x(x_i, y_j) \cdot A$$

$$a_{ij,y} = n_y(x_i, y_j) \cdot A \qquad \textbf{Eq. 5-33}$$

$$a_{ij,z} = n_z(x_i, y_j) \cdot A$$

where $n_x(x_i, y_j)$ represents the x-component of the unitary normal vector at point $(x_i, y_j)$, $n_y(x_i, y_j)$ represents the y-component of the unitary normal vector at point $(x_i, y_j)$ and $n_z(x_i, y_j)$ represents the z-component of the unitary normal vector at point $(x_i, y_j)$.

Although not necessary, it was considered convenient calculate matrix [**B**] (Eq. 5-10) by components. Then,

$$[\mathbf{B}_x] = [\mathbf{\Psi}_x]^T [\mathbf{A}_x][\mathbf{\Phi}]$$

$$[\mathbf{B}_y] = [\mathbf{\Psi}_y]^T [\mathbf{A}_y][\mathbf{\Phi}]$$

$$[\mathbf{B}_z] = [\mathbf{\Psi}_z]^T [\mathbf{A}_z][\mathbf{\Phi}]$$

Finally, each component of [**B**] is obtained as $B_{jk} = \sqrt{B_{jk,x}^2 + B_{jk,y}^2 + B_{jk,z}^2}$ .

The cross-modal participation matrix [**B**] has a very important meaning; each element $B_{jk} = \{\psi_j\}^T [\mathbf{A}]\{\phi_k\}$ is a scalar amount that quantifies the influence of the k-th POD mode (loading mode) on the j-th structural mode. Furthermore, if the amount [**A**]{$\phi_k$} is regarded as a force vector and {$\psi_j$} as a displacement vector, then $B_{jk}$ is the work done by the k-th load vector along the displacements defined by the j-th vibration mode. This concept is depicted graphically in Figure 5.6 for a particular location (x,y).

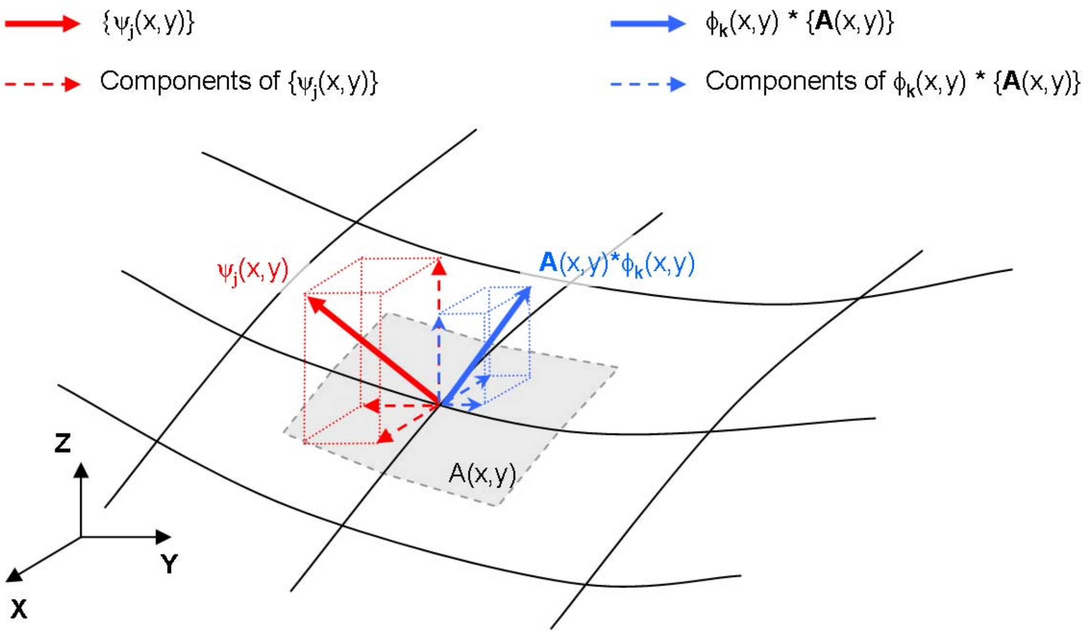

Figure 5.6 Internal product of the components of $\psi_j$ and $\phi_k$ at point (x,y).

It is known that the sign of the inner product of two vectors can be either negative or positive but since the convention for determining the direction of both the POD modes and the structural modes is completely arbitrary, the sign of each element Bjk has no physical meaning and only the absolute values should be considered.

Notice that both matrices [**Ψ**], [**Φ**] can be truncated. In this example, matrix [**Ψ**] contains only 20 structural modes and matrix [**Φ**] contains only 9 POD modes. The result is that the cross-modal participation matrix has dimensions $20 \times 9$.

Given the importance of matrix [**B**], it is considered convenient to present graphically the distribution of its elements. A three-dimensional view of the distribution of each factor $B_{jk}$ is rendered in Figure 5.7, where the magnitude of each inner product is easily observed. In particular, the highest inner product is identified as the combination between the 6th POD mode and the 16th structural mode. The same results are presented in a different way in Figure 5.8, showing the cumulative effects of all 9 POD modes on each structural mode. The individual contribution of each POD mode is identified with the same color code used in Figure 5.7. It can be seen that structural mode number 16 is the most affected by the POD modes.

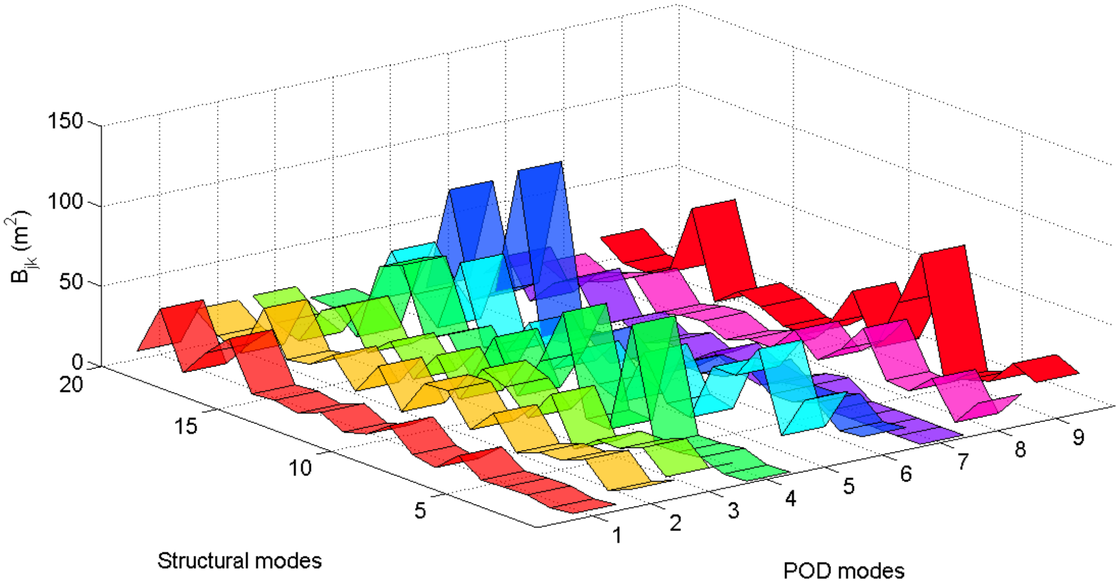

Figure 5.7 3D representation of the cross modal participation matrix, U=37.7 m/s.

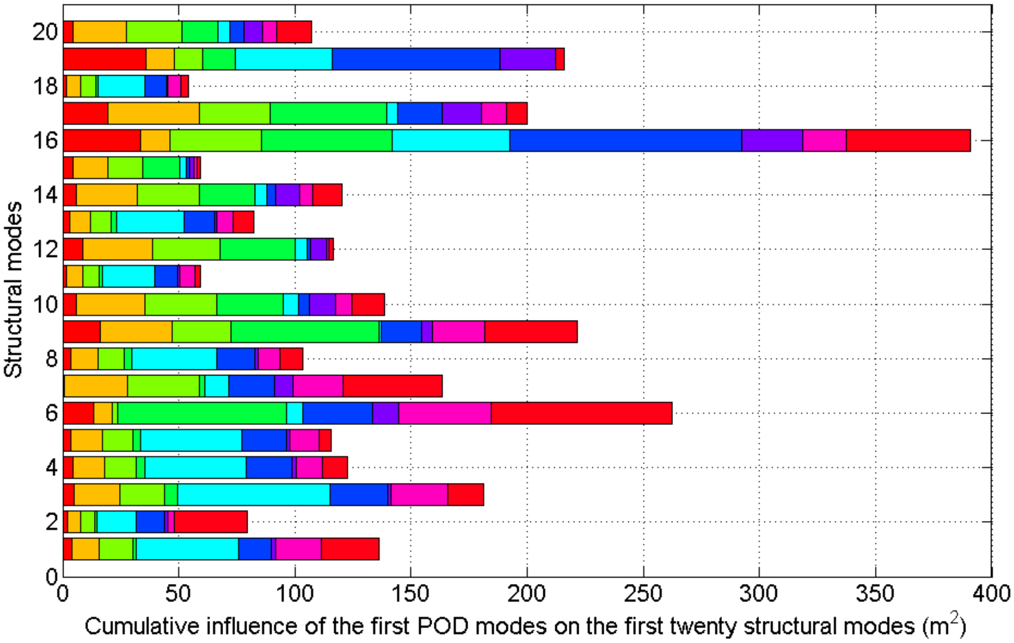

Figure 5.8 Representation of the cumulative influence of 9 POD modes on each structural mode, U=37.7 m/s.

### 5.4.5 Exciting-force spectra for modal oscillators

According to Eq. 5-11, the exciting forces $F_{x,j}(t)$ for each modal oscillator are obtained from the product between the cross-modal participation matrix [**B**] and the pressure histories {$\mathbf{p}_x(t)$} obtained from the POD analysis. The equivalent operation in the frequency domain is given by Eq. 5-17. The power spectral density functions of the nine POD modes used in this example are shown in Figure 5.9. The spectra in the figure include the proper scaling factors to be used in the structural analysis of the prototype. It is evident that the first POD mode provides the dominant signal.

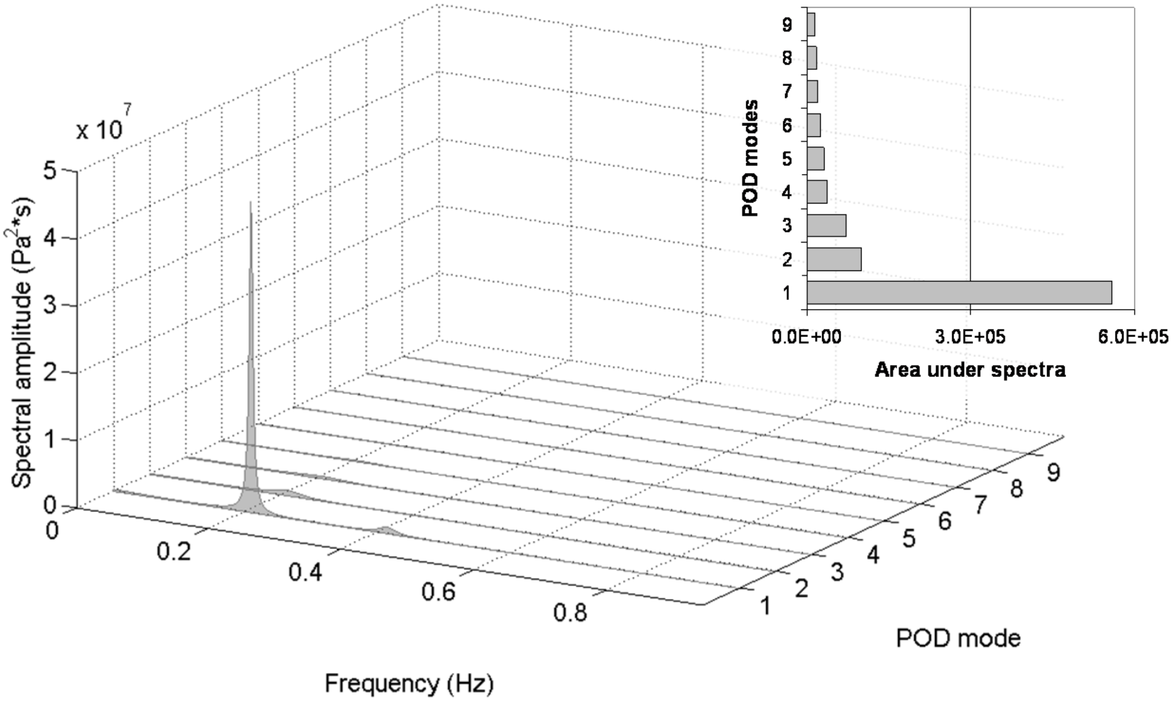

Figure 5.9 Spectra of pressure histories in the modal space defined by [**Φ**].

The application of Eq. 5-17 gives directly the spectra of the exciting forces for each modal oscillator, which are presented graphically in Figure 5.10. It is interesting to note that the spectra with higher intensity are those corresponding to modes 16 and 19. This is explained by observing with more attention Eq. 5-17. Since the first POD mode is the dominant signal, we may disregard for a moment all other POD modes. Then $S_{Fx,j}(f) \cong B_{j1} S_{px,1}(f)$ and therefore the magnitude of $S_{Fx,j}$ is distributed in a similar way as the elements of the first column of [**B**] which are represented by the first ribbon in Figure 5.7.

Since all force spectra $S_{Fx,j}$ are basically a multiple of the spectrum of the first POD mode, then the peaks of $S_{Fx,j}$ correspond to the frequency of vortex shedding (or double this frequency). This frequency can be changed if there is evidence that the prototype would be exposed to a different vortex shedding frequency.

Note also that the large values of $B_{jk}$ for $k \geq 2$ have very little effect on $S_{Fx,j}(f)$ because the spectra of the higher POD modes are small compared with the spectrum of the first POD mode. Of course, this observation may differ for different problems.

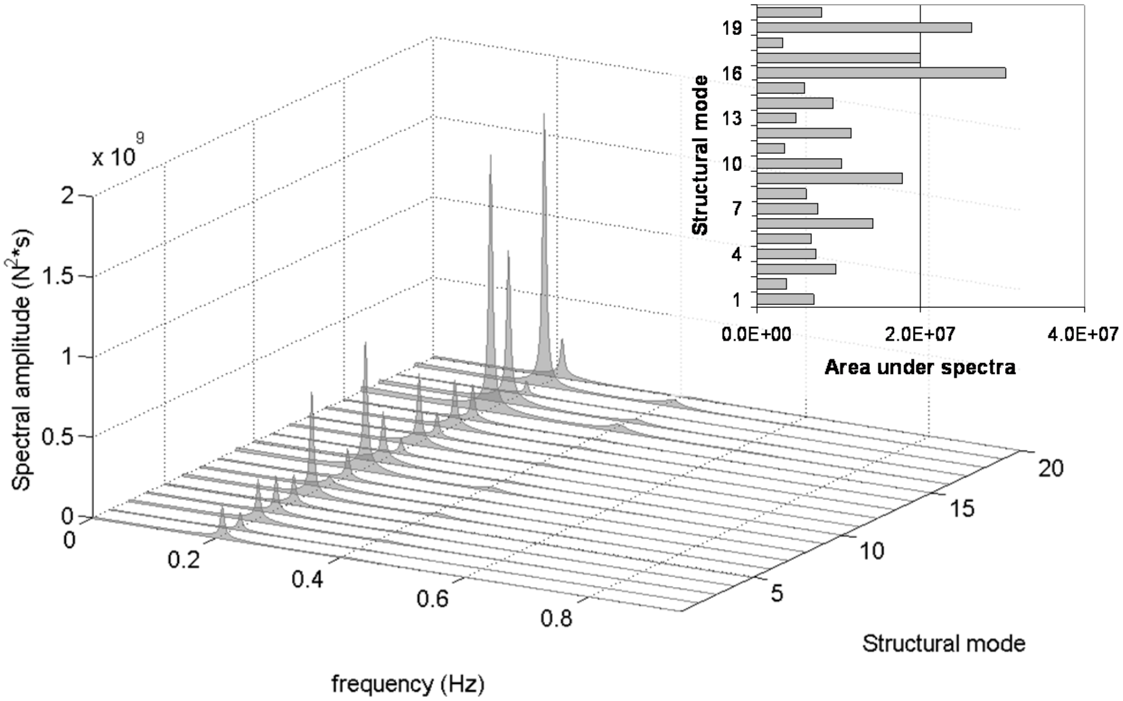

Figure 5.10 Spectra of exciting forces in modal space.

### 5.4.6 Solution of the equations of motion in modal space

Since the equations of motion in modal space are decoupled, their solution is easily achieved by applying Eq. 5-14 to each modal oscillator. The only missing element is the gain function, which is calculated with Eq. 5-15. Notice that each modal oscillator has its own gain function which basically depends on the natural frequency, the modal mass and the damping ratio of each mode.

The damping ratio was arbitrarily assumed equal to 0.02 for all modes. The modal analysis performed by SAP automatically normalizes the eigenvectors with respect to the masses producing unitary modal masses. Since the unit of force used in this example was the ton, therefore all modal masses are equal to 1000 kg. With these values, the gain functions were calculated and they are shown in Figure 5.11. Notice that the amplitude of each gain function decreases with the square of the modal frequency.

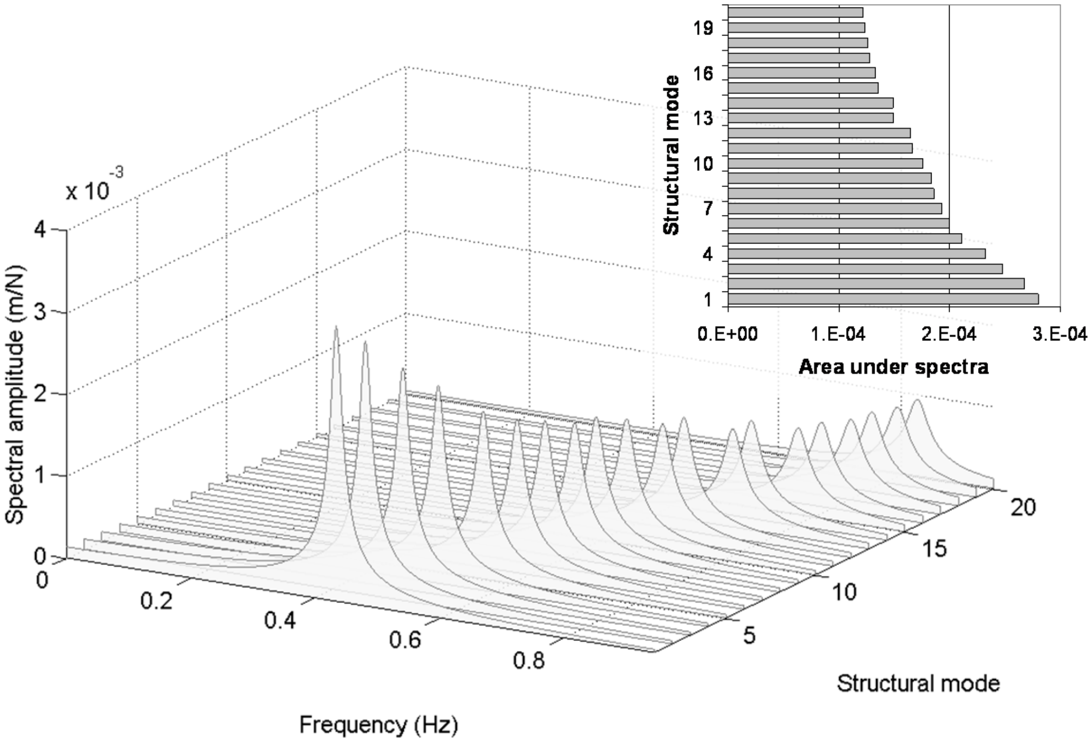

Figure 5.11 Gain functions for each modal oscillator.

The product indicated by Eq. 5-14 produces the response spectrum of each modal oscillator. The results are presented graphically in Figure 5.12. The area under each spectrum is the variance of the displacement $x_j(t)$ of each modal oscillator and these variances are included in the same figure. Notice that the response spectra of the first 10 modal oscillators posses a significant amplitude at a frequency higher than those of the force spectral peaks. This is because the secondary peaks of the force spectra are in resonance with the natural frequencies of the first 10 modal oscillators. Similarly, the significant peaks of the force spectra $S_{Fx,16}$ and $S_{Fx,19}$ have little impact in their respective response spectra $S_{x,16}$ and $S_{x,19}$ because there is no coincidence in frequencies between their force spectra and their gain function.

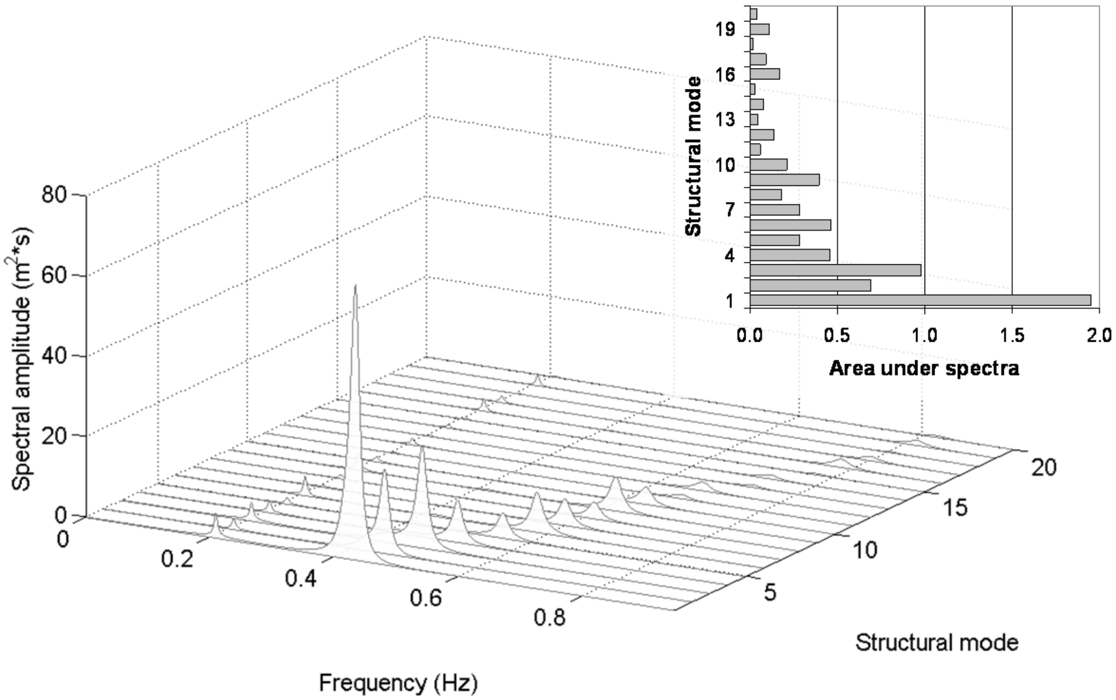

Figure 5.12 Response spectra for each modal oscillator.

### 5.4.7 Solution of the equations of motion in Lagrangian space

With all the elements calculated so far, Eq. 5-27 establishes that it is possible to determine the spectral density function of the displacements in Lagragian space $S_y(f)$ for all 2139 degrees of freedom but this would require significant amount of computer memory. Instead, only the variances of the response $\sigma_y^2$ are obtained according to Eq. 5-28. Finally, the standard deviation of the response is plotted in Figure 5.13. Of course, this figure is the combination of the standard deviation $\sigma_x$ and the structural eigenvectors $[\mathbf{\Psi}]$ but the distribution of $\sigma_x^2$ (Figure 5.12) indicates that the first three structural modes have the largest contribution.

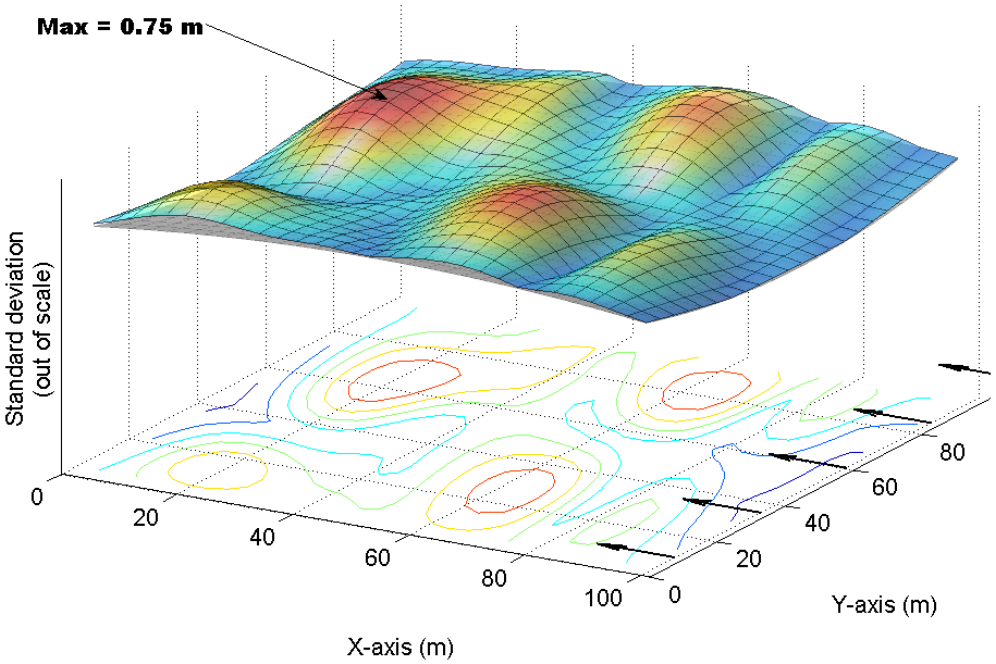

Figure 5.13 Standard deviation of the response in the original coordinates (Lagrangian space), U=37.7 m/s.

### 5.4.8 Dynamic response Vs. Static response

The dynamic effects of the unsteady pressure field are summarized in Figure 5.13, whereas the static effects due to the mean pressure coefficients shown in Chapter 3 are presented in Figure 5.14. The static analysis was carried out in SAP2000 following the procedure explained by Flores-Vera (2003) for structures exhibiting non-linearity due to large displacements. Both analyses were carried out based on the experimental measurements obtained for the hanging roof model immersed in the vortex trail of a square prism at a wind speed of U=37.7 m/s. All parameters were originally normalized and later scaled at the real dimensions of the prototype, for a design wind speed of 35.7 m/s.

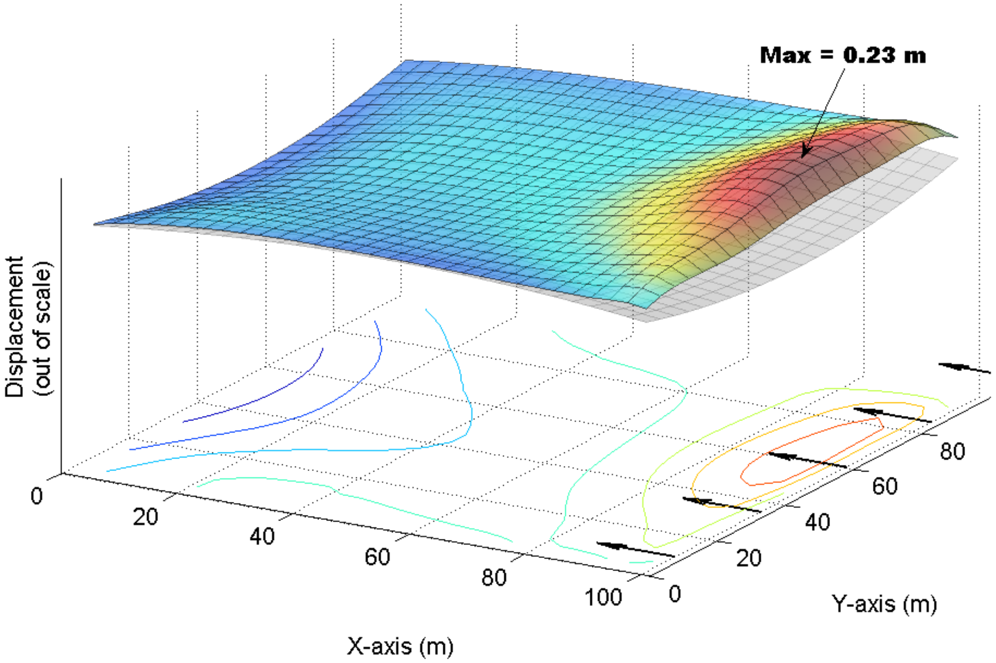

Figure 5.14 Static response of the roof due to mean pressure coefficients.

The static analysis indicates that the maximum displacements on the roof occur near the leading edge with displacements up to 0.23 m. The rest of the roof experience little disturbance with an average of displacements equal to 0.06 m. The dynamic analysis obtained from the double modal transformation method indicates that certain zones of the roof experience significant oscillation with a standard deviation as high as 0.76 m. The average oscillation on the roof is 0.22 m. This results are summarized in the next table.

| ***Static analysis (non-linear)*** | | ***Dynamic analysis (DMT)*** | |
|---|---|---|---|
| Max. displacement (m) | 0.23 | Max. standard deviation (m) | 0.76 |
| Average displacement (m) | 0.06 | Average standard deviation (m) | 0.22 |

This concludes the example of the application of the double modal transformation.

## 5.5 Conclusions

- The previous two chapters dealt completely with the use of the POD analysis to fully describe the wind-induced pressure field around two structures. This chapter introduces the Double Modal Transformation method (DMT) as the application of the POD analysis in the calculation of the response of any type of structure.
- The Double Modal Transformation method is a very appealing technique that fully describes qualitatively and quantitatively the wind-structure interaction. This wind-structure interaction is basically characterized by two mechanisms:
  - (a) The first mechanism is due to the similitude between the frequency content of the loading and the natural frequencies of the structure. The more similitude in frequencies, the larger the structural response, as stated in Eq. 5-14 and represented in Figure 3.1.
  - (b) The second mechanism in which the load affects the structural response is based on the similitude of the structural mode shapes **Ψ** and the load mode shapes **Φ.** The more similitude between the structural mode shapes and the wind load shapes the larger the structural response. This is exactly what is quantified with the cross-modal participation factors $B_{jk} = \psi_j^T \mathbf{A} \phi_k$.
- The numerical application of the DMT method indicates that the dynamic effects of the wind can cause displacements significantly greater than those caused by the static effects.
- It might seem a redundant recommendation but given the large and varied amount of mathematical elements used in the Double Modal Transformation method, it is

worth to point out that careful attention must be observed in the compatibility of units for the final results to be coherent.

- Although the Double Modal Transformation method has been proposed theoretically in different sources, to the knowledge of the author, this is the first application of the method for a real structure immersed in a pressure field which has been measured experimentally. The example presented in this chapter demonstrates in detail each step of the DMT method. In particular, it clarifies the nature of matrix [**A**] and the procedure to construct it. The author expects that this chapter is a valuable resource for those interested in the DMT method.

# Chapter 6 CONCLUSIONS AND RECOMMENDATIONS

The material presented in this thesis emphasizes the use of the Proper Orthogonal Decomposition (POD) for studying unsteady wind-induced pressure fields. Additionally, the POD is used in conjunction with the classical modal analysis in order to evaluate the response of structures exposed to turbulent wind flow. As a result of this research, the following general **conclusions** are obtained.

- Although the formal derivation of the POD method requires a strong mathematical background, the numerical implementation of the method is straightforward.
- Slight asymmetries on structures can produce notorious asymmetries on some POD modes, particularly on the higher modes.
- Since no information can be obtained from flow structures with frequencies higher than half the sampling frequency, it is necessary to determine carefully the sampling frequency.
- The POD method provides mode shapes that suggest real physical structures in some cases but in other cases the modes shapes are only mathematical structures.

Experience, intuition and knowledge in fluid mechanics are necessary for the interpretation of the results. For example, in the case of the study of the telescope model, the POD method was able to confirm and visualize the existence of the free-shear layer modes and to determine the energy content related to each structure. This was achieved relatively easy by knowing that such structures exist, otherwise it would have been difficult to explain the source of the peaks in the spectral density functions of the POD modes.

- Regardless of the physical meaning of the POD modes, the POD method is useful in the numerical evaluation of the wind load effects on structures by converting a multi-variate stochastic pressure field into a series of uncorrelated single-dimensional pressure fields.
- The POD method is well suited to be used in combination with the classical modal analysis, in what is called the Double Modal Transformation method (DMT). The DMT method not only has the ability to give the exact response of a structure exposed to wind action, it also provides a detailed description of the effect of each loading mode on every structural mode.
- The double modal transformation method shows that the similarity between the POD modes and the structural modes increases the structural response. This interaction is nicely condensed into the cross-modal participation matrix.
- The objectives stated at the beginning of the thesis were achieved by proving the effectiveness of the POD method in simplifying the wind loads and by demonstrating the power and generality of the double transformation method as a tool to understand and to evaluate the wind load effects on the response of structures.

- The application of the POD method to wind engineering problems was studied rigorously in the framework of this research. This thesis presents a detailed account of what it is and its benefit on which further development can be build on.
- To the knowledge of the author, the double modal transformation method is the approach that provides the clearest description of how the wind loads interact with the structures and influence their response.

During this research, some interesting observations were made but the time frame restricted their study. Therefore, these observations are left as **recommendations** for future research related to the use of the POD in wind engineering.

- The POD is a process that is both benefited and limited by its linear nature. It is useful in detecting hidden or overlapped pressure fields that can be reconstructed by pressure signals highly correlated in a linear fashion. Nevertheless, the method is less effective for detecting hidden pressure fields when the pressure signals are not linearly correlated. The use of a non-linear correlation coefficient, instead of the covariance, is promising in terms of detecting real pressure fields.
- The distribution of the pressure taps can affect the flow structures that can be captured with the POD method. Therefore, further studies are recommended to determine the optimal distribution of the pressure taps.
- The POD analyses were based on the covariance matrix, which represents the value of the correlation function at the zero-time lag, leaving with no use the rest of the correlation function. Further information might be extracted by working with the complete correlation function, particularly if this is linked to the geometry of the structures and the geometrical distribution of the pressure taps.

- The decision of splitting the covariance matrices of two structures, where the presence of one structure affect the pressure field of the other, was done by simple visual inspection of the energy distribution histograms. Such decision should be better sustained by a more formal procedure that may include the scale of fluctuation of the correlation function.
- The extensive amount of unsteady pressure data collected from reliable wind tunnel tests around the world can be used to perform POD analyses of the wind forces, thus verifying and complementing the results previously obtained.
- It seems promising to use the POD method to study extensively common structural shapes (like the rectangular prism) for different configurations, that may include variable ratios of width-height-depth, variable roughness, variable turbulence, etc. The objective would be to obtain standardized properties of the POD modes and their spectral density functions with the purpose of providing guidelines for structural design. It is believed that these guidelines could provide more accurate results than those obtained by the current design standards.

# APPENDIX A

# The Proper Orthogonal Decomposition (POD)

The fundamental idea behind the proper orthogonal decomposition is simple and its numerical implementation is straightforward. Nevertheless, its formal mathematical definition requires familiarity of concepts related to Hilbert's spaces and calculus of variations.

The POD method is a very powerful tool that can be applied to a field $\{\mathbf{p}^N\}$. The field can be either real or complex and it can also be scalar or vectorial. Each component function can be a function of one or several variables. Although this appendix is addressed specifically to a scalar pressure field {**p**(**x**,t)} over a given surface, the derivation of the method allows complex operations in order for the theory to be used in combination with the Fourier decompositions.

In expanded form, a pressure field can be represented as:

$$\{\mathbf{p}(\mathbf{x},t)\} = \{p_1(\mathbf{x}_1,t), p_2(\mathbf{x}_2,t), \cdots, p_N(\mathbf{x}_N,t)\}^T$$

where **x** represents the spatial coordinates (x,y) and t is the time, measured simultaneously at all points, from t=0 to t=T. The j-th component function $p_j$ is the pressure signal recorded at a location $\mathbf{x}_j$.

The pressure field {**p**(**x**,t)} over a surface can be regarded as a sequence of instantaneous pressure fields {**p**(**x**)} at different times. For example at $t=t_0$ there is a pressure field $\{\mathbf{p}(\mathbf{x},t_0)\}$, at $t=t_1$ there is another pressure field $\{\mathbf{p}(\mathbf{x},t_1)\}$ and so on.

It is assumed that each instantaneous pressure field belong to the infinite dimensional Hilbert space $L^2$ $([\mathbf{0}, \mathbf{X}])$ of square integrable functions with inner product:

$$(f, g) = \int_{\mathbf{0}}^{\mathbf{X}} f(\mathbf{x}) g^*(\mathbf{x}) d\mathbf{x} = \int_0^Y \int_0^X f(x, y) g^*(x, y) dx dy$$

The interval $([0, \mathbf{X}])$ defines the spatial range $([0, X] \times [0, Y])$ where the pressure fields are defined. The function $g^*(x)$ is the complex conjugate of function g(x).

It is desirable to find a spatial basis $\{\phi_j(\mathbf{x})\}_{j=1}^{\infty}$ for $L^2$ that is optimal for the data set in the sense that finite-dimensional representations of the form:

$$p(\mathbf{x}) = \sum_{j=1}^{N} \phi_j(\mathbf{x}) a_j$$

describe typical members of the ensemble better than representations of the same dimension in any other basis. There is an apparent problem given that this expression only represents an instantaneous value of pressure at point **x** but we are interested in reproducing the complete pressure history of pressure at point **x**. The problem is solved by finding a series of coefficients $a_j(t)$ for any time t. Thus, the expression above is further generalized as

$$p(\mathbf{x}, t) = \sum_{j=1}^{N} \phi_j(\mathbf{x}) a_j(t)$$

The word "typical" implies the use of an averaging operation, denoted by $\langle \cdot \rangle$ and which will be assumed to commute with the spatial integral defined for the $L^2$ inner product. The term "optimal" refers to the fact that all vectors $\phi$ should be chosen to maximize the averaged projection of {**p**(**x**,t)} onto each vector $\phi$, which must be normalized. Mathematically this is expressed as:

$$\max_{\phi \in L^2([\mathbf{0}, \mathbf{X}])} \frac{\left\langle |(p, \phi)|^2 \right\rangle}{\|\phi\|^2}$$

where it is understood that $p$ represents the pressure field and it is a function of the spatial coordinates (x,y) and the time t.

Finding the extrema of $\left\langle |(p,\phi)|^2 \right\rangle$ subject to the condition of $\|\phi\|^2 = 1$ is a problem in the calculus of variations. The corresponding functional for this variational problem is:

$$J[\phi] = \left\langle |(p,\phi)|^2 \right\rangle - \lambda\left(\|\phi\|^2 - 1\right)$$

It is known from classical calculus that extreme values of a function are found at points where the first derivative of the function is zero. Similarly, the extrema of functionals are found at 'points'[2] where the functional derivative vanish for all variations $(\phi + \delta\psi) \in L^2([\mathbf{0},\mathbf{X}])$, $\delta \in \Re$:

$$\frac{d}{d\delta} J[\phi + \delta\psi]\bigg|_{\delta=0} = 0$$

Thus,

$$\frac{d}{d\delta} J[\phi + \delta\psi]\bigg|_{\delta=0} = \frac{d}{d\delta}[\langle (p,\phi + \delta\psi)(\phi + \delta\psi, p)\rangle - \lambda(\phi + \delta\psi, \phi + \delta\psi)]\bigg|_{\delta=0}$$

by using the property $(f,g) = \int fg^* dx = \left[\int f^* g dx\right]^* = (g,f)^*$ and performing the functional derivative, the equation above is simplified:

$$\frac{d}{d\delta} J[\phi + \delta\psi]\bigg|_{\delta=0} = 2\,\mathrm{Re}[\langle (p,\psi)(\phi,p)\rangle - \lambda(\phi,\psi)] = 0$$

Considering that the operators $\langle\cdot\rangle$ and $\int \cdot\, dx$ are interchangeable, the expression in brackets can be rewritten as:

---

[2] For functionals, each 'point' of the independent variable is actually a function.

$$\left\langle \int_0^{\mathbf{X}} p(\mathbf{x})\,\psi^*(\mathbf{x})\,d\mathbf{x} \int_0^{\mathbf{X}} \phi(\mathbf{x}')\,p^*(\mathbf{x}')\,d\mathbf{x}' \right\rangle - \lambda \int_0^{\mathbf{X}} \phi(\mathbf{x})\,\psi^*(\mathbf{x})\,d\mathbf{x}$$

$$= \int_0^{\mathbf{X}} \left[ \int_0^{\mathbf{X}} \left\langle p(\mathbf{x}) p^*(\mathbf{x}') \right\rangle \phi(\mathbf{x}') d\mathbf{x}' - \lambda\, \phi(\mathbf{x}) \right] \psi^*(\mathbf{x})\, d\mathbf{x} = 0$$

Since $\psi(\mathbf{x})$ is an arbitrary variation, the equality above is reduced to the condition:

$$\int_0^{\mathbf{X}} \left\langle p(\mathbf{x}) p^*(\mathbf{x}') \right\rangle \phi(\mathbf{x}') d\mathbf{x}' = \lambda\, \phi(\mathbf{x})$$

Thus, the optimal basis is given by the eigenfunctions $\{\phi_j\}$ of the integral equation just derived, whose kernel is the averaged autocorrelation function $R(\mathbf{x}, \mathbf{x}') = \left\langle p(\mathbf{x}) p^*(\mathbf{x}') \right\rangle$. Since usually the pressure field is obtained from measurements, instead of analytical derivations, the eigenfunctions $\{\phi_j\}$ are called empirical eigenfunctions.

# APPENDIX B

# Measurement uncertainty

Although no measurement is exact, it is evident that some measurements are less exact than others are. The lack of exactitude of a measurement is technically called measurement uncertainty. Measurement uncertainty is a non-negative parameter that determines the interval within which the true value of a measurable property lies in with a certain probability. From convention, the uncertainty $U$ of a measured property $x$ is defined in such a way that the experimenter is 95% confident that the true value of the property lies within the interval $[x+u, x-u]$. A measured value is complete only if it is reported with an indication of its related uncertainty.

Measurement uncertainty is affected by different types of errors that can be classified either as bias errors or precision errors. The overall uncertainty is calculated as:

$$U = \sqrt{B^2 + P^2}$$

where $B$ is the bias limit and $P$ is the precision limit.

Bias errors, also known as fixed or systematic errors, are constant throughout the experiment and they would be easy to eliminate if they were identified. Nonetheless, in many cases they are not easily identifiable and therefore contribute to the overall uncertainty. Notice that since bias errors are constant in every measurement, the repetition of the measurement does not decrease the uncertainty introduced by the biases. When biases are introduced through N different steps during the measuring process, the total bias limit is determined as $B = \sqrt{\sum_{i=1}^{N} B_i^2}$, where $B_i$ are the individual bias limits.

Precision errors, also known as random errors, are due to undesirable and inevitable changes in the input variables, which produce changes in the measured output. The repetition of a measurement with the same equipment produces a statistical distribution of the measured value. For measuring devices with negligible bias errors, the more repetitions of the experiment the better the estimation of the true value, i.e., $\mu_x \rightarrow x_{true}$. The dispersion of the measured values determines the precision of the experiment. The smaller the dispersion the more precise the experiment is. The precision limit *P* signifies that for every measurement x, the estimation of the true value has a 95% probability to fall within the interval [*x-P, x+P*]. For a random variable with Gaussian distribution, the precision limit is calculated as $P = 2\sigma_x$.

**Uncertainty of derived properties**

The uncertainty of properties measured directly is calculated as described above. However, in most instances a property *y* is obtained from an analytical expression of the form $y = y(x_1, \cdots, x_M)$, where the subsidiary properties $x_m$ (m=1,2,...,M) are obtained from experimental measurements. Assuming that *y* is a continuous function with partial derivatives with respect to all subsidiary properties, the uncertainty of *y* is calculated as:

$$U_y = \sqrt{B_y^2 + P_y^2}$$

where the bias limit $B_y$ and the precision limit $P_y$ are calculated as follows:

$$B_y = \sqrt{\sum_{m=1}^{M} \left( \frac{\partial y}{\partial x_m} B_{x_m} \right)^2}$$

$$P_y = \sqrt{\sum_{m=1}^{M} \left( \frac{\partial y}{\partial x_m} P_{x_m} \right)^2}$$

If the biases of two subsidiary properties $x_i$ and $x_j$ are correlated and $B'_{x_i}$, $B'_{x_j}$ are the portions of these biases that are perfectly correlated, then the total bias limit of $y$ should include one additional term for each pair of these variables with correlated biases. The expression to calculate the bias limit for these cases is:

$$B_y = \sqrt{\sum_{m=1}^{M}\left(\frac{\partial y}{\partial x_m} B_{x_m}\right)^2 + 2\frac{\partial y}{\partial x_i}\frac{\partial y}{\partial x_j} B'_{x_i} B'_{x_j}}$$

A detailed uncertainty analysis can be difficult to carry out since the bias and precision limits of the subsidiary properties are not always available. Even in this case, it is important to perform an uncertainty analysis with the best estimation of the bias and precision errors in order to observe how sensitive the total uncertainty is with respect to these errors.

**Uncertainty analysis for the telescope model tests**

The measurement uncertainties were estimated for the following experimental quantities of interest: test section dynamic pressure q, test section velocity U, model surface pressure and pressure coefficient. The uncertainties vary with the wind speed, with the measurement accuracies generally improving with increasing wind speed. The uncertainties are derived form the data reduction equations, which are:

$q = k_q \Delta P_p$ dynamic pressure, [Pa]

$U = \sqrt{2q/\rho}$ wind speed, [m/s]

$Cp = \dfrac{\Delta P_i + \Delta P_s}{q}$ pressure coefficient, dimensionless

$\rho = \rho_0\left(\dfrac{P_a}{101.33}\right)\left(\dfrac{288.15}{(T)}\right)$ corrected air density, [kg/m$^3$]

where:

$\Delta P_p$ is the pressure drop between the settling tunnel chamber and the plenum, [Pa]

$\Delta P_i$ is the measured pressure difference between the i-th port and the plenum (room surrounding the test section) reference pressure, [Pa]

$\Delta P_s$ is the offset between the plenum reference pressure and the empty jet static pressure, [Pa]

$k_q$ is the dynamic pressure calibration coefficient

$P_a$ is the dynamic atmospheric pressure measured during test, [Pa]

$T$ is the absolute temperature, [K]

The uncertainties for pressure and pressure coefficient are presented in Table B1 and Table B2, respectively. They are provided as functions of dynamic pressure and applied pressure for a range of pressure coefficients that span those observed. The nominal wind speed of 13.4 m/s is emphasized.

The uncertainties are observed to decrease rapidly with both pressure coefficient and wind speed. The scanners used on the telescope tests have full-scale pressure ranges of either 6895 Pa (used on the external taps), or 2488 Pa, although the measurement accuracies of both are virtually identical. Clearly, the pressures measured at the lower speeds are a small fraction of full scale. As an example, the pressure at 13.4 m/s for a Cp of 1.0 is only 110.0 Pascals. The pressure scanner uncertainties were determined by directly measuring the scanner accuracies through the data system.

Table B1 Pressure uncertainty for tests on the telescope model.

| | | Cp = | 0.10 | 0.50 | 1.00 | 1.50 |
|---|---|---|---|---|---|---|
| q, [Pa] | U, [m/s] | $U_q/q$ | $U_{Pi}/P_i$ | $U_{Pi}/P_i$ | $U_{Pi}/P_i$ | $U_{Pi}/P_i$ |
| 39.2 | 8.0 | 0.0923 | 0.2636 | 0.0516 | 0.0258 | 0.0172 |
| 61.3 | 10.0 | 0.0591 | 0.1662 | 0.0330 | 0.0165 | 0.0110 |
| 95.7 | 12.5 | 0.0378 | 0.1058 | 0.0211 | 0.0106 | 0.0070 |
| 110.0 | 13.4 | 0.0329 | 0.0920 | 0.0184 | 0.0092 | 0.0061 |
| 137.8 | 15.0 | 0.0263 | 0.0734 | 0.0147 | 0.0073 | 0.0049 |
| 187.6 | 17.5 | 0.0193 | 0.0539 | 0.0108 | 0.0054 | 0.0036 |
| 245.0 | 20.0 | 0.0148 | 0.0412 | 0.0082 | 0.0041 | 0.0027 |
| 310.1 | 22.5 | 0.0117 | 0.0326 | 0.0065 | 0.0033 | 0.0022 |
| 382.8 | 25.0 | 0.0095 | 0.0264 | 0.0053 | 0.0026 | 0.0018 |
| 463.2 | 27.5 | 0.0078 | 0.0218 | 0.0044 | 0.0022 | 0.0015 |
| 551.3 | 30.0 | 0.0066 | 0.0183 | 0.0037 | 0.0018 | 0.0012 |
| 647.0 | 32.5 | 0.0056 | 0.0156 | 0.0031 | 0.0016 | 0.0010 |
| 750.3 | 35.0 | 0.0049 | 0.0135 | 0.0027 | 0.0013 | 0.0009 |
| 861.3 | 37.5 | 0.0043 | 0.0117 | 0.0023 | 0.0012 | 0.0008 |
| 980.0 | 40.0 | 0.0038 | 0.0103 | 0.0021 | 0.0010 | 0.0007 |

Table B2 Pressure coefficients uncertainty for tests on the telescope model.

| | | Cp = | 0.10 | 0.50 | 1.00 | 1.50 |
|---|---|---|---|---|---|---|
| q, [Pa] | U, [m/s] | $U_q/q$ | $U_{Cp}/Cp$ | $U_{Cp}/Cp$ | $U_{Cp}/Cp$ | $U_{Cp}/Cp$ |
| 39.2 | 8.0 | 0.0923 | 0.2960 | 0.1913 | 0.1864 | 0.1854 |
| 61.3 | 10.0 | 0.0591 | 0.1878 | 0.1224 | 0.1193 | 0.1187 |
| 95.7 | 12.5 | 0.0378 | 0.1198 | 0.0784 | 0.0763 | 0.0760 |
| 110.0 | 13.4 | 0.0329 | 0.1042 | 0.0682 | 0.0664 | 0.0661 |
| 137.8 | 15.0 | 0.0263 | 0.0831 | 0.0544 | 0.0530 | 0.0528 |
| 187.6 | 17.5 | 0.0193 | 0.0611 | 0.0400 | 0.0390 | 0.0388 |
| 245.0 | 20.0 | 0.0148 | 0.0467 | 0.0306 | 0.0299 | 0.0297 |
| 310.1 | 22.5 | 0.0117 | 0.0369 | 0.0242 | 0.0236 | 0.0235 |
| 382.8 | 25.0 | 0.0095 | 0.0299 | 0.0196 | 0.0191 | 0.0190 |
| 463.2 | 27.5 | 0.0078 | 0.0248 | 0.0163 | 0.0158 | 0.0158 |
| 551.3 | 30.0 | 0.0066 | 0.0208 | 0.0137 | 0.0133 | 0.0133 |
| 647.0 | 32.5 | 0.0056 | 0.0177 | 0.0117 | 0.0114 | 0.0113 |
| 750.3 | 35.0 | 0.0056 | 0.0177 | 0.0117 | 0.0098 | 0.0098 |
| 861.3 | 37.5 | 0.0043 | 0.0134 | 0.0088 | 0.0086 | 0.0085 |
| 980.0 | 40.0 | 0.0038 | 0.0118 | 0.0078 | 0.0076 | 0.0075 |

# REFERENCES

Achenbach, E., (1974). Vortex shedding from spheres, J. Fluid Mechanics, 62:2, 209-221.

Ahmed, N., Rao, K.R., (1975). Orthogonal Transforms for Digital Signal Processing, Springer-Verlag, New York.

Amandolèse, X., Crémona, C., (2005). Analysing fluid loadings on moving bluff bodies using proper orthogonal decomposition, Journal of Fluids and Structures, 20, 577–587.

Armitt, J., (1968). Eigenvector analysis of pressure fluctuations on the West Burton instrumented cooling tower, Central Electricity Research Laboratories-UK, Internal Report RD/L/N 114/68.

Arndt, R.E.A., Long, D.F., Glauser, M.N., (1997). The proper orthogonal decomposition of pressure fluctuations surrounding a turbulent jet, J. of Fluid Mechanics, 340, 1-33.

ASCE/SEI 7-05, (2005). Minimum Design Loads for Buildings and Other Structures, American Society of Civil Engineers.

Asmolov, E.S., (2001). Flow past a sphere undergoing unsteady rectilinear motion and unsteady drag at small Reynolds number, J. Fluid Mechanics, 446, 95-119.

Aubry, N., Holmes, P., Lumley, J.L., Stone, E., (1988). The dynamics of coherent structures in the wall region of turbulent boundary layer, J. Fluid Mech., 192, 115-173.

Baker, C.J., (1999). Aspects of the use of the technique of orthogonal decomposition of surface pressure fields, Wind Engineering into the 21st Century, 393-399.

Banks, D., Meroney, R.N., Sarkar, P.P., Zhao, Z., Wu, F., (2000). Flow visualization of conical vortices on flat roofs with simultaneous surface pressure measurement, J. Wind Eng. Ind. Aerodyn., 84:6, 5-85.

Baskaran, A., Savage, M.G., (2003). Wind pressure measurements on full scale flat roofs, J. of the Roof Consultants Institute, 21:4, 17-21.

Bearman, P.W., (1984). Vortex shedding from oscillating bluff bodies, Annual Reviews on Fluid Mechanics, 16, 195-222.

Berger, E., Wille,R., (1972). Periodic flow phenomena, Annual Reviews on Fluid Mechanics, 16, 313-340.

Berkooz, G., Holmes, P., Lumley, J.L., (1993). The Proper Orthogonal Decomposition in the Analysis of Turbulent Flows, Annual Review Fluid Mechanics, 25, 539-575.

Best, R.J., Holmes, J.D., (1983). Use of eigenvalues in the covariance integration method for determination of wind load effects, J. Wind Eng. Ind. Aerodyn., 13, 359-370.

Bienkiewicz, B., Ham, H.J., Sun, Y., (1993). Proper orthogonal decomposition of roof pressure, J. Wind Eng. Ind. Aerodyn., 50, 193-202.

Bienkiewicz, B., Tamura, Y., Ham, H.J., Ueda, H., Hibi,K., (1995). Proper orthogonal decomposition and reconstruction of multi-channel roof pressure, J. Wind Eng. Ind. Aerodyn., 54:55, 369-381.

Bienkiewicz, B., (1996). New tools in wind engineering, J. Wind Eng. Ind. Aerodyn., 65, 279-300.

Carassale, L., Tubino, F., Solari,G., (2000). Seismic response of multi-supported structures by proper orthogonal decomposition, Proc. Int. Conf. on Advances in Structural Dynamics.

Carassale, L., Piccardo, G., Solari, G., (2001). Double modal transformations and wind engineering applications, J. Engineering Mechanics, 432-439.

Carassale, L., Solari, G., (2002). Wind modes for structural dynamics: a continuous approach, Probabilistic Engineering Mechanics, 17, 157-166.

Chatterjee, A., (2000). An introduction to the proper orthogonal decomposition, Current Science, 78:7, 808-817.

Chen, X., Kareem, A., (2005). Proper Orthogonal Decomposition-Based Modeling: Analysis and Simulation of Dynamic Wind Load Effects on Structures, Journal of Engineering Mechanics, 131:4, 325-339.

Chen, L., Letchford, C.W., (2005). Proper orthogonal decomposition of two vertical profiles of full-scale nonstationary downburst wind speeds [lzcl], J. Wind Eng. Ind. Aerodyn., 93, 187-216.

Cohen, K., Siegel, S., Wetlesen, D., Cameron, J., Sick, A., (2004). Effective Sensor Placements for the Estimation of Proper Orthogonal Decomposition Mode Coefficients in von Karman Vortex Street, J. Vibration and Control, 1857-1880.

Cooper, K.R., Farrell, I., Leclerc, G., Franchi, G., Vezzaro, N., Fitzsimmons, J., (2004). A Wind Tunnel Test on the HIA Very Large Optical Telescope: Phase 0 – Mean and Unsteady Pressure Measurements, Report, National Research Council Canada.

Cosentino, N., Benedetti, A., (2005). Use of orthogonal decomposition tools in analyzing wind effects on structures, Structural Engineering International, 4, 264-270.

Cremona, C., Amandolèse, X., Grillaud, G., Flammand, O., (2002). Simulation numérique des écoulements autour de tabliers de pont, Revue Française de Génie Civil, Volume X – n° X ,1-27.

Davenport, A.G., (1961). The application of statistical concepts to the wind loading of structures, Proceedings of the Institution of Civil Engineers, 19, 449-471.

Davenport, A.G., (1964). Note on the distribution of the largest value of a random function with application to gust loading, Proceedings of the Institution of Civil Engineers, 28, 187-196.

Davenport, A.G., (1967). Gust Loading Factors, Journal of the Structural Division- Proceedings ASCE, 93, 11-34.

Davenport, A.G., (1975). Perspectives on the full-scale measurement of wind effects, J. Wind Eng. Ind. Aerodyn., 1, 23-54.

Davenport, A.G, (1995). How can we simplify and generalize wind loads?, J. Wind Eng. Ind. Aerodyn., 54:55, 657-669.

Davenport, A.G., (2002). Past, present and future of wind engineering, J. Wind Eng. Ind. Aerodyn., 90, 1371-1380.

Delaunay, D., Lakehal, D., Pierrat, D., (1995). Numerical approach for wind loads prediction on buildings and structures, J. Wind Eng. Ind. Aerodyn., 57, 307-321.

Del-Ville, J., Ukeiley, L., Cordier, L., Bonnet, J.P., Glauser, M., (1999). Examination of large-scale structures in a turbulent plane mixing layer: Part 1. Proper orthogonal decomposition, J. of Fluid Mechanics, 391, 91-122.

Devijver, P.A., Kittler, J., (1982). Pattern Recognition: A Statistical Approach, Prentice-Hall-Englewood Cliffs, New Jersey.

Eaton, K.J., (1974). Characteristics of atmospheric turbulence near the ground-Part I, Engineering Science Data Unit, Item 74030.

Eaton, K.J., (1975). Characteristics of atmospheric turbulence near the ground. Part-III, Engineering Science Data Unit, Item 75001.

Feeny, B.F., (1998). On the physical interpretation of proper orthogonal modes in vibrations, J. of Sound and Vibration, 211, 607-616.

Flay, R.G.J., Vickery, B.J., (1995). Pressure correlations on a rough cone in turbulent shear flow , J. Wind Eng. Ind. Aerodyn., 58, 1-18.

Flores-Vera, R., (2003). Respuesta no-lineal de cubiertas colgantes ante la acción del viento, Master's thesis, National Autonomous University of Mexico, Mexico City.

Flores-Vera, R., Larose, G.L., Tanaka, H., (2008). The use of the proper orthogonal decomposition for simultaneously analyzing the pressure fields on two structures, Proceedings VI International Colloquium on Bluff Body Aerodynamics and Applications. Milano, Italy.

Fu, J., Xie, Z., Li, Q.S., (2008). Equivalent static wind loads on long-span roof structures, J. of Structural Engineering, 1115-1127.

Georgiou, I.T., Schwartz, I.B., (1999). Dynamics of large scale structural/dynamical systems: a singular perturbation/proper orthogonal decomposition approach, J. Appl. Math. SIAM, 59, 1178-1207.

Glezer, A., Kadioglu, Z., Pearlstain, A.J., (1989). Development of an extended proper orthogonal decomposition and its application to a time periodically forced plane mixing layer, Physics of Fluids A, 1:8, 1363-1373.

Han, S., Fenny,B., (2002). Enhanced proper orthogonal decomposition for the modal analysis of homogeneous structures, J. Vibration and Control, 8, 19-40.

Han, S., Fenny, B., (2003). Application of proper orthogonal decomposition to structural vibration analysis, Mechanical Systems and Signal Processing, 17, 989-1001.

Hangan, H., Vickery, B.J., (1998). A spectral model for buffeting loading, J. Wind Eng. Ind. Aerodyn., 77:78, 135-145.

Hangan,H., Vickery,B.J., (1999). Buffeting of two-dimensional bluff bodies, J. Wind Eng. Ind. Aerodyn., 82, 173-187.

He, H., Ruan, D., Mehta, K.C., Gilliam, X., Wu, F., (2007). Nonparametric independent component analysis for detecting pressure fluctuation induced by roof corner vortex, J. Wind Eng. Ind. Aerodyn., 429-443.

Holmes, J.D., Best, R.J., (1981). An approach to the determination of wind load effects on low-rise buildings, J. Wind Eng. Ind. Aerodyn., 7, 273-287.

Holmes, J.D., (1988). Distribution of peak loads on a low-rise building, J. Wind Eng. Ind. Aerodyn., 29, 59-67.

Holmes, J.D., (1990). Analysis and synthesis of pressure fluctuations on bluff bodies using eigenvectors, J. Wind Eng. Ind. Aerodyn., 33, 2057-2073.

Holmes, J.D., (1992). Optimized Peak Load Distribution, J. Wind Eng. Ind. Aerodyn., 41:44, 267-276.

Holmes, P., Lumley, J.L., Berkooz, G., (1996). Turbulence: coherent structures, dynamical systems and symmetry, Cambridge University Press, Great Britain.

Holmes, J.D., Sankaran, R., Kwok, K.C.S., Syme, M.J., (1997). Eigenvector modes of fluctuating pressures on low-rise buildings models, J. Wind Eng. Ind. Aerodyn., 69:71, 697-707.

Holmes, J.D., (2002). Effective static load distributions in wind engineering, J. Wind Eng. Ind. Aerodyn., 90, 91-109.

Holmes, J.D., (2007). Wind loading of structures, Taylor and Francis Group.

Igarashi, T., Terachi, N., (2002). Drag reduction of flat plate normal to airstream by flow control using a rod, J. Wind Eng. Ind. Aerodyn., 90, 359-376.

Igarashi., T., (1997). Drag reduction of a square prism by flow control using a small rod, J. Wind Eng. Ind. Aerodyn., 69:71, 141-153.

Irwin, H.P.A.H., Cooper, K.R., (1980). Correction of distortion in fluctuating pressure measurements, National Research Council Canada Technical Report LTR-LA-222.

Jensen, M., (1958). The model law for phenomena in the natural wind, Ingenieörem-International Edition,2.

Jeong, S.H., Bienkiewicz, B., (1997). Application of autoregressive modeling in proper orthogonal decomposition of building wind pressure, J. Wind Eng. Ind. Aerodyn., 69:71, 685-695.

Jeong, S.H., Bienkiewicz, B., Ham, H.J., (2000). Proper orthogonal decomposition of building wind pressure specified at non-uniformly distributed pressure taps, J. Wind Eng. Ind. Aerodyn., 87, 1-14.

Johnson, T.A., Patel, V.C., (1999). Flow past a sphere up to a Reynolds number of 300, J. Fluid Mechanics, 378, 19-70.

Kareem, A., Cermak, J.E., (1984). Pressure fluctuations on a square building model in boundary-layer flows, J. Wind Eng. Ind. Aerodyn., 16, 17-41.

Kasperski, M., Niemann, H-J., (1992). The LRC (Load-response-correlation) method: a general method of estimating unfavourable wind load distributions for linear and nonlinear structural behaviour, J. Wind Eng. Ind. Aerodyn., 43, 1753–1763.

Khanduri, A.C., Stathopoulos, T., Bédard,C., (1998). Wind-induced interference effects on buildings-A review of the state-of-the-art, Engineering Structures, 20, 7, 617-630.

Kikuchi, H., Tamura, Y., Ueda, H., Hibi, K., (1997). Dynamic wind pressure acting on a tall building model-Proper orthogonal decomposition, J. Wind Eng. Ind. Aerodyn., 69:71, 631-646.

Kosambi, D.D., (1943). Statistics in function space, J. Indian Math. Soc., 7, 76-88.

Lajos, T., (1986). Drag reduction by the production of a separation bubble on the front of a bluff body, J. Wind Eng. Ind. Aerodyn., 22, 331-338.

Lawson, T.V., (1985). Characteristics of atmospheric turbulence near the ground-Part II, Engineering Science Data Unit, Item 85020.

Lee, B.E., (1975). The effect of turbulence on the surface pressure field of a square prism, J. of Fluid Mechanics , 69:2, 263-282.

Lesage, F., Gartshore, I.S., (1987), A method of reducing drag and fluctuating side force on bluff bodies, J. Wind Eng. Ind. Aerodyn., 25:2, 229-245.

Lim, H.C., Thomas, T.G., Castro, I.P., (2009). Flow around a cube in a turbulent boundary layer: LES and experiment, J. Wind Eng. Ind. Aerodyn.,in press.

Loeve, M., (1955). Probability Theory, Van Nostrand, New York.

Lorenz, E.N., (1959). Prospects for Statistical whether Forecasting, Final Report, Statistical Forecasting Project, MIT, Cambridge, Massachussets.

Lumley, J.L., (1967). The structure of inhomogeneous turbulent flows, Proc. Int. Coll. on the Fine Scale Structure of the Atmosphere and its Influence on Radio Wave Propagation, Moscow, 166-176.

Lumley, J.L., (1970). Stochastic Tools in Turbulence, Academic Press-New York.

Mayne J.R., Cook N.J., (1978). On design procedures for wind loading, Building Research Establishment, CP25/78.

Mayne J.R., (1979). The estimation of extreme winds, J. Wind Eng. Ind. Aerodynamics, 5:1, 109-137.

Moin, P., Moser, R.D., (1989). Characteristic-eddy decomposition of turbulence in a channel, J. Fluid Mech., 200, 471-509.

Murakami, S., Mochida, A., 1988, 3D numerical simulation of airflow around a cubic model by means of the k-ε model, J. Wind Eng. Ind. Aerodyn., 31, 283-303.

Murakami, S., Mochida, A., Hayashi, Y., Sakamoto, S., (1992). Numerical study on velocity-pressure field and wind forces for bluff bodies by k-ε, ASM and LES, J. Wind Eng. Ind. Aerodyn., 41:44, 2841-2852.

Murakami, S., Mochida, A., (1995). On turbulent vortex shedding flow past 2D square cylinder predicted by CFD, J. Wind Eng. Ind. Aerodyn., 54:55, 191-211.

Nakamura, H., Igarashi, T., (2008). Omnidirectional reductions in drag and fluctuating forces for a circular cylinder by attaching rings, J. Wind Eng. Ind. Aerodyn., 96, 887-899.

O'Donnell, B.J., Helenbrook, B.T., (2007). Proper orthogonal decomposition and incompressible flow: An application to particle modeling, J. Computers & Fluids, 36, 1174-1186.

Paterson, D., Apelt, C., (1990). Simulation of flow past a cube in a turbulent boundary layer, J. Wind Eng. Ind. Aerodyn., 35, 149-176.

Pettit, C.L., Beran, P.S., (2002). Application of proper orthogonal decomposition to the discrete Euler equations, International Journal for Numerical Methods in Engineering, 55, 479-497.

Piccardo, G., Solari, G., 2000, 3D wind-excited response of slender structures: closed-form solution, J. of Structural Engineering, 126:8, 936-943.

Prasad, A., Williamson, C.H.K., (1997). A method for the reduction of bluff body drag, J. Wind Eng. Ind. Aerodyn., 69:71, 155-167.

Rathinam, M., Petzold, L.R., (2003). A new look at proper orthogonal decomposition, J. Numerical Analysis, 41:5, 1893-1925.

Ricciardelli, F., De Grenet, E.T., Hangan, H., (2002a). Pressure distribution & aerodynamic forces and dynamic response of box bridge sections, J. Wind Eng. Ind. Aerodyn., 90, 1135-1150.

Ricciardelli, F., De Grenet, E.T., Solari, G., (2002b). Analysis of the wind loading of a bridge deck box section using Proper Orthogonal Decomposition, Proc. 3rd East European Conference on Wind Engineering.

Rocha, M.M, Cabral, S.V.S., Riera, J.D., (2000). A comparison of proper orthogonal decomposition and Monte Carlo simulation of wind pressure data, J. Wind Eng. Ind. Aerodyn., 84, 329-344.

Saathoff, P.J., Melbourne, W.H., (1997). Effects of free stream turbulence on surface fluctuations in a separation bubble, J. of Fluid Mechanics, 337, 1-24.

Saha, A.K., Muralidhar, K., Biswas, G., (2000). Experimental study of flow past a square cylinder at high Reynolds number, Experiments in Fluids, 29, 553-563.

Sakamoto, H., Saniu, H., (1990). A Study on Wortex Shedding From Spheres in a Uniform Flow, J. of Fluids Engineering, 112, 386-392.

Simiu, E., (1973). Logarithmic profiles and design wind speeds, J. of the Engineering Mechanics Division-ASCE, 99, 1073-1083.

Simiu, E., (1974). Wind spectra and dynamic alongwind response, J. of the Structural Division-ASCE, 100, 1897-1910.

Simiu, E., (1980). Revised procedure for estimating along-wind response, J. of the Structural Division-ASCE, 106:1, 1-10.

Simiu, E., Scanlan, R.H., (1996). Wind Effects on Structures, John Wiley & Sons Inc. Third Edition, p.217.

Solari, G., (1982). Alongwind Response Estimation: Closed Form Solution, J. of the Structural Division-ASCE, 108, 225-244.

Solari, G., (1983a). Alongwind Response Estimation: Structural Classification, J. of the Structural Division-ASCE , 109:2, 575-580.

Solari, G., (1983b). Design wind loads, J. Wind Eng. Ind. Aerodyn., 11, 345-358.

Solari, G., (1983c). Analytical estimation of the alongwind response of structures, J. Wind Eng. Ind. Aerodyn., 14, 467-47.

Solari, G., (1989). Wind response spectrum, J. of Engineering Mechanics, 115:9, 1363-1373.

Solari, G., (1993a). Gust buffeting I: Peak wind velocity and equivalent pressure, J. of Structural Engineering, 119:2, 365-382.

Solari, G., (1993b). Gust buffeting II: Dynamic alongwind response, J. of Structural Engineering, 119:2, 383-398.

Solari, G., Carassale, L., (2000). Modal transformation tools in structural dynamics and wind engineering, Wind & Structures, 3:4, 221-241.

Song, C., Park, S., (2009). Numerical simulation of flow past a square cylinder using Partially-Averaged Navier-Stokes model, J. Wind Eng. Ind. Aerodyn., 97, 37-47.

Stathopoulos, T., (1981). Wind pressure functions for flat roofs, J. of the Structural Mechanics Division-ASCE Proceedings, 107:5, 889-905.

Stathopoulos, T., (1984). Wind loads on low-rise buildings: a review of the state of the art, Engineering Structures, 6, 119-135.

Stathopoulos, T., (1997). Computational wind engineering: Past achievements and future challenges, J. Wind Eng. Ind. Aerodyn., 67:68, 509-532.

Stathopoulos, T., Marathe, R., Wu, H., (1999). Mean wind pressures on flat roof corners affected by parapets: field and wind tunnel studies, J. Engineering Structures, 21, 629-638.

Stathopoulos, T., (2003). Wind loads on low buildings: in the wake of Alan Davenport's contributions, J. Wind Eng. Ind. Aerodyn., 91, 1565-1585.

Sun, D., Owen, J.S., Wright, N.G., (2009). Application ofthe k–ω turbulence model for a wind-induced vibration study of 2D bluff bodies, J. Wind Eng. Ind. Aerodyn., in press.

Szepessy, S., Bearman, P.W., (1993). Analysis of a pressure averaging device for measuring aerodynamic forces on a circular cylinder, J. of Experiment in Fluids, 16, 120-128.

Tamura, Y., Ueda, H., Kikuchi, H., Hibi, K., Suganuma, S., Bienkiewicz, B., (1997). Proper orthogonal decomposition study of approach wind-building pressure correlation, J. Wind Eng. Ind. Aerodyn., 72, 421-431.

Tamura, T., (2008). Towards practical use of LES in wind engineering, J. Wind Eng. Ind. Aerodyn., 96, 1451-1471.

Tang, D., Kholodar, D., Juang, J., Dowell, E.H., (2001). System Identification and Proper Orthogonal Decomposition Method Applied to Unsteady Aerodynamics, J. American Institute of Aeronautics and Astronautics, 39:8, 1569-1576.

Tavoularis, S., (2005). Measurement in fluid mechanics, Cambridge University Press.

Tsutsui, T., Igarashi, T., (2002). Drag reduction of a circular cylinder in an air-stream, J. Wind Eng. Ind. Aerodyn., 90, 527-541.

Tubino, F., Solari, G., (2005). Double Proper Orthogonal Decomposition for Representing and Simulating Turbulence Fields, J. of Engineering Mechanics, 131:12, 1302-1312.

Tubino, F., Solari, G., (2007). Gust buffeting of long span bridges: Double Modal Transformation and effective turbulence, Engineering Structures, 29 , 1698-1707.

Ueda, H., Hibi, K., Tamura, Y., Fuji, K., (1994). Multi-channel simultaneous fluctuating pressure measurement system and its applications, J. Wind Eng. Ind. Aerodyn., 51, 93-104.

Uematsu, Y., Isyumov, N., (1999). Wind pressures acting on low-rise buildings, J. Wind Eng. Ind. Aerodyn., 82, 1-25.

Uematsu, Y., Stathopoulos, T., (2003). Wind loads on free-standing canopy roofs: A review, J. of Wind Engineering, 95, 245-256.

Vickery, B.J., (1966). Fluctuating lift and drag on a long cylinder of square cross-section in a smooth and in a turbulent stream, J. of Fluid Mechanics, 25:3, 481-494.

Wirsching, P.H., Paez, T.L., Ortiz, K., (1995). Random Vibrations, John Wiley & Sons, Inc., p 187.

Xu, Z., (2004). Experimental and analytical modelling of high intensity winds, The University of Western Ontario. Ph. D. thesis. Civil and Environmental Dept.

Yu, Da-hai, Kareem, A., (1997). Numerical simulation of flow around rectangular prism, J. Wind Eng. Ind. Aerodyn., 67:68, 195-208.

Zhou, Y., Kareem, A., Gu, M., (2000). Equivalent static buffeting loads on structures, J. of Structural Engineering, 126:8, 989-992.

Zhou, Y., Kareem, A., (2001). Gust loading factor: new model, J. of Structural Engineering, 127:2, 168-175.

Zhou, Y., Kijewski, T., Kareem, A., (2002). Along-Wind Load Effects on Tall Buildings: Comparative Study of Major International Codes and Standards, J. of Structural Engineering, 128:6, 788-796.

Zhou, Y., Kijewski, T., Kareem, A., (2003). Aerodynamic Loads on Tall Buildings: Interactive Database, J. of Structural Engineering, 129:3, 394-404.